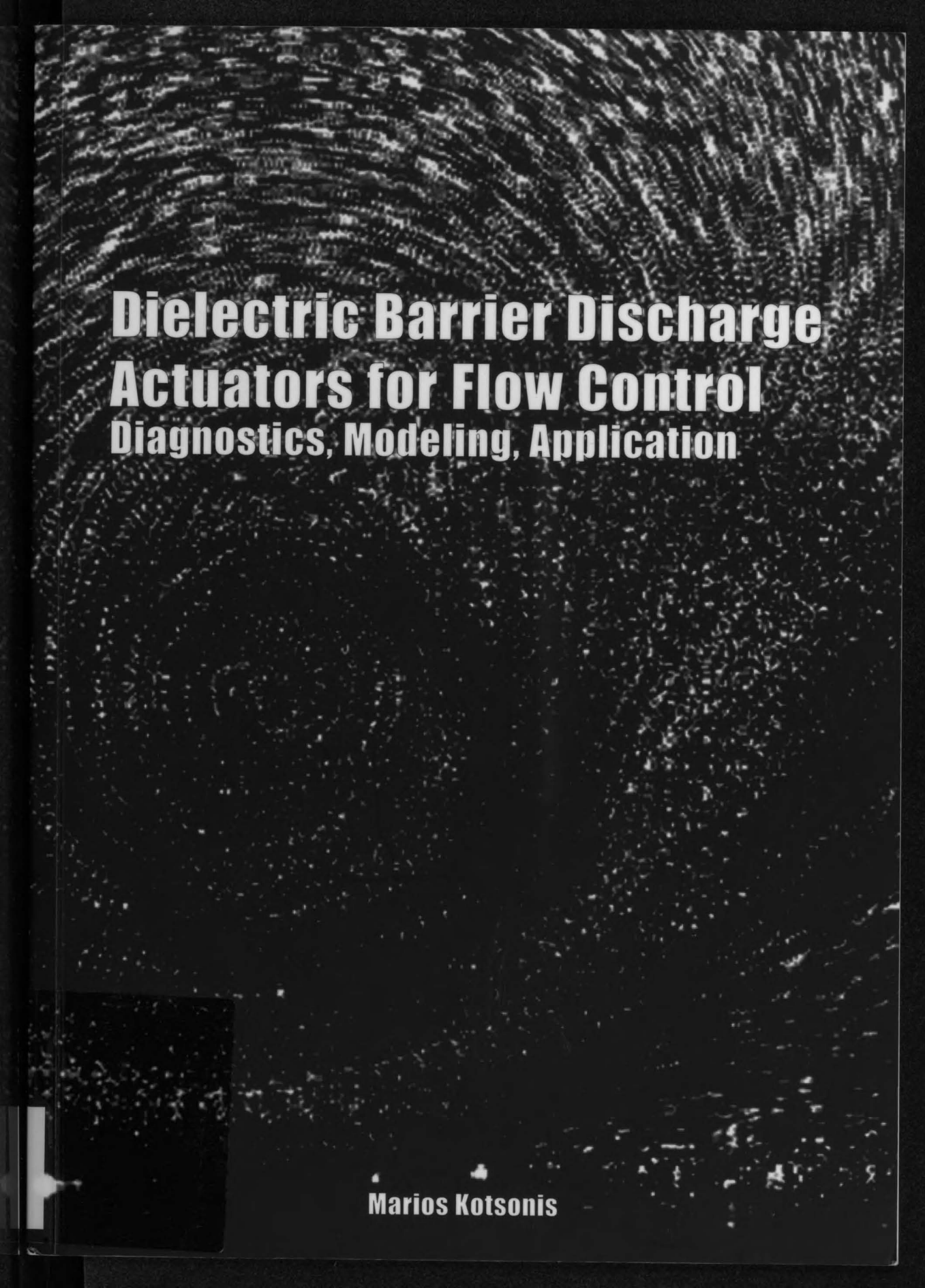
Dielectric Barrier Discharge
Actuators for Flow Control
Diagnostics, Modeling, Application
Marios Kotsonis

Dielectric Barrier Discharge Actuators for Flow Control

Diagnostics, Modeling, Application

Marios Kotsonis

Dielectric Barrier Discharge Actuators for Flow Control

Diagnostics, Modeling, Application

PROEFSCHRIFT

ter verkrijging van de graad van doctor
aan de Technische Universiteit Delft,
op gezag van de Rector Magnificus prof. ir. K.C.A.M. Luyben,
voorzitter van het College voor Promoties,
in het openbaar te verdedigen op dinsdag 13 maart 2012 om 12:30 uur

door

Marios KOTSONIS

Diploma of Mechanical and Aeronautical Engineering,
University of Patras, Greece
geboren te Nicosia, Cyprus.

Dit proefschrift is goedgekeurd door de promotor:

Prof. dr. F. Scarano

Copromotor:

dr. ir. L.L.M. Veldhuis

Samenstelling promotiecommissie:

Rector Magnificus	voorzitter
Prof. dr. F. Scarano	Technische Universiteit Delft, promotor
dr. ir. L.L.M. Veldhuis	Technische Universiteit Delft, copromotor
Prof. dr. ir. J.L. van Ingen	Technische Universiteit Delft
Prof. dr. J. Ekaterinaris	Universiteit Patras, Griekenland
Prof. dr. E. Moreau	Universiteit Poitiers, Frankrijk
Prof. Dr.-Ing. habil. C. Tropea	TU Darmstadt, Duitsland
dr. ir. D.R. van der Heul	Technische Universiteit Delft

This research has been conducted within the framework of the CleanEra project initiated by TU Delft.

ISBN/EAN: 978-94-6191-197-1

Cover design: Marios Kotsonis
Photography: Marios Kotsonis and Sina Ghaemi

Printed in the Netherlands

Summary

Dielectric Barrier Discharge Actuators for Flow Control

Diagnostics, Modeling, Application

The global warming problem is one of the most urgent issues of our time. The majority of modern technology development is now focused on more fuel efficient, green solutions. In the field of aviation an overwhelming effort is pursued for the development of aircraft which are operating with minimum gas emissions and consume less fuel. Specifically in the area of Aerodynamics the main focus turns towards methods for drag reduction. A promising approach involves active flow control using a new kind of actuation device called the Dielectric Barrier Discharge (DBD) or plasma actuator.

DBD actuators operate by ionizing the local area of surrounding air via intense electric field. The ionized gas (plasma) is then subject to electrostatic forces which respectively occur due to the electric field. Under the influence of these forces the ionized gas undergoes movement and, through collisions, transfers momentum to the surrounding neutral air. This momentum transfer results in the acceleration of the air which can be used as an efficient flow control mechanism. An efficient tool for visualizing and modeling the effect of the DBD actuator is a volume distributed body-force field.

This thesis attempts a multi-objective effort in the field of DBD actuators. Firstly, it is concerned with advanced diagnostics towards better understanding of the operational principles of DBDs. Secondly, an attempt on a new effi-

cient way of DBD modeling is performed. Lastly, the attained and developed knowledge is put to application within two distinct practical concepts.

The first part of this work involves the application of a wealth of experimental diagnostic techniques in order to establish a firm description of the operation of DBD actuators. Firstly, several parametric studies are conducted in quiescent air conditions. These aim at establishing correlating relations between geometric or electrical properties and the performance of the DBD. Secondly, studies in conditions of external flow are performed in which the actuator performs in steady and unsteady mode of operation. Last, a study of the spatio-temporal evolution of the DBD forcing mechanism is conducted. This reveals fundamental features of the forcing dynamics which shed light into one of the last controversial issues in DBD actuation.

The second part of the thesis is concerned with the modeling of DBD actuators. For this a novel technique is proposed for the experimental measurement of the body force field. The technique is based on the decomposition of the induced flowfield under quiescent conditions. The technique is formulated and applied for several cases of actuation and results are compared with existing techniques. Force field data are acquired which can efficiently be implemented in numerical flow solvers as models of DBD actuation. Additionally, an initial validation and verification effort of the new model is undertaken. Force distributions are inserted in a numerical flow solver framework and results are compared with experimental data. Moreover, the comparison is extended for cases of unsteady actuation.

The third and last part of the work involves two distinct concepts on application of the gathered knowledge on DBD actuators. The first concept is concerned with the implementation of the actuators in a numerical flow solver framework. The actuators operate within a transitional boundary layer with the final aim of active transition delay. More specifically, they directly attack instability modes via destructive interference, thereby delaying the laminar-turbulent transition process. Their operation is governed by an adaptive feed-forward control system. The second concept attempts to capitalize on the observations of the diagnostic study on the DBD forcing mechanisms. It involves the utilization of asymmetric High Voltage waveforms for the improvement of actuation in terms of strength and efficiency.

Samenvatting

Dielectric Barrier Discharge Actuatoren voor Stromingsbeheersing
Diagnostiek, Modellering, Toepassing

De opwarming van de Aarde is één van de meest urgente problemen van onze tijd. Veel nieuwe technologische ontwikkelingen richten zich daardoor op efficiëntere, groenere oplossingen. In de luchtvaart wordt hard gewerkt aan de ontwikkeling van vliegtuigen die zo min mogelijk schadelijke gassen uitstoten en tevens minder brandstof verbruiken. Binnen de Aerodynamica richt het onderzoek zich vooral op methoden om de luchtweerstand te verminderen. Een veelbelovende techniek maakt gebruik van een nieuw soort actuator voor het actief beïnvloeden van de luchtstroom: de Dielectric Barrier Discharge (DBD) of plasma actuator.

De werking van DBD actuatoren berust op het ioniseren van kleine hoeveelheden lucht met behulp van een sterk elektrisch veld. Dit elektrisch veld veroorzaakt elektrostatische krachten, die op hun beurt weer invloed uitoefenen op het geïoniseerde gas (het plasma). Onder invloed van deze krachten komt het gas in beweging en draagt het, door middel van botsingen, impuls over aan de omringende lucht. Deze impulsoverdracht resulteert in een versnelling van de lucht, waarmee de stroming op een efficiënte manier kan worden beïnvloed. Een goede manier om het effect van een DBD actuator op de luchtstroom te visualiseren en te modelleren is via een zogenaamd ruimtelijk verdeeld "lichaamskrachtveld".

In dit proefschrift wordt een uitgebreid onderzoek naar DBD actuatoren gepresenteerd. Allereerst wordt er getracht beter te begrijpen op welke principes de werking van DBD actuatoren berust. Vervolgens wordt gekeken hoe deze actuatoren het meest efficient kunnen worden gemodelleerd. Tenslotte wordt de verkregen kennis toegepast op twee verschillende praktische concepten.

In het eerste deel van dit proefschrift wordt een groot aantal (experimentele) diagnostische technieken beschreven, die gebruikt worden voor het vaststellen van de werking van DBD actuatoren. Eerst wordt een aantal experimenten uitgevoerd in stilstaande lucht. Het doel van deze experimenten is het vaststellen van de verbanden tussen de geometrische en elektrische eigenschappen en de prestaties van de DBD actuator. Vervolgens wordt een aantal testen gedaan in een externe luchtstroom, waarbij de actuator in stationaire en niet-stationaire modus opereert. Als laatste wordt een studie uitgevoerd naar het ruimte en tijd afhankelijke verloop van het DBD voortstuwingsmechanisme. Hieruit volgt een aantal fundamentele eigenschappen van de door de actuator beinvloede stromingsdynamica, die meer inzicht geven in één van de laatste controversiële kwesties rondom DBD actuatoren.

Het tweede deel van het proefschrift legt zich toe op het modelleren van DBD actuatoren. Hiervoor wordt een nieuwe techniek gebruikt voor het meten van het lichaamskrachtveld, die is gebaseerd op de splitsing van het tijdsgebonden, geïnduceerde stromingsveld en de stilstaande condities. De techniek wordt beschreven en toegepast op een aantal testcases, waarna de resultaten vergeleken worden met bestaande methodes. De gemeten krachtvelddata kunnen gebruikt worden ten behoeve van een model voor een DBD actuator, en zodoende efficiënt worden geïmplementeerd in een numerieke stromingsanalyse. Dit wordt ook gedaan ter validatie en verificatie van het nieuwe model. De krachtverdelingen worden ingevoerd in een numerieke stromingsanalyse en de resultaten worden vergeleken met experimentele data. Deze vergelijking wordt zowel voor een stationaire als een instationaire actuatie uitgevoerd.

Het derde en laatste deel van dit proefschrift gaat over twee verschillende concepten, waarin de verkregen kennis over DBD actuatoren wordt toegepast. Het eerste concept betreft met het implementeren van de actuatoren in een numerieke stromingsanalyse. De actuatoren opereren in het omslaggebied van de grenslaag, met als uiteindelijk doel om het omslagpunt actief naar achteren te verschuiven. In feite worden de instabileitsmodi aangevallen met behulp

van destructieve interferentie, waardoor het omslagpunt van laminaire naar turbulente stroming verschuift. De actuatie wordt gestuurd door een adaptief "feed forward" regelsysteem. Het tweede concept probeert de bevindingen van de diagnostische studie naar het DBD stuwmechanisme te gebruiken. Daarbij wordt gekeken hoe asymmetrische hoogspanningsgolfvormen kunnen worden gebruikt voor het verbeteren van de sterkte en efficiëntie van de aandrijving.

Contents

Acknowledgements

The three month period in which this thesis was put together has been one of the most interesting in the author's life. It started and ended with two motorcycle accidents (both the author's fault) in between which a difficult family moment made him reconsider some of his views on life. The thesis was partly written in Cyprus, The Netherlands, Poland as well as on international waters between Greece and Italy. It has been the end of a wonderful adventure and the start of another.

I would like to express my deepest acknowledgements to a group of individuals without which none of this work would be possible. Firstly I would like to thank my daily supervisor and colleague dr. Leo Veldhuis. His never ending enthusiasm, support and help was always exemplary for me. But he gave me an even greater gift. He provided me with the freedom to find my own way in research, to try my many crazy (and rarely successful) ideas. Never judgmental, always supportive, Leo, dank u wel!.

I would like to express my gratitude to Prof. Fulvio Scarano for his faith towards me and his support towards my work. The many discussions we had have been a source of inspiration and motivation. His enthusiasm for true science has been pleasantly contagious. I hope we can continue on this trail for years to come.

I would also like to express many thanks to colleagues from the department of Aerodynamics. Firstly to my good friend Sina Ghaemi. His expertise in PIV measurements was indispensable for the success of many of the experiments we performed. Secondly, to dr. Steve Hulshoff. His input in numerical simulation topics are greatly appreciated. Last, to the support staff from the Aerodynamic Laboratories for their assistance. Special thanks to Leo Molenwijk and Stefan Bernardy for their help during the months I spent making a mess at the Low Speed Lab.

A doctoral thesis is always the summation of individual pieces of work. As such I feel indebted to the MSc students which I had the privilege to supervise and work together with. Segments of their work can be found in one way or another in the pages of this book. Pieter Boon, Giovanni Nati, Giusseppe Correale, Rogier Giepman and Marcel Hennevelt have all been excellent researchers and colleagues.

Although part of the Aerodynamics group, during my four year PhD study I was also involved in a special group called CleanEra. The extraordinary individuals which I had the honor to share an office with have been a source of inspiration and great fun. I would like to thank all the current and past members of CleanEra, Marcel, Durk, Dipanjay, Chara, Arvind, Gustavo and Sonel.

I would also like to extent my deepest appreciation to my CleanEra colleagues and good friends Michiel Straathof and Hui Yu. Thank you guys for laughing at my bad jokes, arranging my conference trips, cooking me dumplings and putting up with my meditteranean deficiencies. I hope we keep placing entries on the wall of shame for years to come.

I believe CleanEra would not be the same without two special gentlemen. Firstly, Francois Geuskens thank you for being an endless source of joy and offensive remarks. You have made this an unforgettable adventure. Secondly I would like to thank the only true dreamer I have ever met. Ronald van Gent, thank you for keep challenging our cartesian minds.

Work is but a small part of life and many hours over the last four years have been spent with good friends far away from wind tunnels and high voltage amplifiers. I would like to thank my friends in Holland, Greece and Cyprus for being there for me. Special thanks to Pyrrhos, I hope we keep riding motorcycles and arguing over capitalism until we are too old and bored to do it. Thanks to my friends in Cyprus that have never made it boring. Special thanks to Yiannos for calling me at 1 o'clock in the morning from the pub in Nicosia while I'm stranded home in rainy Delft.

Last but not least I would like to thank my family. Andreas, Chrystalla and Natasa it is extremely difficult to express what you mean to me in words. Thank you for giving me what I was never able to give you back.

Nicosia and Delft,
first days of 2012

Había aprendido sin esfuerzo el inglés, el francés, el portugués, el latín. Sospecho, sin embargo, que no era muy capaz de pensar. Pensar es olvidar diferencias, es generalizar, abstraer. En el abarrotado mundo de Funes no había sino detalles, casi inmediatos.

Jorge Luis Borges, *Funes el Memorioso*

O coraçaõ, se pudesse pensar, pararia.

Fernando Pessoa, *Do Livro do Desassossego*

Στην οικογένειά μου και στους φίλους μου.

Without effort, he had learned English, French, Portuguese, Latin. I suspect, nevertheless, that he was not very capable of thought. To think is to forget a difference, to generalize, to abstract. In the overly replete world of Funes there were nothing but details, almost contiguous details.

Jorge Luis Borges, *Funes the Memorious*

Could it think, the heart would stop beating.

Fernando Pessoa, *The Book of Disquiet*

To my family and to my friends.

Prologue

Η αρχή είναι το ήμισυ του παντός.

Πυθαγόρας ο Σάμιος

The beginning is half of everything.

Pythagoras of Samos

Chapter 1

Introduction

This research work attempts to address several fundamental questions on Dielectric Barrier (DBD) actuators. Nevertheless, the overall context within which Dielectric Barrier Discharge actuators are examined is the one of Drag Reduction and more specifically Active Flow Control. This introductory chapter attempts to give a brief overview of these concepts. Additionally, a brief setup of the research goals of the present work is presented along with a general outline of the thesis.

1.1 Towards drag reduction using active flow control

1.1.1 A greener future

One of the emerging problems of our Era is the immense influence human activity has on the global environment. The exponentially growing worldwide economic and social development which is based on an energy driven system is putting global environment dynamics under stress and misbalance. This is further enhanced with the increase of world population, and the improvement of living and social conditions in developing countries.

Due to these reasons, addressing pollution factors has become a necessity in most areas of technology development. In the specific field of aviation, the ef-

forts for more efficient and *green* aircraft has been the major point of research in the last decades. It can be expected that the search for partial or even full elimination of greenhouse gases emissions from aircraft will continue to be the driving force behind current and future research and development efforts. The latter are focused on several aspects of the modern aircraft such as propulsion system, aerodynamic performance, structural weight and operations management. The field of aerodynamic performance is of special interest where a seemingly never ending quest for aerodynamic drag reduction in all aspects dominates the research field. A short description of these efforts is given in the next section.

1.1.2 Aerodynamic drag reduction

The field of aerodynamic drag reduction is vast. Here a brief description of previous efforts is attempted. For more complete overview the reader is directed to the excellent review paper by Bushnell [24] and references within. Aerodynamic drag can be separated into several components based on definition. A common segregation is based on the expression of pressure or form drag, drag due to lift or induced drag, shock wave drag and viscous or friction drag.

All components of drag, as defined above, have been subject to extensive research over the past 50 years. Viscous drag is of special interest in this case since it presents the ideal platform for DBD-based flow control. Viscous drag reduction occupies an extensive area in the research field due to the multitude of proposed solutions. The earliest efforts involved careful shaping of the airfoils and wings in order to achieve favorable pressure gradients which consequently delayed transition. In combination with manufacturing techniques enabling smooth wing surface the collected efforts were placed under the general umbrella of Natural Laminar Flow (NLF) [26, 131, 107]. Later, distributed suction was employed in a hybrid passive (pressure gradient) and active (suction) flow control approach which was named Laminar Flow Control (LFC) [136, 13, 8]. Large gains in drag reduction have been gained using LFC although the practical implementation of many of the proposed solutions was hindered by issues of maintainability, robustness and cost effectiveness. Additionally to extension of the laminar region, Turbulent Drag Reduction (TDR) has also received extensive research effort [34, 44] . Large reduction was achieved using passive skin shaping means such as longitudinal riblets.

Again issues of reliability, maintainability and cost restricted these solutions to mere laboratory exercises.

1.1.3 Active flow control for skin friction drag reduction

The advancement of passive flow control technology has had two major effects on the development of aircraft. Firstly, the last generation of airliners (Boeing 787, Airbus A350) are by far more fuel efficient, environmentally friendly and quiet than the respective first generation jets (Boeing 707). Secondly, it is clear that the next step change in efficiency, and sustainability can only be achieved by active means. In aerodynamics, this automatically translates to applications of Active Flow Control.

In this section a brief description of selected active flow techniques is given. These are restricted to friction drag reduction concepts. For a more complete discussion on general active flow control techniques can be found in [44]. Viscous or friction drag can be separated in two sub-categories related to the state of the developed boundary layer. More specifically there can be drag due to a laminar or turbulent boundary layer with the latter being one order of magnitude larger than the former in cruising Reynolds numbers [118]. In this sense, the first option for skin friction drag reduction is the forced extension of the laminar flow and the simultaneous reduction of turbulent flow. This is typically achieved with the delay of the laminar-turbulent transition.

Laminar-turbulent transition delay

Laminar - turbulent transition delay has been in the research spotlight for several decades due to the large potential it presents for drag reduction. Typically transition occurs due to the amplification of disturbances which enter the laminar boundary layer through a receptivity process [25, 135, 23]. These instability mechanisms pass from an initially linear to a non-linear regime and eventually break down to chaotic motion and thus turbulence [48]. Therefore, successful transition delay comes down to the forced cancellation or damping of the propagating modes. Two distinct approaches for the dampening of transition inducing instability modes exist. These are the manipulation of the mean boundary layer profile and the targeted phase-locked manipulation of the instability modes themselves.

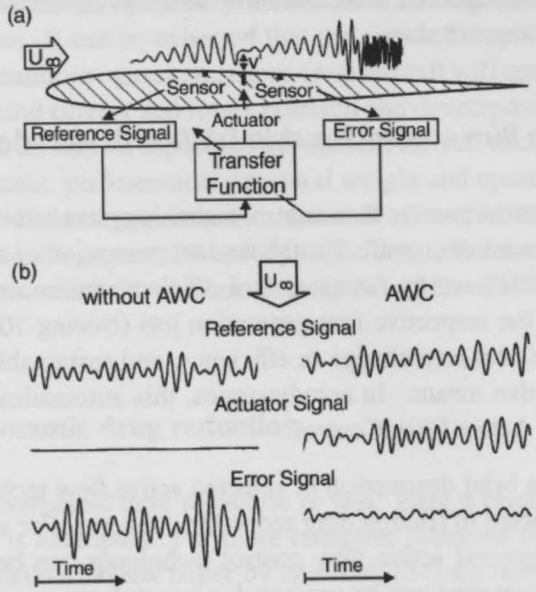

Figure 1.1: Concept of active TS wave control for transition delay (taken from [128]).

The previously mentioned LFC concept is the main representative of the mean flow manipulation approach. After the initial identification of the instability regime several LFC approaches can be explored. Especially in the flow regime typical of subsonic airliners, dominant modes involve the TS waves alongside the crossflow instability. Several extensive and successful LFC flight experiments have been conducted in the USA and in Europe [29, 89, 139, 90, 53]. In prominent position are the experiments conducted by NASA using the Jetstar suction leading edge, which showed successful results in simulated airline service, for a multidude of flight and weather conditions.

The second approach towards transition delay is the direct and phase-locked manipulation of instability modes using active unsteady actuation [132] as demonstrated in Fig.1.1. Chapter 9 of the current thesis is concerned with such concept. The extremely small energy content of the individual instability modes renders such an approach very attractive in terms of actuator power consumption. This is especially interesting in the case of DBD actuator due to their limited momentum input. Several numerical [21, 6, 77] and experimental [133, 100, 128] efforts have been published on direct wave cancellation,

especially focusing on the TS waves due to the simplicity of the test case. In general the basic approach provides positive and promising results, both experimentally and computationally.

Turbulent drag reduction

The second major trend in skin friction drag reduction is the direct attack of the turbulent drag production. The techniques involved are categorized under the umbrella name of Turbulent Drag Reduction (TDR). Following the definitions of Bushnell [24] three approaches to active control of wall turbulence can be defined based on the level of interaction between actuation and turbulent structures. These are respectively steady state, dynamic but not phase locked and dynamic phase-locked approach.

The most obvious and viable steady state approach is the use of massive suction to relaminarize the boundary layer by pulling all of the turbulent flow into the aerodynamic body [103]. A second possibility for active, but not dynamic, TDR methods is the use of combinations of pressure and wall temperature gradients which damp turbulence via baroclinic torque effects.

The second approach to TDR is dynamic but not phase locked techniques. These include oscillatory transverse wall motion [67, 5, 81] and dynamic slot injection [125] with reported drag reduction in the order of 24-45 % in air. A very interesting possibility is opened here for the utilization of DBD actuators as will be shown in Chapter 2.

The third approach for TDR is the dynamic, phase-locked, control of turbulence structure [96, 143, 27] which is approximately analogous to the the instability wave cancellation for transition delay approach discussed earlier. Research thus far has established theoretical feasibility for such an approach and work has been demonstrated on physical actuator development. Again DBD actuators appear to offer a viable alternative to existing actuator concepts for this kind of TDR approaches.

1.2 Thesis aim and objectives

The aim of this thesis is multi-dimensional. Initially an effort is undertaken towards the better understanding of the working principles of the DBD actuator and their capabilities for unsteady actuation common in active flow control with focus on skin friction drag reduction. Additionally this thesis aims at providing a new body force model which, although phenomenological, has the accuracy of numerical first-principles models at a fraction of the cost in time and effort. Last, the work aims at demonstrating the application of the gained knowledge through two concepts. One involves a numerical study on flow control for transition delay while the other offers an approach for the improvement of performance of DBD actuators.

The work is executed following a three step approach corresponding to experimental diagnostics and description of operation, modeling and application. The work in this thesis combines experimental, numerical and theoretical parts. Here the individual objectives are summarized.

- The first objective of this thesis is based on a circumstantial need rather than a scientific question. The current research represents the first effort of TU Delft in the area of plasma actuators. As such, experience with the device and operating procedures was essential before actual original research could be initiated. In this manner the fist objective is to experimentally explore the operation of the actuators in continuous and pulse mode. This is mainly done in quiescent flow using a variety of time resolved or averaged diagnostics.

- Moving towards more original research the second objective of the thesis is the investigation of the pulse mode of operation in quiescent and external flow. Pulse mode refers to unsteady actuation where the actuator is turned rapidly on and off with specific frequencies and duty cycles. The interaction of the actuator with the surrounding fluid in this case has received little attention from the research community although this kind of actuation is fundamental in active flow control. The description of an operational envelope in which the actuator can effectively operate is attempted.

- The last objective in terms of diagnostics involves a high risk and respectively high value attempt to gain insight into one of the most debated and interesting phenomena in DBD actuation. This is the forc-

ing mechanisms within the High Voltage (HV) cycle. As mentioned in the previous sections, it is well established that the forcing which the plasma region exerts on the neutral fluid is unsteady and periodic during the HV cycle. What has been controversial is the actual description of the forcing and how this is related with the HV signal. An experimental campaign is set up toward this goal.

- The next objective involves the modeling of the force field of the actuator. Again this is attempted using a novel technique which increases risk considerably. The technique is purely experimental and it attempts to combine the accuracy of first principles numerical models with the robustness and speed of phenomenological models. More specifically, the objective involves the experimental measurement of the produced body force vector field due to plasma. Additionally, a verification and validation effort of the new model is attempted using a typical numerical solver.

- The application part of this work is separated in two objectives. In general it involves the application of the knowledge which has been gained through the diagnostics and modeling part of the present work. The first concept is addressed numerically. This work involves a flow control scenario in which the plasma actuator operates in pulse mode. More specifically the case involves the active cancellation of TS waves using plasma actuators. Knowledge gathered on the pulse operation of the DBD, along with the body force model are used in conjunction with an automatic control system.

- The second concept, and last objective, departs slightly from the general goal of the thesis. Based on the knowledge gathered on the forcing mechanisms of the DBD, an experimental effort is attempted in order to improve the performance of the actuator. This is done in terms of forcing magnitude as well as power consumption. This objective is set based on the ever increasing needs for stronger, more efficient DBD actuators which would be able to have substantial effects on high Reynolds number flows.

1.3 Thesis outline

Chapter 3 involves a description of the methodology used throughout the thesis work. More specifically, description of the used experimental techniques such as Hot Wire Anemometry (HWA) and Particle Image Velocimetry (PIV) is given regarding basic principles and implementation issues. Additionally, the Proper Orthogonal Decomposition (POD) technique used for data analysis is described. Regarding the numerical techniques a brief overview of the basic theory of Finite Volume (FV) methods is given, followed by a description of the reduced Navier-Stokes (NS) solver which was developed for the purposes of this work. Finally, a theoretical description of the filtered-x LMS control algorithm which is used in Chapter 9 is given.

Chapter 4 presents the experimental effort and diagnostics on the DBD operation in quiescent flow conditions. A description of the experimental setup is given followed by a presentation of results of four separate parametric studies.

Chapter 5 is concerned with the operation of the actuator in conditions of external flow. Special emphasis is given on the pulse mode of operation. Following the description of the experimental setup, discussion on the results in both quiescent and laminar boundary layer external flows is attempted.

Chapter 6 attempts an experimental investigation into the spatio-temporally resolved forcing behavior of the actuator. In order to enhance the observability of the underlying mechanisms, four High Voltage (HV) waveform shapes are tested. A description of the experimental setup as well as the phase shifting technique which is employed is given. Finally results on the four tested waveforms are presented and discussed.

Chapter 7 gives a description on the experimental measurement of the plasma produced force field. Description of the theoretical background of the proposed force estimation techniques is followed by a presentation of the experimental setup. Discussion on the results in terms of body force, thrust, power and efficiency is presented.

Chapter 8 is dealing with the validation of the developed force model from Chapter 7. This involves the implementation of the measured force field in a numerical solver and the comparison of the results with experimental data. A description of the numerical framework is provided followed by a discussion

on the results for both cases of continuous and pulse operation.

Chapter 9 presents the numerical investigation of an active flow control concept involving the use of DBD actuators for the cancellation of Tollmien-Schlichting (TS) waves. The actuators are modeled using the force model described in Chapters 7 and 8. A description of the methodology is presented followed by the presentation of the results in several simulation cases.

Chapter 10 is concerned with an experimental study aimed at the improvement of performance of plasma actuators. This is attempted using asymmetric HV waveforms based on the results of Chapter 6. A description of the experimental setup and methodology is followed by discussion on results.

Finally, Chapter 11 gives a summary of the major conclusions derived from the present work. Additionally a list of recommendations for future research on several issues regarding DBD actuators, flow control and drag reduction is presented.

Chapter 2

Principles of Dielectric Barrier Discharge Actuators

A general review on theoretical, experimental, numerical and application issues concerning DBD actuators is attempted here. Since this subject has become immensely popular during the last 10 years, the existing bibliography is vast. As such it is not possible to fully cover the subject in the limited pages of this work. The interested reader is referenced to the excellent reviews in plasma actuators recently published [32, 94, 33, 61]

2.1 Working principles of barrier discharges

2.1.1 Physical background

The term plasma was introduced in 1928 by Langmuir [84] to describe a region of gas discharge in charge equilibrium. This effectively translates into an approximately equal number of positively and negatively charged species within the plasma region. Over the years the definition has been broadened to that of a system of particles whose collective behavior is characterized by long-range Coulomb interactions. In the specific case of air discharge the fluids under question consist of multiple charged species such as electron, posi-

tive ions, negative ions etc. A major property of air discharges is their collisional character. As will be shown later this property has a profound effect on the momentum transfer processes associated with plasma actuation.

For the so-called *cold plasma discharges* an electric filed of sufficient amplitude is applied to a volume of gas. Under the extreme forces developed in atomic level, ion-electron pairs are formed [78, 79, 88, 109]. A typical arrangement for creating a self-sustained gas discharge at low pressures of a few torr or less has been two separated facing metallic electrodes. Such a configuration is widely used in industry albeit for different reasons than DBD actuators.

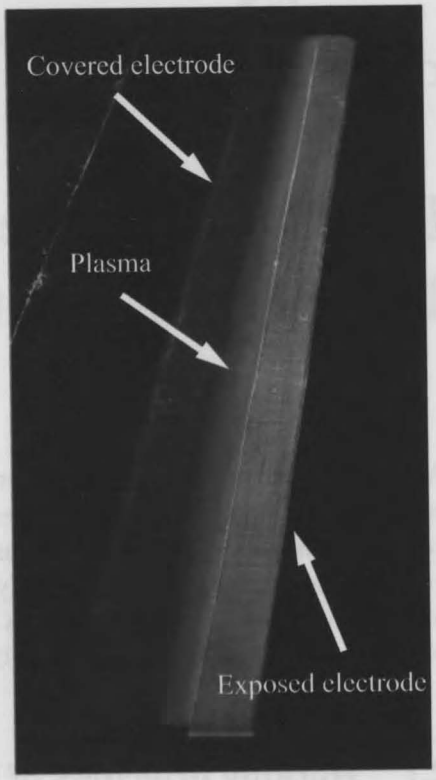

Figure 2.1: Photograph of the DBD actuator during operation (adapted from [19])

The strong electric field is formed by applying high voltage difference between the electrodes which can be direct (DC) or alternating (AC). For given ambient conditions such as pressure, temperature and chemical consistency of the neutral gas, a breakdown electric field value exists which is surpassed by the local applied electric field plasma is formed as shown in Fig.2.1 [78, 79, 88, 109]. In contrast to neutral air, the plasma bulk is consisted of numerous free electrons which have a strong effect on the gas conductivity. As a consequence there is a current, I, which flows between the electrodes. Especially in the case of DBD actuators diagnostic, the instantaneous value of the current I is invaluable to decipher the underlying discharge behavior. This is demonstrated in a range of experimental studies as well as well as in the present work.

Barrier discharges can be initiated and sustained in a large variety of regimes such as diffusive, filamentary, microdischarge etc. A review of the various discharge regimes, modes and associated terminology can be found in [72]. Nevertheless, all barrier discharges share one main feature i.e. one of the electrodes is covered with a dielectric barrier (insulator).

Okazaki and coworkers were among the first to use barrier discharge approach [69, 68, 70, 74, 98, 144]. In the case of the existence of the dielectric layer the utilization of an AC electric field is necessary. Dielectric Barrier discharges have been operated mainly in the microdischarge regime [36, 73]. In this regime, the discharge consists of a number of consecutive filamentary microdischarges (streamers), each of which has a limited lifetime. The passage of the streamer across the gap between the exposed electrode and the dielectric layer locally charges this capacitance, reverses the local field and self terminates. It is due to the self-terminating nature of the discharge that the AC electric field is necessary to sustain barrier discharges over macroscopic time periods.

2.1.2 The asymmetric barrier discharge

The typical configuration for the DBD actuator is highly asymmetric in the placement of the metallic electrodes (Fig.2.2). This in turn creates a strong asymmetry of the discharge between the two half-cycles of the AC actuation. For the entirety of this work the first half of the AC cycle where the exposed electrode is negative shall be denoted as the *forward stroke* while the second half where the exposed electrode is positive shall be denoted as the *backward stroke*. During the *forward stroke* electrons are emitted from the exposed electrode and travel towards the dielectric surface. At the same time charged species of air such as positive ions (O^+, N^+) and negative ions (O^-) are formed through ionization and attachment processes. The negative species move towards the dielectric while the positive species move towards the exposed electrode. Similar processes occur during the *backward stroke* with the direction of the movement of the charged species reversed due to the voltage reversal.

Due to the asymmetry of the discharge between the two half cycles, the ion-neutral momentum coupling is also asymmetric. This point is of fundamental importance to the understanding of the DBD forcing mechanisms and has been

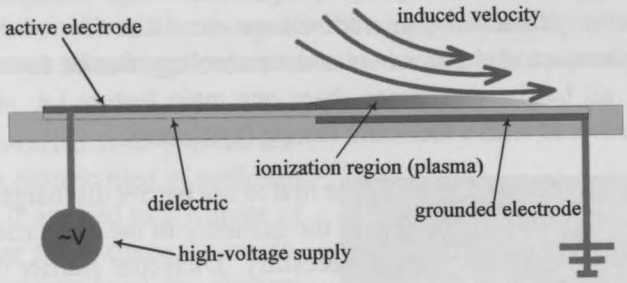

Figure 2.2: Schematic of the DBD plasma actuator (not to scale)

controversial in the past. More discussion on the momentum coupling mechanisms is given in following sections. However, it is widely acknowledged that it is due to this momentum coupling that the actuators induce tangential to the wall velocities. Additionally it has been found that a convenient way of understanding and simulating the effect is via a volume distributed body force acting on the surrounding fluid. A hallmark feature of DBD actuators is that the body force field and hence the induced velocity is always directed from the exposed electrode towards the covered electrode.

2.2 Experimental diagnostics on DBD actuators

The birth of the conventional DBD aerodynamic actuator is placed in the middle of the nineties when the group of Roth developed and patented the so called *One Atmosphere Uniform Glow Discharge Plasma* [114, 110]. This has been the most conventionally used configuration since with the two asymmetric metallic electrodes separated by a dielectric layer. Fig.2.3 shows the original configurations used by Roth.

The actuator, as operated by Roth, is typically composed of two planar electrodes which are flush-mounted on the aerodynamic surface. They are separated by a dielectric layer made of strong insulating material. Usually the exposed electrode is excited by an AC high voltage while the covered electrode is kept at ground potential. Just as in a conventional barrier discharge, above the breakdown threshold voltage V_0, a plasma sheet appears on both sides of the dielectric, resulting in an induced air velocity (electric wind) on

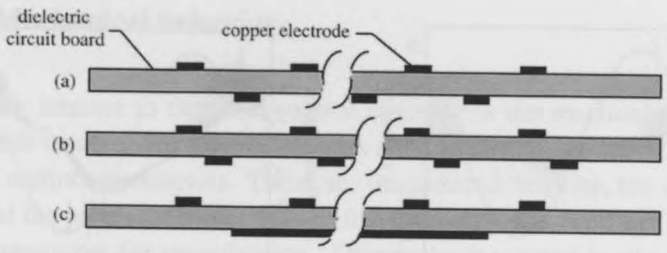

Figure 2.3: Schematic of the first published DBD actuators (taken from [113])

either side.

Typical operational parameters for the DBD actuators are the width of the electrodes, thickness and material of the dielectric layer, horizontal gap between the electrodes, carrier frequency and amplitude of the HV. In most cases, typical values are: electrode width of a few mm, electrode gap equal to zero or a few mm and a dielectric in Teflon, kapton, glass, ceramics or PMMA (Plexiglas). The thickness of the dielectric is usually between 0.1 and a few mm. Amplitude, frequency and waveform of the applied AC HV input change with different research groups and applications, while the typical range of values is: amplitude from a few kV to 20 kV and carrier frequency f_{ac} between 100 Hz and a few tens of kHz.

2.2.1 Electrical behavior

One of the main areas of DBD actuators diagnostics is the measurement of electrical properties. Specifically discharge current measurements are of great interest. It has already been mentioned that the phenomenology of the discharge current can provide useful insights into the regime of the underlying process. Typical behavior of the discharge current within a HV period is presented in Fig.2.4 for the case of exposed and covered grounded electrodes respectively [104].

Similar study has been conducted and confirms these observations [38, 39] where by using a different method, optical measurements which reveal that the structure of the plasma is different in both space and time during the *forward stroke* versus the *backward stroke* were performed. During the *forward stroke*, microdischarges happen in rapid succession with a relatively low

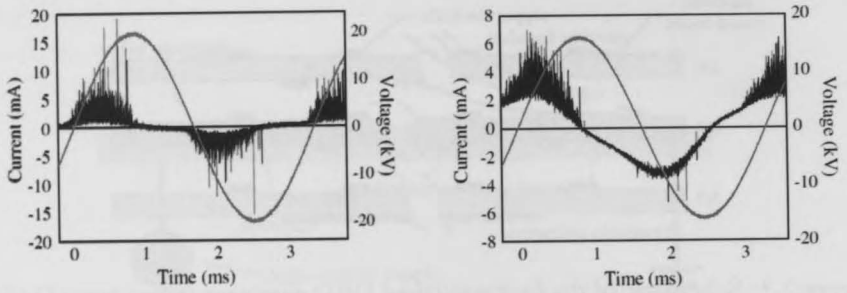

Figure 2.4: Evolution of the discharge current in the case of (a) exposed and (b) encapsulated ground electrode (adapted from [104]).

charge transferred per event whereas during the backstroke, there is a relatively small number of more intense microdischarges.

Additionally, Enloe et al. [39] provide a physical model for the discharge sequence in the DBD. This is summarized in Fig.2.5. During the *forward stroke* the exposed electrode is negative and emits electrons as it is bare metal and hence an infinite electron source. This is signified by the strong but few current peaks registered during this period. Due to the charge buildup on the dielectric surface, the local electric field drops below the breakdown threshold and the discharge is quenched and self-terminates. When the voltage reverses during the *backward stroke*, the electrons move in the opposite direction. At this point however, the electrons are provided by the accumulated species on the dielectric and thus are not so readily available as in the *forward stroke*. This is causing the multitude of weak current peaks during this period.

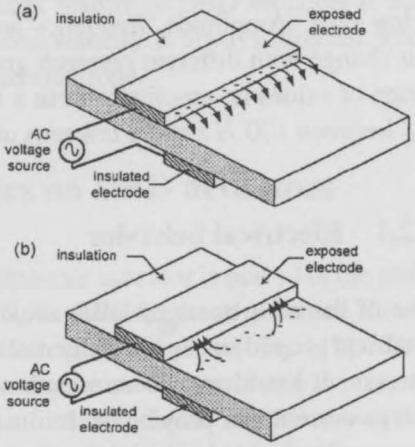

Figure 2.5: Conceptual model of the discharge sequence during the (a) *forward stroke* and (b) *backward stroke* (taken from [39])

2.2.2 Mechanical behavior

Of primary interest to the flow control engineer is the mechanical behavior of the DBD actuator. In general the mechanical effects can be described using three distinct parameters. These are the induced velocity, the mechanical power and the produced thrust. The induced velocity has been by far the most popular parameter for investigation. Originally, measured by the University of Tennessee [114, 111], the now well established tangential wall jet can be seen in Fig.2.6

Since the original measurements from the group of Roth, large contributions to the field have been achieved from the University of Notre Dame in cooperation with the US Air Force (USA) and the University of Poitiers in France. At Poitiers both time averaged and time resolved measurements of the induced velocity have been conducted [43, 42, 12]. On the other hand the groups from the USA have mainly been occupied with the produced thrust from the actuator [134]. Additionally other groups have also been concerned with induced velocity measurements using a variety of diagnostic techniques [120, 3, 35].

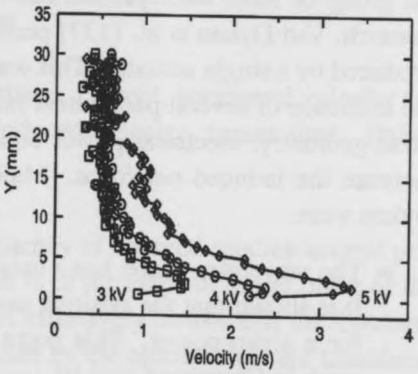

Figure 2.6: The first published record of DBD induced velocity measurements (taken from [114]).

As soon as sufficient experience was developed with the system, researchers attempted to optimize the performance of the actuator using systematic parametric studies. Pons et al. [104] measured velocity profiles in quiescent flow with the help of a glass Pitot tube, while investigating the effect of several parameters such as the applied voltage, carrier frequency, electrode gap, dielectric thickness and dielectric material. This study has been completed by Forte et al. [42] with the ultimate goal of maximizing the induced velocity.

The second characteristic value of interest is the produced thrust due to the plasma operation. A major distinction should be made here as to the nature of produced thrust. In several works [137, 134] and some plasma review pa-

pers [32, 94], the term electric force is used to represent the spatio-temporally averaged body force value produced by the actuator. This is usually in force units such as mN and sometimes normalized with the effective span of the actuator (mN/m). On the other hand several numerical studies [18, 85] as well as Chapters 7 and 8 of the present thesis are conserned with the calculation and modeling of the volume distributed force field rather than the integrated value. In this manner the term *thrust* is used in the present thesis to describe the integrated in space and time force value while the term *body force* is used to describe the volume force vector field.

Regarding thrust measurements several studies have been published. Again the group of Roth were pioneers in this aspect [111]. Folowing this initial research, Van Dyken et al. [137] performed a study concerning the net thrust produced by a single actuator. This was a parametric optimization study where the influence of several parameters (signal waveform, carrier frequency, electrode geometry, electrical power consumption) was investigated in order to increase the induced net force. Major conclusions from the results of Van Dyken were:

- The waveform shape has a major influence on the production of thrust. It is shown that the positive sawtooth shape produces the largest thrust for a given power. This point is discussed extensively in the present work in Chapters 6 and 10.
- Thicker and weaker than Kapton dielectrics such as Plexiglass provide larger net thrust due to the higher voltage values enabled.

Additionally, recent thrust measurements [105] show that:

- The thrust is proportional to carrier frequency.
- Relative efficiency is typically between 0.15 and 0.20 mN per electrical W

2.2.3 Forcing mechanisms within the HV period

One of the most exciting and debated issues within the field of DBD actuators diagnostics is the unsteady behavior of their induced forcing. As already explained, it is widely regarded that collisional processes drive the momentum transfer [16]. This is further supported by an important property of the plasma

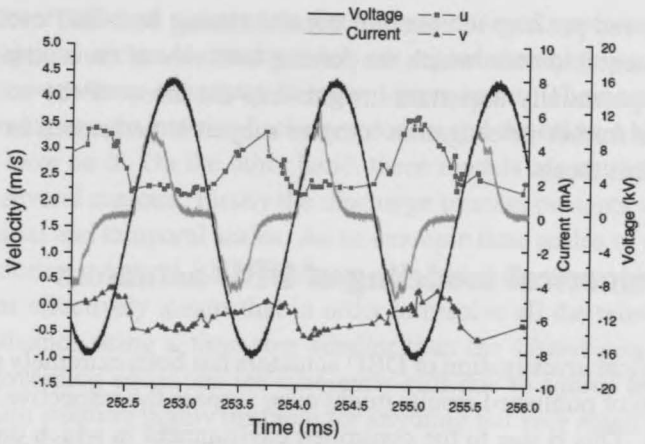

Figure 2.7: Synchronized records of voltage, current, horizontal velocity (u) and vertical velocity (v) of the DBD-induced velocity, versus time. (taken from [42])

discharge in air. This states that the frequency of charged species-neutral particles collisions within the plasma region is of the same or larger order of the electrostatic oscillations frequency. This effectively means that the Coulombian forces exerted on the charged particles by the electric field are transfered entirely to the neutral air. Since the electric field oscillates during the AC HV period, the applied force on the charged species is respectively expected to be unsteady. Yet experimental and numerical information on the influence of each half cycle and more specifically the sign of the applied force at each stroke is controversial. Additionally, the effect of the waveform shape (which as suggested by the results of Van Dyken [137] has a major influence on the performance of the DBD actuator) has not yet been studied systematically in the context of its respective time resolved forcing.

There has been a limited number of experimental investigations on the forcing mechanisms of the actuators. Time-resolved Laser Doppler Anemometry (LDA) measurements were conducted in quiescent air [42] where the asymmetry between the two half cycles is evident (Fig.2.7). Large momentum transfer during the negative half cycle was recorded which corresponds with the recent modeling efforts. In another study [71] phase locked PIV measurements are taken which indicate the dominance of the negative cycle in momentum transfer. Using a different technique Enloe et al.[37] and Font et

al.[40] showed positive momentum transfer during both half cycles. Due to the fundamental interest which the forcing behavior of the actuator presents, as well as potentially important insights into the effect of the voltage waveform shape further investigation into the subject is performed in Chapters 6 and 10 of this thesis.

2.3 Numerical modeling of DBD actuators

The numerical investigation of DBD actuators has been extremely popular and the volume of published results might even surpass the respective experimental studies. This is due to the controlled environment in which the numerical experiments are conducted which gives unlimited access to the, difficult to be physically measured, spatial and temporal metrics associated with the discharge. Additionally, numerical models are seen as the vehicle towards the creation of body force models which can retrospectively be fitted in existing numerical flow solvers in order to simulate the effect of the plasma actuator. In essence numerical investigations on DBD actuators serve primarily a twofold goal:

- To provide insight into the discharge process as a function of macroscopic parameters such as voltage, frequency, geometrical dimensions etc.
- To provide valid, accurate body force models for implementation in numerical flow solvers.

Two main variants of modeling approach have been suggested, each presenting favorable and adverse features. On one hand phenomenological, semi-empirical body force models are proposed usually loosely based on the underlying physics and heavily manipulated and calibrated using experimental evidence. These models are typically low-fidelity since they fail to capture the actual physical background of the discharge nor do they account for a large number of control parameters. They are usually formulated for fixed geometries, electrical parameters and conditions. On the other hand their computational complexity and cost are very low making the ideal for multi-iteration processes such as parametric or optimization studies on flow control.

On the other hand first-principles models are devised where all of the essential physics is captured using usually a combination of Maxwell equations

with the conservation of momentum for various charged species. Although some assumptions are made, these models are regarded as highly accurate especially in cases where chemistry is taken into account. They are primarily used for gaining insight into the discharge process and the effect which several parameters have on it. On the other hand, these models are extremely intensive due to several reasons. Firstly the discharge process presents an extreme range of spatial and temporal scales. As an example time scales of simultaneous events during a typical kHz discharge are spread anywhere between ms and ns. This effectively means that in order to resolve all the relevant scales one must advance using a time step smaller than the fastest process. Secondly the governing equations are inherently stiff due to source terms. This makes explicit solution highly unstable for anything but very small time steps while implicit solutions present increased implementation complexity while the acceleration of solution is still limited due to the first reason mentioned above.

In general phenomenological models produce fast but inaccurate results used mainly as force models while first-principle models are considerably more accurate but so expensive that they can only be used as research tools. A large effort is undertaken in this thesis to develop a new technique of modeling which negates the disadvantages of both variants of numerical models towards the production of force models. This is discussed in Chapters 7 and 8. In this section a review of the major numerical modeling efforts is given. For a more extensive review the reader is referenced to the review paper by Jarayaman and Shyy [61].

2.3.1 Phenomenological models

As with the experimental observations, the group of Roth was also a pioneer on setting the requirements for a body force model able to give a description of the effect of the DBD actuator. Their model [113, 112] has been a simplified approach based on forces in gaseous dielectrics as discussed by [83]. More specifically, the body force is proportional to the gradient of the squared electric field as in:

$$f_b = \frac{d}{dx}\left(\frac{1}{2}\epsilon_0 E^2\right) \tag{2.1}$$

Apart from the restriction of one-dimensionality this model has several issues

as it is based on a static formulation and does not account for the presence of the charged particles, both of which have been shown to be of great importance in experiments. Boeuf and Pitchford [18] give similar comments in their derivation of Eq.2.1. Elaborating, [39] further showed that the body force given by Eq.2.1 can only be valid in the special case of a 1D condition where the electric field has only horizontal components, a scenario which is quite distanced from physical applications relevant to DBD's.

One of the most popular models was published by Shyy et al. [121]. Due to its simplicity this model has been used in a large number of numerical studies. A basic assumption of this model is that the electric field strength, decreases linearly from the edge of the exposed electrode toward the covered electrode. Unfortunately, this assumption does not agree with experimental studies [39, 101, 102], which show an exponential spatial decay. On a different approach Singh and Roy [122] used a combination of results obtained from a first-principles simulation in conjunction with phenomenological observations to develop an approximation for the 2D body force components. Suzen and colleagues [130, 129] used the electrostatic model with an imposed Gaussian distribution for the spatial charge distribution to calculate the plasma body force using a formulation given by [38, 39].

An interesting approach toward an efficient body force model has been proposed by Orlov and colleagues [102, 101]. Their method is a variation of the model proposed by Enloe et al. [39] which is based on the lumped-element circuit model. A schematic of this model is shown in Fig.2.8. The novelty of this model is the division of the domain over the covered electrode into N parallel networks. The properties of each parallel network depend on its distance from the exposed electrode. Each parallel network consists of an air capacitor, a dielectric capacitor, and a plasma-resistive element, as in the earlier model [39, 102]. Zener diodes are used in addition to set a threshold voltage level at which the plasma initiates and to switch into the circuit the different plasma-resistance values based on the current direction, which experiments had shown to be important. The lumped element model is quite efficient in a numerical point of view. On the other hand, the account for the time evolution of the surface voltage provides significant improvement on the achieved accuracy of the force model. In this sense it represents the most viable option for a phenomenological force model.

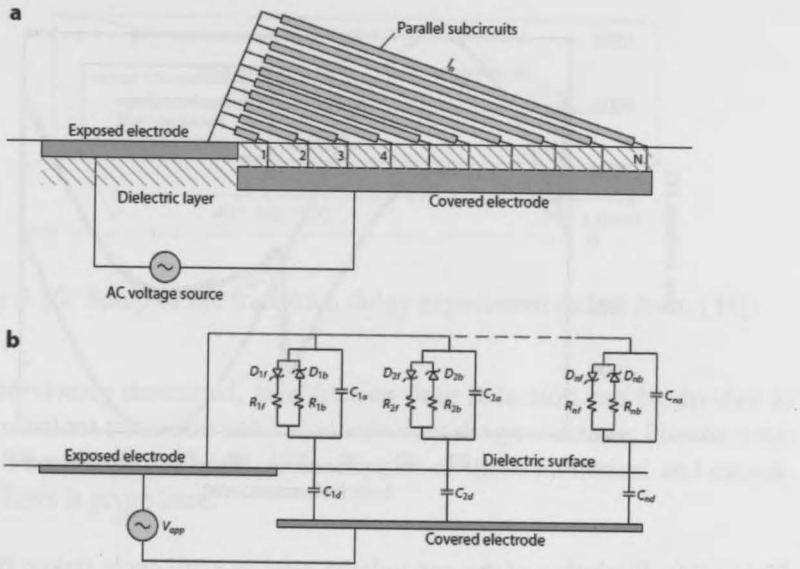

Figure 2.8: Space-time lumped-element circuit model for a single-dielectric barrier discharge plasma actuator that divides the region over a covered electrode into (a) N subregions that (b) each represents a parallel arrangement of circuit elements. (adapted from [32], originally from [102])

2.3.2 First-principles models

One of the first physics-based first-principles models for a DBD plasma actuator was developed by [91]. It consists of a 1D model based on a simultaneous solution of the continuity equations for charged and excited particles and the Poisson equation. The model has also been applied by Jayaraman [61] for the same boundary conditions. The gap voltage evolution for both studies is presented in Fig.2.9 with the peaks indicating the discharge events.

After the initial 1D efforts, it was deemed necessary not only to expand the numerical capability in 2D domains but also to include air chemistry in the resolved charged species. Prior to the advancement of plasma actuators there had been several models developed for DBDs in air that include complicated chemistry. These models have served as the basis for the 2D models involving DBD actuators. To simplify the chemistry, [41] solve for the plasma discharge in a 2D asymmetric plasma actuator that includes only nitrogen and oxygen reactions. Very thorough numerical models have been developed by the group

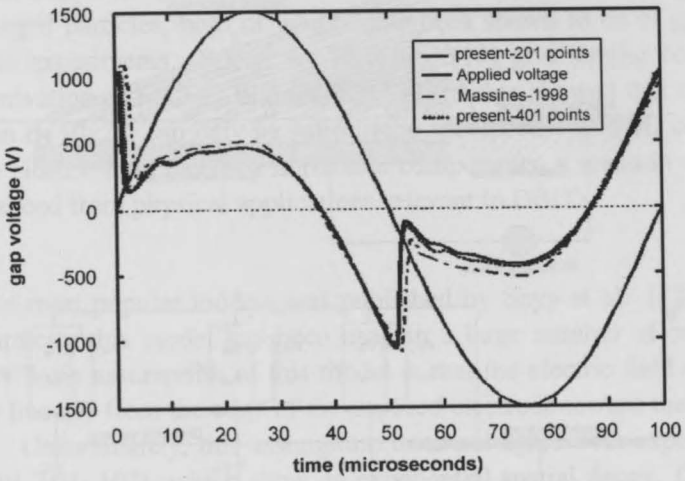

Figure 2.9: Evolution of the gap voltage over one full cycle (taken from [61])

of the Pennsylvania State University [85] and the group of the University of Paul Sabatier [18, 17]. They model the weakly ionized plasma as a mixture of neutral molecules, electrons, and positive and negative ions. They account processes such as ionization and recombination.

It is evident that first principles models can precisely describe all the different processes involved in the plasma actuator. However, they are computationally time-consuming and require significant computer resources. This is especially true if they are applied to air since the number of species to be resolved (and hence equations) increases significantly.

2.4 Applications of DBD actuators

Although no published report of an industrial application of aerodynamic DBD actuators exists to date, the amount of application studies in laboratory conditions has been overwhelming. Considering space and relevance restrictions this section is concerned with only applications of DBDs for drag reduction and more specifically, skin friction drag reduction. For a more detailed review of DBD applications the interested reader is referenced to the extensive reviews been published by Moreau et al. [94] and Corke et al. [32].

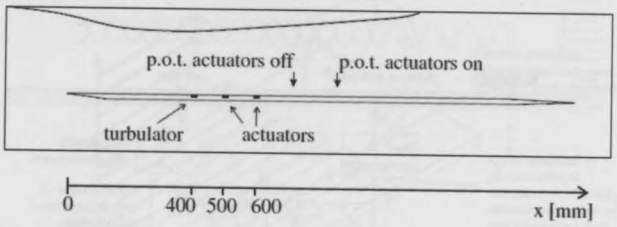

Figure 2.10: Setup of the transition delay experiment (taken from [49])

As was previously described, skin friction drag reduction can be divided to laminar-turbulent transition delay and turbulent drag reduction. Plasma actuators have been used for both. A description of these numerical and experimental efforts is given here.

2.4.1 Transition delay

In the previous description of techniques for transition delay, it was stated that mean flow manipulation is one of the main routes of action. LFC techniques make strong use of this principle although several robustness restrictions have prohibited such methods from industrial application. DBDs present an alternative to LFC and more specifically mean flow manipulation for transition delay. Through their directional, wall parallel forcing they can be used to energize the laminar boundary layer, make the velocity profile more full hence making it more hydrodynamically stable.

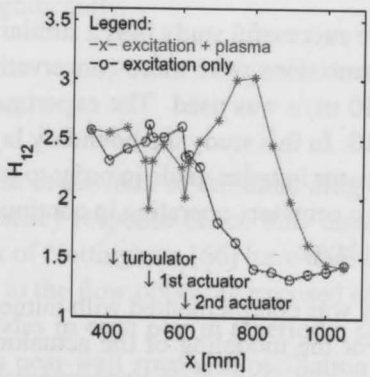

Figure 2.11: Experimental shape factor for actuated and base flows (taken from [49])

The first experimental investigation on this concept has been conducted by

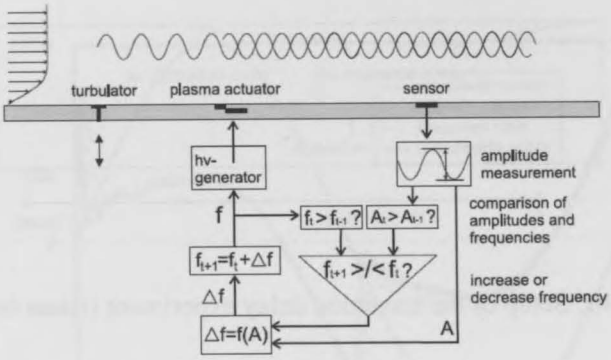

Figure 2.12: The control system for TS cancellation (taken from [51])

ONERA [120]. It involved the utilization of a DBD actuator placed on a flat plate at zero angle of attack. The orientation of the actuator was perpendicular to the mean flow direction and the forcing effect directed downstream. During actuation, the forcing of the actuator is providing momentum to the near-wall regions of the boundary layer which make the profile fuller and damps the amplification of instabilities. Nevertheless, the results of this study were negative as transition was actually promoted than delayed.

On a more successful study [49] a similar investigation was conducted. In this case the ambitions were more conservative and a freastream velocity not exceeding 10 m/s was used. The experimental setup of this study is presented in Fig.2.10. In this study the boundary layer was artificially perturbed using a DBD actuator in pulse mode in order to introduce disturbances. Further downstream two actuators operating in continuous mode were used to accelerate the boundary layer.

The study was complemented with numerical simulations using a RANS flow solver. For the modeling of the actuator a modified version of the model of Jayaraman was used. Both experimental and numerical results have demonstrated transition delay of several cm between base and actuated flows as reflected in the boundary layer shape factor shown in Fig.2.11. The group of Darmstadt has been a leader also in the field of phase-locked wave cancellation techniques using DBDs. In experimental studies which were complementary to their continuous operation cases artificially excited TS waves were damped using plasma actuators operated in pulse mode [50, 51]. The experimental setup has been common between the two studies (Fig.2.10) al-

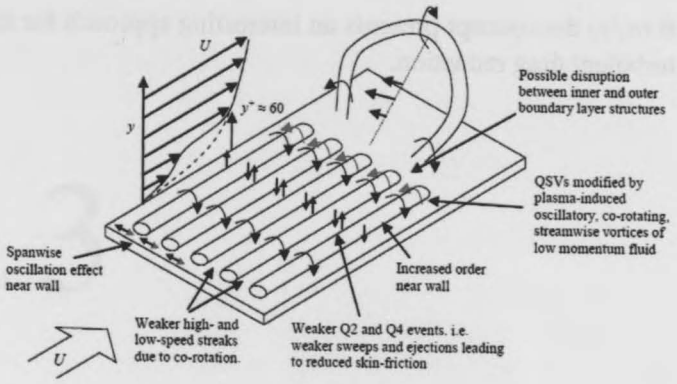

Figure 2.13: Conceptual model for the turbulent boundary layer with oscillatory plasma forcing (taken from [66]).

though the waves were introduced using a vibrating membrane rather than a DBD.

Control plasma actuators positioned downstream of the excitation actuator attenuate the waves by imparting an unsteady force into the boundary-layer as shown in Fig.2.12. As a result the amplitude of the velocity fluctuations at the excitation frequency was reduced significantly.

2.4.2 Turbulent drag reduction

Interesting possibilities for DBDs rise in the field of turbulent drag reduction as well. Utilizing the very fast frequency response of the flow under plasma actuation the group of the University of Nottingham [66] have applied the actuators in a configuration of parallel to the flow opposing exposed electrodes. By energizing one of the two electrodes in each pair in a periodic successive manner, they were able to produce a near-wall spanwise oscillation which is typically known to reduce turbulent friction drag [67, 5, 81] . Drag reduction of up to 45 % was reported for this study.

It was suggested that the plasma forcing resulted in the creation of streamwise co-rotating vortices which could disrupt or cancel the quasi-streamwise vortices occurring near the wall in a turbulent boundary layer. A conceptual sketch of the mechanism as envisioned by this group is shown in Fig.2.13. Although the experimental study was conducted for very small freestream ve-

locities (1.6 m/s) the concept presents an interesting approach for the use of DBDs for turbulent drag reduction.

Chapter 3

Methodology

This chapter is dedicated to the description of the different experimental and numerical techniques used throughout the current investigation. Additionally, the description of the automatic control system used in Chapter 9 is given.

3.1 Experimental and data analysis methods

3.1.1 Hot Wire Anemometry

Hot Wire Anemometry (HWA) is one of the staple techniques used in experimental fluid mechanics. It is based on small heated sensors which are placed in the flow to be measured [30]. The sensor in its most traditional form is made of a thin tungsten or platinum wire supported between two metallic probes. Taking advantage of the Joule effect, the wire is heated by an electric current provided by a Wheatstone bridge circuit. Variations in external flow velocity produce an increase or decrease in the heat which is transfered by the sensor to the fluid. This can be traced back to voltage variations which, through proper calibration can be correlated with velocity. Here a brief description on the working principles of HWA is provided. Details on the experimental setups and measurements parameters are given within each individual chapter concerning HWA.

In general two modes of operation are provided by most HWA systems. These are Constant Temperature Anemometry (CTA) and Constant Current Anemometry (CCA) respectively. In the more common CTA mode, the wire sensor is kept at constant temperature by the Wheatstone bridge circuit. This is done with fast voltage balancing able to follow the fluctuations in heat transfer caused by the external flow. On the other hand, CCA keeps a constant current flowing through the wire. For this study the CTA mode is applied.

The sensor wire is made out of electrically conductive material, meaning that when voltage is applied at the ends, electrical current flows through the wire. Electrical energy is dissipated by the Joule effect which is then transformed into thermal energy, causing the wire to warm up. The rate at which this transformation will take place is governed by the relation:

$$R_w I^2 = \Phi \tag{3.1}$$

where R_w is the resistance of the wire, I is the traveling current and Φ is the heat-loss rate due to thermal convection from the sensor to the flow. To maintain an equilibrium wire temperature, the thermal energy generated, due to the flow of electrical current, should be balanced by heat losses (primarily convective) to the surrounding fluid in motion. The convection heat-loss rate to the flow can be expressed with:

$$\Phi = \pi l k_0 (\Theta_w - \eta T_0) Nu \tag{3.2}$$

where l is the length of the wire, k_0 is the thermal conductivity of the wire in quiescent flow, η is the thermal recovery factor and Nu is the Nusselt number which stands for a non-dimensional heat transfer coefficient. The Nusselt number can be expressed with the semi-empirical relation:

$$Nu = X + Y Re^n \tag{3.3}$$

where X, Y and n are constants. Expanding Eq.3.1 using Ohm's law ($E = IR$) and combining Eqs.3.1 and 3.2 and reformulating Eq.3.3 the calibration formula:

$$E^2 = L + M(\rho u)^n \tag{3.4}$$

where L and M are constants specific to the wire and overheat ration properties. Considering that the King's law expresses the relation for n = 0.5, the

relation between U and E requires at least a fourth order polynomial to be represented accurately during calibration.

HWA has been used in experimental investigations described in Chapters 4 and 5. Since these experiments have been performed at different locations and times, the setup details of the HWA system present some differences which are described within each respective chapter. Here a general description of the equipment used in all experiments is provided.

In the entirety of this work the TSI IFA300 system is used for HWA. As was previously mentioned it is operated in CTA mode. The system provides simultaneously reading of two channels which enables the use of two single hot wire sensors or one double wire sensor. The system provides automatic selection of overheat ratio and the typical operating temperature of the sensors is 250 degrees C.

Bridge voltage is read by a National Instruments CompactDAQ system which employs several modules for fast A/D conversion. Maximum sampling frequency is 100 kHz for each channel at 16 bit resolution. The sampling frequency for each individual experiment is mentioned in the respective chapter's experimental setup section.

The sensor used for the experiments is the TSI model 1201 Standard disposable probes. These are very robust and rigid cylindrical hot film probes. They are constructed from tungsten film wrapped around a glass cylindrical wire. The thickness of the sensing element is 5 μm while the length is 1 mm.

The probes have been calibrated using a dedicated TSI 1127 manual velocity calibrator employing a low velocity nozzle set. More details on calibration process and issues can be found in the thesis work of Pieter Boon [19].

3.1.2 Particle Image Velocimetry

Particle Image Velocimetry (PIV) has been extensively used in this work in Chapters 4, 6 and 10. Here a general description of the working principles of planar PIV is given while details for the individual setups are given at the respective chapters. A review on the PIV working principles can be found in [141].

Working principle

PIV is a nonintrusive technique that measures the velocity simultaneously at numerous points within a fluid volume or area using optical means. The fluid is injected (seeded) with non-transparent tracer particles that are assumed and considered to demonstrate two important properties:

- the tracer particles do not influence or alter the motion of the fluid
- the tracer particles exactly follow the motion of the fluid

The local fluid velocity at location X is obtained indirectly as a displacement D of the tracer particles within a finite time interval of $\Delta t = t_2 - t_1$. This can be expressed as:

$$D(X, \Delta t) = \int_{t_1}^{t_2} \mathbf{v}(X(t), t)dt \tag{3.5}$$

where $\mathbf{v}(X(t))$ is the velocity of the tracer particles along the trajectory X within the time interval Δt. In the case which the tracer particles fulfill the two previously specified properties, the tracer particle velocity $\mathbf{v}$ can be considered equal to the local fluid velocity $\mathbf{u}(X, t)$. It is important to mention that the displacement (D) provides only the average velocity along the particle's trajectory over the time Δt.

The tracer particle position and displacement is established by illuminating and optically capturing the planar measurement domain twice in a short deterministic time interval Δt. This successive illumination is provided by a pulsed laser sheet while the optical capture is performed using fast digital cameras. A statistical analysis is then conducted on the two captured image patterns in order to determine the most likely displacements of the particle ensemble and in extension the instantaneous velocity vector field. A schematic of an experimental arrangement for a typical PIV experiment is shown in Fig.3.1 from [108].

Tracer particles

The tracer particles must fulfill a range of contradicting requirements. On one hand in order to follow the flow with fidelity and unobtrusively typically demands that the particle diameter be sufficiently small. On the other

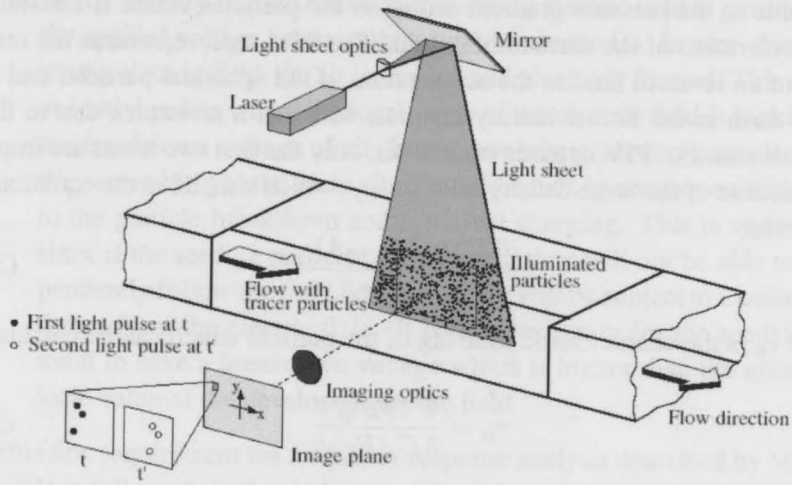

Figure 3.1: Typical experimental setup for planar PIV (taken from [108])

hand, since the detection technique is optical, the particles must also be large enough so that they scatter enough light. Considering the motion of a particle in a continuous medium, in the case which external forces, such as gravitational, and electrostatic forces etc. can be considered negligible, then the ability of the particle to track the flow is a function of its shape, diameter dp, density ρ_p, fluid density ρ_f, and fluid dynamic viscosity μ. If the particles are considered spherical, an expression relating the instantaneous relative velocity ($\mathbf{V} = \mathbf{U_p} - \mathbf{U_f}$) between the particle and the fluid, to the instantaneous velocities $\mathbf{U_p}$ and $\mathbf{U_f}$ of the particle and the fluid, respectively, is given by [92].

$$\frac{\pi d_p^3}{6}\rho_p \frac{d\mathbf{U_p}}{dt} = -3\pi\mu d_p \mathbf{V} + \frac{\pi d_p^3}{6}\rho_f \frac{d\mathbf{U_f}}{dt} - \frac{1}{2}\frac{\pi d_p^3}{6}\rho_f \frac{d\mathbf{V}}{dt} - \frac{3}{2}d_p^2(\pi\mu\rho_f)^{1/2}\int_{t_0}^{t} \frac{d\mathbf{V}}{d\xi}\frac{d\xi}{(t-\xi)^{1/2}} \tag{3.6}$$

where the term in the right hand side (RHS) and the first term in the left hand side (LHS) represent the acceleration force and viscous resistance according to Stokes law respectively. The second term in the LHS term is an additional

force due to the pressure gradient acting on the particles which is a result of the acceleration of the surrounding fluid. The third term represents the resistance of an inviscid fluid to the acceleration of the spherical particle, and the fourth term is the *Basset* history integral, which is a resistance due to flow unsteadiness. For PIV in gases such as air, only the first two terms are important because of the large density ratio ρ_p/ρ_f, which simplifies the equation of motion to:

$$\frac{d\mathbf{U_p}}{dt} = \frac{\mathbf{U_p} - \mathbf{U_f}}{\tau_p} \tag{3.7}$$

where τ_p is the characteristic time lag of the particle which can be calculated from:

$$\tau_p = \frac{4}{3}\frac{\rho_p d_p^2}{C_D Re_d \mu} \tag{3.8}$$

where C_D is the drag coefficient and Re_d is the Reynolds number based on the particle diameter. For the entirety of the measurements in this work olive oil particles are used due to their dielectric strength and small diameter. Nevertheless, due to the extreme electric fileds which the particles are operating as well as the high frequency fluctuations they are requested to follow (Chapter 6) an analysis on their frequency response is given in the next section.

Seeding material considerations

As is already mentioned for the entirety of measurements olive oil droplets have been used as tracer particles in the PIV experiments. Due to the nature of the ionization region inherent in DBD operation several issues are raised on the applicability of the specific seeding particles and in extension of the PIV experiments as a whole. More specifically two main requirements for accurate PIV measurements are formulated:

- It has been previously demonstrated [15, 37] and independently proven by the current work that a highly fluctuating velocity field is developed within the ionization region in the vicinity of the actuator. The main spectral component of these fluctuations corresponds to the carrier frequency f_{ac} of the DBD actuator. In the performed experiments of this work f_{ac} ranges between 0.5 and 4 kHz. The frequency response of the selected seeding material must be enough for the particles to faithfully be able to track velocity fluctuations of up to 4 kHz.

- At the vicinity of the DBD actuator strong electric field is produced by the applied voltage between the actuators electrodes. In turn, due to the strong electric field, the air is ionized and plasma is formed. This occurs at spatial points where the local value of the electric field is higher than the breakdown voltage of air. In the case where seeding particles exist, they are subject to the same electric field which in consequence can lead to the particle breakdown and electrical charging. This is undesirable since if the seeding particles are charged, they will not be able to independently follow the fluid flow since they will be subject to Coulombian forces from the electric field. It is thus necessary for the seeding material to have a breakdown voltage which is higher than the maximum local value of the developed electric field

For the first requirement the frequency response analysis described by Melling [92, 93] is followed. It should be noted here that this analysis is intended for homogenous stationary turbulent motion. This effectively means that the fluid fluctuations are small scale motions. Although the plasma induced fluctuations cannot be considered turbulence in a spectral point of view due to their primary frequency component, they are indeed small amplitude fluctuations. It is therefore assumed that the analysis of Melling is valid in this case.

Initially the Stokes (Sk) number is defined as a non-dimensional representation of the frequency of the particle response:

$$Sk = \left(\frac{\omega}{\nu}\right)^{1/2} d_p \tag{3.9}$$

where ω is the angular frequency of the fluid motion and d_p is the diameter of the particle. Following the assumption made in the previous section regarding large density ratios between tracking particles and fluid, the equation of motion is expressed by Eq.3.7 and can be reformulated as:

$$\frac{d\mathbf{U_p}}{dt} = -C(\mathbf{U_p} - \mathbf{U_f}) \tag{3.10}$$

where C is a characteristic frequency of particle motion defined in terms of drag coefficient C_D as defined in Eq.3.8:

$$C = \frac{3}{4} C_D Re_p \frac{\mu}{\rho_p d_p^2} \tag{3.11}$$

Melling suggests for Stokes resistance $C_D = 24/Re_p$ and:

$$C = \frac{18\mu}{\rho_p d_p^2} = \frac{18\omega}{Sk^2 s} \tag{3.12}$$

where s is the density ratio (ρ_p/ρ_f). Since in this case the particles are liquid (olive oil) and the fluid is air the ratio s can be considered relatively high. For $s \gg 1$ Hjelmfelt and Mockros [54] provide the solution to the equation of motion:

$$\eta = \left(1 + \frac{\omega_c^2}{C^2}\right)^{-1/2} \tag{3.13}$$

where ω_c is the highest fluid frequency of interest. Since the solution to the equation of motion is based on the ratio of amplitude of particle and fluid motion (η) a criterium must be set for the latter. Melling suggests $\eta = 0.99$. Based on this criterium the maximum frequency which the olive oil particles can track can be calculated using Eq.3.12 and 3.13. Based on the specifications of the TSI atomizer used in the experiments the diameter of the produced olive oil droplets is $1\mu m$. Density of olive oil is 970 kg/m^3 while the density ratio s is 617. Based on these values the maximum angular frequency which the particles can follow is ω_c = 47595 rad/s and the maximum physical frequency is $fc = \omega_c/2\pi$ = 7.57 kHz. As such olive oil droplets are deemed sufficient for the intended frequency range (0.5-4 kHz).

The second issue raised on the applicability of olive oil particles as seeding material is its dielectric strength under intense electric field conditions. A very limited amount of work has been published on the subject which is basically confined in two studies [9, 126]. Additionally an in-house investigation is conducted as part of the MSc work of Giovanni Nati [97]. Results from all three studies are used here.

In order to estimate the areas where electrical breakdown of seeding particles might occur the estimation of the electric field distribution is necessary. This is easily approximated by the Poisson equation for the electric potential ϕ

$$-\nabla(\epsilon\nabla\phi) = \rho \tag{3.14}$$

where, ϵ is the dielectric coefficient, and ρ is the space charge density which is set to zero as an approximation. The problem definition, design and boundary conditions is shown in Fig.3.2.

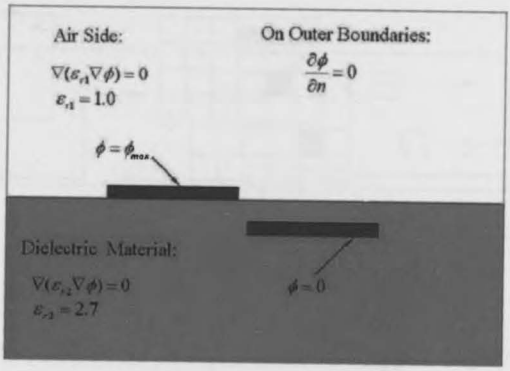

Figure 3.2: Plasma actuator configuration, domain and boundary conditions for determination of the electric field (taken from [97])

The input for the electric potential is chosen to be the maximum voltage used during the experiments of Nati (18 kV_{pp}). It should be noted that this is the maximum value reached during an actuation cycle and not an averaged value. The resulting electric field and electric potential are shown in Fig.3.3.

The strongest electric field is found between the electrodes while the strength of the electric field decays when moving away from away from the exposed electrode. Based on the analyses of Artana et al. [9] the electrostatic forces can be neglected for electric fields below 10^6 V/m for particle diameters of 1 μm. According to Fig.3.3 this is achieved after a quarter of a circle with a 2.5 mm radius away from the exposed electrode. In a $1mm$ radius the maximum electric field is 10^6 V/m which results in a ratio equal to the slipping velocity between the viscous and electrostatic forces. For typical plasma actuator induced velocities of several m/s this means that the viscous forces is several times (O(1)) larger than the electrostatic forces.

The conclusion of Nati's analysis on the electrostatic field induced by a plasma actuator is that in an area (circle of $1mm$ radius) in the immediate of the exposed electrode edge facing the covered electrode the electrostatic force is larger than the body force. Outside this small area the viscous forces are several times larger than the electrostatic forces and seem to dominate the particle motion. Using a different technique Stephen et al. [126] arrives at similar conclusions. More specifically they use independent pitot tube measurements in order to compare a particle-free flow with the PIV study. Again no influence

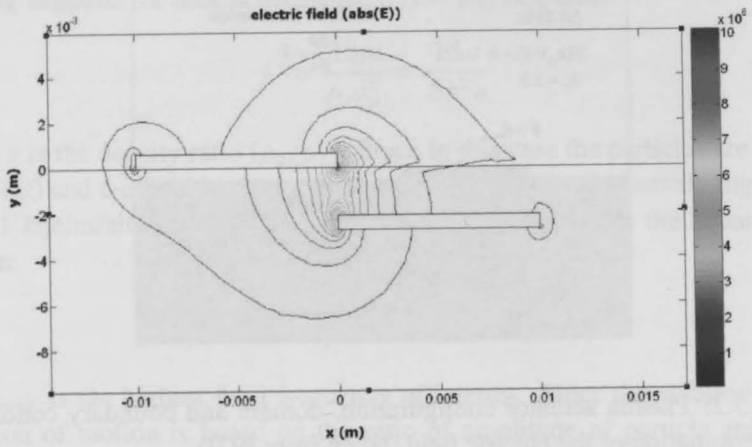

Figure 3.3: Electric field resulting from the investigated plasma actuator configuration, with $18kV_{pp}$ (taken from [97])

on the seeding material has been found.

Imaging

During the imaging process the tracer particles are viewed through a finite aperture lens and as such their image does not appear as a point in the image plane, but forms a Fraunhofer diffraction pattern. This consists of an Airy disk surrounded by Airy rings [108]. The diameter of the Airy disk d_{diff} represents the smallest particle image that can be obtained for a given imaging configuration. The value of d_{diff} for a given aperture diameter D_a and wavelength λ can be calculated by approximating the normalized intensity distribution of the Airy pattern by a Gaussian bell curve and using the thin lens equation given by:

$$\frac{1}{z_0} + \frac{1}{Z_0} = \frac{1}{f} \tag{3.15}$$

where z_0 is the distance between the focal plane and lens, Z_0 is the distance between the lens and the object plane and f is the focal length of the lens. The magnification factor M can then be defined:

$$M = \frac{z_0}{Z_0} \tag{3.16}$$

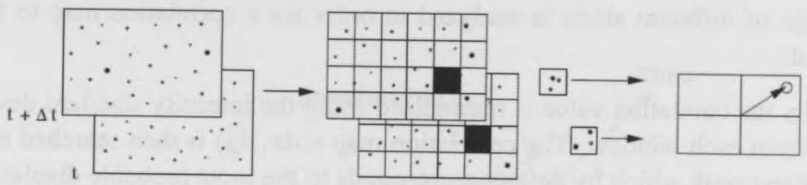

Figure 3.4: Planar PIV cross-corellation process (taken from [108])

and the diffraction limited minimum diameter d_{diff} is expressed as

$$d_{diff} = 2.44 f_{\#}(M+1)\lambda \tag{3.17}$$

where $f_{\#}$ is the f-number of the lens (ratio between focal length (f) and aperture diameter (D_p)).

Image analysis

After acquisition, the gathered digital images are analyzed in order to extract the velocity vector fields. In the course of PIV image analysis, the particle distribution is described in terms of a pattern. The captured particle images show the instantaneous locations of the tracer particles as peaks in the light intensity stored in digital files. For a sufficiently small time interval between two snapshots (Δt), the two consecutive images present intensity distributions with the second exposure slightly shifted with respect to the first. Determining the shift, combined with the knowledge of Δt leads to the estimation of the average velocity field during the respective time interval. The particle shift can be calculated using a correlation technique. The two consecutive particle images at times t and $t + \Delta t$, are shown in Fig.3.4 from [108].

The captured images are first divided into smaller so-called *interrogation windows*, containing local patterns of light distribution. The distributions of light intensity within an interrogation window at times t and $t + \Delta t$ are designated $I_1(i, j)$ and $I_2(i, j)$ respectively, for a two dimensional matrix of pixels counted in i and j. The cross-correlation process involves shifting the first template $I1$ around template $I2$ by a given shift (dx, dy). The sum of the products of all the overlapping pixel intensities at each spatial shift (dx, dy) produces the map of correlation value $C(dx, dy)$, which is essentially a measure of the degree of matching between the two distributions for a given shift.

A range of different shifts is analyzed in order for a correlation map to be formed.

Initially the corelation value is normalized using the intensity standard deviation from each window. The correlation map $c(dx, dy)$ is then searched for the largest peak which by default corresponds to the most probable displacement within the interrogation window. With knowledge of the time separation Δt, the velocity vector field can then be determined. The signal-to-noise ratio is then defined as the ratio between the first and second largest correlation peaks.

3.1.3 Proper Orthogonal Decomposition

Several flow topologies resulting from unsteady actuation are characterized by large coherent structures such as vortices, eddies or shear layers. This is also the case with DBD actuators as is demonstrated in Chapter 4. The presence of these large scale structures and their contribution to the total kinetic energy resulting from the actuation can be determined by using Proper Orthogonal Decomposition (POD) techniques. The decomposition can be carried out using two methods: the *direct* method or the *snapshot* method. A brief description of the mathematical background of the *snapshot* method is presented here since this is the preferred technique for data analysis in Chapter 4. The interested reader is referred to [31] for more information on the *direct* method.

The *snapshot* method was first introduced by Sirovich in 1987 [123] to reduce the memory resources associated with processing large amounts of data. In this technique POD extracts information via a statistical analysis of a set of velocity fields. A typical expample of application is velocity fields resulting from PIV measurements. Snapshot POD relies on the decomposition of the fluctuations of a velocity field in a set of eigenmodes that represent an average spatial description of coherent structures. The criterium of decomposition is based on the energy content of the modes which usually translates into the selection of predominantly large-scale structures [75]. These modes do not necessarily correspond to coherent structures but may also represent events in the flow that contribute the most to the energy of the flow such as turbulence.

POD essentially separates large coherent structures (CS) from small, uncorre-

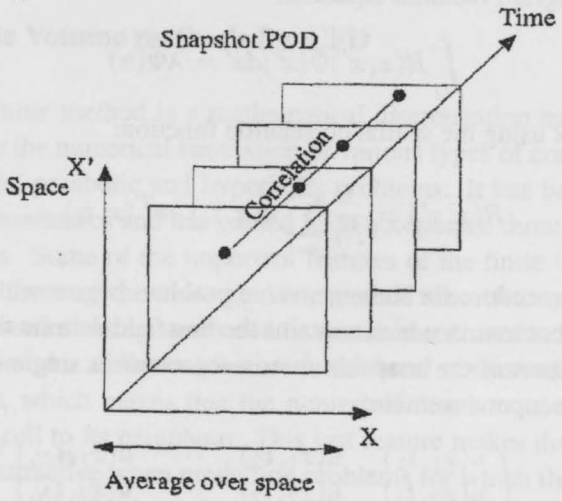

Figure 3.5: Schematic of the *snapshot* POD method (taken from [31])

lated flow features which can be attributed to noise, small scale turbulence and other low energy structures. For this study the snapshot POD method [123] is used which is a modified version of the classical POD technique. More specifically, the flow is assumed to be composed out of a mean component $u_{mean}(x)$ and a a time dependent component $u(x,t)$ which includes the CS as well as the uncorrelated fluctuations. The first step of the POD analysis is to subtract the mean velocity from the total velocity fields which are obtained from the PIV experiment. All subsequent steps will refer to velocity $u(x,t)$ which corresponds to the fluctuating component.

The snapshot POD method (Fig.3.5) consists of an eigenvalue problem from which the resulting eigenfunctions a are the temporal POD modes with corresponding eigenvalues (λ). The spatial modes Φ are then assumed to have a special form with respect to the input field ($u(x,t)$):

$$\Phi(x) = \sum_{k=1}^{N_t} a(t_k) u(x,t_k) \tag{3.18}$$

where $k = 1, 2, \ldots, N_t$ denotes the individual snapshots. The temporal eigen-

functions ($a(t_k)$) are to be determined such that the spatial modes Φ are solutions to the integral Fredholm equation:

$$\int_{\Omega} R(x,x')\Phi(x')dx' = \lambda\Phi(x) \tag{3.19}$$

which in turn is using the spatial correlation function:

$$R(x,x') = \frac{1}{N_t}\sum_{i=1}^{N_t} u(x,t_i)\cdot u^T(x,t_i) \tag{3.20}$$

The solution procedure for the eigenvalue problem begins with the formulation of a snapshot matrix which contains the flowfield data (in this case velocity). Each column of the snapshot matrix represents a single observation or snapshot of the input ensemble:

$$A = \begin{pmatrix} u(x_1,t_1) & u(x_1,t_2) & \cdots & u(x_1,t_{N_t}) \\ u(x_2,t_1) & u(x_2,t_2) & \cdots & u(x_2,t_{N_t}) \\ \vdots & \vdots & \ddots & \vdots \\ u(x_M,t_1) & u(x_M,t_2) & \cdots & u(x_M,t_{N_t}) \end{pmatrix} \tag{3.21}$$

where M is the number of all points of observation within one snapshot while N_t is the number of snapshots. Matrix A is used to build the two point correlation matrix R needed for the formulation of the eigenvalue problem. Specifically for the snapshot POD method, stationarity and ergodicity assumptions are applied in the estimation of the spatial correlation tensor R:

$$R = \frac{AA^T}{N_t} \tag{3.22}$$

The integral Fredholm equation (3.20) can be reformulated into the eigenvalue problem:

$$RV = \lambda V \tag{3.23}$$

where: $V_i = \begin{pmatrix} a^i(t_1) \\ a^i(t_2) \\ \vdots \\ a^i(t_{N_t}) \end{pmatrix}$ for $i = 1,2,\ldots,N_t$ The set of eigenvalues (λ) can provide the contribution of each mode to the total energy content of the fluctuating flowfield:

$$E_i = \frac{\lambda_i}{\sum_{i=1}^{N_t}\lambda_i} \tag{3.24}$$

3.2 Numerical Methods

3.2.1 Finite Volume methods for CFD

The finite volume method is a mathematical discretization method which is well suited for the numerical simulation of various types of conservation laws such as elliptic, parabolic and hyperbolic problems. It has been extensively used in fluid mechanics and has gained wide acceptance through commercial CFD packages. Some of the important features of the finite volume method are similar to those of the finite element method since it it may be used on arbitrary geometries, using structured or unstructured meshes, and it leads to robust schemes. An additional feature is the local conservativity of the numerical fluxes, which means that the numerical flux is conserved from one discretization cell to its neighbour. This last feature makes the finite volume method quite attractive when modelling problems for which the flux is of importance, such as in fluid mechanics. The finite volume method is locally conservative because it is based on a *balance* approach: a local balance is written on each discretization cell which is often called *control volume*. Using the divergence theorem, an integral formulation of the fluxes over the boundary of the control volume is then obtained. The fluxes on the boundary are discretized with respect to the discrete unknowns.

The finite volume is the primary spatial discretization technique used in OpenFOAM and as such a brief description of its mathematical background is given here. The interested reader is referenced to [28] for a more detailed description of the method. In the following subsections the method is described using the simple example of the linear transport equation.

Example 1. Transport equation

The first example considers the one-dimesnional transport equation for given initial conditions:

$$u_t(x,t) + \nabla \cdot (\mathbf{v}u)(x,t) = 0 \tag{3.25}$$

with initial conditions:

$$u(x,0) = u_0(x) \tag{3.26}$$

where u_t is the time derivative of u. Consider the discretization over a mesh Σ of polygonal bounded convex subsets, namely control volumes. Then, Eq.3.25

can be integrated over a volume $K \in \Sigma$ yielding the *balance equation* over K:

$$\int_K u_t(x,t)dx + \int_{\partial K} \mathbf{v}(x,t) \cdot \mathbf{n}_K(x) u(x,t) d\gamma(x) = 0 \quad (3.27)$$

where $\mathbf{n}_K$ is the normal vector to ∂K, outward to K. If k is a constant time discretization step and $t_n = nk$ then Eq.3.27 can be further discretized in time using the explicit Euler scheme:

$$\frac{1}{k}\int_K (u^{(n+1)}(x) - u^{(n)}(x))dx + \int_{\partial K} \mathbf{v}(x,t) \cdot \mathbf{n}_K(x) u^{(n)} d\gamma(x) = 0 \quad (3.28)$$

where $d\gamma$ is the one dimensional Lebesgue measure (in this case equivalent to dx) on ∂K and $u^(0)(x) = u_0(x)$. Using the divergence theorem the second term of the RHS of Eq.3.28 is expressed as a sum of surface integrals where σ denotes the face subset of the finite volume cell:

$$\int_{\partial K} \mathbf{v}(x,t) \cdot \mathbf{n}_K(x) u^{(n)} d\gamma(x) = \sum_\sigma \int_\sigma \mathbf{v}(x,t_n) \cdot \mathbf{n}_{K,\sigma} u^{(n)}(x) d\gamma(x) \quad (3.29)$$

setting:

$$v_{K,\sigma}^{(n)} = \int_\sigma \mathbf{v}(x,t_n) \mathbf{n}_{K,\sigma} d\gamma(x) \quad (3.30)$$

the final discretized transport equation can be set:

$$\frac{m(K)}{k}(u_K^{(n+1)} - u_K^{(n)}) + \sum_\sigma v_{K,\sigma}^{(n)} u_{K,\sigma}^{(n)} = 0 \quad (3.31)$$

along with the boundary condition:

$$u_k^{(0)} = \int_K u_0(x)dx \quad (3.32)$$

where $m(K)$ denotes the measure of the control volume K.

3.2.2 Reduced Navier-Stokes solver in OpenFOAM

OpenFOAM is a widely documented open source package and as such the interested reader is referenced to [2, 1] for more information on the selection of solvers and issues of implementation and validation. Here only a description of the specially developed solver for the needs of this study is given. This includes governing equations, implementation in the source code and a description of the boundary conditions.

Governing equations

In order to resolve all the spatial and temporal scales involved in the Tollmien-Schlichting waves (TS) propagation and amplification problem, a full Navier-Stokes solution is pursued. Furthermore a reduced approach is followed in which the base flow (laminar boundary layer) is considered fixed while the NS equations are solved for the TS perturbations. Here an overview of the flow solver is given.

Since the pimary interest of the study is the interaction of the DBD actuator with TS waves propagating in the laminar boundary layer, a 2-dimensional approach is taken in order to reduce complexity and numerical cost. It is of course only a first step towards a complete transition control application. Nevertheless, the methods, tools and conclusions related to this study can easily be expanded to generalized 3D cases.

Consider the 2D incompressible Navier Stokes equations in the presence of body forces:

$$\frac{\partial \mathbf{U}}{\partial t} + \mathbf{U} \cdot \nabla \mathbf{U} - \nu \nabla^2 \mathbf{U} = -\frac{\nabla P}{\rho} + \frac{\mathbf{F_b}}{\rho} \tag{3.33}$$

In the context of hydrodynamic stability it is often convenient to express the flow as the sum of a base mean flow ($\mathbf{U_0}$,P_0) and a fluctuating component ($\mathbf{u}$,p). The mean flow which is steady in time can be calculated beforehand using either analytical solutions of the Falkner-Skan equations or numerical solutions of the NS equations. In this case the standard incompressible NS solver in Open FOAM (icoFoam) is used. More details in implementation and validation of this solver as well as the results for the mean flow can be found in the thesis work of Rogier Giepman [45]. The velocity, pressure and force fields are expressed as:

$$\begin{aligned} \mathbf{U}(x,y,t) &= \mathbf{U_0}(x,y) + \mathbf{u}(x,y,t) \\ P(x,y,t) &= P_0(x,y) + p(x,y,t) \\ \mathbf{F_b}(x,y,t) &= \mathbf{f_b}(x,y,t) \end{aligned} \tag{3.34}$$

To be noted here that the body force term is of major importance since it provides an efficient way to introduce the effect of the plasma actuator in the flow. A model for this is developed in Chapters 7 and 8. Here, no mean force component is assumed since it is desirable to keep the force as one single

term for simplicity in the calculations. Instead, $\mathbf{f_b}$ contains both the mean and fluctuating components of the body force.

Substituting (3.34) into (3.33) produces the expression for the mean and perturbed flowfield:

$$\frac{\partial(\mathbf{U_0}+\mathbf{u})}{\partial t}+(\mathbf{U_0}+\mathbf{u})\cdot\nabla(\mathbf{U_0}+\mathbf{u}) \\ -\nu\,\nabla^2(\mathbf{U_0}+\mathbf{u})=-\frac{\nabla(P_0+p)}{\rho}+\frac{\mathbf{f_b}}{\rho} \tag{3.35}$$

It can now be assumed and enforced that the mean flowfield $(\mathbf{U_0}, P_0)$ is also a solution of the NS:

$$\frac{\partial\mathbf{U_0}}{\partial t}+\mathbf{U_0}\cdot\nabla\mathbf{U_0}-\nu\,\nabla^2\mathbf{U_0}=-\frac{\nabla P_0}{\rho} \tag{3.36}$$

Subtracting Eq.3.36 from Eq.3.35 provides with the final formulation for the perturbations:

$$\frac{\partial\mathbf{u}}{\partial t}+(\mathbf{u}\cdot\nabla)\mathbf{u}+(\mathbf{U_0}\cdot\nabla)\mathbf{u}+(\mathbf{u}\cdot\nabla)\mathbf{U_0}-\nu\nabla^2\mathbf{u}=-\frac{\nabla p}{\rho}+\frac{\mathbf{f_b}}{\rho} \tag{3.37}$$

To be noted that no linearization has been applied to the NS equations. Instead the overall solution can be visualized as a two-step approach where the mean and fluctuating flowfields are calculated independently.

The set of governing equations is implemented and solved within the computational framework of OpenFOAM. The platform employs second order finite volume discretization in space and a variety of finite difference methods for temporal advancement. The laminar boundary layer base flow (U_0) is calculated using the boundary layer equations or the Falkner-Skan solutions. Nevertheless in this study the incompressible viscous solver of OpenFOAM (icoFoam) is used since the computational cost is minimum for a 2D study [45]. The source code for the reduced NS solver is presented in Appendix A.

Boundary and initial conditions

The boundary conditions for the stability problem are Dirichlet conditions of zero perturbation velocity at the flat plate wall and top boundary while a Neumann condition of zero gradient is imposed at the outflow. For pressure, Neumann conditions of zero gradient are imposed on all boundaries except the top where fixed zero pressure is imposed.

In order to investigate the boundary layer stability problem the disturbance in question must be introduced in the numerical domain. This can be done in a multitude of ways such as imposed fluctuating velocity at the inflow, unsteady suction and blowing at the wall or fluctuating distributed body forces [4, 21, 63]. It is generally a good choice to introduce the disturbance upstream of the first neutral curve to allow any transient noise to damp out. In this study two techniques for introducing the disturbance are employed. Firstly a fluctuating velocity component is imposed at the inflow. The shape of the fluctuation corresponds to the eigenfunction of the TS wave calculated from Linear Stability Theory (LST) for the given frequency. Details on the LST calculations are given in the next subsection. Zero net mass is achieved since the imposed velocity has zero mean value. This technique is useful for verification purposes as well as single frequency control cases. Nevertheless it presents some difficulties when wavetrains of more than one frequencies must be introduced. For these cases an unsteady horizontal body force ($f_g(x, y, t)$) is used in the form of:

$$f_g(x, y, t) = \sum_{i}^{n} (W_i \cdot sin(2\pi\omega_i t)) \cdot sin\left(\pi \frac{x}{x_2 - x_1}\right) \cdot sin\left(\pi \frac{y}{y_2 - y_1}\right) \tag{3.38}$$

where $x_1 < x < x_2$, $y_1 < y < y_2$.

The differences $(x_2 - x_1)$ and $(y_2 - y_1)$ define the spatial wavelengths of the force in x and y direction. For the current case the x wavelength is approximately half the wavelength of the desired TS wave while the vertical wavelength is approximately a quarter of the TS wavelength. The temporal variation of the fluctuating force is controlled by the sum of n sinusoidal modes

with corresponding amplitudes (W_i) and frequencies (ω_i). In general, the numerical study in Chapter 9 makes use of the imposed inflow for the single frequency cases while the imposed body force is used for all multi frequency cases.

Verification and Validation

The numerical framework in Chapter 9 is comprised of three discreet computational modules which are coupled together in order to achieve the final transition control goal. These are the flow solver, the forcing mechanism and the adaptive control system. Due to the multiple models used in this approach, it is desirable to identify, evaluate and address possible sources of error. This is done via a verification and validation approach wherever is possible. For more details on the validation and verification issues address to the Master thesis of Rogier Giepman [45].

The flow solver is the most straightforward component to verify and validate since accurate solutions exist for both the mean and the fluctuating velocity components in the form of the Blasius equations and Linear Stability Theory (LST) respectively. It should be noted here that both the Blasius solution for the boundary layer and LST are solutions of a different set of equations than the ones the solver of this study handles. Modeling errors are therefore expected.

Firstly some notations are introduced in the framework of hydrodynamic stability. For the entire numerical study in Chapter 9, flat plate boundary layers with zero pressure gradient at two freestream velocities are considered. These correspond to 10 and 30 m/s. For all cases a Reynolds number based on the inflow displacement thickness is defined:

$$Re_0^* = \frac{U_\infty \delta_0^*}{\nu} \tag{3.39}$$

A TS wave frequency number is set based on the Reynolds number at the inflow:

$$F = \frac{\omega_0}{Re_0^*} \times 10^6 \tag{3.40}$$

where $\omega = \frac{2\pi\delta^*}{Uf_r}$ is the local non-dimensional frequency of the mode.

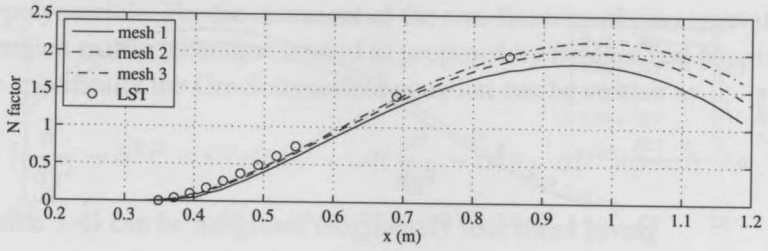

Figure 3.6: N factor for the three tested grids ($F = 86$) along with LST prediction.

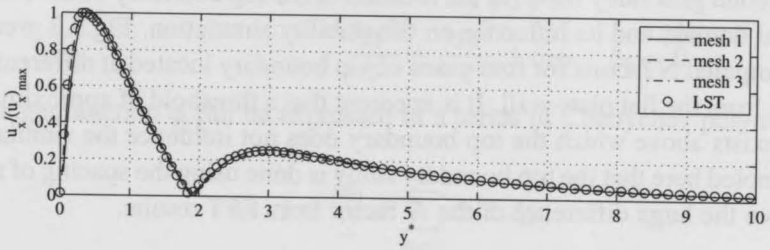

Figure 3.7: TS eigenfunction shape for the three tested grids ($F = 86$) along with LST prediction.

For verification purposes two grid studies are employed. Firstly a mesh refinement study is conducted. Three computational meshes of different sizes (106×544, 141×727, 211×1090 cells denoted mesh 1, mesh 2 and mesh 3 respectively) are created employing the same physical dimensions and cell clustering ratio. The h factor between the three meshes is 1, 1.5 and 2 respectively. To be noted that the cell spacing of mesh 2 is the one used in this study for the investigation of the selected test cases. For all three meshes, a two stage sequence of cases is run. More specifically, for each mesh a mean flow is calculated using the standard full Navier-Stokes solver (icoFoam) and subsequently the stability case is run for a single frequency case using the reduced NS solver (Eq.3.37). Velocities at several spatial positions are calculated in order to estimate the observed order of accuracy as defined by Roy [115]. Fig.3.6 presents N factors for the three different meshes for the case of $F = 86$. The observed order of accuracy for the N factor at $x = 0.8$ is 2.03. Additionally a comparison between the shape of the propagating TS wave is given in Fig.3.7.

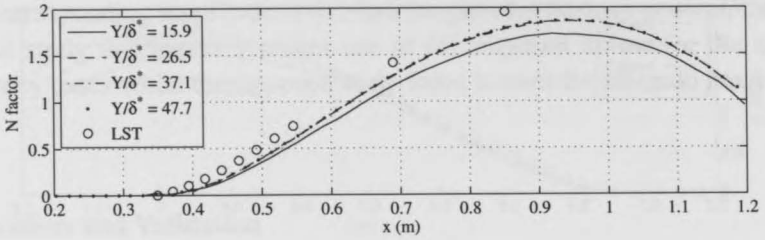

Figure 3.8: N factor for different top boundary location. ($F = 86$, mesh 1)

The second grid study involves the location of the top boundary of the computational domain and its influence on the stability simulation. Fig.3.8 presents the computed N factors for four cases of top boundary located at different distances from the flat plate wall. It is apparent that a threshold of approximately $25\delta^*$ exists above which the top boundary does not influence the simulation. To be noted here that the top boundary study is done using the spacing of mesh 1, hence the large difference of the N factor from LST results.

3.2.3 Linear Stability computations

Linear Stability Theory results are used for validation of the developed flow solver as well as for generation of initial conditions for the simulation. Here, only a brief discussion is given on the solution of the Orr-Sommerfeld equation as well as some details on the e^N method. For a more detailed account on LST see the work of Van Ingen [57, 58].

Disturbances in the laminar boundary layer are described by a stream function :

$$\psi(y) = \phi(y)e^{i(\alpha x - \omega t)} \tag{3.41}$$

Various quantities are non-dimensonalized using the velocity at the edge of the boundary layer (U) and the momentum loss thickness (θ) as scales. Boundary conditions for ϕ follow from u' and $v' = 0$ at the wall and for $y \to \infty$:

$$\phi(0) = \phi'(0) = \phi(\infty) = \phi'(\infty) = 0 \tag{3.42}$$

The Orr-Sommerfeld code used in the present investigation is based on the global solution of the spatial stability problem using an expansion in Cheby-

chev polynomials. For the treatment of the non-linearity of the eigenvalue the companion matrix technique is used as proposed by Bridges and Morris [22]. More specifically the Orr-Sommerfeld equation can be written as

$$[(\frac{d^2}{dy^2} - \alpha^2)^2 - iRe((\alpha U - \omega)(\frac{d^2}{dy^2} - \alpha^2) - \alpha U'')]\phi = 0 \tag{3.43}$$

Equation 3.43 can be integrated indefinetely four times giving

$$\phi - (i\omega Re - 2\alpha^2) \iint \phi - i\alpha Re \iint U\phi + 2i\alpha Re \iiint U'\phi +$$
$$(\alpha^4 - i\alpha^2 \omega Re) \iiiint t\phi + i\alpha^3 Re \iiiint U\phi +$$
$$\frac{b_1 y^3}{6} + \frac{b_2 y^2}{2} + b_3 y + b_4 = 0 \tag{3.44}$$

The eigenfunction ϕ can be expressed in a series of Chebychev polynomials as:

$$\phi(y) = \frac{\alpha_0}{2} + \sum_{n=1}^{N} \alpha_n T_n(y) \tag{3.45}$$

Equation 3.45 is substituted into Equation 3.44 along with the formula for Chebychev multiplication and integration. Finally the system is solved by a standard eigensolver to obtain the global spectrum of eigenvalues (α) for a given combination of frequency (ω) and Reynolds number (Re).

In the spatial mode of the stability analysis the circular frequency ω is assumed to be real and the wave number α to be complex. Also ϕ and ψ are complex but in the present study it is only important to specify $\alpha = \alpha_r + i\alpha_i$.

Introducing α into Eq.3.41 leads to:

$$\psi(y) = \phi(y) e^{(-\alpha_i x)} e^{i(\alpha_r x - \omega t)} \tag{3.46}$$

It follows from Eq.3.46 that disturbances grow, remain constant or decrease with x for $\alpha_i < 0$, = 0 and > 0 respectively, meaning that the given flow is unstable, neutral or stable against the given disturbance. As can be seen from Eq.3.46 the rate of amplification or damping is determined by $-\alpha_i$.

The amplitude a of the disturbance can be computed as a function of x using Eq.3.46 .The ratio of the amplitudes a and $a + da$ at x and $x + dx$ is given by:

$$\frac{a + da}{a} = \frac{e^{-\alpha_i (x + dx)}}{e^{-\alpha_i x}} = e^{-\alpha_i dx} \tag{3.47}$$

or:

$$ln(a+da) - ln(a) = d(ln(a)) = -\alpha_i dx \tag{3.48}$$

and after integration:

$$n = ln(\frac{a}{a_0}) = \int_{x_0}^{x} -\alpha_i dx \tag{3.49}$$

where x_0 is the station where the disturbance with frequency ω and amplitude a_0 first becomes unstable. The quantity n will be denoted as the "amplification factor" while $-\alpha_i$ is the "amplification rate". Then e^n gives the "amplification ratio". In applications Eq.3.49 is written as follows:

$$n(x,\omega) = (10^{-6} U_\infty \frac{c}{\nu}) \int_{x_0/c}^{x/c} 10^6 \frac{-\alpha_i \theta}{Re_\theta} \frac{U}{U_\infty} d(\frac{x}{c}) \tag{3.50}$$

or by denoting $T = 10^6(\frac{-\alpha_i \theta}{Re_\theta})$

$$n(x,\omega) = (\frac{10^{-6} U_\infty c}{\nu}) \int_{x_0/c}^{x/c} T(\frac{U}{U_\infty}) d(\frac{x}{c}) \tag{3.51}$$

The factors 10^6 and 10^{-6} have been introduced for convenience. If n is calculated as a function of x for a range of frequencies ($F_\infty = \frac{\omega \nu}{U_\infty^2}$) a set of n-curves is derived. The envelope of these curves gives the maximum amplification factor N as a function of x. The e^N method assumes that transition occurs when N has reached a critical value (of the order of 9) but dependent (as determined by experiment) on the disturbance environment in the flow such as turbulence level, external noise, surface roughness etc.

3.3 Filtered-x LMS automatic control system

Chapter 9 is focused on the numerical investigation of control of TS waves using DBD actuators. As is explained in the specific chapter, the robust and autonomous control of TS waves must rely in a capable automatic control system. Since this work is coupled to future experimental work, the control system must also work under realistic implementation conditions. This translates to the need for simple arithmetics which can enable the control algorithm to work in fast real-time Digital Signal Processors (DSP). One of the best suited

algorithms to fulfill the requirements is the filtered-x LMS (FXLMS). In this subsection mathematical overview of the working principles is given. An excellent introduction in the field of active noise control and related techniques (including FXLMS) is given in the book by Hansen [52].

As is previously mentioned for the control system the filtered-x LMS (FXLMS) [80] adaptive algorithm based on FIR filters is applied. The concept is derived from active noise cancellation techniques and it involves a feed-forward loop for the estimation of the control signal which drives the actuator (in this case the voltage amplitude of the DBD actuator). More specifically, the system uses a reference and an error signal which in the investigated case are pressure values at the flat plate wall. In the numerical framework these are read directly within Open FOAM. The reference signal is read upstream of the actuator in order to sense the incoming instabilities while the error sensor is downstream of the actuator in order to sense the instability after manipulation. A schematic of the working principle is given in Fig.3.9.

The system is using a primary Finite Impulse Response (FIR) filter:

$$\mathbf{w}(k) = [w_1(k), w_2(k), \dots w_{L-1}(k)]^T \tag{3.52}$$

through which the reference signal ($\mathbf{x}$) is passed as follows[1]:

$$y(k) = \mathbf{w}(k)^T \cdot \mathbf{x}(k) = \sum_{i=0}^{L-1} w_i(k) x(k-i) \tag{3.53}$$

where k is the time instant of the last sample of the reference signal and L is the length of the primary FIR filter $\mathbf{w}$. To be noted here that $\mathbf{x}(k) = [x(k) \quad x(k-1) \dots x(k-L+1)]^T$ is a vector containing the L last samples of the reference signal. Through this process the output signal $y(k)$ which is sent to the actuator is produced. In order to achieve the desirable cancellation effect the weights of the primary filter $\mathbf{w}$ must be adapted. This is achieved through a Least Mean Square (LMS) approach which compares a filtered version of the reference signal with the error signal at time instant k in order to compute an updated set of primary filter coefficients for time instant $k+$:

$$\mathbf{w}(k+1) = \mathbf{w}(k) - 2\mu e(k)\mathbf{f}(k) \tag{3.54}$$

[1]For the description of the controller algorithm the notation of Hansen [52] is followed throughout.

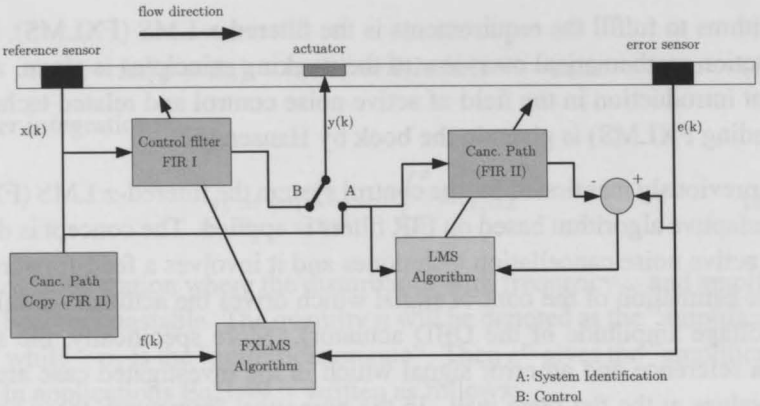

Figure 3.9: Schematic of the working principle for the filtered-x LMS control algorithm.

where the convergence coefficient μ is a constant used to increase or decrease the convergence of the adaptation process. The choice of μ is extremely important for the final control performance. As will be shown in Chapter 9 too small μ leads to slow convergence and reduced performance while too large μ renders the algorithm unstable. For this study a variation of the standard FXLMS algorithm is used where μ is normalized by the strength of the reference signal in order to increase the robustness of the convergence process and decouple partially the stability of the algorithm from the absolute values of the reference signal:

$$\mu = \frac{\beta}{\mathbf{x}^T(k)\mathbf{x}(k)} \tag{3.55}$$

where β is a predifined constant.

In the control algorithm $\mathbf{f}(k)$ is produced by filtering the reference signal with a secondary FIR filter (FIRII) which is a digital representation of the natural cancellation path:

$$f(k-j) = \sum_{i=0}^{M-1} \hat{c}_i(k)x(k-i-j) \tag{3.56}$$

where $\mathbf{c}(k) = [c_1(k), c_2(k), \ldots c_{M-1}(k)]^T$ and M is the length of $\mathbf{c}$. This is

done in order to have a valid comparison between reference and error signals for the update process. The cancellation path copy (FIRII) is obtained using a system identification routine based on a modified version of the LMS adaptive algorithm. More specifically the actuator is driven by a predetermined signal which in this case is the reference signal $\mathbf{x}(k)$. At the same time $\mathbf{x}(k)$ is passed through the secondary filter. The produced signal is then subtracted from the error signal and used in the LMS routine to update the coefficients of FIRII. By using the difference of the two signal to update FIRII, the final weight coefficients of the secondary filter are such that $f(k) = e(k)$. This effectively means that FIRII, in its final converged state, can model the natural cancellation path as it was initially required by the primary control system. The control sequence starts first by running a System Identification procedure (circuit A in Fig.3.9). As soon as the system ID algorithm converges and FIRII is available the actual control can begin (circuit B).

Both the system identification and control algorithms are implemented in the Open FOAM framework and operate in parallel to the flow solver. Several parameters of the algorithm such as primary and secondary filters lengths, sampling rate, weights update rate and convergence values (β) are set prior to the simulation.

Part I

Diagnostics

Felix, qui potuit rerum cognoscere causas.

Publius Virgillius Maro, *Georgica*

Fortunate who was able of things to know the causes.

Virgil, *Georgics*

Chapter 4

Actuation in Quiescent Flow Conditions

The simplicity in construction and operation which is so typical of DBD actuators, is able to provide a wealth of possible configurations in terms of geometrical, electrical and operational properties. Prior to any attempt in utilizing DBD actuators in a flow control application, a clear view of the operating principles must be established. Furthermore, the influence of many geometric and electrical properties on the actuation effect should be investigated and mapped. Through appropriate parametric studies, an operational envelope for the actuators can be created which can serve as the starting basis for any intended flow control effort.

This chapter is dedicated on the establishment of a clear description and understanding of the phenomenological actuation effect of the DBD actuators and the dependence of their performance on several operational parameters. The investigation is performed in conditions of quiescent fluid in order to isolate the effect of the actuator. Several parameters are investigated using a multitude of measurement techniques and diagnostic tools. Two major campaigns are initiated to this goal. Firstly, a large parametric study is performed with the use of HWA and direct thrust measurements. This choice is made due to the robustness and time efficiency these measurement techniques can provide, properties which are essential for mapping a large number of parameters. Sec-

ondly, fewer selected cases are investigated with the used of time resolved PIV in order to provide further insight into several steady and unsteady phenomena occurring during actuation.

4.1 Experimental Setup

4.1.1 The actuator

The actuators consist of thin rectangular copper electrodes made out of self-adhesive copper tape separated by a dielectric layer. The thickness of the electrodes is 60 μm while the width varies between 5 mm and 25 mm depending on the test case. Their effective spanwise length (along which plasma is generated) is 200 mm for the majority of measurements. Longer actuators (300 mm) are used for the thrust measurements. The electrodes are separated by one to three Kapton tape layers depending on the test case. The thickness of each layer is 2 mil (50.8 μm). The electrodes and dielectric are supported by a 10 mm thick, 200x100 mm rectangular POM plate. The free ends of both electrodes are folded around the POM plate. The plate is then fixed on a rectangular POM base carrying two aluminum connectors which contact the electrodes. The connector of the upper electrode is connected to the HV output cable of a TREK 20/20C HV amplifier ($\pm 20\ kV$, $\pm 20\ mA$, $1000\ W$) while the connector of the lower electrode is grounded. The design of the actuator is specifically chosen to be modular for the easy interchange of different configurations of electrodes.

The actuator operation is controlled remotely via a computer workstation were the driving signal is created by software (LabView) and is sent to the amplifier via a Digital/Analog (D/A) converter. The amplifier provides direct readings of the output voltage and current through internal measurement probes. While the internal voltage probe gives sufficiently accurate readings the internal current probe has been found to be too slow to resolve high frequency current fluctuations such as the discharge currents typically found in plasma actuators. To resolve this, a resistance is placed between the lower electrode and the grounding cable and voltage is measured across it indicating the traveling current.

When the actuator is activated, plasma appears near the inner edge of the two electrodes in the form of a uniform purple glow cloud with decreasing inten-

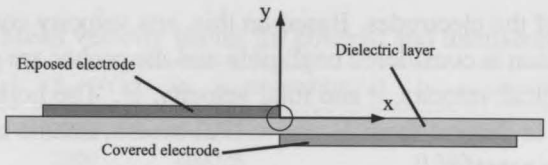

Figure 4.1: The actuator layout and coordinate system (not to scale)

sity towards the covered electrode. The ionization region appears to be uniform and constant along the length of the electrodes although it is known that it consists of multiple nanosecond discharges of high current flow [102].

4.1.2 Measurement techniques

To reduce the effect of any external disturbances on the measurements, the tests are ran in still air. This approach has the advantage of increasing the accuracy of the measurements since the induced velocities are expected to be in the order of 1 m/s as well as giving more insight to the 'pure' induced velocity field. A major drawback of this approach is the lack of insight into the interaction process of the actuator and a given external flow. Although this is not a major issue for the parametric study of this chapter, experiments in a low-turbulence boundary-layer tunnel are conducted and described in a following chapter. For ensuring an environment of still air a test box is constructed from clear Plexiglas for optical access. The box has the shape of a cube with a 500 mm long side. The base of the box has a rectangular slot were the actuator fits in, flushed with the base of the box thus minimizing any effects of roughness on the induced velocities. The box is equipped with ventilation due to the large amounts of ozone produced from the ionization process.

Hot Wire Anemometry

For the flow diagnostics the use of Hot Wire Anemometry (HWA) is selected. HWA has been found best suited for a parametric study as it combines sufficient accuracy with relative ease of use. Furthermore, with the use of an x-probe or two single wire probes resolving of both horizontal and vertical velocity components is possible. Based on an initial two-dimensionality study the flow has been identified as uniform and constant along approximately 80

% of the span of the electrodes. Based on this, any velocity component in the spanwise direction is considered negligible and the probes are placed in order to measure vertical velocity, v and total velocity, U. The horizontal velocity component, u, is derived from U and v. All measurements are taken at the half-span of the actuator.

High frequency interference

In the experimental studies described in this and the following chapters, the first measurement point is placed at 7 mm from the actuator. In such close proximity, the hot-wire readings present a strong fluctuating component at the carrier frequency f_{ac} of the actuation signal, which in this case is 2 kHz. It is known from other investigations [15] that in the plasma formation area velocity fluctuations appear, corresponding to the carrier frequency.

These are due to the physical interaction between charged and neutral particles. It is thus important to establish that the fluctuations in our signal are due to EM noise and not due to physical effects such as the plasma-flow interaction. To this goal high-speed (10 kHz) PIV data from the experimental campaign described in in the next section are used. As can be seen from Fig.4.2 the high frequency fluctuations appear very near the inner electrode edge (plasma formation area) but damp out and eventually disappear prior to the first hot-wire measurement point (at x = 7 mm). Based on these observations the high frequency fluctuations which remain in the velocity signal will be considered as EM noise and filtered out using a low pass filter.

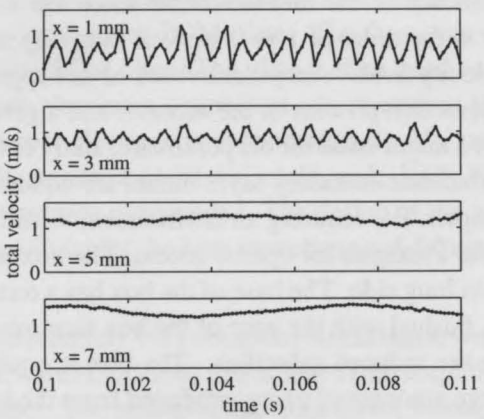

Figure 4.2: Time trace of total velocity for different x positions (V_{app} = 10 kV_{pp}, f_{ac} = 2 kHz). High-speed PIV measurements. All data sampled at y = 0.75 mm.

Table 4.1: Mean velocity values for covered and uncovered actuators.

V_{app} (kV_{pp})	f_{ac} (Hz)	u_{mean} covered (m/s)	u_{mean} uncovered (m/s)
6	2000	-0.0035	0.2493
8	2000	-0.0026	0.3820
10	2000	-0.0030	0.4723
8	1000	-0.0046	0.3502
8	3000	-0.0032	0.4264
8	4000	0.0011	0.4581

An additional consideration is the effect of the EM noise on the time averaged value of velocity which cannot be corrected using filtering. In order to investigate this effect, HWA measurements are conducted in the vicinity of the actuator. The actuator is then covered with a plastic sheet in order to obstruct the induced flow field from reaching the hot wire sensor and the measurements are repeated. Care has been taken in the design of the cover as to not interfere with the plasma region. A comparison between the covered and uncovered actuator is presented in Fig.4.3. Additionally, the mean values of velocity for different voltages and frequencies are presented in Tab.4.1. It is clear that the EM noise has no significant effect on the time averaged value of induced velocity.

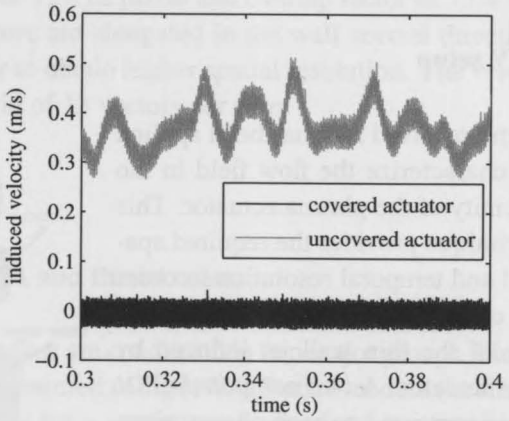

Figure 4.3: Induced velocity for covered and uncovered actuators for V_{app} = 10 kV_{pp}, f_{ac} = 2 kHz. Sampled at x = 7 mm, y = 0.75 mm.

Load cell

For the direct thrust measurements an electronic ME-messsysteme ®KD-40S strain-gage load cell is used. The nominal force range is $\pm$ 2 N with an accu-

racy of 0.1% (2 mN). A light PMMA (Plexiglass) plate of 5 mm thickness, which carries the electrodes and dielectric, is directly mounted on the load cell. The connection of the electrodes to the HV and ground connectors is via thin copper wires to minimize signal contamination from external vibrations. Tests are repeated three times to minimize any error due to load cell relaxation. The measurement is continued for ten seconds before actuation and thirty seconds after in order to ensure that the steady flow regime is achieved. The sampling rate of the thrust measurement system is 100 Hz. The thrust is then calculated by comparing the time averaged readings from the two time periods.

PIV setup

Time-resolved PIV has been applied to characterize the flow field in the vicinity of the plasma actuator. This technique provides the required spatial and temporal resolution in order to characterize the transient behavior of the thin wall jet induced by the actuator. A two component PIV configuration has been chosen since the large span of the actuator ensures minimal 3D effects.

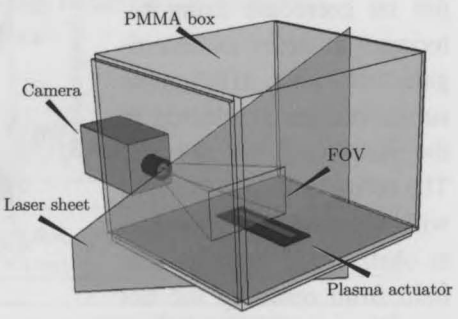

Figure 4.4: The PIV experimental setup (not to scale)

The plasma actuator is placed flushed on the bottom of the Plexiglas box. A Photron Fastcam SA1 high speed CMOS camera of 1024×1024 pixels (full sensor size) is used to image the field-of-view (FOV). Image acquisition has been conducted at 10 KHz rate in single-frame mode. This implies a time separation of 100 μs between successive images. A Nikkor 105 mm objective is set at f-stop 4 and is used along with extension tubes in order to achieve 0.8 magnification and a FOV of 15×6 mm. To achieve the high sample rate needed for these measurements, the sensor is cropped to a size of 1024×512 pixels. The air in the Plexiglas box is seeded with olive oil droplets of approximately 1 μm diameter generated by a TSI atomizer. The particles at the mid span of the actuator are illuminated by a light sheet of $2mm$ thickness generated by a Quantronix Darwin-Duo laser

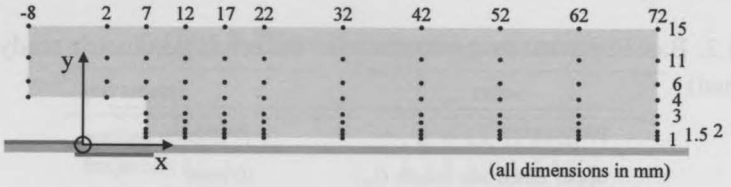

Figure 4.5: The locations for the measurement mesh points

system with an average output of 80 W at 3 kHz. The images are analyzed using Davis 7.4 (Lavision GmbH) by cross-correlating successive images. Final interrogation window size of 12×12 pixels and overlap factor of 75% are used. The interrogation windows are elongated in the wall normal direction using a 4:1 aspect ratio in order to obtain higher spatial resolution. The velocity vectors are returned on a grid of 13 vectors per mm.

4.1.3 Test cases

Broad parametric study: HWA and thrust cases

The measurements in quiescent flow are conducted in two major groups. Firstly a large number of test cases is measured using HWA. Statistical data (i.e time-averaged velocities) are obtained for a spatial mesh of points covering most of the downstream area of the actuator as well as a small part of the upstream area (Fig. 4.5). Due to the nature of the ionization region, a small area near the inner edge of the electrodes cannot be approached by the hot-wires due to short-circuiting hazard. The mesh consists of 89 non-uniformly positioned nodes for better resolution of the flow-field near the wall as well as near the actuator itself. The coordinate system presented here will be used throughout this work. The origin is located horizontally at the inner edge of the upper electrode and vertically on the wall.

Additionally to the induced velocities, thrust measurements are taken by directly measuring the reaction force on the actuator due to the acceleration of the induced flowfield. For this, an electronic strain-gage load cell is used. In order to perform accurate thrust measurements some minor modifications are made to the experimental setup. The POM base is replaced by a light Plexiglas plate of 5 mm thickness which is directly mounted on the load cell. The spanwise length of the electrodes is also increased from 200 mm to 300 mm

Table 4.2: Baseline actuator parameters for the broad parametric study (HWA and thrust)

parameter	value
upper electrode length (l_u)	10 mm
lower electrode length (l_l)	25 mm
horizontal gap (g)	0 mm
dielectric thickness (t_d)	0.06 mm
electrode thickness (t_u, t_l)	0.06 mm
electrode material	copper
dielectric material	Kapton ®polyimide
applied voltage (V)	8 kV_{pp}
carrier frequency (f_{ac})	2 kHz
voltage waveform	sine
duty cycle (D)	100 %
pulsed frequency (f_p)	0

Table 4.3: Geometrical control parameters.

parameter	test values
upper electrode length (l_u)	5, 10, 20 mm
lower electrode length (l_l)	5, 10, 15, 20, 25 mm
horizontal gap (g)	-5, -2.5, 0, 1.5 mm
dielectric thickness (t_d)	0.06, 0.12, 0.17 mm

to increase the total value of the thrust and thus the accuracy of the measurement. Furthermore, the connection of the electrodes to the HV and ground connectors is done via thin copper wires to minimize disturbances coming from the cables. Each test case is measured three times in order to minimize the influence from any load cell relaxation.

For the majority of the HWA test cases a *ceteris paribus* assumption methodology is used, keeping all other parameters fixed except the control parameter. A baseline actuator (Table 4.2) can be defined in this way indicating all the fixed parameters. For each test case the fixed values of the actuator correspond to the baseline values unless stated otherwise and only the control parameter is changed. The experiments are divided in two sub groups for time-averaged velocity measurements and thrust measurements respectively.

The first experimental sub-group involves a parametric study on several geometrical and electrical parameters of the plasma actuators. Time-averaged

Table 4.4: Electrical control parameters.

parameter	value
applied voltage (V)	6, 8, 10, 12 kV_{pp}
frequency (f_{ac})	1, 1.5, 2, 2.5, 3 kHz
duty cycle (D)	12.5, 25, 50, 100 %
(@ f_p = 100 Hz)	
pulsed frequency (f_p)	50, 100, 150, 200 Hz
(@ D = 25 %)	
electrode lengths [l_u, l_l]	a: [5, 10 mm], b: [10, 10 mm],
for V and f_{ac} cases	c: [5, 15 mm]
electrode lengths [l_u, l_l]	
for D and f_p cases	[5, 15 mm]
dielectric thickness (t_d)	
for all cases	0.12 mm

velocity measurements are taken for each case at the nodes of the defined mesh (Fig.4.5). The investigated geometrical properties are shown in Fig.4.6 and consist of the lengths of the two electrodes l_u and l_l, the thickness of the dielectric layer t_d and the horizontal gap g between the inner edges of the electrodes. The values for the respective test cases are shown in Table 4.3.

For the electrical properties investigation the tested parameters involve the applied voltage V_{app} and the frequency of the applied voltage f_{ac}. In contrast to the geometrical study the electrical properties investigation does not require the physical modification of the actuator. This shortens the testing time considerably enabling the investigation of three actuators for voltage and frequency. All the test parameters with respective values are presented in Table 4.4.

The second experimental sub-group involves direct thrust measurements using the load cell. Thrust measurements are taken for three geometrical parameters of the plasma actuator, namely upper and lower electrode lengths and horizontal gap. For each test case a sub-matrix of applied voltages between 6 kV_{pp} and

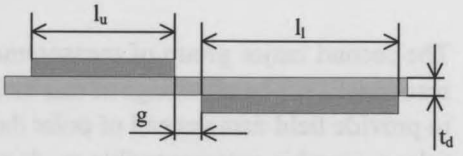

Figure 4.6: The investigated geometrical parameters of the actuator.

Table 4.5: Test cases for thrust investigation

parameter	**value**
upper electrode length (l_u)	5, 10, 15 mm
lower electrode length (l_l)	5, 10, 15 mm
horizontal gap (g)	-2.5, -1.5, 0, 1.5, 2.5 mm
applied voltage (V_{app})	5 to 15 kV_{pp} (steps of 0.5 kV_{pp})
frequency (F)	0.5 to 4 kHz (steps of 0.25 kHz)
for geometrical test cases all possible combinations of:	
applied voltage (V_{app})	6, 8, 10, 12, 14 kV_{pp}
	×
frequency (F)	0.5, 1, 1.5, 2, 2.5, 3 kHz
for voltage and frequency test cases:	
electrode lengths [l_u, l_l]	[5, 15 mm]

14 kV_{pp} and frequencies between 0.5 kHz and 3 kHz is constructed and all combinations are tested. Furthermore, two dedicated test cases are performed for voltage and frequency variation respectively. These involve a fine grid of voltages for three different frequencies and a respectively large number of frequencies for three different voltages. Simultaneously to the measurements, voltage and discharge current are measured in order to calculate the power consumption. Due to the extremely small values of the vertical component (within the accuracy limits of the load cell) of the produced body-force, only the horizontal component of thrust is considered accurate enough to be presented here. The overview of the parameters tested is shown in Table 4.5.

Refined parametric study: PIV cases

The second major group of measurements is performed with the use of time resolved PIV. The advantage of this technique compared to HWA is the ability to provide field data instead of point data, can resolve areas of high ionization (plasma) and is not susceptible to electromagnetic interference. On the other hand the produced amount of data and the post processing time are limiting factors on the number of test cases that can be performed. In order to remain within time efficient limits, only one actuator is tested. This is identical with

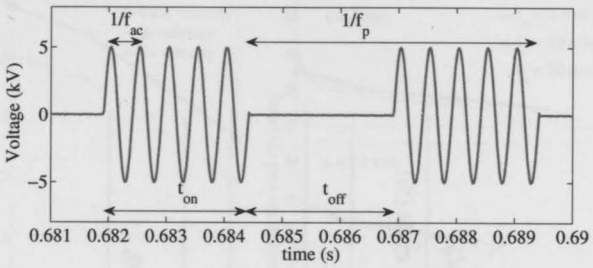

Figure 4.7: Sample of the voltage signal with the characteristic actuation values. (V_{app} = 10 kV_{pp}, f_{ac} = 2 kHz, f_p = 50 Hz, D = 50%)

actuator described in Tab.4.4

The investigation is conducted in two parts. These involve the continuous and pulse operation respectively. For the continuous operation the parameters which are tested are the applied voltage (V_{app}) and the carrier frequency (f_{ac}). Two sub-sets of measurements are taken, the first for a fixed f_{ac} and varying V_{app} and the second for a fixed V_{app} and fixed f_{ac}. For the pulse operation V_{app} and f_{ac} are kept fixed while the pulsation parameters are varying. These consist of the pulse frequency (f_p) and the duty cycle (D). Throughout this study the duty cycle is defined as the percentage of time (t_{oper}) the plasma actuator is operating in a single pulsation period (τ_p):

$$D = \frac{t_{oper}}{\tau_p} \times 100 = t_{oper} \times f_p \times 100 \tag{4.1}$$

A schematic of a typical actuation signal is shown in Fig.4.7.

Table 4.6: Test cases and parameters for the refined parametric study (PIV)

test case	**applied voltage** $[kV_{pp}]$	**carrier frequency** $[kHz]$	**pulse frequency** $[Hz]$	**duty cycle** [%]
continuous operation				
applied voltage (V_{app})	8, 10, 12, 14, 16	2	0	100
carrier frequency (f_{ac})	10	1, 2, 3, 4	0	100
pulse operation				
pulse frequency (f_p)	10	2	50, 200, 350	50
duty cycle (D)	10	2	50	25, 50, 75

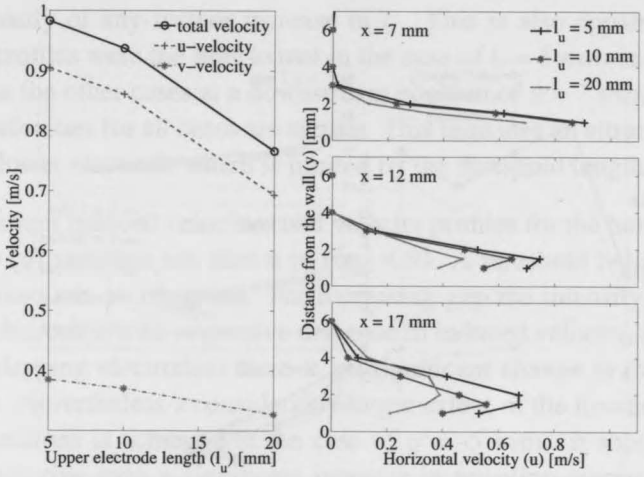

Figure 4.8: Maximum induced velocities (left) and u-velocity profiles (right) for upper electrode length (l_u) variation

4.2 Results

4.2.1 Broad parametric study using HWA

The induced flow velocities under the variation of the length of the upper electrode (l_u) is shown in Fig. 4.8. It is apparent that the maximum induced velocity is moderately affected by l_u. This is also evident in the development of the flow to more downstream stations. The slight increase in the velocities with decreasing electrode length can be attributed to the strengthening of the electric field caused by the shorter electrode. It should be noted here that higher velocities are occurring in the close vicinity of the actuator where the hot wire probe cannot approach. This area will be resolved by the subsequent PIV measurements.

For the variation of the length of the lower electrode (l_l) it is apparent that a threshold length of about 5 mm exists, above which there is no significant influence on the induced flow (Fig. 4.9). For short lower electrodes the plasma region is physically limited by the length of the grounded electrode below the dielectric. For cases in which the length of the lower electrode exceeds the threshold, electron-ion recombination processes limit the plasma region

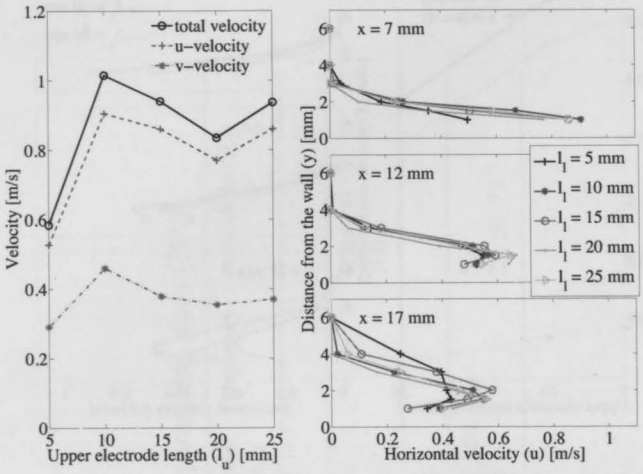

Figure 4.9: Maximum induced velocities (left) and *u*-velocity profiles (right) for lower electrode length (l_l) variation

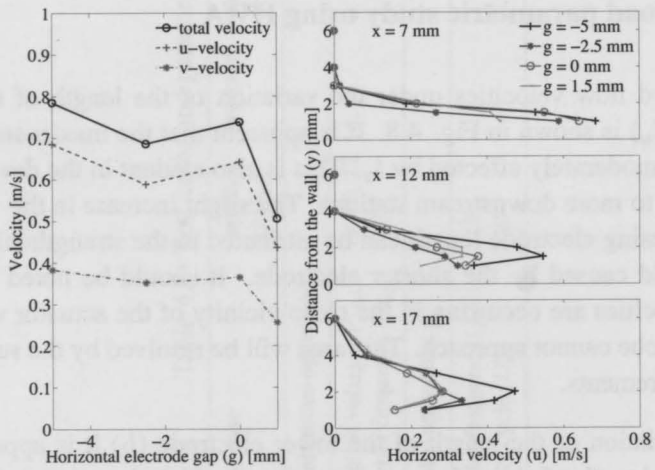

Figure 4.10: Maximum induced velocities (left) and *u*-velocity profiles (right) for horizontal electrode gap (g) variation

independently of any further increase in l_l. This is also apparent from the velocity profiles were the flow extent in the case of l_l = 5 mm is significantly lower than the other cases at a downstream position of x = 7 mm. Yet by x = 12 mm velocities for all cases are similar. This indicates an attractor behavior from the lower electrode which is limited by the threshold length.

The maximum induced velocities and velocity profiles for the horizontal electrode gap (g) variation are shown in Fig. 4.10. A threshold behavior similar to the l_l case can be observed. For increasing gap the intensity of the electric field decreases with respective decrease in induced velocity. For negative gap (overlapping electrodes) there is no significant change in the maximum velocities. Nevertheless a considerably larger extent of the flowfield in downstream positions is achieved in the case of g = -5 mm. It should be noted that for negative gaps a significant increase in traveling current and subsequently consumed power has been registered. This leads to faster degradation of the dielectric and should be taken under consideration in future applications.

The dielectric thickness (t_d) (Fig. 4.11) is also directly related with the distance between the two electrodes which has a clear impact on the intensity of the electric field and the induced velocity. The relation between maximum velocities appears to be linear. On the other hand this is not to the case for more downstream positions as can be seen from the velocity profiles. This suggests that the influence of the dielectric thickness on the electric field is only local at the inner electrode edges. In general it seems that thinner dielectrics produce locally strong velocity components near the inner electrode edge, while thicker dielectrics give a more uniform flow in downstream direction.

The influence of the applied voltage (V_{app}) is presented in Fig. 4.12. Both the maximum velocity and the downstream evolution is in direct relation with the applied voltage for the tested range of 6 to 12 kV_{pp}. In contrast to the dielectric thickness variation, the effect on the electric field here seems to be global and directly scales up the entire induced flowfield. During this test case, the value of approximately 5 kV_{pp} is identified as the discharge breakdown threshold below which no ionization is observed for the current geometrical configuration.

Similar to the applied voltage behavior, an increase in the frequency f_{ac} leads to increase in maximum velocities and downstream evolution of the flowfield (Fig. 4.13). Also evident from this test case is the rapid degradation of the

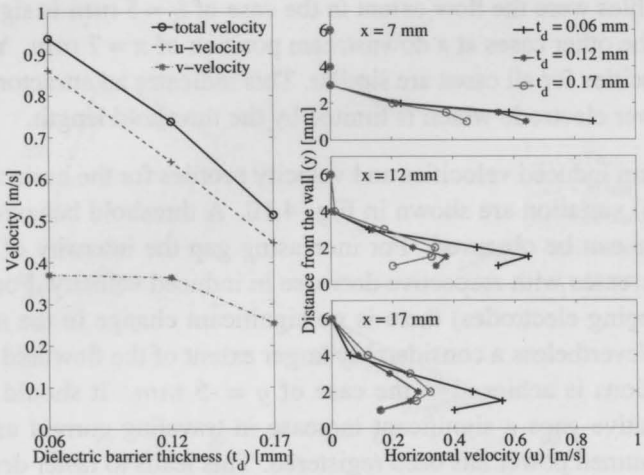

Figure 4.11: Maximum induced velocities (left) and u-velocity profiles (right) for dielectric thickness (t_d) variation

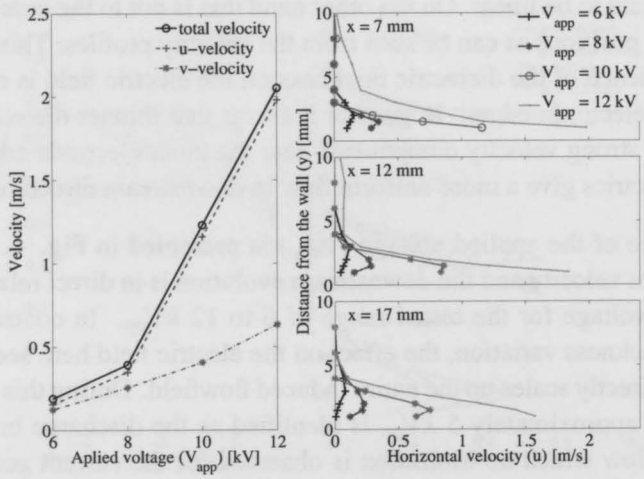

Figure 4.12: Maximum induced velocities (left) and u-velocity profiles (right) for applied voltage (V_{app}) variation

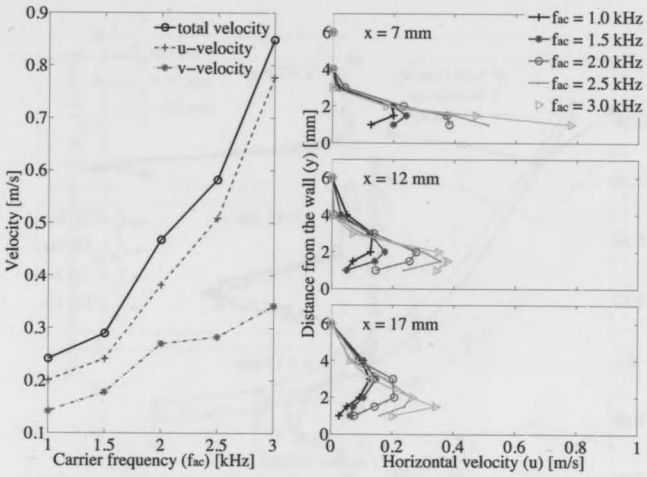

Figure 4.13: Maximum induced velocities (left) and *u*-velocity profiles (right) for frequency (f_{ac}) variation

dielectric layer with increased frequency. Although irrelevant to the scope of this study this is an important factor in the case of any feasible application and should be taken into account.

Until this point the operation of the actuator has been in continuous mode. Additionally, several cases have been tested in pulsed mode and the respective time averaged quantities have been measured. For the pulsed operation velocities are shown in Fig. 4.14 for pulse frequency f_p and Fig. 4.15 for duty cycle (D). It is interesting to note that there is no significant influence on the velocity value from variations in pulse frequency. Also apparent is the relatively large *v*-velocity component for larger duty cycles which could indicate some form of vortical structures. Although these test cases involve pulsed operation, the velocity measurements are time-averaged giving rise to the need for a time resolved study in order to clarify some outstanding issues, such as the large vertical velocities, as well as to gain more insight to the process. This is achieved using the time resolved PIV measurements and is presented in the following section.

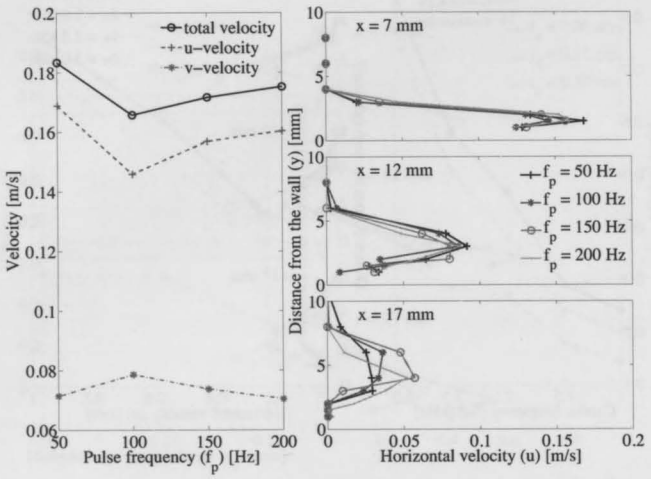

Figure 4.14: Maximum induced velocities (left) and u-velocity profiles (right) for pulse frequency (f_p) variation. The duty cycle (D) is 25 %

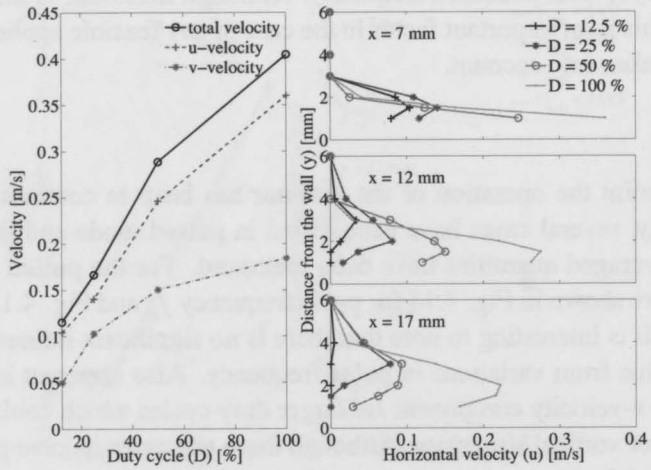

Figure 4.15: Maximum induced velocities (left) and u-velocity profiles (right) for duty cycle (D) variation. The pulse frequency (f_p) is 100 Hz

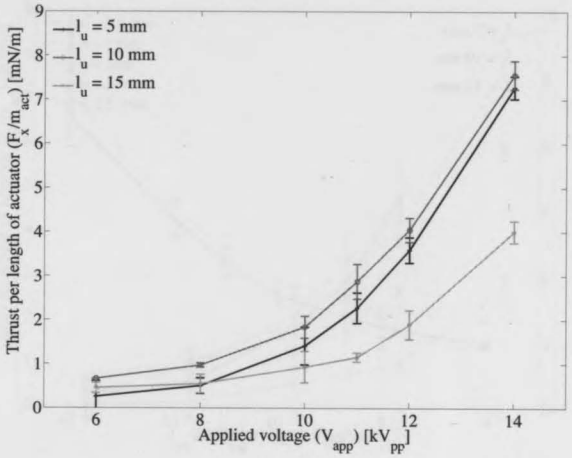

Figure 4.16: Thrust measurements for upper electrode length (l_u) variation. Frequency (f_{ac}) is 2 kHz

4.2.2 Broad parametric study using thrust measurements

Thrust measurements for variation of the upper electrode length are shown in Fig. 4.16. There is little influence on the thrust apart from the case of l_u = 15 mm were the values at high voltages are smaller. The behavior of the thrust with voltage appears to follow a power law. This property is investigated in more detail in following test cases.

For the lower electrode length variation (Fig. 4.17) the thrust appears to be entirely independent to any change in length. This corresponds well to the time-averaged velocity measurements. Although the time-averaged data indicate a decrease in maximum velocity for the case of l_l = 5 mm the downstream evolution of the flowfield, which in integrated form reduces to the total thrust, is uniform among the test cases.

Measurements for the variation of the horizontal electrode gap are shown in Fig. 4.18. As it is already shown from the time-averaged data, positive gaps have a reducing effect on the intensity of the electric field and all induced quantities including thrust. For negative gaps no significant dependence of the thrust exists although the traveling current and thus the power consumption increase considerably. For the case of 14 kV_{pp} no negative gap measurements

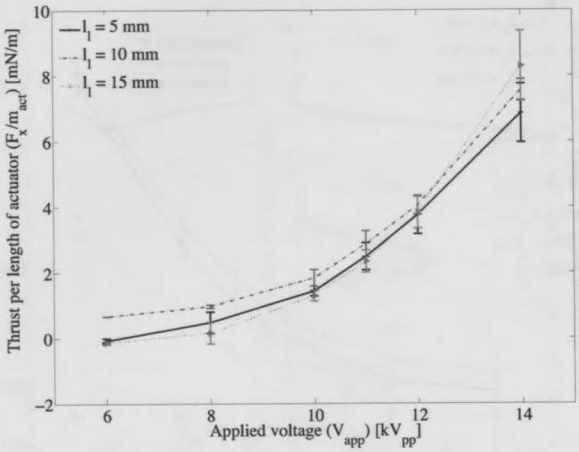

Figure 4.17: Thrust measurements for lower electrode length (l_l) variation. Frequency (f_{ac}) is 2 kHz

are taken due to the destruction of the dielectric by the increased discharge current.

So far it is clear that there is a strong thrust dependence on applied voltage. Geometrical parameters are also influencing the thrust magnitude albeit to a lesser degree. Thrust measurements for the applied voltage (V_{app}) variation are shown in (Fig. 4.19). The sequence of voltages is tested for three different frequencies. Additionally, the current traveling through the actuators is measured simultaneously to the thrust enabling the calculation of the dissipated power (Fig. 4.20). A power law seems to govern both the thrust and power behavior under different voltages.

For the variation in frequency (f_{ac}) the thrust measurements are shown Fig. 4.21. The sequence of frequencies is tested for four different voltages. The power curves are shown in Fig. 4.22. As with the voltage variation, thrust behavior seems to be almost linear with frequency. The dispersion in the results is caused due to the inherent difficulties in measuring the thrust more accurately. In contrast, the measurements of the current show minimum dispersion allowing a more safe speculation on the governing relation. Careful examination of the power curves reveals a weak power law connecting frequency and power. More accurate thrust measurements are needed in order to verify if the

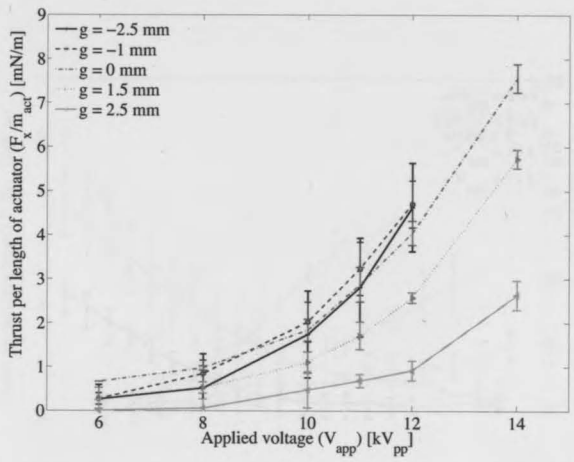

Figure 4.18: Thrust measurements for horizontal electrode gap (g) variation. Frequency (f_{ac}) is 2 kHz

same law applies for thrust behavior.

To this point it is clear that there is a thrust dependence on applied voltage. Geometrical parameters are also influencing thrust magnitude albeit to a lesser degree. In order to gain more insight into the relation of thrust and voltage, a fine grid of frequencies and voltages is devised and a new actuator is tested. The tested actuator has an upper electrode length (l_u) of 5 mm, lower electrode length (l_l) of 10 mm and zero horizontal electrode gap (g). Dielectric thickness (t_d) is 0.1 mm. As with the previous investigations, the spanwise length of the actuator (l_a) is 300 mm. The frequency range lies between 0.5 and 4 kHz with a step size of 0.25 kHz while the applied voltage values span from 5 to 15 kV_{pp} in steps of 0.5 kV. The upper right area of the grid, which consists of high voltages and high frequencies, is not tested due to the HV amplifier slew-rate limitations. Simultaneous to the thrust measurements, discharge current is also measured in order to calculate the power consumption.

From the results of the fine grid investigation, several observations can be made on the behavior of thrust and power consumption. Thrust and in extension body force appear to be connected with voltage through a power law as it is already observed from the geometrical properties investigation, while

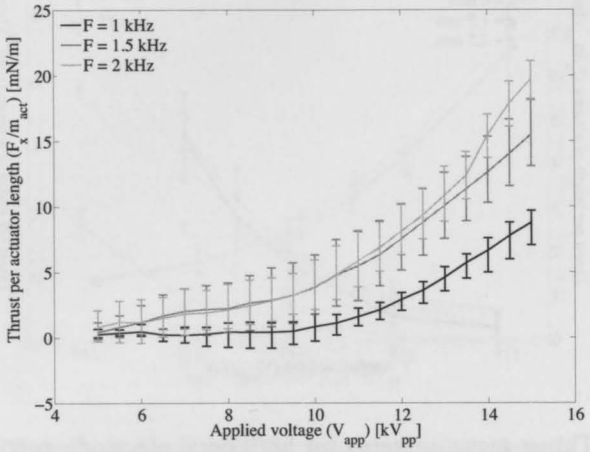

Figure 4.19: Thrust measurements for applied voltage (V_{app}) variation

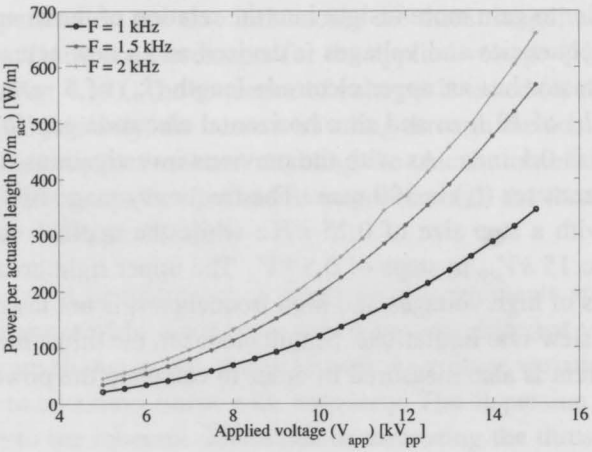

Figure 4.20: Consumed power for applied voltage (V_{app}) variation

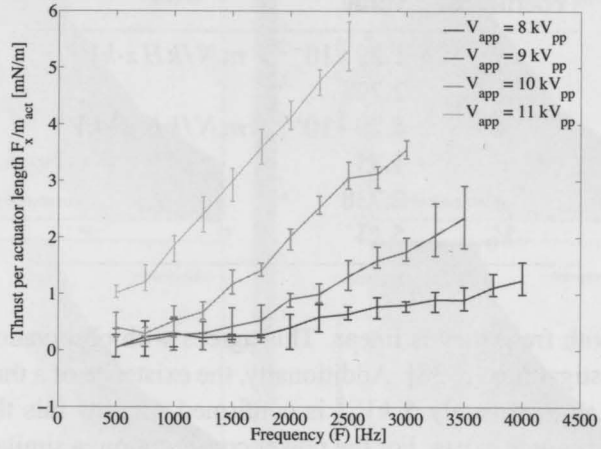

Figure 4.21: Thrust measurements for frequency (f_{ac}) variation

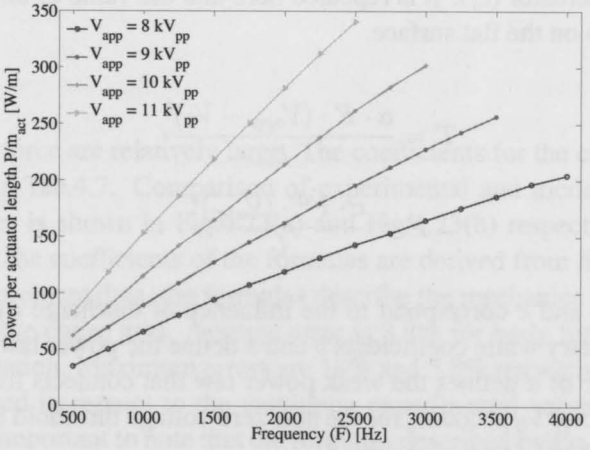

Figure 4.22: Consumed power for frequency (f_{ac}) variation

Table 4.7: Fitting coefficients for the fine grid investigation

coefficient	value	
a	$1.29 \cdot 10^{-2}$	$mN/kHz{\cdot}kV^b$
b	2.798	
c	$4.29 \cdot 10^{-2}$	$mN/kHz^d{\cdot}kV^e$
d	1.35	
e	2.738	
V_0	$5\ kV$	

the relation with frequency is linear. This agrees with observations made by previous investigations [3, 38]. Additionally, the existence of a threshold voltage value of approximately 5 kV_{pp} is confirmed. Below this threshold, no detectable body force exists. For the power consumption, a similar power law exists in relation to the applied voltage. Diverging from the body force case, a weak power law applies also in relation to the frequency. This weak power law dependence has not been reported by any previous investigations. Based on the observed behavior, two fitting formulas can be derived connecting voltage (V_{app}) and frequency (f_{ac}) with thrust (T) and power consumption (P) respectively. F_b and P are considered to be normalized with the spanwise length of the actuator (l_a). It is repeated here that the value of thrust includes the shear force on the flat surface.

$$T = \frac{a \cdot F \cdot (V_{app} - V_0)^b}{l_a} \tag{4.2}$$

$$P = \frac{c \cdot F^d \cdot (V_{app})^e}{l_a} \tag{4.3}$$

Coefficients a and c correspond to the influence of discharge dynamics and actuator geometry while coefficients b and e define the power law on the voltage. The value of d defines the weak power law that connects frequency and power. The factor V_0 accounts for the non-zero voltage threshold below which no significant body force is observed.

For deriving the coefficients of Eq.4.2 and Eq.4.3, data from the fine grid investigation is fitted only for a range of frequencies from 0.5 to 1.25 kHz were high voltage values can be reached by the amplifier and thus the values

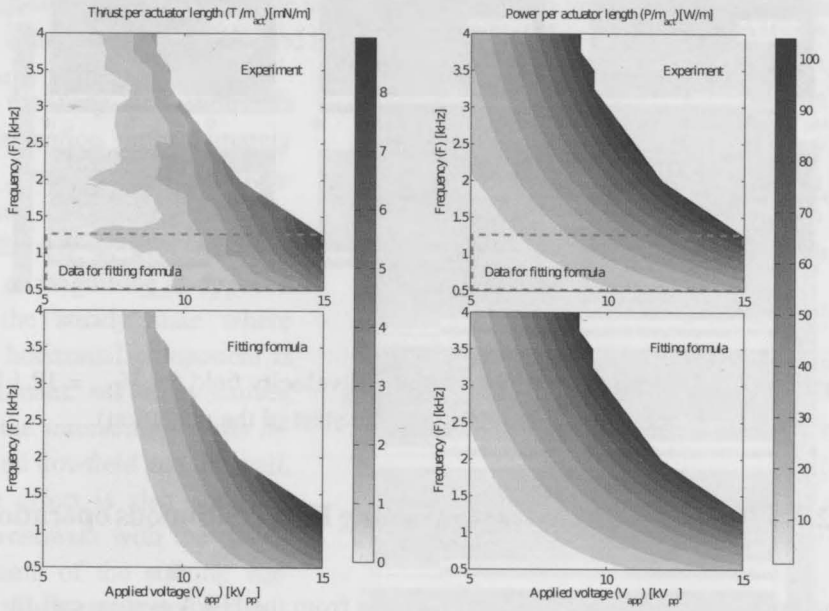

(a) (b)

Figure 4.23: Experimental and modeled thrust (a) and power (b) for voltage and frequency variation.

of the body force are relatively large. The coefficients for the current actuator are shown in Tab.4.7. Comparison of experimental and modeled thrust and power values is shown in Fig.4.23(a) and Fig.4.23(b) respectively. Despite the fact that the coefficients of the formulas are derived from fitting only part of the measurement data, the formulas describe the mechanics of the actuator well across the entire grid. Average error is 3.8% for body force and 2% for power estimation. Maximum errors are 14% and 5.8% respectively. All errors are referenced in respect to the maximum experimental values of force and power. It is important to note that the formulas described by Eq.4.2 and Eq.4.3 are only valid for the tested range of frequencies and voltages. Regarding the power law connecting voltage with thrust and power, the values of the exponent (coefficients b and e) lie between similar reported values [38, 35, 42], although these researchers used thicker dielectrics.

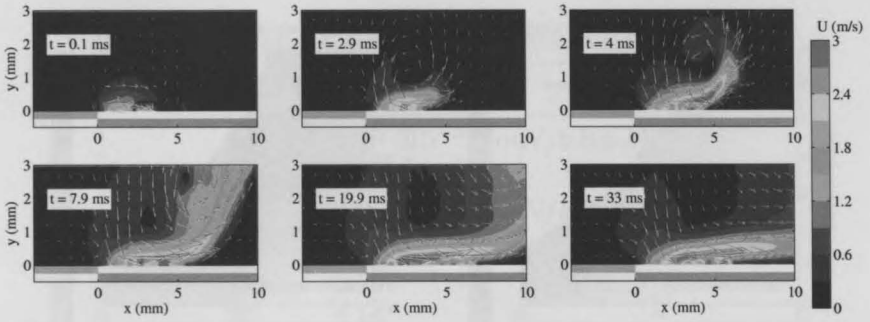

Figure 4.24: Snapshots of the evolving total velocity field for $V_{app} = 12\ kV_{pp}$, $f_{ac} = 2\ kHz$ (time values are relative to the start of the actuation).

4.2.3 Refined parametric study using PIV: continuous operation

The limitations in spatial resolution arising from the HWA system call for the use of more global diagnostic techniques in order to fully resolve the induced flowfield. The most ideal method for such cases is time resolved PIV although care must be taken in the selection of test cases due to the complexity and time consumption inherent is this technique. The actuator is initially tested in continuous operation mode where the applied voltage is alternating with a fixed carrier frequency (f_{ac}). Several voltages and frequencies are tested in order to establish the dependence of the induced flowfield on these parameters. In all cases the measurements are taken prior to the start of the actuation in order to resolve the initial transient of the induced jet. The measurements are continued until after the flowfield has reached a quasi steady state in order to acquire statistics information as well.

The transient development of the induced flowfield is presented in Fig.4.24 for the case of 12 kV_{pp}. The flow reacts faster than the PIV resolution time (0.1 ms) since velocity components are present already at the second PIV frame after actuation. The development is similar to that of a wall jet with a typical starting vortex forming within the first 5 ms of actuation. Through interaction with the wall, the vortex convects out of the FOV in the downstream direction. After the starting vortex is at a sufficient distance from the actuator, the flowfield settles into a wall jet with the dominant velocity component established parallel to the wall. A weak suction effect is observed at an upstream

location where fluid from the still flow is drown in a vertical direction towards the actuator and then injected forward.

At the very first moments of actuation (approximately the first 5 ms) the horizontal and vertical components are of the same order of magnitude as opposed to the steady state where the horizontal component is dominant. This is caused by the interaction of the induced flowfield and the wall. The effect is also observed downstream with the development of the starting vortex. Such events present particular interest in flow control applications where both horizontal and vertical velocity components might be of use. Since this effect appears only in the transient phase of development, the continuous operation of the actuator seems not to be the optimum for achieving this kind of effects. In contrast, a pulse mode of operation where the actuator forces the flow in an 'on' and 'off' manner would suggest that this transient behavior can be repeatable and controllable. The pulse operation will be addressed in more detail in a subsequent section of this chapter.

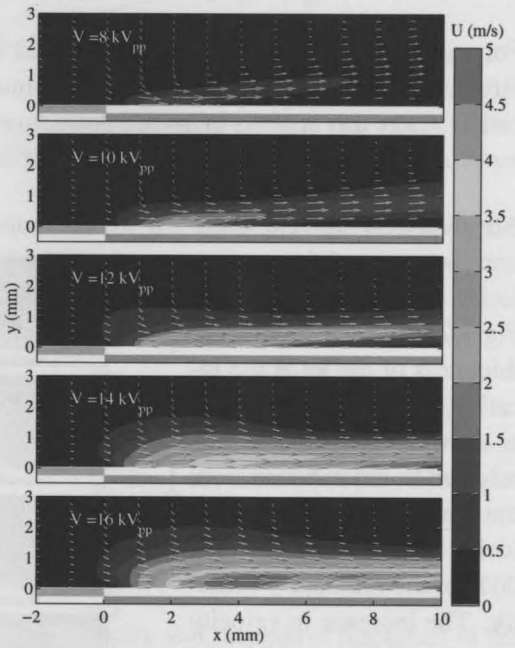

Figure 4.25: Average total velocity fields for different applied voltages (continuous operation, $f_{ac} = 2\ kHz$).

The PIV measurements are taken for a time span which extents well into the region where the flow is fully developed to the familiar wall jet structure. This allows the averaging of several frames in order to calculate the mean flow for each tested case. The averaged velocity field for the different tested voltages is presented in Fig.4.25 while the averaged velocity field for the different tested carrier frequencies is shown in Fig.4.26. The flowfields are averaged over

1000 frames (1 s) for all cases. The jet is clearly a function of applied voltage and carrier frequency as is already verified from the HWA study. Maximum velocity for different voltages and frequencies is shown in Fig.4.27.

For varying applied voltage the jet changes in velocity magnitude as well as direction. For increasing voltage the maximum velocity increases and the location where this appears is moved downstream. Furthermore, the jet thickens especially in close proximity to the edge of the exposed electrode.

An overview of the location where maximum velocity occurs is given in Fig.4.28. Additionally the thickness of the jet at the location of maximum velocity is shown. The thickness is selected as the distance from the wall where the total velocity becomes smaller than 20% of the maximum velocity. The increase in velocity as well as thickness of the jet can be explained by taking into account the strengthening with voltage of the electric field in both magnitude and spatial extent. This is directly reflected on the produced thrust which in turn defines the jet strength and shape.

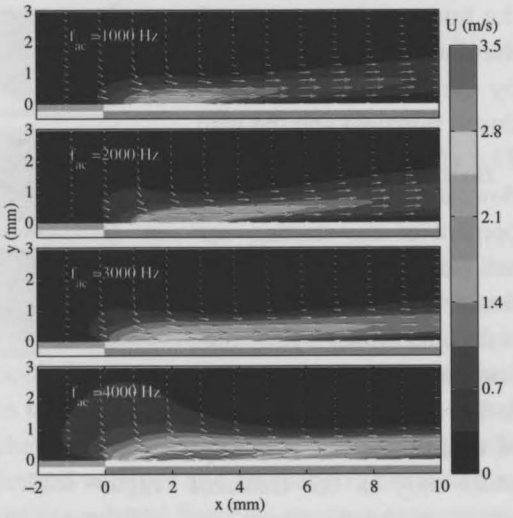

Figure 4.26: Average total velocity fields for different carrier frequencies (continuous operation, V_{app} = 10 kV_{pp}).

One more aspect is the downstream displacement of the location where maximum velocity occurs with increasing voltage. This is an indication of the lengthening of the plasma region over the covered electrode due to the previously mentioned strengthening of the electric field. Finally, of interest is the direction of the jet downstream. For low voltages the jet seems to have a pronounced upward component indicating a deflection due to the thick boundary layer the jet itself creates. As the jet velocity increases, the boundary layer be-

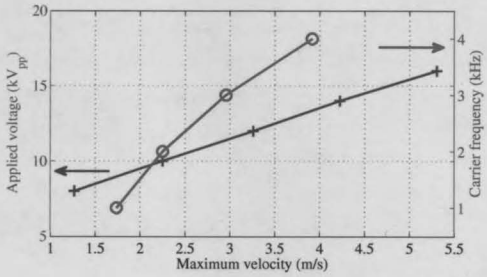

Figure 4.27: Maximum total velocities for the applied voltages and carrier frequencies in continuous operation.

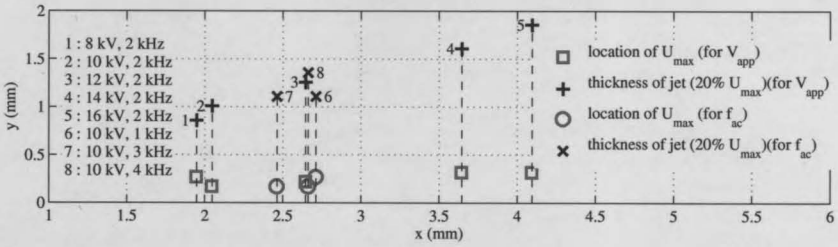

Figure 4.28: Locations of maximum velocity and respective thickness of the jet for the test cases in continuous operation

comes thinner and the inertial forces dominate over the viscous effects. Above 12 kV_{pp} no perceivable upward deflection is registered.

In the case of varying carrier frequency major differences exist with respect to the voltage variation case. The jet velocity increases with frequency but no major difference is observed in the location where the maximum velocity occurs or the thickness of the produced jet (Fig.4.28). This behavior suggests a different mechanism of influence that the carrier frequency has on the performance of the actuator. More specifically it appears that the increase of velocity is the product of increased momentum transfer rate, rather than increased momentum value. For a fixed applied voltage the thrust does not change in magnitude. Yet, the rate of momentum transfer to the flow increases with carrier frequency since more HV cycles occur within a given time span. Macroscopically, however, this is perceived as an increase in the actuator produced body force. Additionally, from Fig.4.27 it is apparent that the velocity

is not a linear function of frequency. As the carrier frequency increases an optimum must exist where the discharge current will limit the value of the produced body force. This limit is defined by the capacitance of the actuator [101].

In general, two different mechanisms can be identified here regarding the influence of applied voltage and carrier frequency on the performance of the actuator:

- Increased applied voltage strengthens the electric field, which in turn increases the magnitude and spatial extent of the induced jet.
- Increased carrier frequency increases the momentum transfer rate while leaving the time averaged electric field unaltered. This essentially increases the velocity of the jet without changing its spatial properties.

4.2.4 Refined parametric study using PIV: pulse operation

The pulse operation of the plasma actuator presents some interesting aspects regarding flow control applications. Mainly the extremely short response of the external flow to the actuation signal enables high frequency actuation approaches for a variety of flow control scenarios. Using the experimental setup previously described, a time resolved investigation of the pulse actuation has been performed in order to gain insight into the control authority of the actuator.

The actuator is operated with fixed applied voltage (10 kV_{pp}) and carrier frequency (2 kHz) to ensure consistency in power output. Three different pulse frequencies (f_p) are tested (50, 200, 350 Hz) at fixed duty cycle (D) of 50 %. Additionally the 50 Hz case is repeated for duty cycles of 25 and 75 %. To characterize the pulse actuation cycle, snapshots of the flowfield have been phased averaged over 20 pulse cycles. For the case of f_p = 200 Hz the phase averaging produces 50 points equally spaced over the pulse period. The history of total velocity along with the applied voltage signal is shown in Fig.4.29. Furthermore, snapshots of the velocity field are presented for 6 characteristic locations in the pulse period. The behavior within one HV cycle appears to be similar to the one observed by previous investigations [15]. The acceleration of the flow occurs mainly in the negative half cycle of HV. The overall acceleration appears to be accumulative through successive HV cycles

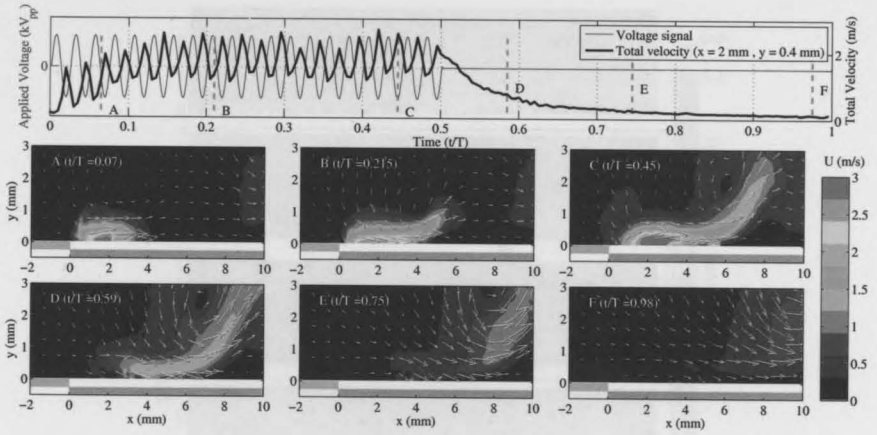

Figure 4.29: History of total velocity evolution through a full pulse period (f_p = 50 Hz, D = 50 %)

that occur in the first half of the pulse period. In the second half of the period the flow decelerates smoothly due to the hydrodynamic stresses.

One interesting aspect is the differences between the two halves of the pulse period apart from the apparent horizontal acceleration. During the first half (actuator is 'on') the flowfield exhibits an almost parallel to the surface downstream motion while for the second half a vertical component towards the wall is evident. This can be attributed to the sudden disappearance of the produced body force when the actuator turns 'off' (at this case t/T = 0.5). During the actuation phase the high velocity area in the plasma region is low in pressure. As the body force disappears, the flow reacts to the residual low pressure region and is drawn to the wall.

Such behavior should be considered in flow control scenarios where the forcing and the respective flow reaction must be highly deterministic. Such situations are typically boundary layer instabilities control. It must be stressed here that these results correspond to flow in quiescent conditions. Further investigations of similar type should be conducted in the presence of an external flow in order to obtain a higher degree of generality of these observations.

Applying the POD analysis on the results gives some insight into the large coherent structures involved in the induced flowfield for each actuation case. Fig.4.31 shows the energy percentage of the first 5 modes for all tested cases.

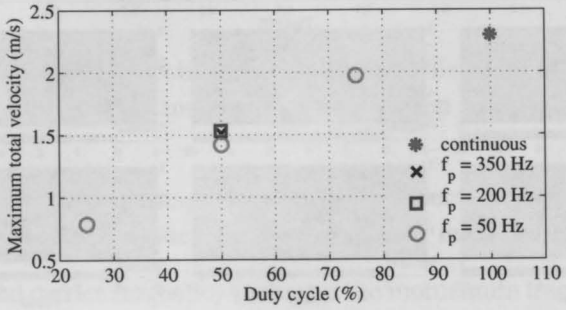

Figure 4.30: Maximum time-averaged velocity for the test cases in continuous and pulse operation (V_{app} = 10 kV_{pp}, f_{ac} = 2 kHz).

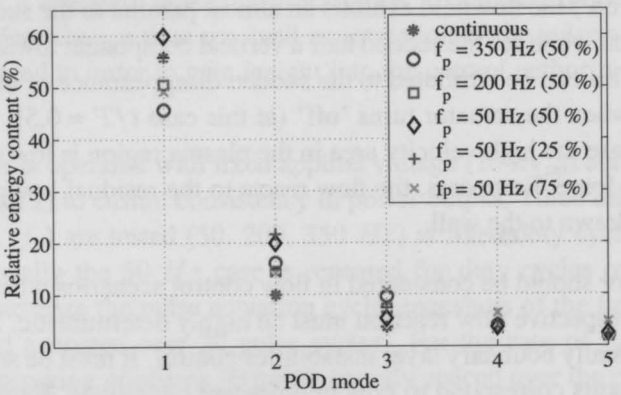

Figure 4.31: The energy content of the first five fluctuating modes as calculated form the POD analysis.

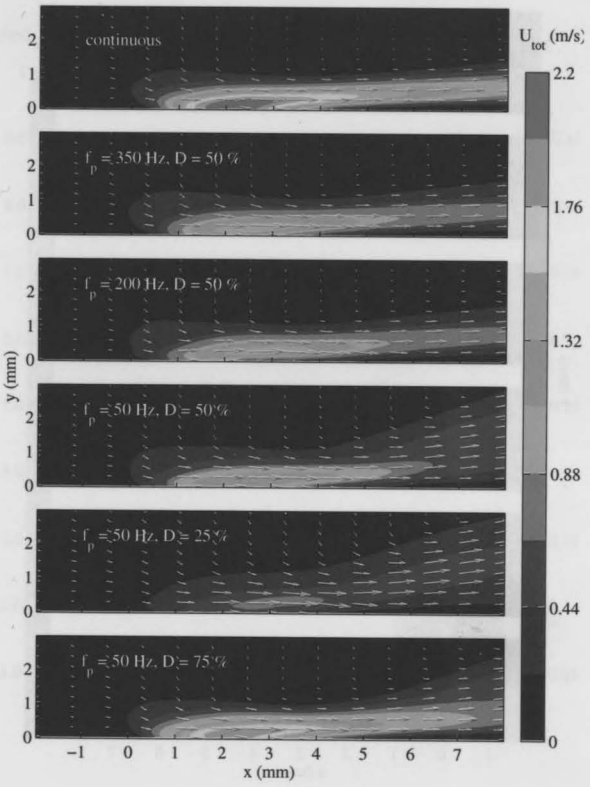

Figure 4.32: Mean component (Φ_0) for the test cases in continuous and pulse operation ($V_{app} = 10\ kV_{pp}$, $f_{ac} = 2\ kHz$.

It is obvious that the majority of the energy is carried out by the first two modes. The mean flow mode (Φ_0) for the different pulse operation cases is presented in Fig.4.32 along with the respective case of continuous operation.

It is evident that the mean induced field is significantly weaker compared to the continuous operation. This is to be expected as for the pulse operation the input power is lower than the continuous operation. This is further established by observing the cases of $D = 25$ and 75 % respectively. Compared with the 50 Hz, $D = 50$ % case the duty cycle appears to affect the mean flow velocity in almost a linear relation, as can be observed in Fig.4.30. On the contrary pulse frequency (f_p) appears not to influence the mean flow considerably.

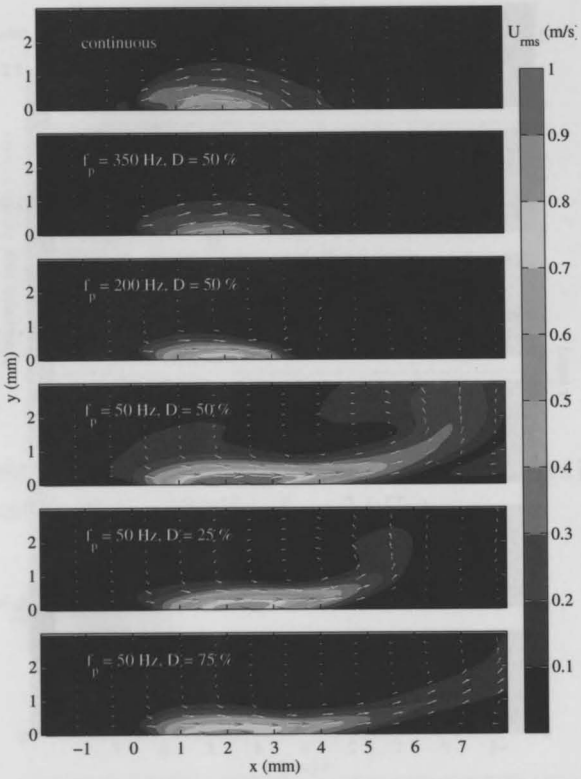

Figure 4.33: First fluctuating mode (Φ_1) for the test cases in continuous and pulse operation ($V_{app} = 10\ kV_{pp}$, $f_{ac} = 2\ kHz$.

The first fluctuating mode (Φ_1) is presented in Fig.4.33. In the majority of cases it is represented by largely transversal components in the vicinity of the actuator. For the low f_p cases a downstream extension is observed with some indication of rotational flow. This mode appears to correspond to the initial strong acceleration of the flow close to the actuator. Since the POD analysis differentiates the modes based on their energy content, no information on the spectral content can be extracted as such.

It is nevertheless apparent that the first and most energetic mode for the plasma actuator in pulse mode corresponds to a fluctuating and mostly parallel to the surface induced jet. Additionally, a strengthening of the jet is observed for decreasing f_p. This behavior presents some interest in terms of the flow con-

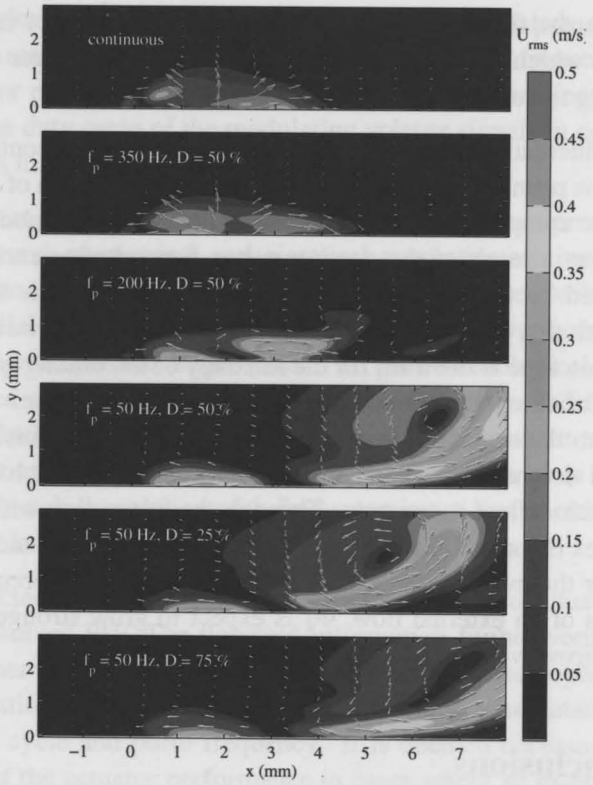

Figure 4.34: Second fluctuating mode (Φ_2) for the test cases in continuous and pulse operation ($V_{app} = 10\ kV_{pp}$, $f_{ac} = 2\ kHz$).

trol authority of the actuator. It becomes apparent from the available results that for lower pulse frequencies the flow presents stronger fluctuating components.

The reasoning behind this effect is the relaxation time of the flow for a given disturbance input. For lower pulse frequencies the flow has more time to relax to the 'actuator off' conditions after the ending of the pulse ('actuator on'). For higher f_p the flow simply does not have enough time to decelerate before the next pulse. For the case of 350 Hz the fluctuation intensity simply collapses on the respective values for continuous operation. It must be stressed here that the influence of the pulse frequency on the intensity of fluctuations is also a function of the external flow conditions. As will be shown in the

following chapter, for the case of an external laminar boundary layer the upper limit of f_p at which the fluctuations are still perceived is larger than the limit corresponding to quiescent flow.

The second fluctuating mode (Φ_2) is shown in Fig.4.34. In contrast to Φ_1 the nature of Φ_2 is primarily rotational. It is observed in the form of a large vortex with stronger components in the near wall region. This mode is captured by the POD as a result of the starting vortex formed after each pulse. This is also verified by the increased intensity of the vortex with decreasing f_p. Similarly with Φ_1, for larger f_p the vortex is significantly weaker since the flow relaxation time is the limit for the intensity of fluctuating quantities. The significance of external flow conditions is also apparent here. The vortex is created due to the acceleration of flow in quiescent conditions. The wall jet is developed downstream where it meets regions of low velocity and high pressure which deflect it upwards. Through the interaction with the wall the starting vortex is formed. In the case of external flow (i.e. boundary layer) the road map for the evolution of the jet is expected to be different. In general, in conditions of an external flow, Φ_1 is expect to grow stronger while Φ_2 is expected to grow weaker.

4.3 Conclusions

In this chapter an experimental parametric study is conducted on the operation of plasma actuators aimed at active boundary-layer control applications. Three main groups of experiments are done focusing on time-averaged velocity measurements using HWA, direct thrust measurements and time resolved PIV measurements respectively. Complementary readings of electrical quantities such as voltage and current is also performed.

The study on time-averaged velocity reveals the dependence of the induced flow field on geometrical properties such as lower electrode length, horizontal electrode gap and dielectric thickness. Threshold levels are identified for lower electrode length and horizontal gap that limit the intensity of the plasma field and consequently the maximum values of induced velocities. The locality of the induced velocity is found to be dependent on dielectric thickness. Thicker dielectrics produce more uniform flow fields in the downstream direction than thinner dielectrics, although they require larger voltage values.

Several electrical operational conditions are also investigated. A direct relation between maximum velocity and applied voltage and frequency has been identified. For pulsed operation the induced quantities are found to depend directly on the duty cycle of the modulating voltage signal. In contrast, pulse frequency has minimum influence.

The second test group involves measurements of the thrust produced by the actuator. Several geometrical and electrical properties are investigated. A large dependance of the thrust has been found on applied voltage and frequency. Parallel current measurements also give the power consumption for the respective voltages and frequencies. Two phenomenological models have been identified connecting thrust and power with voltage and frequency respectively. The thrust seems to follow a power law in respect to the voltage while its relation with frequency is linear. Similar behavior is observed for the power although the relation with frequency is not linear, rather following a weak power law.

Finally a selected group of cases in continuous and pulsed actuation is tested using time resolved PIV. The flowfield information further verifies the findings of the other two test groups. POD analysis on the pulsed operation results reveals translational and rotational coherent structures associated with the respective duty cycle and pulse frequency. It is deemed necessary to expand the analysis of the actuator performance in cases where an external flowfield exists.

Chapter 5

Actuation in External Flow Conditions

The characteristics of the plasma induced flowfield in quiescent flow have been investigated in the previous chapter. A clear dependence of the induced flowfield has been found on several operating parameters. Furthermore the pulse operation regime was analyzed and the produced unsteady flowfield examined. Based on the findings, it was made clear that the general topology of the induced flow should not only be evaluated as a function of the actuator performance but also of the external flow conditions. This is particularly important in cases of unsteady actuation. Special care must be given in these cases since the existence of an external flow gives rise to natural instabilities which can be manipulated favorably or unfavorably by the actuator.

In order to efficiently control natural external flows with a small momentum input, one must turn to the secondary structures or instabilities of the global flow dynamics. One typical example of low power flow control is the delay of laminar-turbulent transition by means of Tollmien-Schlichting (TS) wave cancellation which will be addressed numerically in the application part of this work (Chapter 9). This technique aims at tackling the instability waves while still at linear amplification stage. At this stage the waves have little energy content with typical amplitudes of 0.01 % of the freastream velocity [118]. By controlling these instabilities at the initial low-energy stages,

the evolution of the global hydrodynamic chain can be changed with minimum actuation energy. Similar technique has already been investigated with the use of vibrating membranes as actuators [128]. In recent studies [50, 51] artificially introduced TS waves were successfully cancelled using plasma actuators. These structures are typically unsteady and as such require unsteady actuation for optimal control. Investigations on manipulating other unsteady structures such as shedding vortices using the actuator in pulse mode have been performed [64, 106].

Although the pulse mode has been verified to be equally or in some cases more effective than continuous operation [87, 64], plasma actuators under pulse operation and the resulting flowfield have yet to receive detailed investigation as a stand alone phenomenon especially in cases of external flows. A limited number of studies [15, 12, 20] have been published on the subject. The aim of this chapter is to further investigate the behavior of the plasma actuator and the response of the surrounding flow under pulse operation. More specifically, this will be done both for the case of still air as well as for the case of the actuator operating in a laminar boundary layer. The quiescent flow cases serve as a reference and comparison basis while the laminar boundary layer case is designed to resemble the general conditions for the TS wave cancellation scenario. Furthermore, the sensitivity and behavior of the induced flow, under the variation of the pulse frequency and duty cycle of actuation is analyzed. This will provide an insight on the potential and limitations of these devices for applications that involve low power flow control based on manipulation of instabilities or other secondary flow structures. .

5.1 Experimental Setup

5.1.1 The actuator

For this study the conventional Dielectric Barrier Discharge (DBD) actuators are used in a similar (but not identical) setup as with the investigation in Chapter4. The actuators consist of thin rectangular copper electrodes made out of self-adhesive copper tape separated by a dielectric layer (Fig.5.1). The thickness of both electrodes is 60 μm and the width is 10 mm. Their effective spanwise length (along which plasma is generated) is 200 mm. The electrodes are separated by two Kapton tape layers. The thickness of each layer is

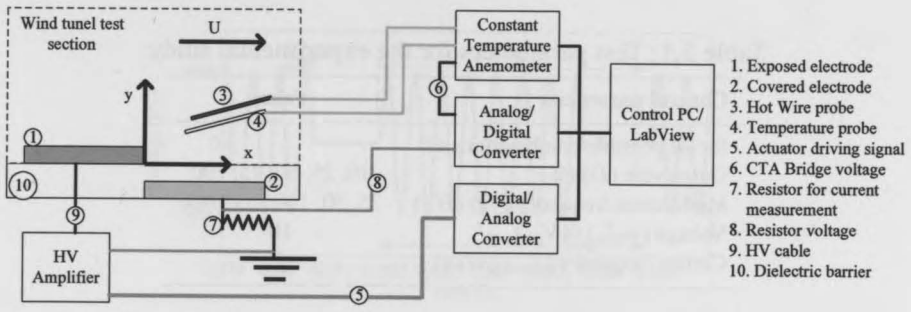

Figure 5.1: The experimental setup and coordinate system (not to scale)

2 mil (50.8 μm). The total thickness of the dielectric (including adhesive) is approximately 110 μm.

The electrodes and dielectric are supported by a 10 mm thick, 200x100 mm rectangular POM (Polyoxymethylene) plate carrying two aluminum connectors. The connector of the upper electrode is connected to the High Voltage (HV) output cable of a TREK 20/20C HV amplifier ($\pm 20\ kV$, $\pm 20\ mA$) while the connector of the lower electrode is grounded. The actuator operation is controlled remotely via a computer workstation were the driving signal is created by LabView software and is sent to the amplifier via a Digital/Analog (D/A) converter. The amplifier provides direct readings of the output voltage while the output current is measured using the voltage across a resistance (100 Ω) placed between the lower electrode and the grounding cable.

5.1.2 Measurements setup

The measurements are conducted in the test section of the Boundary Layer Tunnel (BLT) at the TU Delft. This wind-tunnel is of the closed type with a test section of 1.5 x 0.3 x 5 m. The tunnel incorporates a flexible wall which allows the creation of a large variety of pressure gradients. The boundary layer is formed on the opposite smooth plate. A knife edge protruding slightly into the flow ensures that the incoming turbulent boundary layer, formed in the contraction ratio, is bled out and a clean laminar boundary layer is initiated at the leading edge. The velocity range of the tunnel ranges from 1 to 40 m/s while freestream turbulence intensity is lower than 0.09 %.

Table 5.1: Test parameters for the experimental study.

Control parameter	**Value**
for all possible combinations of:	
Duty cycle (D) (%)	10, 25, 50, 75, 100
Modulation frequency (f_p) (Hz)	25, 50, 100, 200, 400
Voltage (V_{app}) (kV_{pp})	10
Carrier frequency (f_{ac}) (kHz)	2

For the flow diagnostics the use of Hot Wire Anemometry (HWA) is selected. HWA has been used in previous studies involving plasma actuators [66, 65] and has been found best suited for a parametric study as it combines sufficient accuracy, high sampling rate and relative ease of use. During the measurements, temperature readings in the proximity of the sensor are taken for velocity correction. Typical ΔT for a single measurement sequence is in the order of 0.5 $^{\circ}C$ for quiescent flow. No measurable difference has been found in the case of boundary layer flow. The hot-wire probe is traversed using a manual three-component traversing system with a 0.1 mm accuracy in each direction.

Based on the results from Chapter 4, the vertical velocity component v is considered negligible in the downstream region compared to the horizontal component u. Nevertheless, all measurements will be presented in the form of total velocity. All mesurements are taken at the half-span of the actuator. For all distance references in this chapter the coordinate system presented in Fig.5.1 is used. The origin of the axes is located at the downstream edge of the exposed electrode. To sufficiently resolve the temporal evolution of the flow and increase the accuracy of the spectral analysis, a sampling rate of 50 kHz is chosen with varying sampling time, depending on the distance of the hot-wire probe from the actuator.

Three x positions are selected at 7, 12 and 17 mm downstream the actuator. At these positions measurements are taken at selected y positions near the wall. Additionally, for the case of the laminar boundary layer, two more downstream positions at 43 and 93 mm are measured in order to track any convecting structure that might be initiated from the operation of the actuator.

For the entire study the high-voltage signal is kept fixed at V_{pp} = 10 kV with

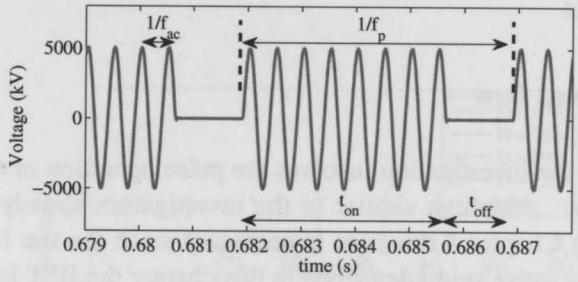

Figure 5.2: Sample of the voltage signal with the characteristic actuation values. (f_p=200 Hz, D = 75%)

a carrier frequency (f_{ac}) of 2 kHz. The operation of the actuator in pulse mode is essential for the manipulation of unsteady flow structures. As such the actuation period can be separated into the 'on' and 'off' stage. The pulse frequency (f_p) is defined as the number of times the actuator switches 'on' and 'off' while the duty cycle (D) is the percentage of the time period the actuator is 'on' over one full actuation period (Eq.5.1).

$$D = \frac{t_{on}}{t_{on} + t_{off}} \cdot 100 = t_{on} \cdot f_p \cdot 100 \tag{5.1}$$

A schematic of a typical actuation signal is shown in Fig.5.2. To investigate the sensitivity of the induced flow to pulse frequency and duty cycle, a test grid is devised. This involves the measurement of the induced velocity for all possible combinations of a series of D and f_p's. An overview of all parameters involved in the measurement is given in Tab.5.1

Similar to the HWA measurements described in Chapter 4 the high frequency fluctuations which remain in the velocity signal are considered as EM noise and filtered out using a low pass filter.

5.2 Results

5.2.1 Quiescent flow

The first case in the investigation involves the pulse operation of the actuator in quiescent flow. Although similar to the investigation already performed and described in Chapter 4 this case is necessary since the test location has changed. For the entire study described in this chapter the BLT is used. This case, although far from any practical application, provides an overview of the true control authority of the actuator over the fluid as demonstrated in Chapter 4. By ensuring a quiescent ambient flow environment, the only momentum input is provided by the actuator. Fig.5.3 and Fig.5.4 show the time evolution of the velocity at $x = 7\ mm$ and $y = 0.75\ mm$ for pulse frequencies $f_p = 50\ Hz$ and $200\ Hz$ respectively. The velocity measurement is started prior to the actuation and continues for several seconds after actuation. The initiation of each pulse is denoted in these and all subsequent figures with the vertical dashed line and their respective number. The EM noise in the velocity signal is removed with a 4^{th} order low pass Butterworth filter with cutoff frequency of $1\ kHz$.

The resulting flow accelerates from the initial still conditions to a quasi-steady state where it fluctuates around a mean value, seemingly at the frequency of the actuation. It is evident that the response of the flow under the actuation is relatively fast with a quasi-steady oscillatory state already reached after the first few actuation cycles. Also apparent is a time lag between each voltage pulse and the respective accelerating response of the flow. This is of course due to the finite distance of the measurement probe from the actuator. The time lag is simply the time it takes for the accelerated fluid to cover this distance. The flow appears to be self limiting in the maximum attained velocity where a balance between the actuator produced body force and hydrodynamic stresses is reached. As soon as the pulse is finished and the actuator is 'off' the flow starts decelerating. If no other forcing is applied the flow reaches zero with typical relaxation time of 20-30 ms.

Looking at the first few actuation cycles into more detail, an accumulative effect on the overall velocity is observed. This differs between cases of different duty cycles. For lower duty cycles the momentum transfer between the ionized particles and the neutral air during one actuation cycle is not enough to bring the flow to the maximum velocity. Nevertheless, inertial forces keep the

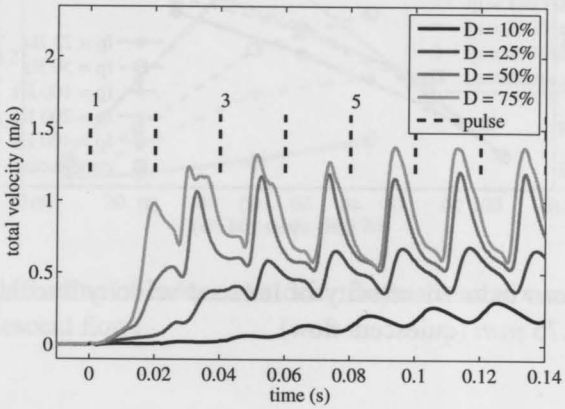

Figure 5.3: Time evolution of induced velocity for pulse frequency f_p = 50 Hz. Measurements at x = 7 mm, y = 0.75 mm

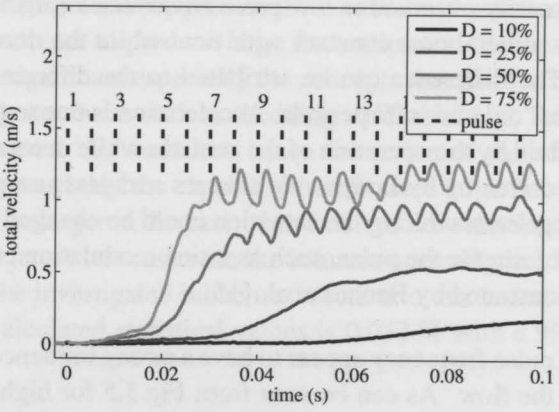

Figure 5.4: Time evolution of induced velocity for pulse frequency f_p = 200 Hz. Measurements at x = 7 mm, y = 0.75 mm

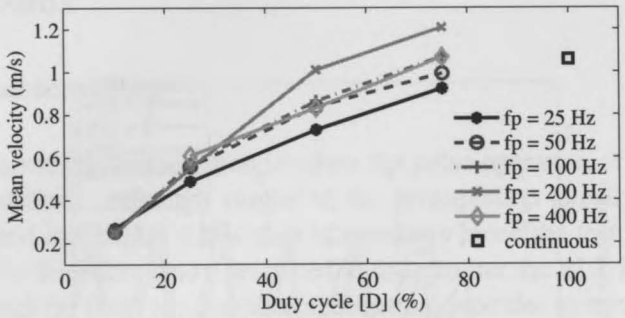

Figure 5.5: Mean induced velocity of induced velocity fluctuations at x = 7 mm and y = 0.75 mm (quiescent flow)

flow from decelerating to zero before the next actuation thus creating the accumulating effect on velocity. The relaxation time of the flow after each pulse seems to define the overall appearance of the fluctuating field. This also implies that for different external flow (such as a boundary layer) the fluctuations will differ since the relaxation time will also change.

Another aspect of the flow evolution is the difference between the accelerating part of the flow (the actuator is 'on') and the decelerating part (the actuator is 'off'). More easily observed at low pulse frequencies (Fig.5.3), the acceleration appears to be almost constant with time while the deceleration is of higher order. The difference can be attributed to the different mechanisms acting during the 'on' and 'off' periods. Acceleration is due to the body-force exerted on the fluid by the operation of the actuator while deceleration is more conventionally driven by hydrodynamic stresses and pressure gradients. The way the flow accelerates during the actuation could be changed by employing a different waveform for the pulse, such as a sine modulation or a trapezoidal wave as is demonstrated by Benard et al. [15].

Duty cycle and pulse frequency appear to have a strong influence on the quasi-steady state of the flow. As can be seen from Fig.5.5 for higher duty cycles the mean flow velocity increases and even surpasses the respective continuous actuation values in some cases. Pulse frequency seems to have less influence on the mean velocity, as is expected since the provided power does not change with f_p. Nevertheless, differences still appear which indicate that mechanisms directly related to the flow such as hydrodynamic instabilities and resonance

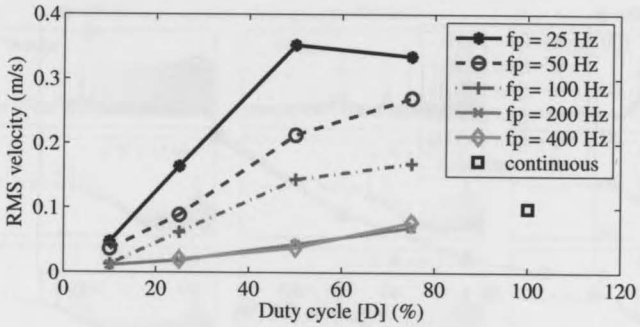

Figure 5.6: RMS value of induced velocity fluctuations at x = 7 mm and y = 0.75 mm (quiescent flow)

are in action and potentially can be used for flow control. For the quiescent flow an optimum appears near f_p = 200 Hz.

The rms fluctuation of the flow is also a function of pulse frequency and duty cycle as shown in Fig.5.6. For higher f_p the fluctuations become weaker since the pulses become shorter in duration and repeat more often thus approaching the continuous operation. It is interesting to note that for the cases of f_p =200 Hz and 400 Hz the fluctuations of the flow are of the same order and their trend of increase with D collapses on the continuous operation point. This inability of the actuator to produce large fluctuations on the flow for high pulse frequencies is significant especially for concepts that involve manipulation of fast developing structures such as shedding vortices or high Reynolds number unstable TS waves. Nevertheless, since the action of the actuator is directional, it is expected that the capability to introduce large fluctuations at high frequency can be larger in the case of an external flow moving in the direction of the induced jet. A test case with the actuator operating in a laminar boundary layer will be investigated in the next section to this cause. The maximum error for the calculated statistical values is 0.053 % with a 99 % confidence level.

The power consumption of the actuator is shown in Fig.5.7. A power law seems to govern the relation between power and duty cycle giving more ground to the utilization of the actuator in pulsed operation rather than in continuous mode. For instance at f_p = 200 Hz and D = 75 % the mean velocity is higher than the continuous actuation while power consumption is 40 % less.

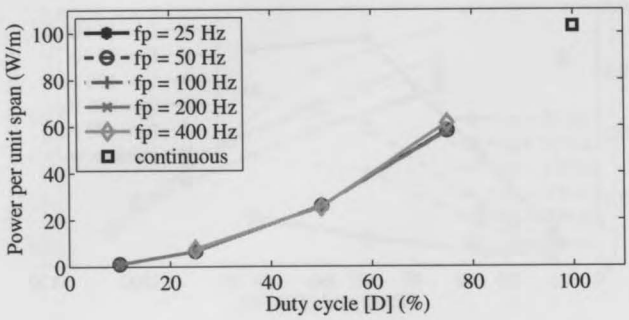

Figure 5.7: Power consumption of the plasma actuator for the series of tested f_p and D

Since the actuators are mainly focused on manipulating instabilities and unsteady structures of the flow a look in the spectral content of the induced flow is necessary. This will provide an insight into the corellation between the provided input signal, which in this case is the HV, with the produced velocity field. Power spectral densities (PSD) of the voltage signal and the induced flow field are shown in Fig.5.8 for different pulse frequencies. These are calculated using Welch's method [140] using eight segments over the entire signal with 50 % overlap. The number of points taken for the Fast Fourier Tranform (FFT) is 2^{16}. The PSD is presented here for the unfiltered signals. To be noted here that the average power in the signal is the integral of the PSD over a given frequency band. The peaks in this spectra do not reflect the power at a given frequency.

The voltage signal content is inherently rich in harmonics of the pulse frequency. Of interest is the lack of the even frequency harmonics of the pulse frequency. For example in the f_p=100 Hz case the harmonics of 200, 400, 600 Hz and so on are missing. This is an artifact of the modulation of the carrier frequency signal with a square wave pulse at a fixed duty cycle of 50% and will be shown to change for different duty cycles. The carrier frequency (2 kHz) is also apparent with an almost continuous subspectrum on its sides.

The velocity signal shows strong components at the main pulse frequency and its first few harmonics. A peak at the carrier frequency with a sideband subspectrum indicates the EM noise previously mentioned. At position $x = 7\ mm$

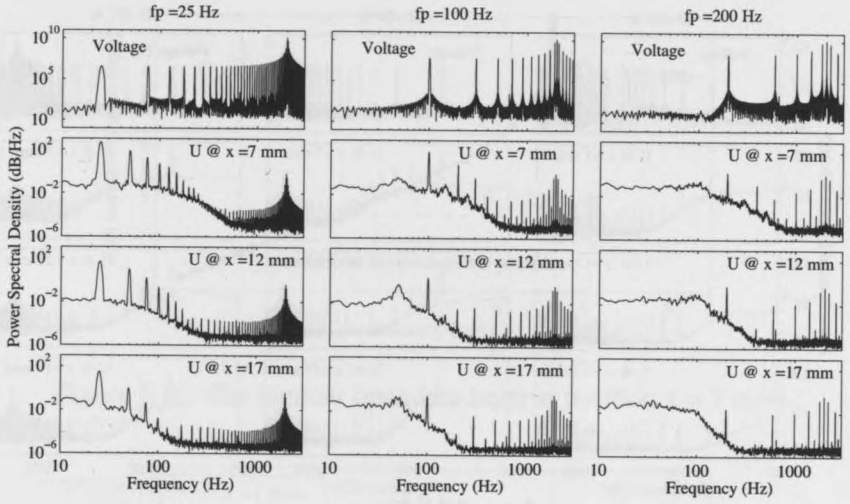

Figure 5.8: Power Spectral Density of voltage and velocity for D = 50 % (quiescent flow)

the average power of the signal is calculated using a rectangle approximation of the integral of the PSD. 97.9, 97.6 and 76.9 % of the average signal power is contained in the first three harmonics for the cases of f_p = 25, 100 and 200 Hz respectively. The pulse harmonics decrease with distance faster than the main frequency. A secondary effect can be observed here, in the existence of even harmonics in the velocity signal that are absent in the voltage signal. These harmonics appear to decrease in power with distance, at a larger rate than the odd harmonics.

The spectral densities of the voltage and velocity signals are shown in Fig.5.9 for different duty cycles. Similarly to the previous case, specific harmonics are absent from the input signal depending on the duty cycle for a fixed pulse frequency of 50Hz. For the case of 50% all the even harmonics are absent while for the cases of 25% and 75% every fourth harmonic (f_{4n}) is absent. Similar to the pulse frequency variation, the velocity spectra correspond to the input signal. It is verified that the harmonics that have no counterpart in the input signal decay faster in the downstream distance.

Since the initial voltage signal is created using only two frequencies (f_p and f_{ac}), the fact that the flow presents a larger set of harmonics could be cru-

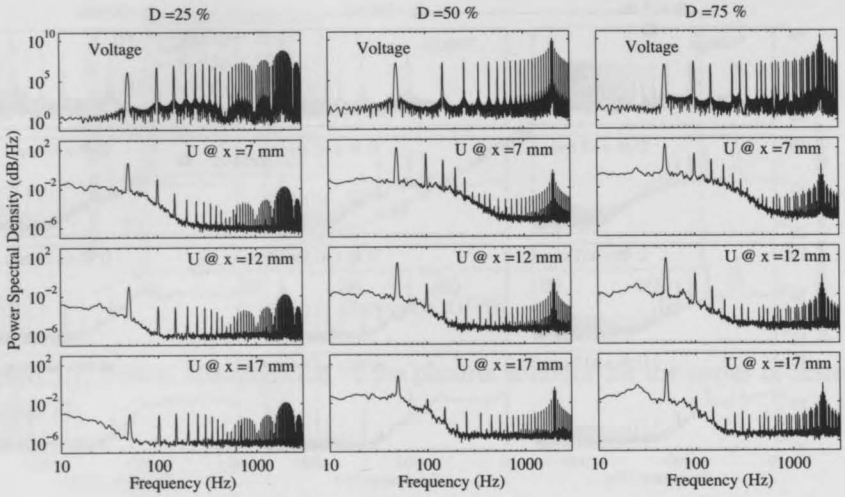

Figure 5.9: Power Spectral Density of voltage and velocity for $f_p = 50\ Hz$ (quiescent flow)

cial to some flow control approaches which involve unstable structures. For instance, if the actuator is operating in a laminar boundary layer at a pulse frequency which corresponds to a stable mode, the subharmonics in the induced flowfield might be well within the unstable region and eventually cause transition.

5.2.2 Laminar boundary layer

Through the introduction of steady or unsteady disturbances in the flow the plasma actuators can manipulate, enhance or accentuate flow instabilities, unsteady vortical structures and other secondary flow mechanisms. As such, it is essential to identify the behavior of the actuator and the resulting flow in the case of an external and already developed flow field. As an initial test case a low velocity laminar boundary layer is selected. This choice is made based on the low energy content of such a flow which would in turn increase the experimental observability of any effect the actuator might have. Additionally, this type of boundary layer forms the basis for the intended demonstration application of TS wave cancellation. Since the convecting instabilities which in the case of unswept wings are Tollmien-Schlichting waves have the form

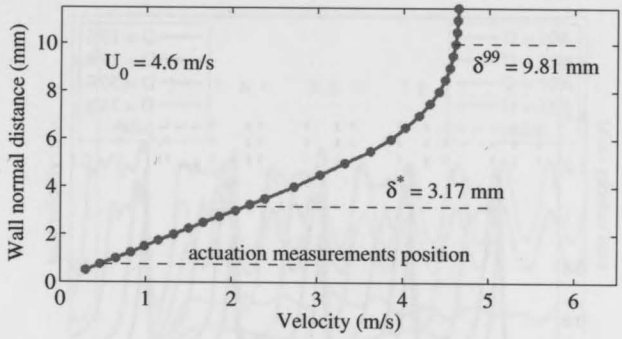

Figure 5.10: The laminar boundary layer at position x = 7 mm

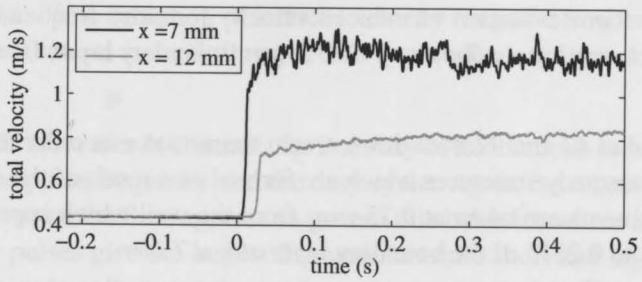

Figure 5.11: Velocity evolution for continuous operation at two downstream positions

of a multi frequency wave train, the actuator is required to operate in pulse or burst mode [51]. A similar investigation as with the quiescent flow cases is conducted to this goal.

The BLT tunnel is used to create a laminar boundary layer in which the actuator is operating in pulse mode. The freestream velocity is intentionally kept low at 4.6 m/s in order to avoid boundary layer instabilities to grow to levels that would interfere with the induced velocity components of the actuator. The boundary layer velocity profile is presented in Fig.5.10. The boundary layer is naturally growing downstream although for the first three x positions the growth is minimal.

For the pulse operation the same combination of duty cycles and pulse frequencies as with the quiescent flow are tested. Two additional x positions

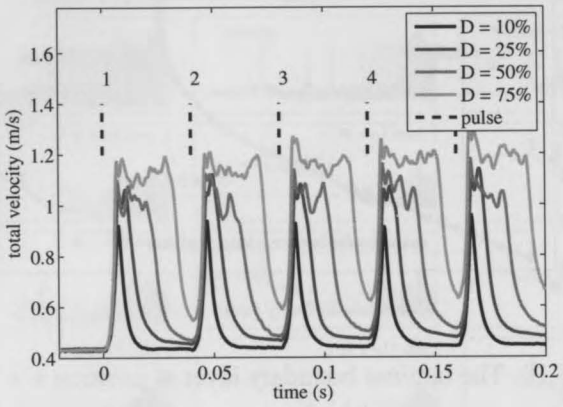

Figure 5.12: Time evolution of induced velocity for pulse frequency f_p = 25 Hz. Measurements at x = 7 mm, y = 0.75 mm (boundary layer, U = 4.6 m/s)

are measured at 47 and 97 mm downstream the actuator in order to track the convecting unsteady structures which are formed as a result of the actuation.. All measurements are taken at 0.75 mm from the wall which approximately corresponds to 0.25δ^* of the boundary layer at x = 7 mm.

Prior to the pulse operation a test case of continuous actuation is performed in order to establish a reference flowfield. This is shown in Fig.5.11. It is apparent that the flow accelerates significantly downstream the actuator.

The velocity measurements for pulse frequencies of 25 and 200 Hz and different duty cycles are presented in Fig.5.12 and Fig.5.13 respectively. A similar to the quiescent flow case behavior can be observed. In the vicinity of the actuator velocity consists of a mean component which is considerably larger than the unperturbed boundary layer velocity and strong fluctuating components. The individual velocity oscillations correspond to the respective actuator pulses and appear at the specific pulse frequency. Additionally, the time lag associated with the convection time between the actuator and the HWA probe is observed. The mean velocity and rms value of the fluctuations are shown in Fig.5.14 and Fig.5.15 respectively. Of interest is the insensitivity of the mean flow to changes in pulse frequency. This differs from the respective case in quiescent flow and can be attributed to the shorter relaxation time of the flow. This suggests that the mean velocity increase from the operation of the actuator is purely a function of the energy input the latter is capable, for

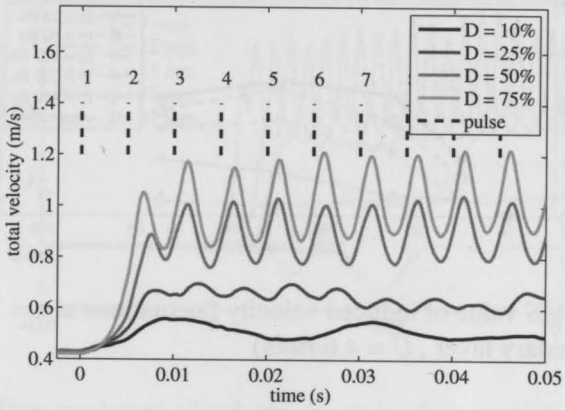

Figure 5.13: Time evolution of induced velocity for pulse frequency $f_p = 200$ Hz. Measurements at x = 7 mm, y = 0.75 mm (boundary layer, $U = 4.6$ m/s)

this specific test case. In contrast, the intensity of fluctuations seems to depend on both the pulse frequency and the duty cycle. Again the relatively short relaxation time of the flow appears to govern this behavior where long and low frequency pulses give the largest fluctuations while short and high frequency pulses appear to collapse on the continuous actuation point. The maximum error for the calculated statistical values here is 0.037 % with a 99 % confidence level. To be noted here that for the investigated cases, the power consumption of the actuator is found to be independent of the external flow.

The intensity of the velocity fluctuations appears to be dependent on the duty

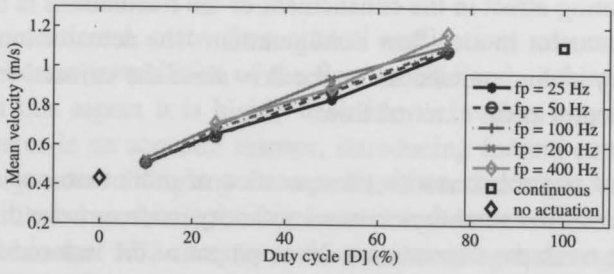

Figure 5.14: Mean induced velocity and at x = 7 mm and y = 0.75 mm (boundary layer, $U = 4.6$ m/s)

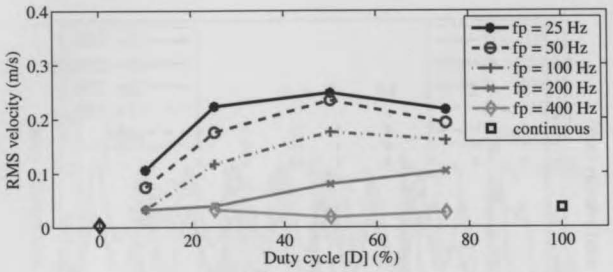

Figure 5.15: RMS value of induced velocity fluctuations at x = 7 mm and y = 0.75 mm (boundary layer , U = 4.6 m/s)

cycle with the same energy accumulation mechanism as in the quiescent flow seemingly governing the operation. More specifically the full development of the field to its quasi-steady state is achieved after several actuation cycles especially for low duty cycles and high pulse frequency. Nevertheless, comparing with the respective case in quiescent flow, as shown in Fig.5.4, maximum velocity is achieved in a much shorter time from the start of the actuation. An effect that can additionally be observed is the fact that larger fluctuations appear for higher pulse frequencies than in quiescent flow. For instance at f_p = 200 Hz and D = 25% the induced velocity in quiescent flow almost lacks any coherent fluctuating component and rather resembles the flowfield from continouous operation. For the boundary layer case, as can be observed from Fig.5.13, the flow still excibits fluctuations corresponding to the pulse frequency at D = 25%. This can be explained taking account that the velocity of the external flow whith no actuation is larger than the case of quiescent flow (zero velocity). This in turn makes the relaxation time of the flow less. One more contributing effect in the enhancment of the fluctuations is the arrangement of the actuator in a co-flow configutation. The actuator introduces the fluctuations by adding momentum to the flow since the induced velocity is in the same direction as the external flow.

In several flow control scenarios the operation of more than one actuators is proposed in order to extent their control authority in streamwise distance. It is thus useful to track the downstream development of the induced fluctuations from the operation of the actuator. In this manner the effective downstream region for a single actuator can be defined. A track of the evolution of the fluctuating field can be seen in Fig.5.16 for pulse frequency of 50 Hz and duty

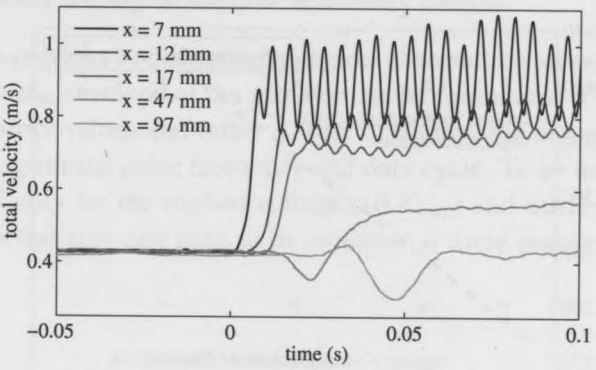

Figure 5.16: Time evolution of velocity for pulse frequency $f_p = 50\ Hz$, $D = 50\%$ and different downstream positions (measurement at y = 0.75 mm)

cycle of 50 %. Similar behavior is observed for the rest of the tested pulse frequencies. The effect of the actuator is local as strong fluctuations appear only at the first 3 measurement positions or within 10 mm from the actuator. Further downstream, at 47 mm, the mean velocity acceleration is evident but the fluctuating components have almost disappeared. At 97 mm only a very weak increase in velocity is registered. In the case of the laminar boundary layer the distance in which the forcing of the actuator can be perceived is highly dependent on the freestream conditions and the hydrodynamic stability of the flow. In this case, it is obvious that 50 Hz corresponds to a stable TS mode at this Reynolds number. This can also be verified by linear stability theory. Nevertheless it seems that independent of forcing frequency the actuator can introduce strong fluctuations at least in the first 10 mm downstream.

As already mentioned, many flow control applications rely on the manipulation of inherent instabilities of the flow to efficiently achieve the desired control. In this aspect it is highly desirable to be able to control any potential actuator in an accurate manner, introducing forcing components that are necessary and avoiding any unwanted artifacts that might be additionally introduced. Based on this, some comments can be made on the pulse operation of the actuator. It is clear from the continuous operation of the actuator Fig.5.11 that the induced flowfield is unsteady with the velocity signal being almost stochastic in time. This behavior can also be observed in pulse operation for low pulse frequencies and high duty cycles. For instance at $f_p = 25$

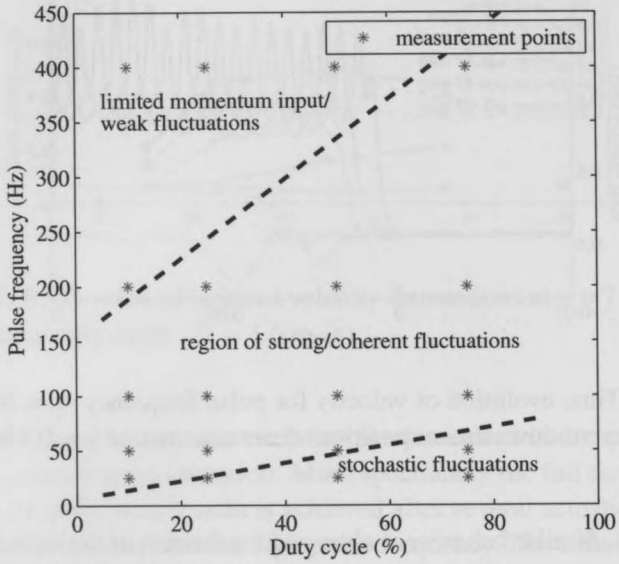

Figure 5.17: Empirical operational envelope for the plasma actuator operation in a low speed laminar boundary layer.

Hz and $D = 75\%$ (Fig.5.12) the flow accelerates after each pulse begins until it reaches its self limiting maximum velocity. This is reached before the end of the pulse and for the remaining duration of the pulse the flow essentially behaves as in the continuous operation. This could potentially be unwanted since the stochastic velocity signal might trigger instabilities in the flow in a random and uncontrolled fashion. It is thus important to limit the duration of the pulse to the point where a 'clean' forcing is imposed on the flow. Furthermore, reduction of the duty cycle could contribute positively in the reduction of consumed electrical power.

One additional feature which is important in efficient flow control is the actual intensity of the fluctuating components. Especially for high pulse frequencies and low duty cycles such as the case of $f_p = 200\ Hz$ and $D = 10\%$ (Fig.5.13) the momentum input from the actuator is too little and the relaxation of the flow is too slow to respond to the actuation. This results in a flowfield which resembles the continuous operation case albeit with a lower mean velocity since the input energy is limited. For these cases the ability of the actuator to

impose unsteady forcing on the flow is severely limited.

Based on the previous two phenomenological observations an empirical model for the operating envelope of the actuator can be formulated (Fig.5.17). This is far from strict values and rather a 'rule of thumb' for the useful range of the actuator operating pulse frequency and duty cycle. To be noted that these values apply only for the applied voltage (10 kV_{pp}) and carrier frequency (2 kHz) of this test case and have to be redefined if these parameters are to be varied.

5.3 Conclusions

An experimental study has been conducted on the operation of the plasma actuator in pulse mode. The actuator used was a conventional DBD incorporating copper electrodes and Kapton dielectric. The high voltage and carrier frequency were kept fixed at $V_{app} = 10\ kV_{pp}$ and $f_{ac} = 2\ kHz$ respectively. Total velocity was measured for the cases of quiescent flow and laminar boundary layer. Several combinations of pulse frequency and duty cycles were tested in order to evaluate the sensitivity and form of the resulting flowfield.

From the tests it became apparent that the plasma actuator is capable in introducing mean and fluctuating components of velocity to the surrounding air when operated in pulse mode. In most cases a quasi-steady situation is reached after a few cycles of actuation. For the quiescent flow a strong dependence connecting pulse frequency and duty cycle with mean velocity and fluctuation intensity has been found. An upper limit in pulse frequency and a lower limit in duty cycle seem to define the useful operating range of the actuator. The respective tests in the laminar boundary layer reveal the importance of the outer flow and especially the relaxation time in the final form of the fluctuating field. Differences between the two cases suggest that results from tests in quiescent flow might not be suitable for correct prediction of the actuator performance in other flows.

An additional spectral analysis has been performed on the velocity signal from the test in quiescent flow. As shown the induced velocity field presents a slightly different spectral content than the forcing signal. This is important in applications dealing with hydrodynamic stability where the exact spectral content of the forcing must be precisely controlled.

For the laminar boundary layer cases the measured velocities present distinct differences from the respective quiescent flow cases. Due to the existing energy content of the boundary layer as well as the directional forcing of the actuator the control authority over the flow is increased. This is especially important when high frequency actuation is required. Nevertheless, due to the same reasons some unwanted effects are also identified. For large duty cycles and low pulse frequencies a similar to the continuous actuation field is measured for part of the actuation pulse. This consists of random and uncorellated velocity fluctuations which potentially could degrade the performance of the actuator. One more important aspect is the lower limit in duty cycle which was previously identified in the quiescent case. Depending on the pulse frequency the actuators seems to lack the necessary power to induced strong and coherent fluctuations when operating below a certain value of duty cycle. This is particularly pronounced in high pulse frequencies. Based on these observations an empirical operational envelope is proposed for the implementation of the actuator in pulse mode flow control techniques. The envelope is specific to the operating parameters and external flow for the test case under investigation but similar approach in deriving 'situation specific' envelopes could be followed for any other case.

Chapter 6

Forcing Mechanisms within the Actuation Period

The exact mechanism of momentum transfer from the weakly ionized gas created by the DBD actuator to the ambient air is partly unclear. It is widely regarded that collisional processes drive the momentum transfer [16]. This is further supported by an important property of the plasma discharge in air. This states that the frequency of charged species-neutral particles collisions within the plasma region is of the same or larger order of the electrostatic oscillations frequency. This effectively means that the Coulombian forces exerted on the charged particles by the electric field are transfered entirely to the neutral air. Yet the influence of the heavy species to the net momentum transfer and how this affects the direction of the force during the HV cycle is still debated. Early numerical models [62] suggest that during the *forward stroke* (exposed electrode is negative) positive ions are drawn towards the exposed electrode and impart negative momentum to the air. During the *backward stroke* (exposed electrode is positive) the ion movement is reversed and momentum transfer is positive. The net momentum transfer for the entire HV cycle is positive due to the asymmetry in species density between the two strokes. This scenario has been challenged by more recent modeling efforts as well as experimental investigations. Particularly the consideration of air chemistry and more specifically the existence of negative ions (O^-) in simulations [85, 18] is important since in such case, the forcing scenario is completely altered. In models where

negative ions are considered, both cycles contribute positively in momentum transfer with the negative half cycle responsible for the majority of the momentum input.

There has been a limited number of experimental investigations on the forcing mechanisms of the actuators. Time-resolved Laser Doppler Anemometry (LDA) measurements were conducted in quiescent air [42] where the asymmetry between the two half cycles is evident. Large momentum transfer during the negative half cycle was recorded which corresponds with the recent modeling efforts. In another study [71] phase locked PIV measurements are taken which indicate the dominance of the negative cycle in momentum transfer. Using a different technique Enloe et al.[37] and Font et al.[40] showed positive momentum transfer during both half cycles.

The current status of experimental research into the forcing mechanisms of the plasma actuator is restricted to either spatial [71] or temporal [42, 37] resolution of the flowfield. The experimental investigation in this chapter is aimed at combining the previously missing information using advanced diagnostic techniques. Results are obtained through the simultaneous spatial and temporal resolution of the induced flowfield from the operation of the plasma actuator within one period of forcing. The knowledge of the exact nature of the forcing within the HV cycle is of high importance for several reasons. This information will provide insight into the forcing mechanisms of the actuator and the nature of the momentum transfer process which can potentially be used in deterministic flow control transfer functions. Additionally, the results can further be used for comparison and validation of first-principles plasma actuator models as well as optimization of some operating parameters such as the waveform shape for the improvement of the performance of the actuator.

6.1 Experimental Setup

6.1.1 The actuator

In this investigation conventional DBD actuators are used, employing thin rectangular copper electrodes made out of self-adhesive copper tape. The electrodes are 10 mm in length (x direction), with zero horizontal gap. Their

Table 6.1: Test parameters for the experimental investigation.

Parameter	Value
upper electrode length (l_u)	10 mm
lower electrode length (l_l)	10 mm
dielectric thickness (t_d)	110 μm
horizontal gap (g)	0 mm
applied voltage (V_{app})	10 kV_{pp}
carrier frequency (f_{ac})	625 Hz
waveform	sine, square, sawtooth, negative sawtooth

thickness is 30 μm including adhesive. The effective spanwise length (z direction) of the electrodes (along which plasma is generated) is 200 mm. The electrodes are separated by two dielectric layers of polyimide Kapton tape. The thickness of each layer is 50.8 μm. The total thickness of the dielectric, including adhesive, is approximately 110 microns. The geometrical properties of the actuator are presented in Tab.6.1. The upper electrode is energized using a TREK 20/20C HV amplifier (20 kV, 20 mA) while the lower electrode is kept grounded.

The amplifier provides direct readings of the output voltage and current through internal measurement probes. While the internal voltage probe gives sufficiently accurate readings the internal current probe has been found to be too slow to resolve high frequency current fluctuations. To resolve this, a resistance (100 Ω) is placed between the lower electrode and the grounding cable and voltage is measured across it indicating the discharge current. The voltage and current signals are measured using a Tektronix TDS 2004B oscilloscope using a sampling frequency of 10 MHz.

6.1.2 PIV setup

Tests are conducted in a closed box made from Plexiglass (PMMA) to provide optical access in the same context as described in Chapter 4. Time-resolved PIV is used in conjunction with a phase shifting technique (described further below) to characterize the flow field in the vicinity of the plasma actuator. A two component PIV configuration has been chosen since the large span of the actuator ensures minimal 3D effects.

The plasma actuator is placed flushed on the bottom of the Plexiglas box. A Photron Fastcam SA1 high speed CMOS camera of 1024×1024 pixels is used to image the field-of-view (FOV). Image acquisition has been conducted at 6 KHz rate in double-frame mode. Time separation of 50 μs has been applied between successive images. A Micro Nikkor 200 mm objective is set at f-stop 4 and is used along with extension tubes in order to achieve 2.1 magnification and a FOV of 9.7×4.7 mm over a cropped sensor of 1024×496 pixels. The air in the Plexiglas box is seeded with olive oil droplets of approximately 1 μm diameter generated by a TSI atomizer. The particles at the mid span of the actuator are illuminated by a light sheet of $2mm$ thickness generated by a Quantronix Darwin-Duo laser system with an average output of 80 W at 3 kHz. The images are analyzed using Davis 7.4 (Lavision GmbH) by cross-correlating successive images. Final interrogation window size of 16×16 pixels and overlap factor of 75% are used. The interrogation windows are elongated in the wall normal direction using a 4:1 aspect ratio in order to obtain higher spatial resolution. The velocity vectors are returned on a grid of 26×26 vectors per mm^2.

6.1.3 Phase shifting technique

For DBD actuators employing thin dielectric layers such as Kapton tape, typical carrier frequencies f_{ac} are typically between 0.5 and 10 kHz. This range corresponds directly to the characteristic electrostatic oscillation frequency of the HV signal. As such it is desirable to accurately capture the response of the induced flow within these time scales in order to safely deduce the features of the forcing mechanism. The desired sampling rate of any data acquisition system should at least be one order of magnitude larger than the respective operating frequency for each test case. As already mentioned, it is the goal of this study to simultaneously resolve the spatial and temporal characteristics of the velocity field. The spatial requirement is fulfilled using a 2D PIV system operating at a high optical magnification (M = 2.1). The PIV system is capable of high speed acquisition up to 10 kHz limited by the repetition frequency of the laser. Yet this is deemed not sufficient for cases of carrier frequencies larger than 0.5 kHz.

In order to redeem the problem of limited sampling rate, a phase shifting technique is employed to increase the effective sampling frequency of the PIV system. The technique is based on the periodicity of the plasma forcing ef-

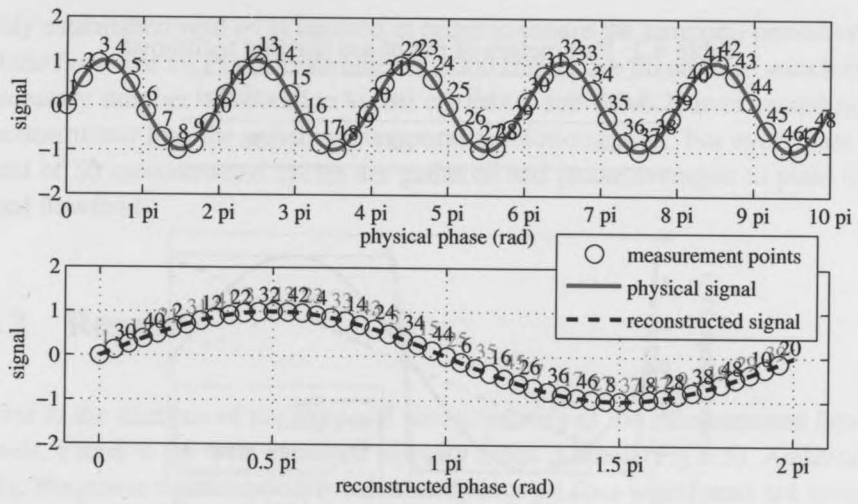

Figure 6.1: Example of physical and reconstructed signals using the phase shifting technique (f_{samp} = 6 kHz, f_{ac} = 625 Hz).

fect as proved in numerous previous studies [15, 76]. More specifically the sampling rate f_s is kept fixed at 6 kHz while the actuator carrier frequency f_{ac} is chosen such that the ratio $r = f_s/f_{ac}$ is not an integer value. In this manner, the phase of every measured point is slightly shifted between successive actuation signal cycles. This implies that a number of signal cycles c will contain n points with distinct phases which can be combined into a single reconstructed cycle with higher temporal resolution. An example of the phase shifting technique is presented in Fig.6.1 with the settings used in the experimental investigation (f_s = 6 kHz, f_{ac} = 625 Hz). The achieved phenomenal frequency is then given by the product $f_{eff} = n \cdot f_{ac}$.

An overview of the parameters of the phase shifting method as used in this study is presented in Tab.6.2. The carrier frequency is chosen such that for every case the final reconstructed signal would consist of 48 points. Although the phenomenal acquisition frequency is 30 kHz the temporal resolution of the system is based on the 50 μs time separation between the PIV image pairs. This translates into a 34% overlap between successive measurement points.

Table 6.2: Parameters of the phase shifting technique.

$f_{ac}\,(Hz)$	$f_s\,(kHz)$	n	c	$f_{eff}\,(kHz)$
625	6	48	5	30

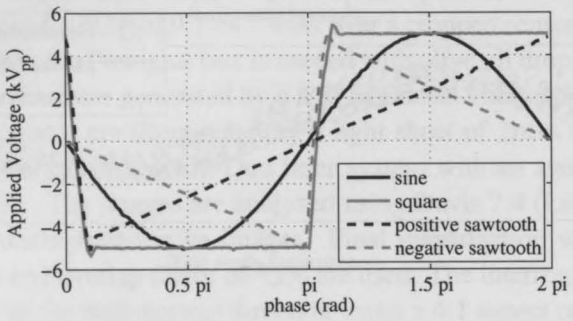

Figure 6.2: The HV waveforms tested in this investigation.

6.1.4 Test cases

Due to the advantages in spatio-temporal resolution the selected measurement techniques provide, a series of different waveform shapes is selected for the actuation signal. The selected waveforms include the widely used sinusoidal signal, a square, a sawtooth and a negative sawtooth. All the waveform cases are ran using a fixed carrier frequency $f_{ac} = 625\ Hz$ and fixed applied voltage $V_{app} = 10\ kV_{pp}$. This implies a different power consumption for each waveform which renders the comparison of their performance problematic. As such, no direct performance comparison between the test cases will be currently performed. In contrast the scope of this study is focused on individual forcing mechanisms within each waveform which are treated as individual test cases.

A schematic of the different waveforms is presented in Fig.6.2. The slight deviations from the ideal shapes are due to the limited slew rate of the HV amplifier ($350\ V/\mu s$). An overview of the test parameters, including the geometric properties of the actuator, is presented in Tab.6.1.

All measurements are taken for continuous operation of the actuator. This implies that the initial transient stage of acceleration from quiescent flow to the

fully established wall jet is omitted in order to ensure the temporal periodicity of the flow. For all PIV measurements, 3000 frames are taken from which the necessary number of actuation signal cycles (c, see Tab.6.2) is extracted and reconstructed into the enhanced temporal resolution cycle. For every case a total of 50 reconstructed cycles are gathered and phase averaged to yield the final flowfield.

6.2 Results

Prior to the analysis of the temporal characteristics of the reconstructed flowfields, a look at the time averaged velocity fields is taken (Fig.6.3). Additionally, the power consumption is calculated since all four waveforms are tested for the same geometrical configuration, applied voltage and carrier frequency. The power consumption is calculated using the integral:

$$P = \int_{t_1}^{t_2} |I(t) \cdot V(t)| dt \tag{6.1}$$

where $V(t)$ is the instantaneous voltage, $I(t)$ is the instantaneous current and $t_2 - t_1$ is a time interval containing an integer number of actuation periods (100). Power consumption for the four tested waveforms is presented in Tab.6.3

Table 6.3: Time average power consumtion for the four tested waveforms.

Waveform	Power (W)
sine	1.8
square	3.5
pos. sawtooth	2.0
neg. sawtooth	2.9

The general topology of the flowfield is similar to a typical wall jet. A suction effect is observed slightly downstream of the edge of the exposed electrode (x = 0), where flow is entrained towards the wall and then is injected downstream. The sine and square waveforms produce the highest velocities in amplitude. The positive and negative sawtooth actuation is substantially weaker.

The power consumption of the four waveforms reveals additional differences between the waveform shapes. The most energy consuming shape is square while sine requires almost half the power in comparison. Of special interest is

the power consumption of the positive and negative sawtooth shapes which is relatively high considering the weak character of the induced flowfield from these two shapes.

Considering the differences in both the induced flowfield and the power consumption for the tested waveforms some remarks must be made here. It must be stressed that care should be taken in comparing the four waveforms.

This is due to the differences in power consumption between the four cases. As such no conclusion on the performance or efficiency as a function of the waveform shape can be obtained by comparing these cases. In the case of a parametric study for performance improvement through waveform shape manipulation a metric of efficiency should be devised taking into account the strength as well as the power consumption of each shape. In contrast, the scope of this study involves the independent spatio-temporal analysis of the waveforms as stand-alone cases. An effort to define forcing mechanisms related to the features of each waveform shape is thus undertaken.

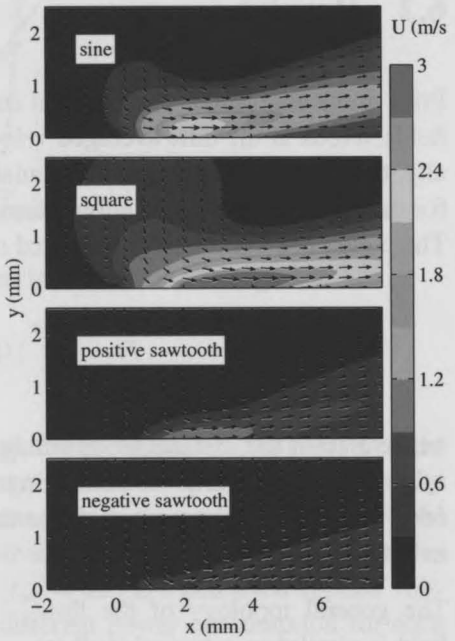

Figure 6.3: Average total velocity field corresponding to the four tested waveforms

In order to obtain a general insight into the underlying scales governing the HV cycle, an initial dimensional analysis is conducted. This is based on the decomposition of the incompressible two-dimensional Navier-Stokes equations based on the available velocity data. More specifically, The NS equations are:

$$\frac{\partial \mathbf{U}}{\partial t} + \mathbf{U} \cdot \nabla \mathbf{U} - \nu \, \nabla^2 \mathbf{U} = -\frac{\nabla p}{\rho} + \frac{\mathbf{F}}{\rho} \tag{6.2}$$

where $\mathbf{U}$ is the 2D velocity field, $\mathbf{F}$ is the plasma body force field, p is the static pressure, ν is the kinematic viscosity of the fluid and ρ is the density.

In the present study, all the left hand side terms of Eq.6.2 are available through the PIV measurement. On the other hand the pressure gradient and body force terms cannot be uncoupled without erroneous assumptions. This renders the interpretation of the time resolved flowfields more difficult. Fig.6.4 shows the temporal evolution of the value of the three left hand side terms in Eq.6.2 integrated over the spatial domain for the sinusoidal waveform case. Similar results are also obtained for the other waveforms. It is apparent that for both the x and y directions, the unsteady acceleration term ($\frac{\partial \mathbf{U}}{\partial t}$) dominates the convective acceleration ($\mathbf{U} \cdot \nabla \mathbf{U}$) and the viscous stresses ($-\nu \nabla^2 \mathbf{U}$). This is partly expected as the flow is not confined, it is driven purely by the plasma body force and is largely inviscid. This implies that the pressure gradient might also be small compared to the body force term although no conclusions can be made at this point. For the present study the dominant term of unsteady acceleration shall be considered as a combined effect of the pressure gradient and the plasma body force.

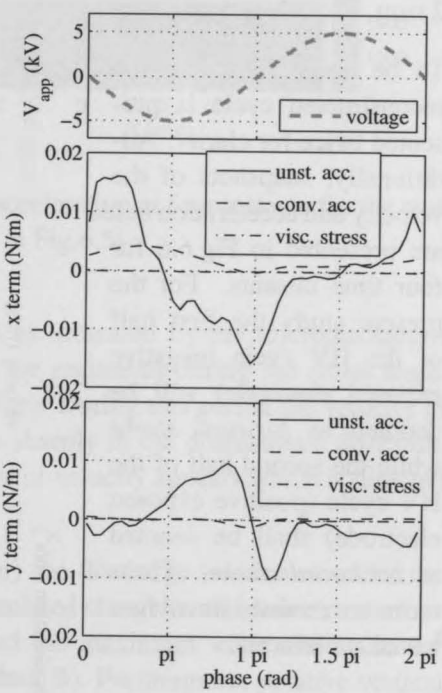

Figure 6.4: Dimensional analysis of the measured x and y terms of the Navier-Stokes equations. All terms are integrated over the spatial domain at each time frame.

6.2.1 Sine waveform

The majority of experimental [37, 71, 15, 42] and numerical [17, 85] investigations on the DBD forcing mechanisms discuss the sine waveform, albeit for different carrier frequencies and applied volatges. The temporal evolution of velocity and acceleration in the plasma region is presented in Fig.6.5 along the measured voltage and current. All flowfield values are probed at approximately the position where the maximum values of velocity are registered (x = 2 mm, y = 0.2 mm).

To be noted here that the reconstructed cycle is presented twice for clarity. Additionally, snapshots of the velocity and acceleration fields are presented in Fig.6.6 for four time instants. For the present study the first half of the HV cycle (negative exposed electrode) will be denoted as *forward stroke* while the second half of the HV cycle (positive exposed electrode) shall be denoted as *backward stroke*. These terms are retained for all four tested waveforms.

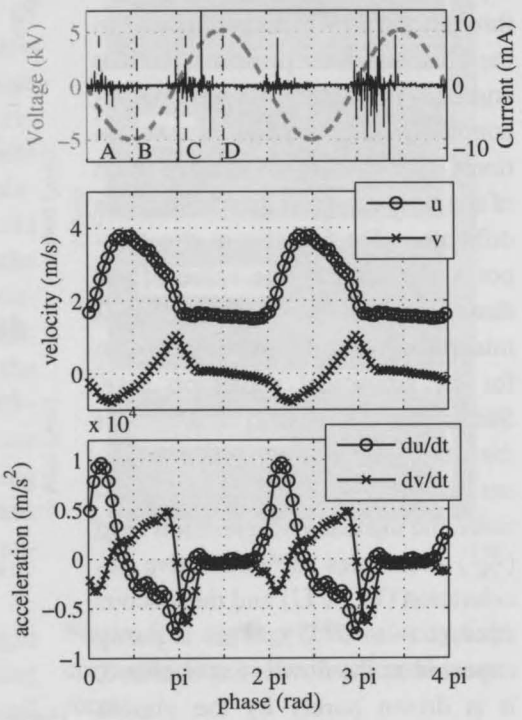

Figure 6.5: Temporal evolution of velocity (u, v) and acceleration ($\partial u/\partial t$, $\partial v/\partial t$) during the HV cycle for the sine waveform (values probed at x = 2 mm, y = 0.2 mm).

It is evident from the velocity evolution for the sine waveform that the forcing due to the plasma is unsteady and periodic within the HV cycle. Moreover a strong asymmetry exists between the two strokes. The velocity evolution closely resembles results obtained by Forte et.al.[42]. At the initial phases of the *forward stroke* the voltage of the exposed electrode starts to drop (instant A).

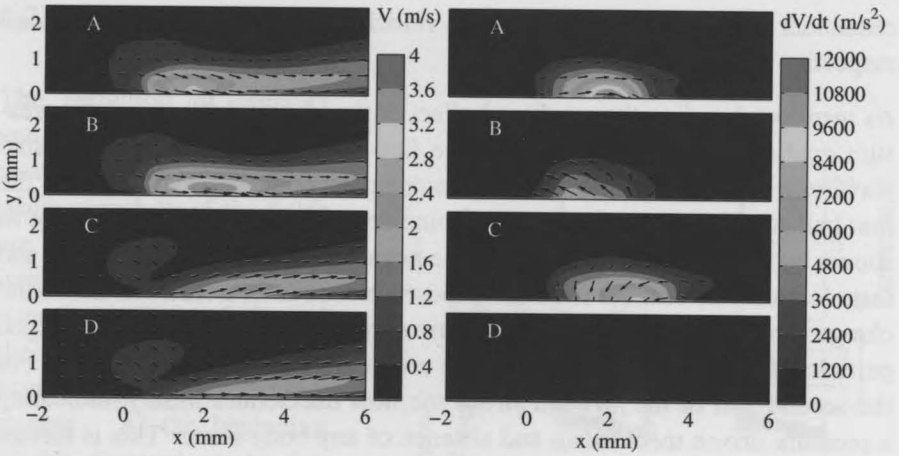

Figure 6.6: Snapshots of velocity and acceleration at four instants for the sine waveform. (instants A-D are indicated in Fig.6.5)

Simultaneously, the plasma is ignited as indicated by the microdischarges corresponding to current peaks which are registered during the entire negative going portion of the stroke (0 - 0.5 π). During this period the velocity in the region of the discharge accelerates sharply in the downstream direction. Additionally, a weak vertical component of velocity appears which is directed towards the wall.

At the peak of negative voltage (0.5 π) the discharge terminates under the self limiting effect caused by the accumulated charge on the dielectric surface [85, 38, 17]. The velocity has reached the maximum value and starts decelerating as the voltage increases (instant B). Furthermore, positive vertical acceleration is registered causing fluid to move away from the dielectric wall. It is interesting to note that the slope of change of velocity, and thus negative acceleration is significantly weaker than the first half of the *forward stroke*. Nevertheless, at 0.9 π a sharp increase in negative acceleration is registered.

For the *backward stroke* no significant change in horizontal velocity is registered (instant C) although the current peaks from π to 1.5 π indicate the positive discharge. On the other hand the vertical velocity starts decreasing and drops to zero by 1.2 π. This is also indicated by the moderate acceleration vectors towards the wall evident at the snapshot of instant C. For the

remainder of the *backward stroke* both velocity components are constant and respective acceleration drops to zero.

As mentioned earlier, the combined effect of the plasma forcing and the pressure gradient appears to be driving the flowfield acceleration. For the sine waveform it is apparent that strong momentum addition occurs during the first half of the *forward stroke*. This coincides with the negative discharge as shown by the current peaks. During the negative discharge negative ions and fast electrons are emitted from the exposed electrode in a series of microdischarges and accumulate on the dielectric surface. The movement of charged particles downstream couples positive momentum to the neutral fluid. For the second half of the *forward stroke* the flow decelerates mildly, indicating a pressure driven mechanism and absence of any body force. This is further supported by the positive vertical velocity components which indicate an area of high pressure created at the area where the discharge took place in order to fulfill the momentum deficit the sudden disappearance of the body force has created. In contrast, the *backward stroke* appears not to change significantly the flow although a discharge is occurring. This implies the existence of a moderate positive forcing from the plasma. This is enough to keep the flow from decelerating until the next end of the stroke. One event that is currently unclear is the sharp negative acceleration at 0.9 π. This might indicate the existence of accumulated negative ions on the dielectric surface which begin to travel upstream as soon as the voltage of the exposed electrode starts increasing. This would imply a small negative body force at the beginning of the *forward stroke*. No definitive conclusion can be made at this point.

Summarizing, the sine waveform appears to produce significant positive forcing during the *forward stroke* with very weak but still positive forcing during the negative stroke. Following the terminology of Corke [32] the action appears to be a PUSH-push effect. This agrees well with the experimental study of Enloe et al. [37] where a 97 % of momentum addition was registered during the *forward stroke*. Furthermore the numerical predictions of Boeuf et al. [17] are confirmed for the case of low carrier frequency and high voltage amplitude. As they suggest, for these operating conditions, the momentum transfer is dominated by the negative ions movement during the *forward stroke*.

6.2.2 Square waveform

The evolution of velocity and acceleration for the square waveform is shown in Fig.6.7 while snapshots of the fields are given in Fig.6.8. Qualitatively similar to the sine waveform, the evolution of the flowfield suggests an asymmetry between the two strokes. At the beginning of the *forward stroke* (instant A) the voltage drops sharply. This is accompanied by strong current peaks indicating a respectively strong and short negative discharge. During this event, the velocity rises sharply and strong acceleration in the downstream direction is observed. The area of strong acceleration is located well downstream of the exposed electrode with maximum values around x = 3 mm and is considerably larger than the respective sine case. Similarly the flow is accelerated vertically towards the dielectric surface.

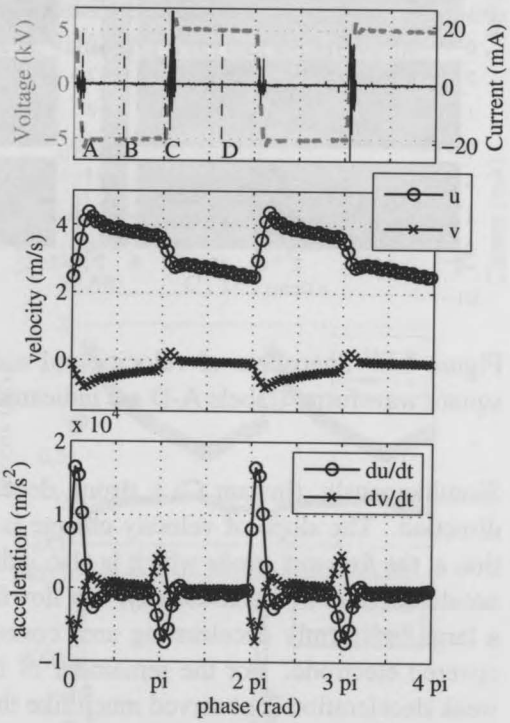

Figure 6.7: Temporal evolution of velocity (u, v) and acceleration ($\partial u/\partial t$, $\partial v/\partial t$) during the HV cycle for the square waveform (values probed at x = 3 mm, y = 0.2 mm).

During the remainder of the *forward stroke* the flow remains at relatively high velocities but constantly decelerates. Respectively the negative velocity is reduced and approaches zero by the end of the stroke. During this period no discharge is registered as suggested by the lack of current peaks.

At the beginning of the *forward stroke* (π) the voltage sharply reverts and large current peaks signify the positive discharge.

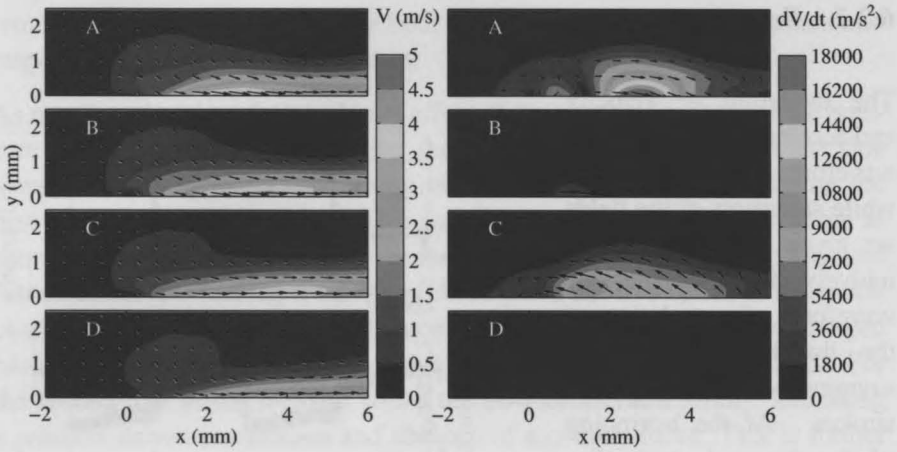

Figure 6.8: Snapshots of velocity and acceleration at four instants for the square waveform. (labels A-D are indicated in Fig.6.7)

Simultaneously, (instant C) a strong deceleration occurs in the streamwise direction. The slope of velocity change is less than the respective acceleration at the *forward stroke* which is also indicated by the value of the negative acceleration at π. Additionally, the flowfield snapshot at instant C reveals a large, uniformly decelerating area covering almost half the length of the covered electrode. For the remainder of the *backward stroke* (1.2 π - 2 π) weak deceleration is observed much like the respective period of the *forward stroke*.

The square waveform appears to gather the two active phases in short time periods at 2 π and π. Strong events seem to dominate both voltage reversals occurring within the HV cycle. During the voltage drop (2 π) the plasma appears to produce strong positive forcing while at the voltage rise (π) the forcing is negative (upstream). During the long periods of flat high voltage the discharge is quenched and the flow appears to decelerate by pressure alone although at less rate than the respective sine periods. This is attributed to the increased momentum transfered to the flow during the plasma forcing periods which in turn renders the flow more resistant to adverse pressure gradients. In general a PUSH-pull event can be identified from the waveform shape.

The concentrated discharge events during the voltage reversal instants appear to be the main mechanism behind the increased power consumption of this

waveform. This is due to two simultaneously acting features of the current and voltage evolution respectively. Firstly, the fast change of voltage from relatively constant positive value to an also relatively constant negative value *compresses* the discharge sequence (avalanche ionization) in a very short time span which in sequence increases its intensity. Secondly, the instantaneous voltage is theoretically always at peak values for a perfect square shape.

This is practically not the case here since the slew rate of the HV amplifier gives a slight slope to the shape. Nevertheless the instantaneous voltage during the discharge events is generally higher than the respective sine case. The combined effect of both increased voltage and discharge current during the active phases is transfered into the product of these values which in turn produces the relatively high consumed power value.

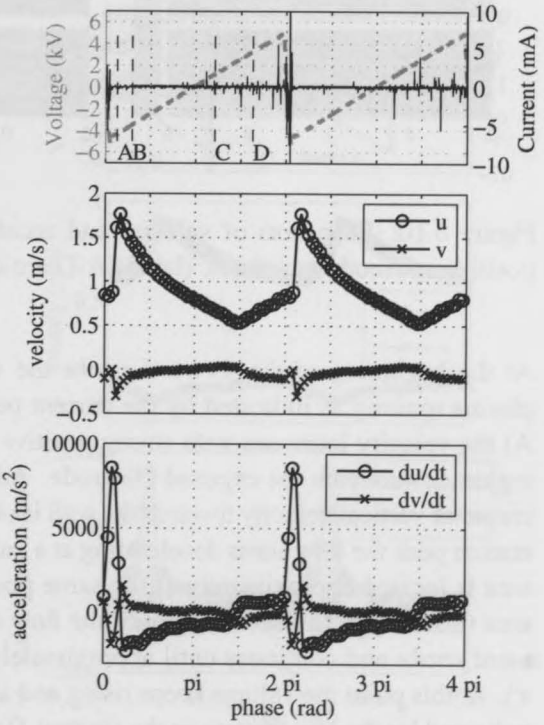

Figure 6.9: Temporal evolution of velocity (u, v) and acceleration ($\partial u/\partial t$, $\partial v/\partial t$) during the HV cycle for the positive sawtooth waveform (values probed at $x = 3\ mm$, $y = 0.2\ mm$).

6.2.3 Positive sawtooth waveform

Positive and negative sawtooth waveforms have been investigated, albeit in a time averaged way [11, 38]. Additionally, the rising and sinking ramp voltage has been investigated numerically as stand alone cases [16]. The evolution of velocity and acceleration for the positive sawtooth waveform is shown in Fig.6.9 while snapshots of the fields are given in Fig.6.10.

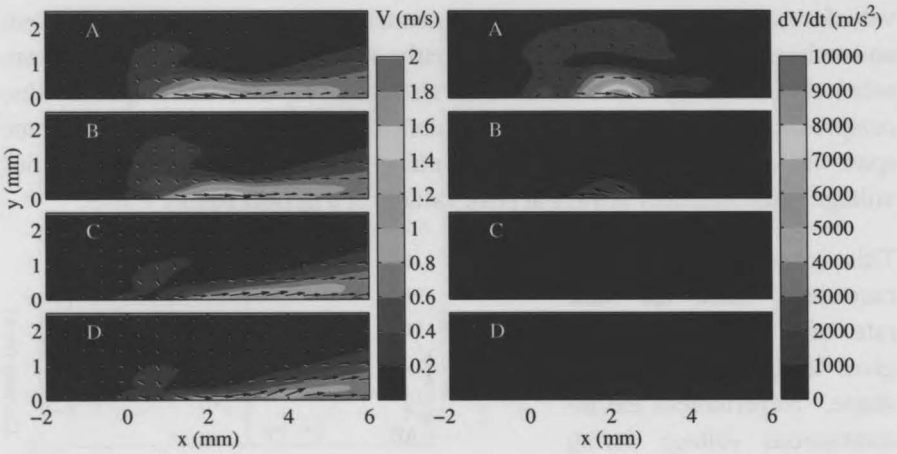

Figure 6.10: Snapshots of velocity and acceleration at four instants for the positive sawtooth waveform. (labels A-D are indicated in Fig.6.9)

At the beginning of the *forward stroke* the voltage drops sharply with the plasma igniting as indicated by the current peaks. At the same time (instant A) the velocity increases with strong positive acceleration located in a small region downstream the exposed electrode. Additionally a small but sharp increase of vertical velocity towards the wall is observed. Shortly after the acceleration peak the flow starts decelerating at a much lower rate. The deceleration area is located approximately at the same position as the initial acceleration area (instant B). The deceleration of the flow covers the remainder of the *forward stroke* and continues until approximately half the *backward stroke* (1.5 π). At this point the voltage keeps rising and a weak discharge is registered as indicated by the low current peaks (instant D). Furthermore the flow accelerates weakly again although at a much lower rate compared to the event at the beginning of the *forward stroke*. This weak acceleration continues until 2 π where it's superseded by the strong acceleration of the next HV cycle.

The positive sawtooth waveform exhibits an asymmetry between the two strokes. The *forward stroke* produces strong positive forcing during the negative discharge associated with the sharp voltage drop. Subsequently the flow appears to decelerate on pressure alone until the end of the *forward stroke*. The deceleration continues unaffected, as the *backward stroke* begins and carries on until 1.5 π. At this point weak current peaks are registered indicating the pos-

itive discharge. Simultaneously a moderate positive acceleration occurs signifying weak but still positive forcing from the plasma. The positive waveform appears to produce a PUSH-push effect.

6.2.4 Negative sawtooth waveform

The evolution of velocity and acceleration for this waveform is shown in Fig.6.11 while snapshots of the fields are given in Fig.6.12. At the beginning of the *forward stroke* the voltage is gradually decreasing (instant A). The flow remains largely unaffected until approximately 0.3 π where a moderate positive acceleration is observed in the region of the plasma (instant B) along with weak current peaks indicating the negative discharge. The snapshot of instant B also indicates a large area of negative acceleration above the exposed electrode although the velocity components in the same area are relatively small. At 0.7 π the flow starts decelerating smoothly until the end of the *forward stroke*.

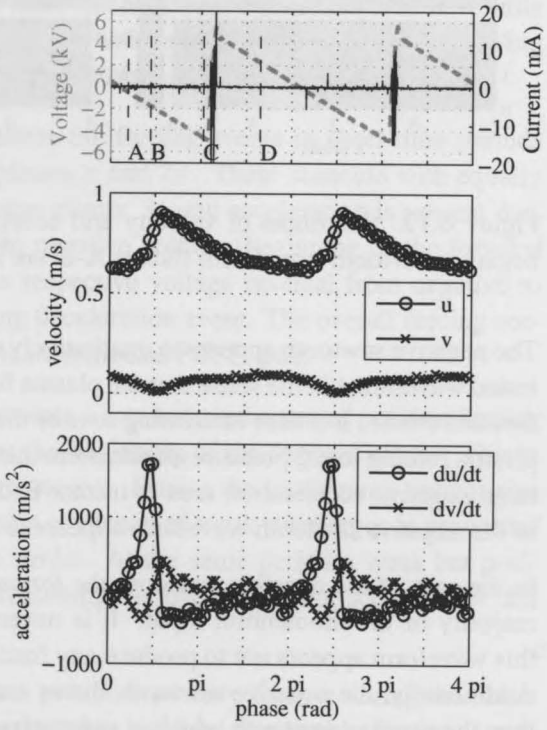

Figure 6.11: Temporal evolution of velocity (u, v) and acceleration $(\partial u/\partial t, \partial v/\partial t)$ during the HV cycle for the negative sawtooth waveform (values probed at $x = 3\ mm$, $y = 0.2\ mm$).

During the *backward stroke* the flow continues to decelerate and seems largely unaffected from the sharp voltage rise, although strong current peaks indicate the occurrence of the positive discharge (instant C). The smooth deceleration continues throughout the *backward stroke*.

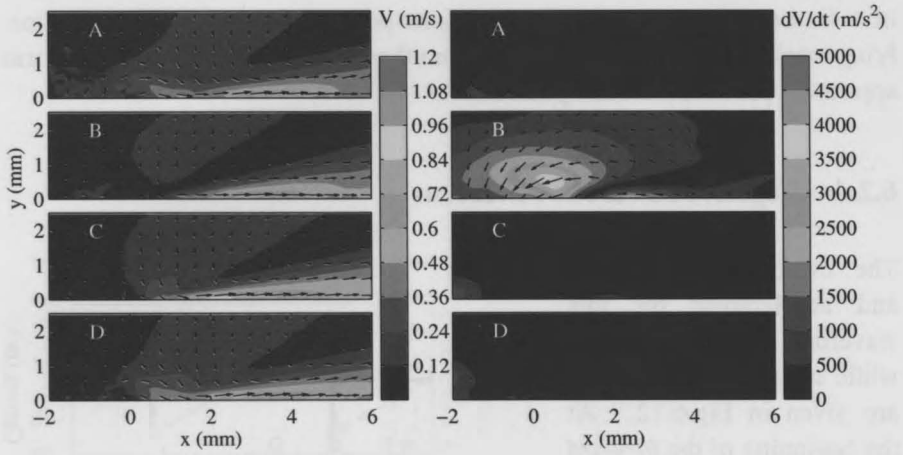

Figure 6.12: Snapshots of velocity and acceleration at four instants for the negative sawtooth waveform. (labels A-D are indicated in Fig.6.11)

The negative sawtooth appears to qualitatively differentiate from the rest of the tested waveforms in the sense that the plasma forcing is visible only during the *forward stroke*. It is also interesting to note that due to the weak nature of the plasma forcing itself, pressure effects seem more pronounced as evident by the large negative acceleration area at instant B. In general the forcing behavior of the negative sawtooth waveform appears to be a PUSH-none effect.

In the case of the negative sawtooth the *forward stroke* is responsible for the majority of the momentum input. It is nevertheless interesting to note that this waveform appears not to produce any forcing during the *backward stroke*. Additionally, the negative sawtooth shows a more uniform acceleration area than the positive sawtooth which is suggestive of the negative ion dominance during the *forward stroke*. Although the power consumption of the two cases is not the same the general flow topology agrees with previous observations [11].

6.3 Conclusions

Recent experimental studies indicate that the discharge associated with DBD's is highly asymmetric between the positive and negative half-cycles [42, 38].

This has been verified in the present study. Furthermore four different waveform shapes have been investigated in order to gain insight in the asymmetry and its influence on the plasma forcing.

The sine waveform produces strong acceleration of the flow during the active period of the *forward stroke*. This is associated with the negative discharge where fast electrons and negative ions are emitted from the exposed electrode and accumulated on the dielectric surface [85] coupling momentum to the flow at the same time. On the other hand the *backward stroke* seems to have little effect in momentum addition although still produces positive force rendering the overall forcing scenario to PUSH-push.

The square waveform concentrates the forcing events in short time periods during the voltage reversal at phases π and 2π. These coincide with equally short in time but intense discharge events. Strong acceleration is present during the reversal from positive to negative voltage (beginning of the *forward stroke*). On the other hand the respective voltage reversal from negative to positive values produces a strong deceleration event. The overall forcing scenario for the square waveform is identified as PUSH-pull.

The positive sawtooth shape presents a concentrated event of positive forcing during the steep voltage drop at the beginning of the *forward stroke*. This is accompanied by strong discharge events. During the linear ramp voltage rise from π to 2π (*backward stroke*) a sequence of weak discharges is registered during the entire period of the stroke. At the same period a weak but positive acceleration is registered rendering the overall forcing scenario for this waveform as PUSH-pull.

The negative sawtooth waveform produces positive forcing during the linear ramp from phases 2π to π. On the other hand no perceivable forcing is registered during the sharp voltage rise at the beginning of the *backward stroke* π even though strong discharge current is measured. The overall forcing scenario for the negative sawtooth shape can be identified as PUSH-none.

The results of the present study are suggestive of ways to improve the performance of the plasma actuators. The key seems to be the *forward stroke*, where negative ions are emitted downstream imparting momentum to the flow. While charge equilibrium must remain between the two half cycles, waveforms which present an asymmetry in shape between *forward* and *backward stroke* are expected to enhance the overall performance in terms of forcing

strength as well as power consumption. An application of assymetric waveforms for the improvemnt of performance of the DBD actuator is described in Chapter 10.

Part II

Modeling

Jakoż zasiedli do eksperymentowania. A polegałlo na tym, iż sporządzili model króla Okrucyusza i potwora, oba wszakże tylko na papierze, bo sposobem matematycznym, Trurl zawiadywa? pierwszym, Klapaucjusz zaś drugim. I starły sięoba na wielkich arkuszach białych, zalegających stół, z takąmocą, aź grafiony pękły naraz w ołówkach.[...] Pędziłkról wszystkimi swoimi współczynnikami okrutnymi, błądził w lesie znaków poszóstnych, wracał własnymi śladami, potwora atakował do siódmego potu i ósmej silni, ów zaś rozpadł sięna sto wielomianów, zgubił jednego iksa i dwa ypsylony, wlazł pod kreskęułamkową, rozpoczwarzył się, machnął pierwiastkami i jak królewskiej osobie zmatematyzowanej z boku nie zajedzie! - aź zatrzęsło sięcałe równanie, tak na odlew trafione.

Stanislawa Lema, *Cyberiada*

So they rolled up their sleeves and sat down to experiment by simulation, that is mathematically and all on paper. And the mathematical models of King Krool and the beast did such fierce battle across the equation-covered table, that the constructors' pencils kept snapping. [...] The King rushed forward with all his cruel coordinates and mean values, stumbled into a dark forest of roots and logarithms, had to backtrack, then encountered the beast on a field of irrational numbers (F_i) and smote it so grievously that it fell two decimal places and lost an ϵ, but the beast slid around an asymptote and hid in an n-dimensional orthogonal phase space, underwent expansion and came out, fuming factorially, and fell upon the King and hurt him passing sore.

Stanislaw Lem, *Cyberiad*

Chapter 7

Measurement of the Plasma Induced Force Field

It is commonly accepted that collisional processes between the heavy plasma species (mostly ions) and neutral air are responsible for the momentum transfer [86]. At a macroscopic scale the model of an exerted body force on the fluid seems to describe the effect with reasonable accuracy. A large amount of simulation studies has been conducted in order to simulate the underlying physics of the ionization process [60, 82, 18] and calculate the exerted body force.

The experimental investigation on the actuator's operation has also received substantial attention. Several studies focus on the investigation of the induced velocity field [37, 42, 99] and the produced thrust from the actuators [3, 35, 55]. These methods are robust and fast but they present some drawbacks which render the results difficult to be used as an input in flow solvers, an area that so far has been served only by numerical plasma modeling studies. A shortcoming is their inability to provide any information on the spatial distribution of the force field, information that is vital in cases of discrete, unsteady and localized actuation. In a recent study Wilke [142] attempted to estimate the spatio-temporal evolution of the force field. His results are discussed in later sections of this chapter. To the authors knowledge no other experimental investigation on the determination of both the magnitude and

the spatial distribution of the body force vector field has been published to this time.

A plasma body force model is of great importance for a successful flow control application. This chapter is focused on the development of a novel experimental approach for determining the amplitude and spatial distribution of the body force exerted on the flow by a plasma actuator. Such approach provides considerable advantages over existing numerical models. Firstly, it is relatively faster to implement even considering the complexity of the experimental setup while the results are deemed more accurate since they are based on experimental data. Furthermore, the model represents DBD actuators in true operating conditions with no simplifications in the geometry, dimensions or operating parameters which are usually made in numerical modeling. The proposed method will be evaluated against well established thrust measurement techniques demonstrated in Chapter 4 which are used as a benchmark.

7.1 Methodology

The determination of the induced body force can be done experimentally in several ways. Due to the nature of the momentum transfer mechanisms direct measurements of the ionized species density in the plasma region can only be obtained using molecular level diagnostics. The species density can be used to derive the Coulomb forces exerted by the electric field. Taking into account the complexity of such approach, only indirect methods based on the induced flow field or reaction forces can be feasibly employed in the time span such an experiment allows.

In this study two benchmark techniques are applied to determine thrust produced by the operation of the actuator. These will be used as benchmark cases for validating and verifying the developed force estimation technique. More specifically the techniques employed are: direct thrust measurements using a highly sensitive load cell and thrust calculation via momentum balance of the induced flow field. Both induced flow and thrust measurements results are explained in detail in Chapter 4.

7.1.1 Body Force estimation

The proposed body force measurement technique determines the spatial distribution of the plasma induced body force from time-resolved velocity field. The required information is obtained using a high-speed PIV system as it is shown in a subsequent section of this chapter. Detailed description on the induced flowfield is given in the refined parametric study section of Chapter 4. An analysis of the velocity field using the full Navier-Stokes (NS) equations can provide the body force. The 2D incompressible NS equations in the presence of body forces read as:

$$\frac{\partial \mathbf{U}}{\partial t} + \mathbf{U} \cdot \nabla \mathbf{U} - \nu \, \nabla^2 \mathbf{U} = -\frac{\nabla p}{\rho} + \frac{\mathbf{F}}{\rho} \tag{7.1}$$

where $\mathbf{U}$ is the 2D velocity field, p is the static pressure, ν is the kinematic viscosity of the fluid and ρ is the density.

A first approach in deriving the body force ($\mathbf{F}$) is to apply Eq.7.1 only for the first moments after the actuation. During this stage the flow is expected to accelerate only around the region of the exerted body force where the rest of the field is still relatively quiescent. For initial conditions of zero velocity the convective, viscous and pressure gradient terms are assumed relatively small and can be neglected. This reduces Eq.7.1 to:

$$\frac{\partial \mathbf{U}}{\partial t} = \frac{\mathbf{F}}{\rho} \tag{7.2}$$

which is basically Newton's second law. This method will be referenced as the *reduced method* throughout this study.

A second approach is to use the full NS equations to derive the force. For this it is necessary to calculate all the terms involved. The acceleration, convective and viscous terms are obtained from the available spatio-temporal data of the velocity field. In the absence of body force terms the only unknown is the pressure gradient which can be obtained using Eq.7.1 from the measured velocity field. In the case of the plasma actuator, the body force term appears as one extra unknown. Physically, the pressure gradient term and the body force term are equivalent and one can be used to explain the phenomena related to the other. Nevertheless, the expression of the plasma effect through a volume distributed body force is a convenient way of imposing the effect in a flow solver. To be able to bypass the problem of one extra unknown,

two major assumptions must be made: 1) the body force remains quasisteady over a large number of HV cycles and 2) the pressure gradient prior to the actuation is zero. The assumption for a quasisteady force is justified by taking into consideration the difference in time scales involved between one HV cycle and the acceleration of the flow. It has been demonstrated in Chapter 6 that the forcing within the actuation period is not constant. This has also been demonstrated by Enloe et al. [37] and numerous other related studies. Nevertheless, the high frequency of operation (order of kHz) and the hydrodynamic 'inertia' of the flow reduce the effect to quasisteady in time. A more detailed discussion on this assumption is given in a following section. In general, if the time scales which the force oscillates are sufficiently separated from the external flow time scales, the force can be assumed as time invariant. With these assumptions, Eq.7.1 is differentiated in time:

$$\frac{\partial^2 \mathbf{U}}{\partial t^2} + \frac{\partial(\mathbf{U} \cdot \nabla \mathbf{U})}{\partial t} - \nu \frac{\partial(\nabla^2 \mathbf{U})}{\partial t} = -\frac{\partial(\nabla p)}{\partial t} \cdot \frac{1}{\rho} \tag{7.3}$$

The first assumption states that the body force is steady in time and its time derivative is reduced to zero. Eq.7.3 now involves only one unknown which is the time derivative of the pressure gradient. Integrating Eq.7.3 back in time the pressure gradient can be calculated from:

$$\int_0^t (\frac{\partial^2 \mathbf{U}}{\partial t^2} + \frac{\partial(\mathbf{U} \cdot \nabla \mathbf{U})}{\partial t} - \nu \frac{\partial(\nabla^2 \mathbf{U})}{\partial t}) dt = -\frac{\nabla p}{\rho} + A \tag{7.4}$$

In the process of integration a constant A appears which has to be defined. At this point the separation between the pressure gradient due to the flow and the plasma body force is established. Based on the second assumption ($(\nabla p)|_{t=0} = 0$) the integration constant is set to zero. Eq.7.4 is plugged back into Eq.7.1 and leaves the body force term as the only unknown. Since the time gradient of the NS is used, this method will be referenced as the *gradient method* throughout this paper.

In contrast to the two benchmark techniques the *reduced* and *gradient* methods have the advantage of providing spatial distribution of body force vectors instead of an integrated thrust value. The results from such analysis can be

valuable for validation of numerical models of plasma actuators as well as an input into flow solvers investigating flow control concepts. An application of this force model is demonstrated in Chapter 9.

7.1.2 Direct thrust measurement

Direct thrust measurement is a straightforward technique which involves attaching the actuator to a load cell and measuring the force exerted by the induced flow on the actuator. By means of Newton's third law this force is equal and opposite to the total force the actuator exerts on the flow. For clarity the integrated force shall be referred to as thrust. The value of thrust can be valuable for parametric and optimization studies aiming at improving the actuator such as the broad parametric study in Chapter 4. Nevertheless, further clarifications must be made on what exactly is being measured. It has been reported repeatedly and also verified in this work that the induced flow field from the continuous operation of the actuator resembles a typical wall jet. As such, shear forces developing between the wall surface of the actuator and the accelerating fluid are also included in the load cell measurement. Another issue with this technique and in general with integral techniques is the lack of spatial information. A complete description on the use of this technique is given in Chapter 4.

7.1.3 Thrust calculation from velocity measurements

The second benchmark technique is based on measurements of the velocity field in the vicinity of the plasma actuator, obtained by PIV. The measured flowfields are described in the refined parametric study section in Chapter 4. The technique involves the definition of a control volume in the flow where the momentum flux is calculated at the boundaries of the domain and equilibrium with the internal forces is assumed (Fig. 7.1)[1]. This approach is well established in experimental and numerical investigations for the calculation of aerodynamic drag of airfoils and wings [7]. In a recent experimental study [55], it was used for estimating the thrust of plasma actuators. The calculated

[1]For all figures and references to spatial dimensions and distances in this chapter, the displayed coordinate system is used. The origin lies at the downstream end of the exposed electrode and on the flat surface

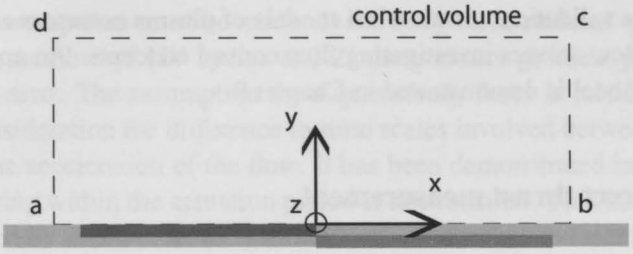

Figure 7.1: The control volume for the momentum balance equations.

thrust includes both the body force from the actuator and also the friction force at the wall. This technique also suffers from lack of any information on the spatial distribution of the body force. More specifically applying the momentum balance equation on the control volume gives:

$$\mathbf{T} = \oint_{abcd} (\rho \mathbf{U} \cdot dS)\mathbf{U} + \oint_{abcd} p dS \tag{7.5}$$

where $\mathbf{T}$ is the integrated in space force exerted on the fluid. Eq.7.5 is developed for the boundaries taking account the no-slip condition at the wall. This implies that the momentum flux across the wall is zero. Note that the boundaries where the unit vector perpendicular to the surface (dS) is negative take a minus sign:

- x -direction

$$T_x = \rho \int_{da} {u_x}^2 dy + \rho \int_{cd} u_x u_y dx - \rho \int_{bc} {u_x}^2 dy + \int_{da} p dy - \int_{bc} p dy \tag{7.6}$$

- y -direction

$$T_y = \rho \int_{da} u_x u_y dy + \rho \int_{cd} {u_y}^2 dx - \rho \int_{bc} u_x u_y dy + \int_{cd} p dx - \int_{ba} p dx \tag{7.7}$$

Due to the fact that pressure is not readily available from velocity data, a further assumption needs to be made for the accurate calculation of the momentum budget. This states that if the control volume boundaries are far enough

from the bulk of the plasma body force (near the inner electrode edge) pressure at the boundaries can be considered uniform and equal. Similar assumption is typically made in the case of airfoil drag estimation. It should also be noted here that for the x-direction the calculated force (T_x) contains not only the contribution of the plasma actuator (T_x^p) but also the shear force between the flow and the surface (T_x^s). These assumptions reduce Eq.7.6 and Eq.7.7 to:

- x -direction

$$T_x^p + T_x^s = \rho \int_{da} {u_x}^2 dy + \rho \int_{cd} u_x u_y dx - \rho \int_{bc} {u_x}^2 dy \tag{7.8}$$

- y -direction

$$T_y = \rho \int_{da} u_x u_y dy + \rho \int_{cd} {u_y}^2 dx - \rho \int_{bc} u_x u_y dy \tag{7.9}$$

7.2 Experimental Setup

Since the measurements which are used to demonstrate the developed techniques are the ones described in Chapter 4 the plasma actuator is respectively the same. An overview of the actuator and test parameters for all measurements is shown in table 7.1. The direct thrust measurements are sourced from the broad parametric study described in Chapter 4. Respective to the actuator, the PIV setup is identical to the one used in Chapter 4.

7.3 Results

7.3.1 Load cell thrust measurements

The load cell measurement offers a robust approach and has been applied to a large number of test cases. Detailed results can be found in Chapter 4. In this study the load cell results are only presented for the voltage (V) and carrier frequency (f_{ac}) values identical to the one used for the PIV measurement.

Table 7.1: Test cases for thrust and body force investigation.

Parameter	Value	Base value
upper electrode length (l_u)	10 mm	-
lower electrode length (l_l)	10 mm	-
dielectric thickness (t_d)	110 μm	-
horizontal gap (g)	0 mm	-
Load cell measurements		
applied voltage (V_{app})	8 to 14 kV_{pp} (steps of 0.5 kV)	8, 9, 10, 11 kV_{pp}
carrier frequency (f_{ac})	0.5 to 4 kHz (steps of 0.25 kHz)	1, 1.5, 2 kHz
PIV measurements		
applied voltage (V_{app})	8 to 16 kV_{pp} (steps of 2 kV)	10 kV_{pp}
carrier frequency (f_{ac})	1 to 4 kHz (steps of 1 kHz)	2 kHz

The test cases studied in this chapter are shown in Tab.7.1. For voltage variation three cases with base frequency of 1, 1.5, and 2 kHz are done, while for frequency variation four cases with base voltage of 8, 9, 10 and 11 kV_{pp} are performed. For the frequency variation the maximum tested frequency is limited by the slew rate of the HV amplifier ($350V/\mu s$) and is reduced with increase of voltage amplitude. For the entire study, a sinusoidal waveform has been used for the high voltage signal.

Thrust results for voltage and frequency variation are presented in Fig.7.2. Both voltage and frequency seem to influence the magnitude of thrust albeit in different manners. Thrust is related to voltage with a power law. Similar behavior has been previously observed by Abe et al. [3]. In contrast, the relation with frequency is linear.

7.3.2 PIV measurements: estimation of thrust

The dataset from the high speed PIV measurement is used for the thrust estimation using the momentum balance technique. After the initial acceleration stage, the induced flow field develops into a wall jet. In the steady state regime the momentum balance equations do not require evaluation of the acceleration terms. Steady state is reached in approximately 30 ms after actuation for the case of 8 kV_{pp} . In this respect it is safe to average for approximately 400 frames spanning from 43 ms after the actuation to 83 ms. Apart from the

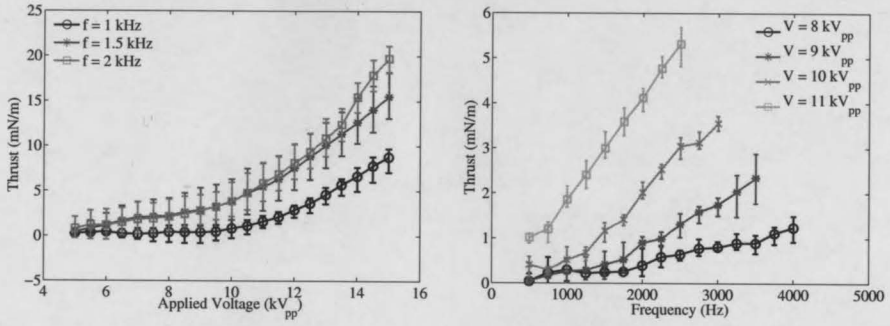

Figure 7.2: Thrust (T_x) per length of actuator for different applied voltages and frequencies, as measured by the load cell.

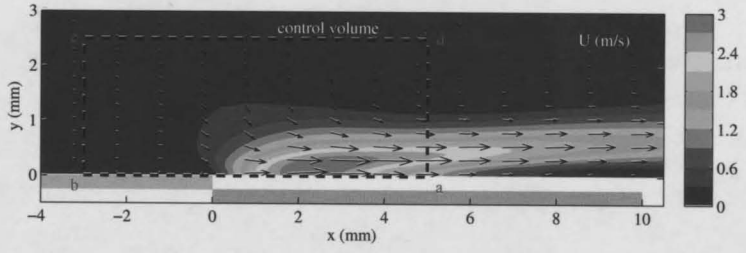

Figure 7.3: Time averaged velocity field and control volume for momentum balance ($12kV_{pp}$, 2 kHz).

processing of the raw PIV data and time averaging no other data processing is required.

The time averaged flow field with the selected control volume is shown in Fig.7.3 for the case of 12 kV_{pp}. The momentum increase mainly occurs in the x direction while a weak suction effect is observed upstream of the inner edge of the electrodes. The suction effect is an indication of a pressure gradient which is potentially strong in the vicinity of the actuator. As mentioned, any existing pressure gradient cannot be readily resolved using the time averaged velocity data. It is therefore necessary to choose the con-

Table 7.2: Section contribution in thrust (mN/m_{act}) for case of 12 kV_{pp}, 2 kHz.

section	T_x	T_y
da	-0.131	0.0015
cd	0.0160	-0.1344
bc	3.9828	-0.0235
$total$	3.8673	-0.1564

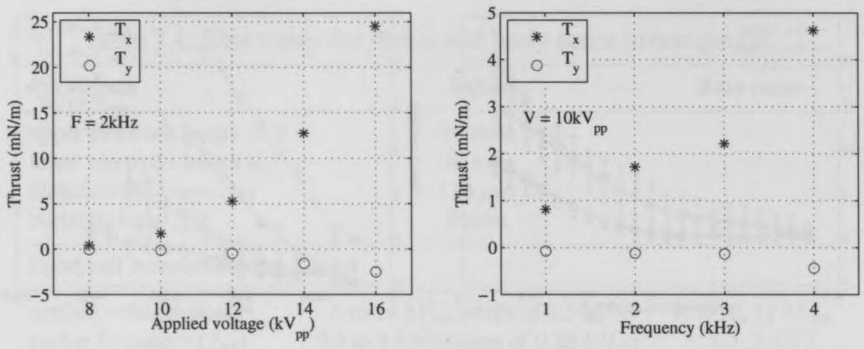

Figure 7.4: Thrust per length of actuator for different applied voltages and frequencies, as calculated by momentum balance on the PIV data.

trol volume such that the pressure effects are minimized. The chosen control volume is a rectangular area spanning form x = -3 to x = 5 mm and y = 0 to y = 2.5 mm.

The momentum balance equation in x and y directions calculated using the terms in (7.8) and (7.9) reveals the significance of each boundary of the control volume. As it is shown in Tab.7.2 and also apparent from the velocity field, the maximum contribution to thrust comes from the outflowing horizontal velocity from section bc. This implies that the very simple approach of calculating thrust from only one cross section of the jet would still deliver satisfying results. Nevertheless, since field data are available the method used herein takes into account all sections of the control volume.

The thrust as a function of both applied voltage and frequency are shown in Fig.7.4. The same power law behavior as observed in the direct thrust measurements is observed here for thrust in x direction with different voltages. A slight increase of thrust magnitude in y direction is observed with increase of the applied voltage. For different frequencies, the linear dependence of thrust appears to hold. A more concise comparison of the results from different techniques is performed at a subsequent section.

7.3.3 PIV measurements: estimation of body force

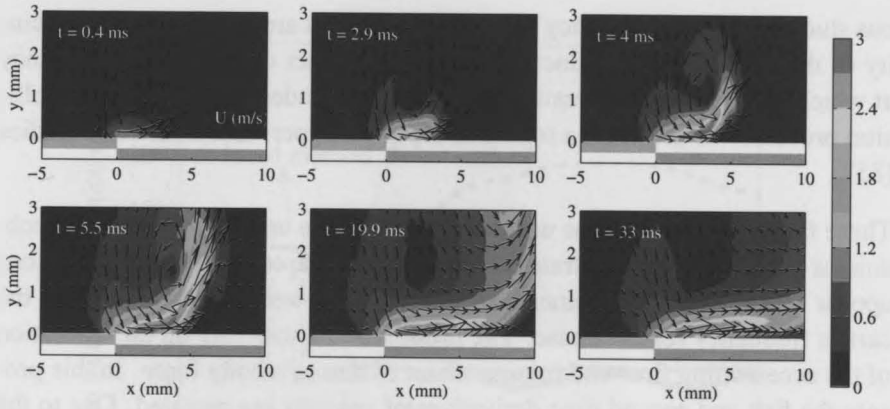

Figure 7.5: Temporal evolution of the total velocity field (U) for the actuation case of 12 kV_{pp}, 2 kHz.

The two described approaches, (*reduced* and *gradient method*), are applied to the velocity field measured using PIV. Instantaneous snapshots of the evolving flowfield are presented in Fig.7.5. The time values indicate elapsed time from the start of the actuation. The flow reacts immediately to the actuation with initial velocity components already starting to appear approximately 0.1 ms after the start of the actuation. The flow accelerates in a region starting from the end of the upper electrode and extending over half the covered electrode (x = 0 to 5 mm). The impulsive forcing on the flow creates a starting vortex which develops and moves out of the FOV in less than 40 ms after the start of the actuation. It is apparent that the general forcing of the actuator produces a wall jet which in turn creates a secondary weak suction effect upstream.

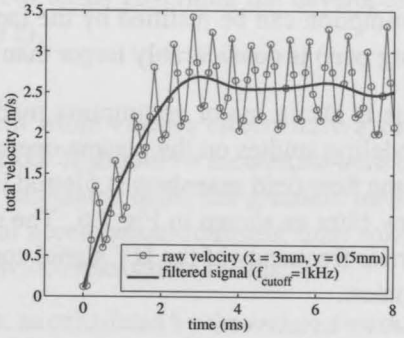

Figure 7.6: Raw and filtered signal of velocity in the developing flowfield.

At this point, some specific features of the induced flow field should be discussed due to their effect on the results of the proposed technique. In a previ-

ous study [15], high frequency velocity fluctuations are registered in the vicinity of the actuator. These fluctuations are a product of the carrier frequency at which the actuator is operating and reflect the underlying ion-neutral collision processes in the plasma region as reported in previous numerical studies [85].

These fluctuations reveal the unsteady nature of the underlying forcing mechanisms which was demonstrated in detailed in Chapter 6. These fluctuations appear in the PIV measurements of this work as well, corresponding to the carrier frequency for each case. The proposed methods rely on the resolution of the accelerating flow and interpretation of that to a body force. In this process the first and second time derivatives of velocity are required. Due to the high frequency fluctuations, these terms cannot be explicitly resolved without large artifacts. Based on the large difference between the time scale governing the acceleration of the flow and the time scale of these fluctuations one further assumption must be made. This states that although the flow, and in extent the body force, fluctuate in time the latter can be considered as quasi steady. This assumption can be justified by the fact that the rise time of the flow (accelerating part) is considerably larger than the fluctuation period.

This is also a major assumption made in a large majority of first-principles modeling studies on the plasma operation. Based on this, the PIV time-series of the flow field snapshots is filtered in time with a 6th order low-pass Chebychev filter as shown in Fig.7.6. The cutoff frequency is chosen based on the carrier frequency of the HV signal corresponding to the test case under investigation.

For the majority of cases the cutoff frequency is half the carrier frequency. By filtering the high frequency fluctuations, the development of the velocity field occurs smoothly and the time derivatives can be calculated with reasonable accuracy.

The *reduced method* involves the utilization of the very first moments (first 0.5 ms) after actuation when all other terms apart from acceleration are negligible. The acceleration, convective, viscous and pressure gradient components of the NS are shown in Fig.7.7 as a function of time after actuation ($t = 0$). The terms are calculated in x direction from the time-filtered PIV data for a given point located well into the expected force field. As anticipated, the acceleration term dominates the very first moments of actuation with a high and almost constant value. Convection and pressure gradient are initially neg-

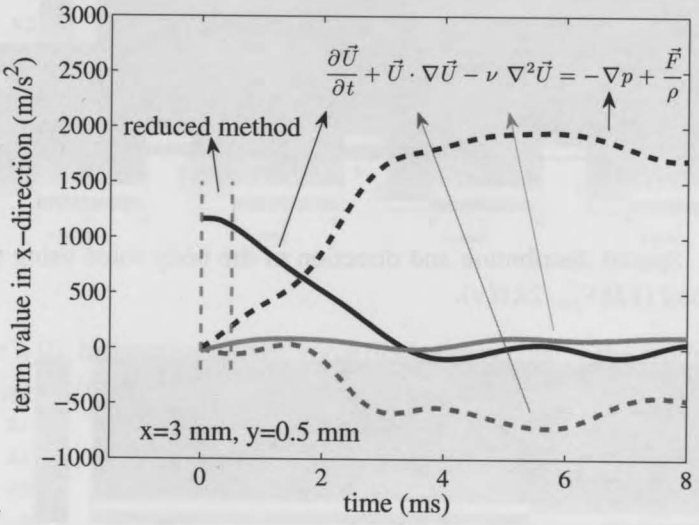

Figure 7.7: Temporal evolution of the NS terms governing the development of the flow in x direction ($12kV_{pp}$, $2kHz$).

ligible and eventually dominate the event while viscous effects have a small influence during the entire actuation period. It should be mentioned here that the pressure gradient term in Fig.7.7 is calculated using the *gradient method* as discussed in section 7.1.1. The initial acceleration-dominant time span is visually confirmed to be 0.5 ms and provides reasonable results.

The spatial distribution of the body force, as calculated by the *reduced method*, is shown in Fig.7.8 for the case of $12kV_{pp}$ applied voltage and $2kHz$ carrier frequency. The PIV snapshots used for this case cover the first 0.5 ms after actuation and the force field is simply averaged over this span. The bulk of the force appears to be just downstream the inner electrode edge while the horizontal extent spans almost a quarter of the covered electrode. In the wall normal direction the force field extends no more than 1 mm which confirms the very thin wall jet reported by this and numerous other investigations. The vertical force seems to be very weak compared to the horizontal component. Its major direction is towards the wall especially near the edge of the exposed electrode. For this case the cutoff frequency of the Chebychev filter is 1000 Hz.

For the same case (12 kV_{pp}, 2 kHz), the spatial distribution of the body force

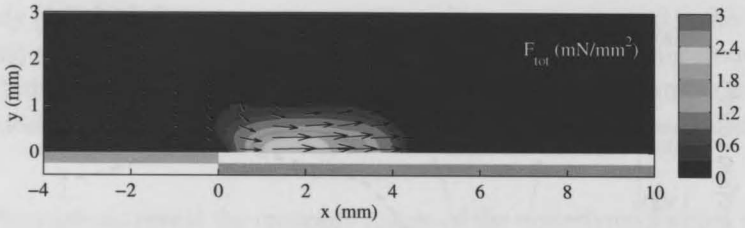

Figure 7.8: Spatial distribution and direction of the body force using the *reduced method* ($12kV_{pp}$, $2kHz$).

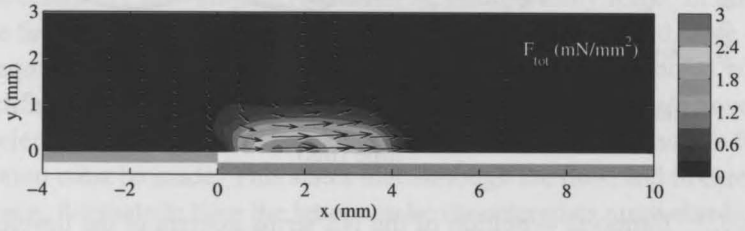

Figure 7.9: Spatial distribution of the body force using the *gradient method* ($12kV_{pp}$, $2kHz$).

using the *gradient method* is shown in Fig.7.9. The first 20 ms after actuation are used and the force field is averaged over this time span. The general shape of the field is identical to the results from the *reduced method*. Nevertheless, the magnitude of the force attained with the *gradient method* is slightly larger than the *reduced method's* result. This small discrepancy can be attributed to modeling errors inherent in the eliminated terms of the *reduced method* as well as the ambiguity in selecting the initial acceleration time span. These facts support the higher accuracy of the *gradient method*.

One additional advantage of the *gradient method* over the *reduced method* is its relative independence on the time span used for the force calculation. In contrast to the *reduced method* there is no term elimination involved and no consideration should be made in the dominance of one term or another. Applying this method for the first 20 ms after actuation gives an almost steady in time body force. Several snapshots of the instantaneous total force field are shown in Fig.7.10. The temporal coherence of the force distribution is an extra indication of the validity of the method as this was an important assumption made during the formulation of the technique.

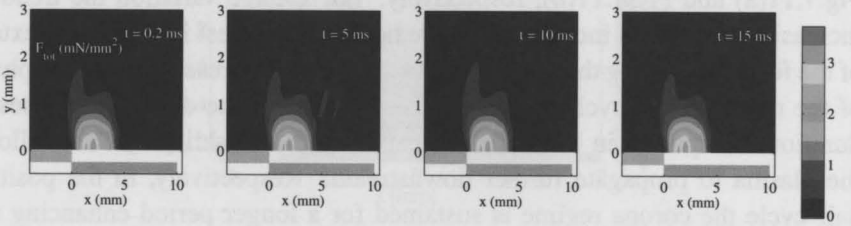

Figure 7.10: Instantaneous total force field obtained using the *gradient method* ($12kV_{pp}$, $2kHz$).

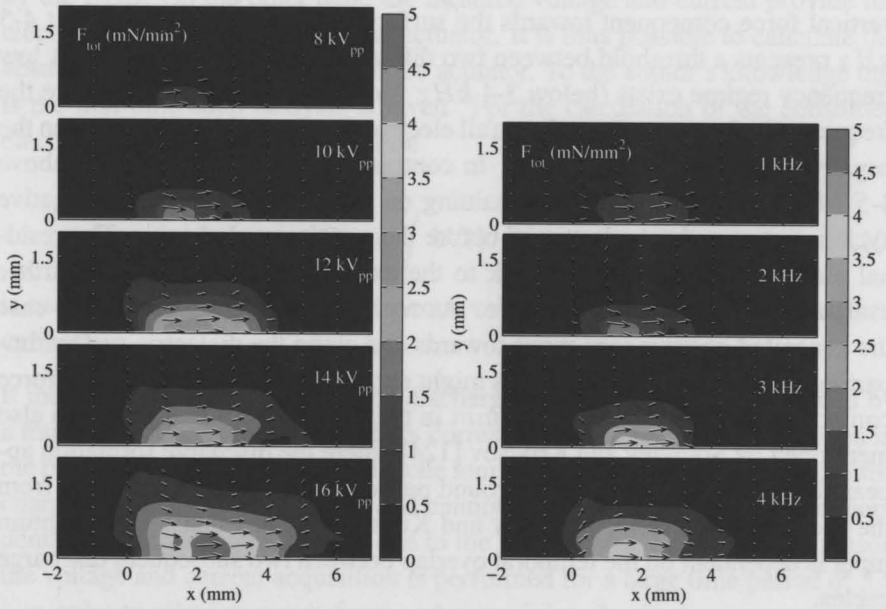

(a) (b)

Figure 7.11: The measured body force distributions for the tested (a) voltages and (b) frequencies

The force distributions for different voltage and frequencies are presented in Fig.7.11(a) and Fig.7.11(b), respectively. For voltage variation the trend of increasing force with increased voltage holds. Of interest is the spatial extent of the force field along the dielectric. As the voltage increases, the active phase of the negative half cycle, where the electron avalanche occurs, increases in duration as reported in the excellent paper by Likhanskii [85]. This allows the plasma to propagate further downstream. Respectively, in the positive half cycle the corona regime is sustained for a longer period enhancing the movement of positive ions downstream. This is also verified by the force distributions for different frequencies.

In this case, the spatial extent of the plasma cloud remains almost the same as the applied voltage is fixed. The magnitude of the force, nevertheless, is increased since the momentum exchange between the ionized gas and neutral air is performed at a higher rate. Furthermore, a jump in maximum force also occurs from the case of 3 kHz to the case of 4 kHz as well as a secondary vertical force component towards the surface. This is an indication that 4-5 kHz presents a threshold between two different regimes of operation. A low frequency regime exists (below 3-4 kHz for these plasma scales), where the frequency is slow enough to allow full electron-ion recombination between the negative and positive half cycles. In contrast, for higher frequencies (above 4-5 kHz) the electron cloud remaining on the dielectric from the negative cycle is not completely destroyed before the positive cycle begins. The residual electrons are then pulled back to the exposed electrode causing further avalanche ionization as they move. As reported by Likhanskii, in this case the generated positive ions move towards and along the dielectric surface imparting momentum to the air. This might explain the secondary vertical force components located around $x = 3mm$ in the 3 and 4 kHz cases. This is also mentioned by Soloviev and Krivtsov [124] where the discharge formation appears to be affected by the background particle concentration fields left from the previous HV cycles. Soloviev and Krivtsov suggest that the momentum input is dependent on the temporal overlap between two subsequent discharge cycles.

7.3.4 Power consumption and efficiency

Through the resolution of the body force fields, some interesting possibilities are presented in the analysis of the power budget of the actuator. More specif-

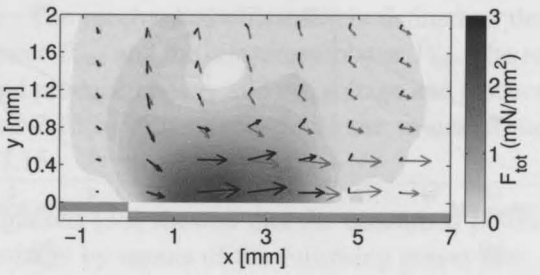

Figure 7.12: The body force and the velocity field ($t = 15\ ms$) for the case of $V_{app} = 12\ kV_{pp}$ and $f_{ac} = 2\ kHz$. The gray vectors indicate the velocity field and the black vectors the body force.

ically, the availability of actual field data for velocity and body force vectors in the vicinity of the actuator can provide the pure mechanical power given by the DBD. On the other hand the mesured voltage and current provide the electrical power consumed by the actuator. It is thus possible to calculate the absolute mechanical efficiency of the actuator. To the author's knowledge this is the first time such analysis is given. For the calculation of the consumed electrical power the integral relation

$$P_{in} = \int V(t) \cdot I(t) dt \tag{7.10}$$

is used where $V(t)$ is the instantaneous voltage and $I(t)$ is the instantaneous current.

It must be stressed here that DBD discharge current is typically governed by a multitude of high frequency peaks corresponding to the microdischarges in the plasma region during the avalanche ionization phase [38]. These microdischarges occur in ns time scales and cannot be accurately measured independently of electromagnetic noise due to the high electric field. For this reason the voltage and current acquisition is performed for a large time period of 3.5 s in order to alleviate errors from under resolving the discharge current. For the power consumption P_{in}, the instantaneous voltage and current signals are multiplied and the result is integrated over time to produce the final value for P_{in}.

On the other hand both the velocity field and the two dimensional body force field is available in order to calculate the mechanical power P_{out} that is pro-

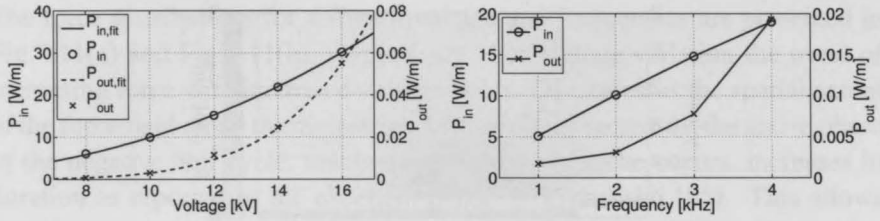

(a) (b)

Figure 7.13: The power consumed P_{in} and produced P_{out} by the plasma actuator for the range of (a) voltages and (b) frequencies

duced by accelerating the flow. This can be done by means of Eq.7.11

$$P_{out} = \int_{\Omega} \mathbf{F_b} \times \mathbf{U} d\Omega \tag{7.11}$$

Where Ω is the integration region around the plasma actuator, F_b is the body force and U the velocity. Eq.7.11 practically expresses the spatial integration of the inner product of the body force and the velocity field in Fig.7.12.

One of the major assumption made during the derivation of the force estimation technique is the time invariance of the body force. As a consequence the temporal evolution of the mechanical power output is solely defined by the evolving flowfield. Fig.7.14 presents the case where the plasma actuator is operated at a voltage of 12 kV_{pp} and a frequency of 2 kHz. It takes about 6 ms for the power output to reach a quasi-steady level of approximately 12 mW per meter of actuator length. Changing the input voltage and frequency of the plasma actuator does not have a profound effect on the settling time that is recorded. For all cases that were tested, a settling time of about 6 ms was recorded.

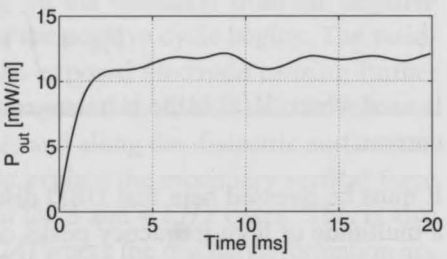

Figure 7.14: The power produced by the actuator as a function of time. ($V_{app} = 12\ kV_{pp}$ and $f_ac = 2kHz$)

All the information is available to calculate the mechanical efficiency η of the

plasma actuator. The mechanical efficiency is defined as the ratio between the produced power P_{out} and the consumed power P_{in}. The relation between the consumed and produced power and the voltage and frequency is shown in Figs. 7.13(a) and 7.13(b) respectively while the values of the efficiency are depicted in Fig.7.15.

Previous investigations [38] showed that the consumed power can be related to the applied voltage by means of the following power law: $P_{in} \sim V^n$. In [38] a value of $n = 3.42$ was found at an operating frequency of 6 kHz and for an operating frequency of 3 kHz a value of $n = 3.35$ was found. The same fitting function can also be applied to the data of the current investigation as can be seen in Fig.7.13(a). The standard deviation between the fit and the consumed power is 0.4% of the power that is consumed at a voltage of 16 kV_{pp}. Although the fit is of a good quality, the value that is found for the exponent $n_{P_{in}}$ is only 2.35. This is significantly smaller than the values that were found in [38].

The same fitting function can also be used for the produced power and the efficiency. In both cases reasonably accurate fits are obtained. The standard deviation equals 1.69 % and 3.86 % respectively, these values are normalized with the maximum values that were recorded for the produced power and the efficiency. For the produced power, a high value of $n_{P_{out}} = 6.13$ is found and for the efficiency $n_\eta = 3.82$. Note that, $n_{P_{out}} - n_{P_{in}} = 6.13 - 2.35 = 3.78 \approx n_\eta$, which demonstrates the quality of the fit.

The relation between the absolute mechanical efficiency, voltage and frequency is shown in Figs.7.15. It is interesting to note that efficiency is not a monotonically increasing function with frequecny, rather it exhibits a minimum at 2 kHz. This behaviour also cannot be approximated by means of the power law relation from [38].

From the point of view of mechanical efficiency it seems beneficial to operate at a high voltage and / or high frequency. This will however reduce the lifespan of the plasma actuator due to increased degradation of the dielectric. Another important point to be noticed is the magnitude of the mechanical efficiency, which is very small. The largest value that is found is 0.183 %, for the case where the actuator is operated at a voltage of 16 kV_{pp} and a frequency of 2 kHz. The smallest value for the efficiency is only 0.013 %, for a voltage of 8 kV_{pp} and a frequency of 2 kHz. This low mechanical efficiency however does not imply that the DBD plasma actuator is not effective as a flow control

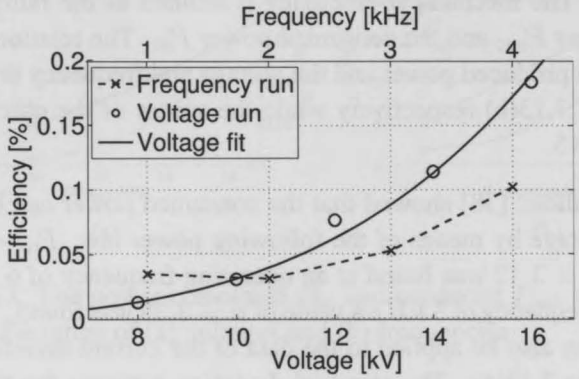

Figure 7.15: Efficiency as a function of the frequency f_{ac} and voltage V_{app}. For the frequency run the voltage is kept at a fixed value of 10 kV_{pp} and for the voltage run the frequency is kept at a fixed value of 2 kHz.

device. It merely expresses the lack of capabilities in efficiently accelerating flow, much like an engine. Although it is interesting to analyze the actuator from the point of view of its mechanical efficiency, this is not the only measure of capabilities. In its role as a flow control device the main question is how effective it is in exciting or damping certain flow structures. In [50] it is for instance used to damp artificially introduced Tollmien-Schlichting waves. High attenuation rates are reached, which in turn produce a significant drag reduction. Although the mechanical efficiency as defined in this study is very low, its efficiency as a flow control device can still be excellent.

7.3.5 Comparison of thrust and force estimation techniques

An overall comparison between the thrust values attained by the proposed body force estimation methods and the two benchmark techniques is presented in Fig.7.16 for different voltages and frequencies. It should be noted here that the thrust value from the proposed PIV techniques is calculated by integrating the body force value over the spatial domain.

For different voltages, a good agreement is observed between the different techniques. In x direction (horizontal body force) the momentum balance is located at the lower error margin of the load cell measurements. The thrust es-

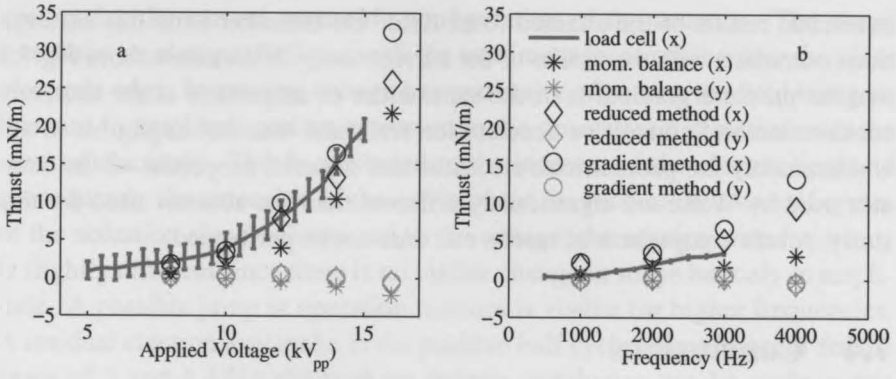

Figure 7.16: Thrust values from the tested methods as a function of applied voltage (a) and frequency (b).

timated by the body force methods is systematically larger than the two other techniques although still in the error margin of the load cell for the majority of cases. This is expected as both, the load cell measurements and the momentum balance calculations contain the shear stress at the wall. Additionally, the previously mentioned difference between the reduced and gradient methods is observed. This is attributed to the term elimination inherent in the reduced method.

For different frequencies, the absolute error stays in the same level while the relative error between the different methods is larger. This is partly due to the low applied voltage of 10 kV_{pp} that is used for this test series as the slew rate of the currently used HV amplifier is the limiting factor in increasing both voltage and frequency. The low voltage results in lower body force and the results are more susceptible to interference from external sources and other measurement errors. It is expected that the relative error would decrease with higher applied voltage.

As was mentioned in the beginning of this chapter, a study with similar objectives has been performed by Wilke [142]. Although using similar techniques for measurement of the induced flowfield, Wilke's study differentiates in the assumptions made towards the decoupling of the body force term and the pressure gradient term in the NS decomposition. More specifically he regards the pressure gradient term as negligible compared to the body force. This assumption is based on good agreement between the measured flowfield and

numerical results of the attained force field. On the other hand this assumption contradicts with the results of the current study. It is evident from Fig.7.7 that the pressure gradient is of the same order of magnitude as the unsteady acceleration and convective acceleration term and thus not negligible at all. Unfortunately the geometrical, electrical and material properties of the actuator used by Wilke are significantly different than the actuator used for this study. A safe comparison of results can thus not be performed.

7.4 Conclusions

A novel technique for the estimation of the body force field of plasma actuators is developed and tested. This involves the use of time-resolved PIV data on the evolving flowfield during actuator operation. The force amplitude and spatial distribution can be calculated through the estimation of the individual terms of the 2D incompressible NS equations and is conducted in two distinct ways. First, a dimensional analysis is performed on the temporal and spatial evolution of the velocity field. An initial period dominated by pure acceleration is identified and the latter is expanded explicitly in body force terms. Second, the full NS is estimated. The decoupling between the force and pressure gradient terms is performed based on the temporal stability of the body force and the initial zero pressure gradient.

The results from the tested methods are compared against well-established thrust measurement techniques and demonstrate sufficient agreement. Based on the comparison several comments can be made on the proposed techniques. The *reduced* and *gradient* techniques produced consistently larger values of horizontal force than direct thrust measurements or momentum balance on the velocity data. This is mainly attributed to the inherent inclusion of the wall shear force, opposite to the plasma body force, in the total thrust value obtained by the two benchmark techniques. The proposed techniques negate this effect since the calculation is done in the fluid volume not including the wall effects. Furthermore, a comparison can be made between the reduced and gradient methods. Although attractive because of its simplicity, the reduced method presents some drawbacks in respect to the gradient method. These are based on term elimination as well as on the semi arbitrary choice of applied time length.

The general shape of the force field seems to be dictated by voltage and fre-

quency for the current geometric configuration of the actuator. The shape resembles an elongated ellipse with the maximum force arising near the inner electrode edge. Increasing voltage has two major effects on the field being an increase in amplitude and an extension in the downstream direction over the covered electrode. This is attributed to the increase of the electric field and consequently the extension of the active phase for each of the two half cycles of the actuation signal. Compared to the voltage, the relation with frequency is slightly different since there is no visible change in shape but only in amplitude. A possible jump in operation regimes is visible for higher frequencies. A residual electron avalanche in the positive half cycle seems to occur for the cases of 3 and 4 kHz although no definite conclusion can be made at this point.

Finally, using simultaneously measured values of voltage and current the consumed electrical power is calculated. Additionally, the power output of the actuator is estimated using the inner product of the force and velocity fields. The absolute mechanical efficiency of the actuator is then calculated, indicating the lack of capabilities in accelerating bulks of fluid from the actuator part. In contrast the use the actuators as instability manipulators seems to be the only efficient way of operation.

The measured body force distributions using the *gradient method* will be used in Chapter 9 as models of the DBD actuator in a numerical framework. Prior to this, the models are validated in Chapter 8.

Chapter 8

Validation of the Plasma Force Model

In the previous chapter the *gradient method* was proposed and implemented for the measurement of the body force field of the plasma actuator. The method is based on the measurement of the evolving velocity field originating from the impulsive start of the actuation in initially quiescent air. The measurement is achieved with the use of a time-resolved two-component particle image velocimetry (2C-PIV) system, able to resolve both the temporal and spatial features of the induced jet. By assuming a quasi-steady body force in time and through reconstruction of the terms of the incompressible Navier-Stokes equations, an estimation of the applied body force is possible. In contrast to other experimental techniques the use of this method provides the estimation of the plasma body force in amplitude as well as spatial distribution. Most importantly, the attained body force distributions can be used directly into a numerical flow solver with no further calibration. Although good agreement was found between the results of the *gradient method* and other reference thrust measurement techniques, open questions remained regarding the applicability of the body force distributions in a numerical solver. More specifically, in order to ensure a global and robust character for the body force distributions as a plasma actuator model, several key requirements must be fulfilled:

- Implementation of the experimental body force distributions in a numerical flow solver should result in the original flowfield for the same initial (quiescent flow) and actuator design conditions.

- The experimental body force distributions should provide accurate representation of the actuator effect in operational regimes which are independent from the original force measurement experiment.

- The force estimation technique assumes that the body force is quasi-steady in time. This assumption must not affect the numerical results.

In general the differences between the numerical and experimental results are expected to reveal the effects of the assumptions involved in the body force model as well as the operational envelope in which the force model can accurately capture the plasma actuator effect.

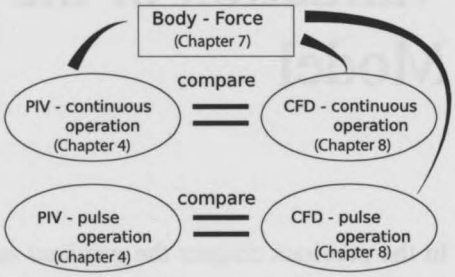

Figure 8.1: The methodology of comparison followed towards model validation.

This chapter is aimed at the implementation and validation of the body force distributions as DBD actuation models. The experimentally derived body force distributions are implemented in the framework of a well established flow solver and the results are compared with the respective experimental cases. Two modes of operation are discussed, namely, continuous and pulse operation. The continuous operation cases correspond to the original experimental campaign that led to the force distributions. The pulse operation cases aim at proving that the force distributions can be applied in cases which are independent from the original force measurement cases. A summary of the followed methodology is presented in Fig.8.1.

The structure of this chapter involves a section with details on the numerical framework. In the following section results are presented and the final section discusses some conclusions and outlook.

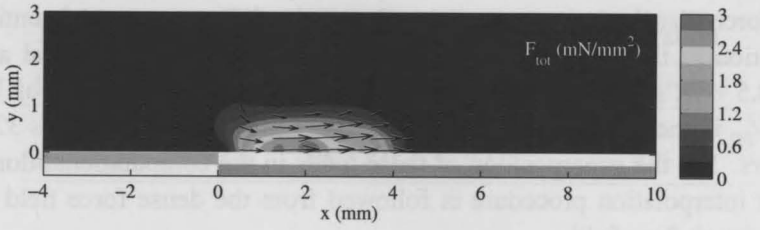

Figure 8.2: The experimental body force distribution for the case of V_{app} = 12 kV_{pp} and f_{ac} = 2 kHz (from Chapter 7).

8.1 Numerical Framework

8.1.1 Flow solver

The validation is performed entirely in the framework of the open-source CFD code OpenFOAM. This code employs finite volume discretization over structured or unstructured grids and is able to handle complex geometries. A variety of specialized solvers is provided, covering a large spectrum of possible applications. In this study the full unsteady incompressible Navier-Stokes equations are solved with the inclusion of predefined body forces. The velocity-pressure coupling is achieved using the PISO (Pressure Implicit with Splitting of Operators) [59] algorithm while the advancement in time is performed using a second order accurate implicit Euler algorithm.

8.1.2 Force implementation

The plasma actuator effect on the flow is expressed in terms of body forces imposed within the NS equations. In a 2D framework these read:

$$\frac{\partial \mathbf{U}}{\partial t} + \mathbf{U} \cdot \nabla \mathbf{U} - \nu \nabla^2 \mathbf{U} = -\frac{\nabla p}{\rho} + \frac{\mathbf{F}}{\rho} \tag{8.1}$$

where $\mathbf{F}(\mathbf{X}) = [F_x(\mathbf{X}) \quad F_y(\mathbf{X})]^T$ are the body force components of the actuator action and $\mathbf{X} = [x \quad y]^T$ are the spatial coordinates in the 2D domain. $\mathbf{U} = [u \quad v]^T$ is the velocity field while p is pressure, ν is kinematic viscosity and ρ is density.

The force distributions are available for all the different cases of continuous operation in the form of force vectors (2 components) in a spatial area of 15×3.5 mm starting at x = -4 mm. The force field for the case of V_{app} = 12 kV_{pp} is shown in Fig.8.2 as an example. The force field contains 322×74 vectors. For the superposition of these fields in the computational domain a linear interpolation procedure is followed from the dense force field to the more rough flow field.

For continuous operation the force is imposed as a time invariant quantity at every time step. Additionally, provision for the pulse operation is implemented in the flow solver. This involves the multiplication of the force field by a square waveform function which oscillates between values of 0 (actuator 'off') and 1 (actuator 'on'). The oscillation is performed at the required pulse frequency f_p while the ratio of the 'on' and 'off' periods is defined by the duty cycle D.

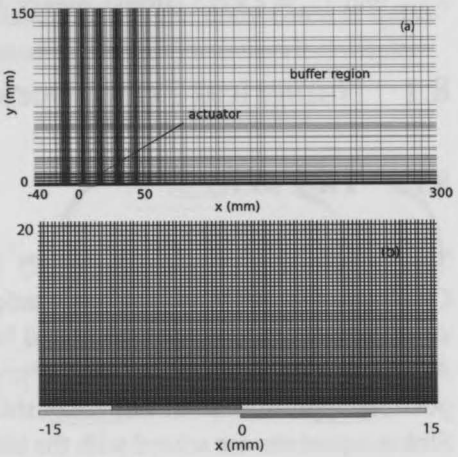

Figure 8.3: (a) Computational mesh used for the continuous cases and (b) detail in the vicinity of the actuator.

8.1.3 Simulation parameters

The simulation is executed using a modified version of the icoFoam transient incompressible solver incorporated in OpenFOAM. The modification involves the inclusion of the body force fields. It is well established from the experimental results that the developed jet from the plasma actuation is laminar at least within the PIV field of view. In this manner no turbulence modeling is employed in the simulation and the full laminar NS equations are solved.

After initial grid convergence studies, two grids are selected for the simulation. The first grid is used for the continuous operation cases. It is consisted of structured hexahedral cells clustered near the wall in order to increase accuracy in the vicinity of the actuator (Fig.8.3). Additionally the mesh employs

Table 8.1: Mesh parameters for the numerical investigation

case	**size** (mm)	**cells**	$dx\|_{y=0}(mm)$	$dy\|_{y=0}(mm)$
continuous	340×150	310×160	0.35	0.1
pulse	70×40	400×200	0.175	0.05

an outer buffer layer of more roughly spaced cells. This is used in order to keep the boundaries of the computational domain at sufficient distance from the actuator without increasing the number of cells beyond practical values. Furthermore, the physical limits of the computational domain are chosen such that the starting vortex, from the impulsive plasma actuation, does not cross them during the simulation time. This precaution is taken in order to avoid unwanted reflections of velocity or pressure that can interfere with the flowfield near the actuator.

For the pulse operation a grid similar to the continuous case is used. The outer buffer region is omitted since the simulation is ran for less time and the starting vortex is smaller due to the lower strength of the actuator compared to the continuous operation. Due to the smaller physical size of the second mesh, a more fine spacing is chosen for increased accuracy. The dimensional properties of the two meshes are shown in Table.8.1. All simulations are conducted with initial conditions of zero velocity and pressure in order to replicate the respective experimental conditions of the PIV measurement. Neumann boundary conditions of zero gradient are imposed on the velocity at the open boundaries while no-slip conditions are imposed at the wall. For pressure, zero gradient conditions are imposed at all boundaries except the left hand side boundary where a Dirichlet condition of $p = 0$ is applied. All cases are ran using a fixed time step of $1\times10^{-4}\ s$

8.2 Results

8.2.1 Continuous operation

The first group of test cases involves the continuous operation of the actuator. The time resolved PIV experiment serves a double purpose. As summarized in Fig.8.1 the measurements firstly provide the body force distribution as de-

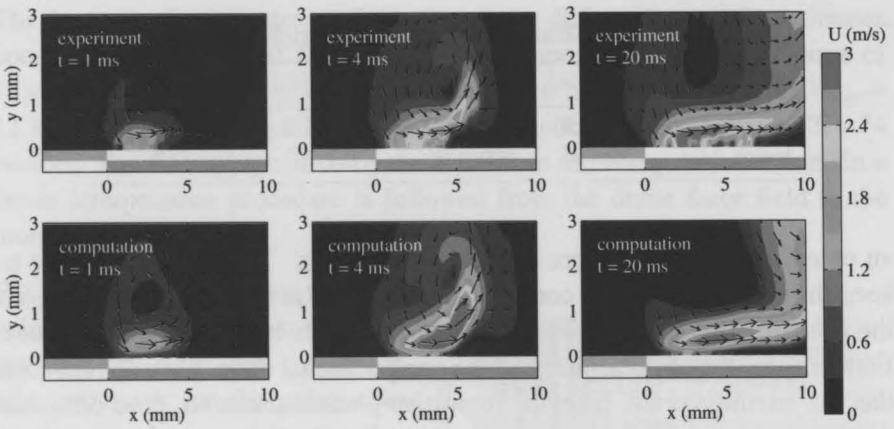

Figure 8.4: Snapshots of the evolving total velocity field for $V_{app} = 12\ kV_{pp}$, $f_{ac} = 2\ kHz$ (time values are relative to the start of the actuation).

scribed in Chapter 7. Secondly, the measured velocity fields under continuous operation present the first group of benchmark measurements which can serve as a comparison to the respective numerical results. Several voltages and frequencies are tested in order to establish the dependence of the induced flowfield on these parameters. In all cases the measurements are taken prior to the start of the actuation in order to resolve the initial transient phase of the induced jet. The measurements are continued until after the flowfield has reached a quasi steady state in order to acquire time averaged information as well. On the numerical side, the test cases are run with the conditions specified in section 8.1. For every voltage or frequency case the respective experimentally determined body force is used as a time invariant vector field and the simulation is executed for the first 0.5 s after the start of actuation.

The experimentally resolved transient development of the induced flowfield is presented in Fig.8.4 for the case of 12 kV_{pp} and 2 kHz along with the results from the respective numerical simulation. Additionally, a comparison of the time history of velocity in several spatial locations is presented in Fig.8.5.

Shortly after actuation, flow is accelerated tangentially to the wall in the direction of the covered electrode. The flow topology is similar to that of a wall jet with a typical starting vortex forming within the first 5 ms of actu-

ation. Through interaction with the wall, the vortex advects out of the FOV in the downstream direction. When the starting vortex is at a sufficient distance from the actuator, the flowfield settles into a wall jet with the dominant velocity component established parallel to the wall.

A weak suction effect is observed at an upstream location where fluid moves in a vertical direction towards the wall just upstream of the actuator. Some discrepancies appear between experimental and numerical results in Fig.8.4 especially in regions near the wall. This is attributed to wall reflections present in the PIV measurements which limit the near-wall resolution of the system. It is evident in Fig.8.5 that additionally to the large coherent structures associated with the impulsive start of the actuation, secondary velocity fluctuations appear in the vicinity of the actuator ($x = 2\ mm$). These fluctuations are attributed to electrostatic oscillation of the body force and are not captured by the body force model as described in Chapter 6. Additionally, a relatively large error is apparent in position $x = 6\ mm$ between the experimental and numerical result. This can be attributed to modeling errors inherent in the body force estimation techniques as well as reflection from the wall during the PIV measurement. A more detailed discussion on the measured velocity fluctuations and modeling error is given in Section 8.3. A look at the time averaged flowfield is taken in order to establish the capability of the experimental body force to reproduce

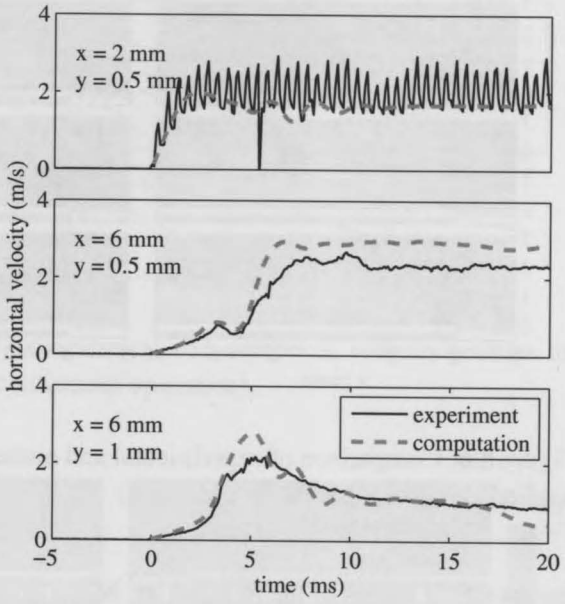

Figure 8.5: Time history of the horizontal velocity in three spatial positions near the actuator for $V_{app} = 12\ kV_{pp}$ and $f_{ac} = 2\ kHz$ (time values are relative to the start of the actuation).

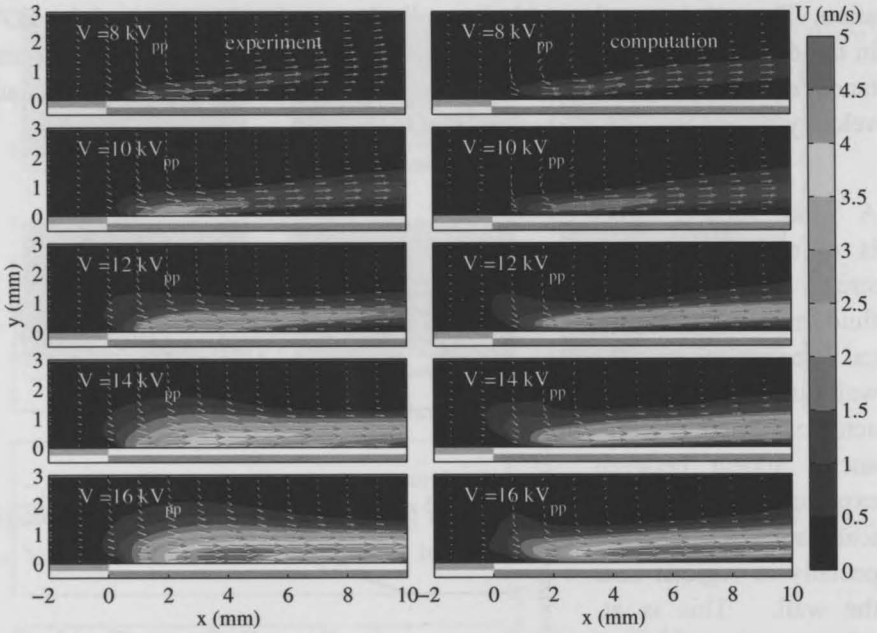

Figure 8.6: Comparison of experimental and numerical flowfields for different applied voltages (continuous operation).

the statistical values of the induced jet. Mean flowfields are calculated by taking the time average of a series of PIV snapshots which starts well after the flowfield has reached the fully developed state of the tangential to the wall jet. The time averaging also levels out the effect of the high frequency fluctuations attributed to electrostatic oscillation (see Section 8.3).

The experimental flowfields are averaged over 1000 frames (0.1 s) for all cases. The series of 1000 frames is taken 0.4 s after the start of the actuation in order to ensure minimum bias of the time averaged results from the initial transient period. The numerical flowfields correspond to snapshots at 0.5 s after actuation which approximates the steady state. The averaged flowfields for different voltages and frequencies are presented in Figs. 8.6 and 8.8 respectively. Additionally, averaged velocity profiles in different x position are presented for the cases of varying applied voltage in Fig.8.7 and varying carrier frequency in Fig.8.9 along with the respective numerical results.

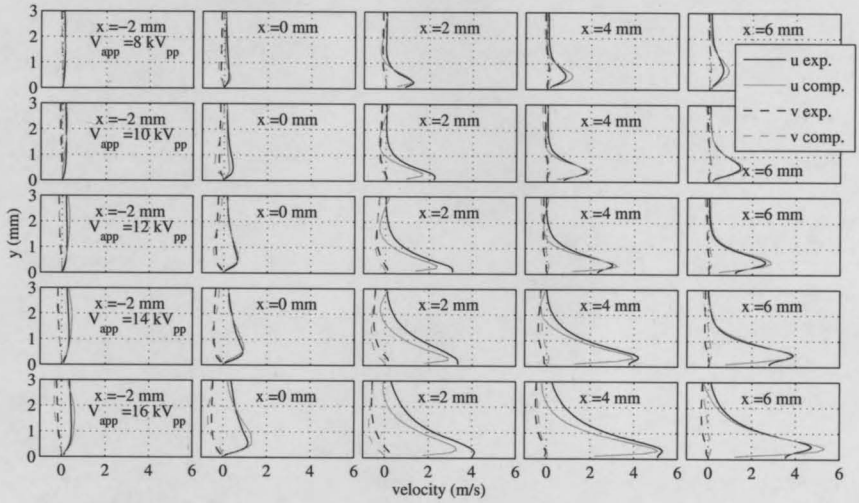

Figure 8.7: Comparison of experimental and numerical velocity profiles for different applied voltages (continuous operation).

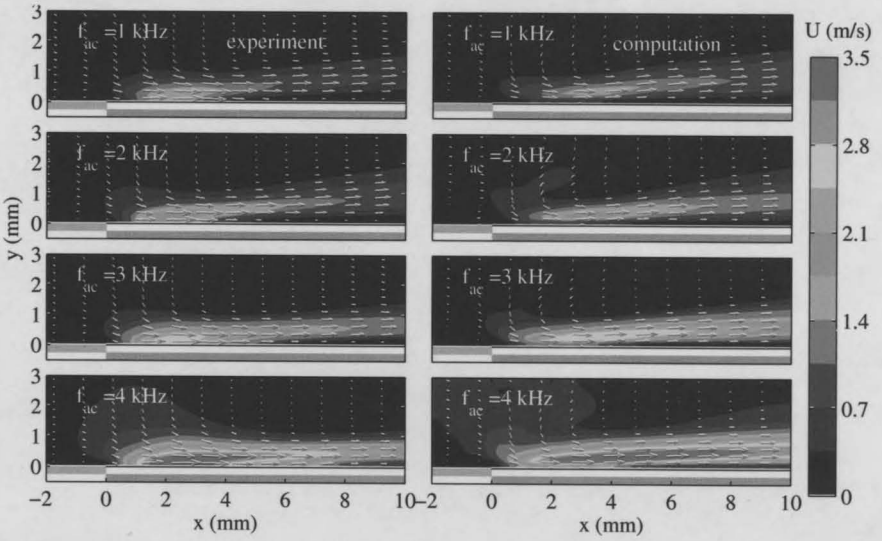

Figure 8.8: Comparison of experimental and numerical flowfields for different carrier frequencies (continuous operation).

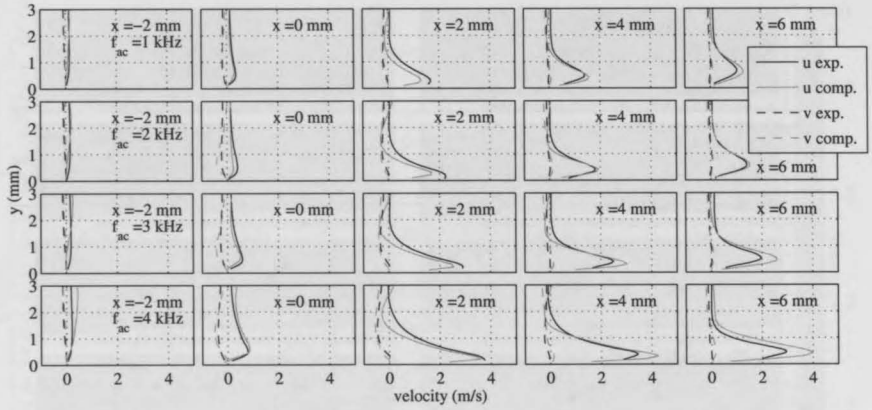

Figure 8.9: Comparison of experimental and numerical velocity profiles for different carrier frequencies (continuous operation).

Differences between numerical and experimental results rise especially in regions within the body force extent. These are accentuated for strong actuation cases such as 16 kV_{pp}, 2 kHz and 10 kV_{pp}, 4 kHz. These are attributed to the modeling assumptions inherent in the force estimation technique. The error is calculated as the average of the difference between numerical and experimental velocities at every vector point within the PIV field of view. This is then normalized with the maximum experimental velocity of the specific test case. The error for all test cases is shown in Tab.8.2 More detailed discussion on the modeling error is given in Section 8.3.

Table 8.2: Average error between numerical and experimental velocities for all cases in continuous operation.

Test case	**error** (%)
8 kV_{pp}, 2 kHz	8.8
10 kV_{pp}, 2 kHz	5.2
12 kV_{pp}, 2 kHz	6.9
14 kV_{pp}, 2 kHz	7.9
16 kV_{pp}, 2 kHz	8.6
10 kV_{pp}, 1 kHz	8.0
10 kV_{pp}, 3 kHz	9.6
10 kV_{pp}, 4 kHz	9.8

For the case of varying applied voltage the jet changes in velocity magnitude as well as spatial extent. The maximum velocity increases and the location where this appears is moved downstream for increasing applied voltage. A comparison between experimental and numerical maximum velocities ($U_{max} = max[\sqrt{u^2 + v^2}]$) is given in Fig.8.10. An overview of the loca-

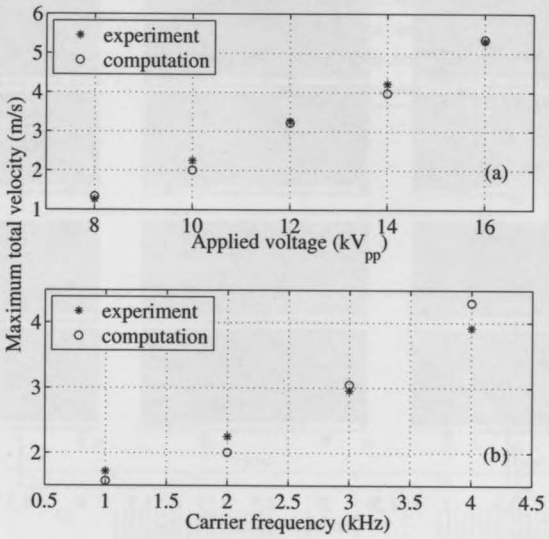

Figure 8.10: Maximum total velocities for the tested cases of continuous operation.

tion where maximum velocity is achieved is given in Fig.8.11. Small differences between the experimental and numerical results could be attributed to increased viscosity near the wall due to seeding particles accumulation. The increase in velocity as well as the downstream displacement of the maximum velocity point can be explained by taking into account the strengthening of the electric field in both magnitude and spatial extent with increasing voltage. This is directly reflected on the produced body force which in turn defines the jet strength and shape. Of interest is the direction of the jet downstream. A seen in Fig.8.6, for low voltages the jet seems to have a pronounced upward component indicating a deflection due to the thick boundary layer the jet itself creates.

In the case of varying carrier frequency some differences exist with respect to the voltage variation case. The jet velocity increases with frequency but no major difference is observed in the location where the maximum velocity occurs (Fig.8.11).

This behavior suggests a different mechanism of influence that the carrier frequency has on the performance of the actuator. More specifically it appears

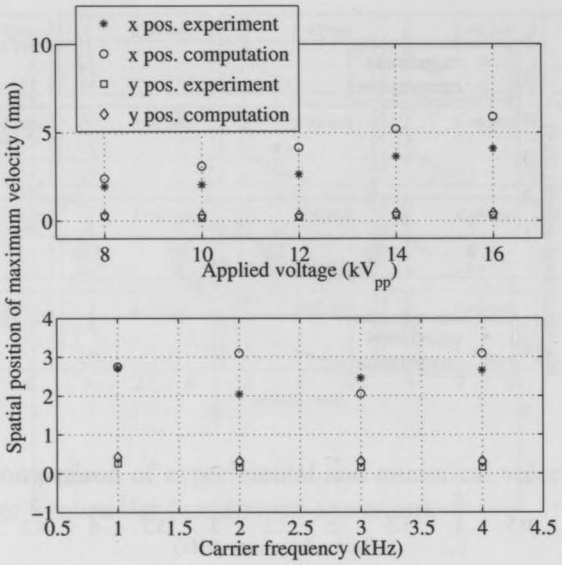

Figure 8.11: Spatial position where maximum velocity occurs for the tested cases of continuous operation.

that the increase of velocity is the product of increased momentum transfer rate over multiple HV cycles, rather than increased net momentum over a single HV cycle. For a fixed applied voltage the instantaneous body force does not change in magnitude. Yet, the rate of momentum transfer to the flow increases with carrier frequency since more HV cycles occur within a given time span.

8.2.2 Pulse operation

The pulse operation of the plasma actuator presents some interesting aspects regarding flow control applications. Mainly the short response of the external flow to the actuation signal enables high frequency actuation for a variety of flow control scenarios. Following the roadmap of the current investigation as shown in Fig.8.1, several cases of pulse operation are experimentally tested and subsequently simulated using the experimental body force distribution.

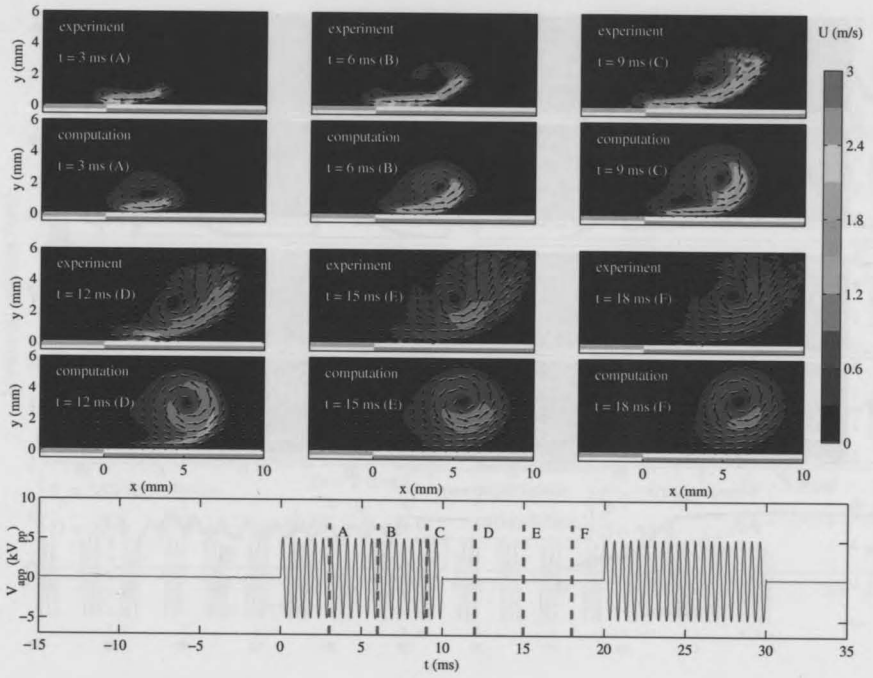

Figure 8.12: Snapshots of total velocity evolution through a full pulse period ($f_p = 50\ Hz$, $D = 50\ \%$)

The actuator is operated with fixed applied voltage (10 kV_{pp}) and carrier frequency (2 kHz) to ensure consistency in power output. Three different pulse frequencies (f_p) are tested (50, 200, 350 Hz) at fixed duty cycle (D) of 50 %. Additionally the 50 Hz case is repeated for duty cycles of 25 and 75 %. For the simulations, only the body force distribution originating from the continuous case of $V_{app} = 10\ kV_{pp}$ and $f_{ac} = 2\ kHz$ is used, at the respective pulse frequency and duty cycle.

Snapshots of the evolving field during different instances of a pulse are shown in Fig.8.12 for the case of $f_p = 50\ Hz$, $D = 50\ \%$ and in Fig.8.13 for the case of $f_p = 350\ Hz$, $D = 50\ \%$. Some intrinsic features of pulsed actuation can be observed here. More specifically, pulse frequency appears to severely affect the evolution of the induced flowfield. In the case of pulsation at 50 Hz the impulsive forcing of the actuator accelerates the flow in the vicinity of the inner electrode during the active period. Due to the initial quiescent

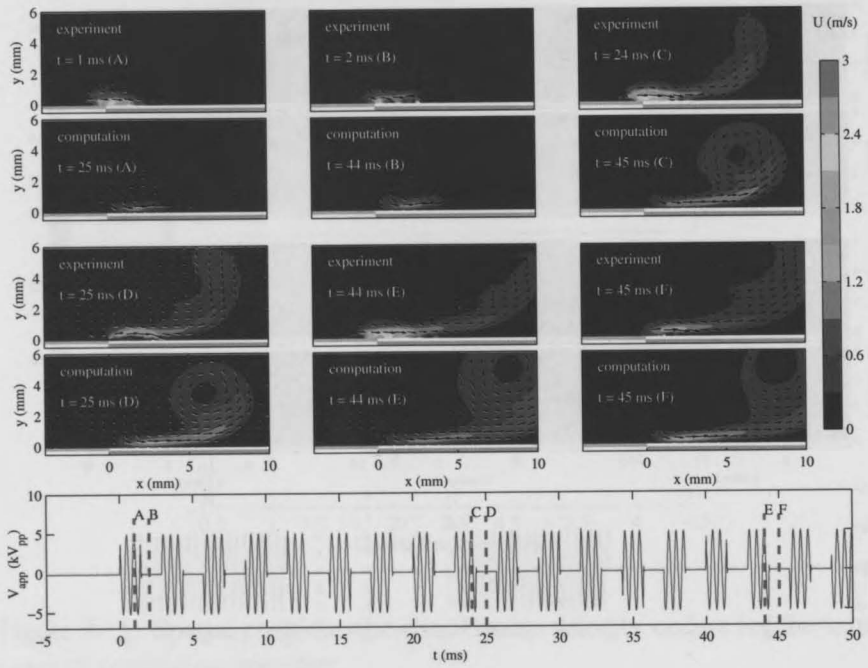

Figure 8.13: Snapshots of total velocity evolution through a full pulse period ($f_p = 350\ Hz$, $D = 50\ \%$)

conditions and the existence of the wall, a large starting vortex is created. During the "off" period the vortex decouples from the actuator forcing region and convects downstream. The process is repeated for every pulse and results in the continuous production of discreet vortices which convect downstream. This is further eveident in Fig.8.14 where the temporal trace of velocity at discreet points is shown.

In contrast, pulsed actuation at 200 and 350 Hz provides a different evolution for the flowfield. As shown in Fig.8.13 the actuator is entraining and accelerating fluid in the vicinity of the upper electrode during the "on" period. Nevertheless, no discreet structures other than the initial starting vortex are observed. This is explained taking into account the time scale of the flow under external forcing. The pulse frequency is simply too high for the developed flowfield to recover to its initial unperturbed state. As such, the starting vortex has not enough time to distance itself from the forcing region before the next

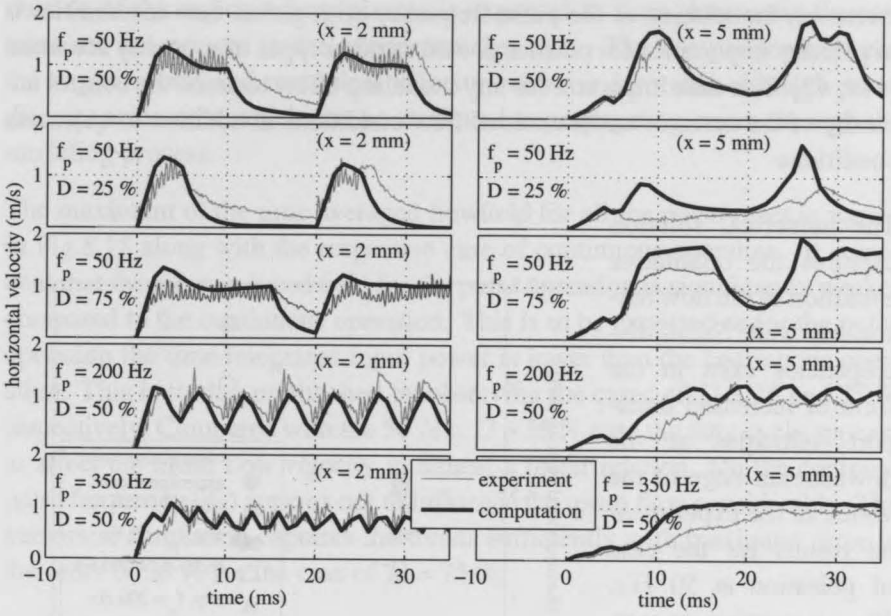

Figure 8.14: Temporal history of the evolving velocity field for pulse operation at two different x positions ($y = 0.5\ mm$)

actuation pulse. In this way the actuator continuously adds momentum to the single starting vortex with each pulse rendering the evolving field similar to continuous actuation. Further indication is shown in Fig.8.14 where for the cases of 200 and 350 Hz the flow in the vicinity of the actuator never fully relaxes to zero velocity prior to the next pulse.

The differences in the evolution of the flowfield between cases of different pulse frequencies suggest the intrinsic dependance of the actuator effect on the flow time scales. As similarly demonstrated by previous investigations [116] the form of the induced unsteady flowfield is dependent on the relation between the primary forcing time scale of the actuator and the respective time scale of the external flow. An important note to be made here is that the time scales of initially quiescent flow are not representative of actual flow control scenarios. As was shown in Chapter 5 in the case of an externally imposed flow field the maximum frequency at which the actuator has a measurable unsteady effect on the flow increases with increasing freestream velocity. Fur-

thermore, the relation of the pulse frequency with global flow instabilities is of primary importance for plasma as well as other types of unsteady actuation [119, 47]. It is thus important for any modeling effort to asses the control authority of the actuator under external flow conditions in addition to quiescent conditions.

The numerical solution captures the qualitative evolution of the flow reasonably well. Small discrepancies exist in the form of increased transport velocities at the downstream edge of the vortex in the experimental results for the case of pulsation at 50 Hz. The respective numerical snapshots show a cleaner rotational flow. These differences could reflect the small but non-zero initial velocity conditions in the experimental box caused by thermal convection and external vibrations.

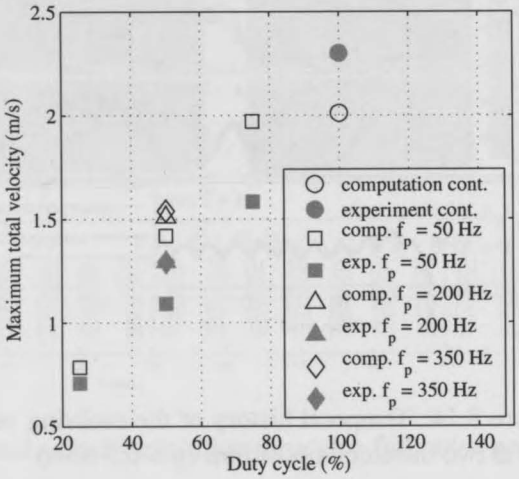

Figure 8.15: Maximum velocity for time averaged flowfields in pulse operation.

A quantitative comparison of the time history of the evolving field is shown in Fig.8.14 for all the pulse test cases. The velocity history is presented for two different spatial positions in the vicinity of the actuator ($x = 2$, $y = 0.5$ mm) and further downstream ($x = 5$, $y = 0.5$ mm).

The used body force distributions are implemented in a time averaged form. For the simulation of the pulse operation the force is simply multiplied by 0 or 1 depending on the pulse frequency and duty cycle. Similarly to the continuous operation the high frequency velocity fluctuations which are present in the first spatial position are not captured by the numerical solver. Nevertheless the mean values of the velocity as well as the temporal evolution show reasonable agreement. The downstream position ($x = 5$ mm) is located well

outside of the region where plasma is expected to form, hence the fluctuations are not present in the experimental results. The comparison between the experimental and numerical velocity values is favorable although some discrepancies exist which can be attributed to propagating errors through the modeling process.

The maximum of the time averaged flowfield for all the pulse cases is shown in Fig.8.15 along with the respective case of continuous operation. It is evident that the mean induced field for the pulse operation is significantly weaker compared to the continuous operation. This is to be expected as for the pulse operation the time integrated input power is lower than the continuous operation. This is further established by observing the cases of $D = 25$ and $75\ \%$ respectively. Compared with the $50\ Hz$, $D = 50\ \%$ case the duty cycle appears to affect the mean flow velocity in almost a linear relation. On the contrary, pulse frequency (f_p) appears not to influence the mean flow considerably. The numerical simulation captures the trends sufficiently with maximum error in the order of $30\ \%$ for the case of $D = 75\ \%$.

8.2.3 Laminarity of the wall jet

The issue of the laminarity of the wall jet has been raised in the previous sections due to the importance of accounting for turbulence or not in the numerical flow solver. Here a brief analysis is performed on the developed wall jet due to plasma actuation in order to establish the state of the flow. The analysis is presented here for the highest voltage case ($16\ kV_{pp}$) which exhibits the highest velocities and in extension the highest Reynolds number. Similar results are obtained for the other cases.

Two main requirements must be fulfilled for a positive confirmation of laminar flow. Firstly it must be proven that the developed wall jet is not subject to natural transition. An initial approach is the visual inspection of the temporal evolution of the flowfield. Bajura et al. [10] and Hsiao and Sheu [56] have performed comprehensive studies on natural transition of plane wall jets. The main transitional mechanism observed in these studies is the existence of an outer layer instability in the form of vortex pairs which lift off the solid wall and initiate self sustaining turbulence production. This is not observed in the measurements of the present study giving a first indication for laminar flow.

In order to further secure this observation the flowfield is compared against the analytical similarity solution for a laminar plane wall jet first presented by Glauert [46]. The horizontal velocity (u) profiles are non-dimensionalised with the maximum local velocity (U_m) while the wall normal coordinate y is non-dimensionalised with the half width of the jet (the distance from the wall at which $u = 0.5 \times U_m$). The comparison between the experimental results of the present study with the analytical solution of Glauert is presented in Fig.8.16. The profiles indicate a laminar boundary layer from positions downstream of $x = 4\ mm$. Differences exist in the outer regions of the jet ($y/y_{1/2} \leq 1$) due to the negative wall normal velocity components inherent in the specific flowfield. For positions within the force field ($x \leq 4\ mm$) the profiles present additional discrepancies from the theoretical profile in the near-wall region. This can possibly be accounted to one of the major assumptions of Glauert based on the existense of zero pressure gradient in the x direction. This is of course the case with traditional wall jets where the momentum and mass of the injected fluid is supplied through a small (infinitesimal in theory) orifice. On the other hand in the case of the plasma actuator the exerted body force is equivalent to a strong pressure gradient which negates this assumption. In contrast, moving further downstream and outside of the plasma (and body force) region, the profiles compare well with the laminar solution of Glauert since the zero pressure gradient condition is met. In general it appears that the developed wall jet does not undergo natural transition downstream of the body force area.

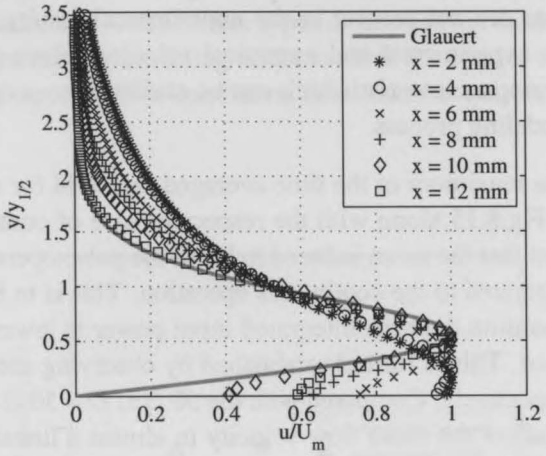

Figure 8.16: Non-dimensionalized velocity profiles in several x stations against the analytical similarity solution of Glauert (V_{app} = 16 kV_{pp}).

From the previous observations, the state of flow within the forcing region

($x < 5mm$) remains unclear and must be estimated using a different approach. Here the second requirement for laminarity of the flowfield is set where it must be proven that the oscillatory behavior of the force does not act as a local 'turbulator' of the flow. Statistical quantities such as rms values of the velocity fluctuations would show not only possible existence of turbulence but also the deterministic velocity fluctuations described in Section 8.3. As such a spectral analysis using a Fast Fourier Transformation (FFT) algorithm is performed on the unsteady velocity signal at various locations in the flowfield. Results for three such locations are shown in Fig.8.17. It is apparent that strong peaks are registered in the upstream x stations corresponding to the plasma induced primary frequency and its first harmonic. On the other hand no broad spectrum region is apparent, indicative of the diffusive character of possible turbulence. Furthermore, fluctuation intensity for the uncorelated spectrum is preserved below 4 % of the local maximum velocity at all stations which according to observations of Hsiao and Sheu [56] is characteristic of a laminar wall jet in similar conditions. Station $x = 10mm$ is of special interest since it has already been shown to lie close to the laminar profile while its uncorrelated spectral content is similar to more upstream stations.

The general conclusion of the laminarity analysis is that indeed the flow is laminar at the conditions of the present experimental study. Similar assumption was apparently made by similar model validation works [117, 49, 138]. On the other hand it must be stressed that the existence or not of turbulent flow should be known prior to application of any plasma model. Indeed in the case of turbulence (due to either external conditions or the plasma itself), the plasma force model should be carefully calibrated and checked against the chosen turbu-

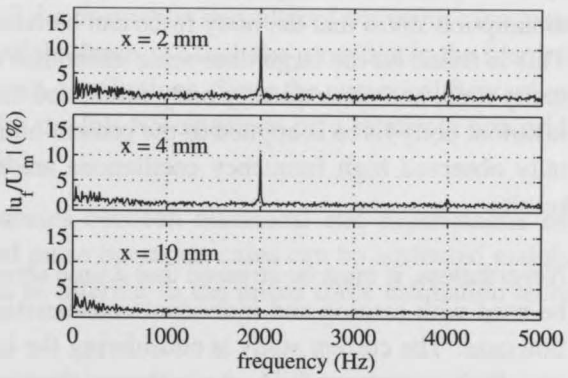

Figure 8.17: Spectral content of velocity fluctuations (u_f) (in % of the local maximum velocity U_m) at three x stations (all values probed at y = 0.5 mm).

lence model used in the flow solver.

8.3 Modeling considerations

8.3.1 Electrostatic velocity fluctuations

As previously mentioned, the experimental results present, a secondary effect in the vicinity of the actuator, additionally to the large coherent structures such as the formed wall jet and the starting vortex. This consists of high frequency velocity fluctuations occurring mostly over the first half of the covered electrode. The RMS of the total velocity fluctuations for the case of 10 kV_{pp} and 1 kHz is presented in Fig.8.18. These high frequency fluctuations are the result of the underlying ion-neutral momentum transfer mechanism as was examined in [15, 37].

In the experimental body force estimation technique (Chapter 7), one major assumption states that the body force can be considered quasi-steady in time. This is based on the large time-scale difference of the oscillations of the velocity field, and consequently body force, and the external flow. Since a time invariant body force is applied in the present numerical study, the experimentally observed high frequency oscillations are not present in the numerical results.

Nevertheless, it must be stressed that a time invariant body force model must be used with caution and individual consideration depending on the simulation case. The current study is considering the impulsive start of actuation in an initially quiescent fluid. As is shown, the time scales governing the large coherent structures due to actuation are significantly separated from the high frequency velocity fluctuations. This time scale separation is an essential requirement for the applicability of the model. In contrast, in cases where the actuator is operating in areas of high receptivity bounded within a frequency spectrum which includes the carrier frequency, account for the high frequency velocity fluctuations must be taken through a different or modified body force model.

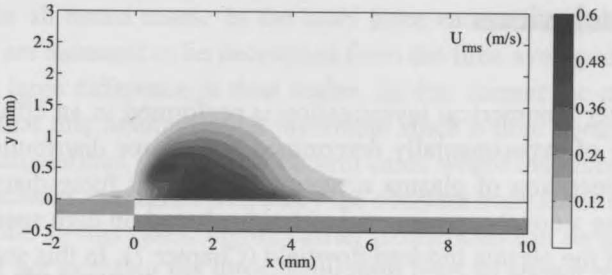

Figure 8.18: Experimentally determined RMS of total velocity fluctuations (continuous operation, $V_{app} = 10\ kV_{pp}$, $f_{ac} = 1\ kHz$).

8.3.2 Model assumptions and error

As stated earlier the major assumption in the technique which is proposed in Chapter 7 is the treatment of the force field as a time invariant value in relation to the electrostatic oscillations. This is a source of error which propagates through the modeling process and is reflected in the comparison of experimental and numerical results. As shown by the experimental results (Fig.8.5), the force field actually fluctuates at the carrier frequency of the applied voltage. In the techniques in Chapter 7 the fluctuation was filtered out using a low pass filter prior to the estimation of the force. As such the error due to the filtering process is transfered to the force distributions. Since the numerical flow solver in the present study solves for the full NS equations on a relatively fine grid, no additional error is expected.

In this manner the discrepancies between numerical and experimental results for both continuous and pulse operation cases can be attributed mainly to the propagating error due to filtering in the initial force estimation technique.

At this point some comments must be made in the context of the overall modeling process. The proposed model has not been subject to a calibration procedure. As such, it is self-standing and independent of empirical factors which are usually used to fine-tune phenomenological models (such as the Debye length [121]). This of course increases the risk of error since no a-priori control on the performance of the model exists through calibration of force amplitude or shape. On the other hand the model ensures applicability in a range of scenarios without the need for further experiments for calibration.

8.4 Conclusions

In this chapter a numerical investigation is performed in an effort to test the applicability of experimentally determined body force distributions as models for the operation of plasma actuators. The body force distributions are attained using a novel experimental technique based on high speed PIV measurements of the plasma induced flowfield (Chapter 7). In this study the force distributions are implemented in a numerical flow solver. Several test cases are simulated in order to clarify several issues of implementation and applicability of the body force distributions.

The first set of test cases involves the continuous operation of the plasma actuator. Several applied voltages and carrier frequencies are tested. These cases are the same as the ones that provide the body force distributions. The operation of the actuator produces a wall-parallel jet with intensity and spatial extent being functions of applied voltage and carrier frequency. Additionally, due to the impulsive start of the actuation, a starting vortex is formed and advects downstream. The characteristics of the induced flowfield are captured well by the numerical solver. Maximum velocities, locations of maximum velocity and general topology of the jet show reasonable agreement. It is resolved from these test cases that the body force distributions can reproduce the original experimental data in the numerical framework.

The second group of test cases involves the pulse operation of the actuator. These cases serve the purpose of establishing the robustness of the force distribution model in cases different to the original experiment. The actuator is pulsed in an 'on-off' regime using several pulse frequencies and duty cycles. The same cases are simulated in the numerical framework. The general evolution of the flow as well as the temporal history show agreement within the expected error margins. This verifies the capabilities of the body force distributions in representing the effect of the actuator in cases unrelated to the original body force experiment.

Additionally to the general evolution of the field, a secondary effect is observed in the experimental results. An area of strong velocity fluctuations exists in the vicinity of the upper electrode edge. It is evident that these fluctuations reflect the underlying plasma collisional processes through which momentum is transfered to the surrounding fluid as observed in previous studies [15] as well as in Chapter 6. These fluctuations correspond to the carrier

frequency for all tested cases. In the body force estimation technique, these fluctuations are assumed to be decoupled from the time averaged momentum input due to large difference in time scales. In this chapter the numerical results prove that this assumption is justifiable since a time invariant force is used in the simulations. Yet in flow control cases where the receptivity range is close or includes the carrier frequency the constant body force model might not be suitable. In this cases, higher carrier frequencies can be used with the constraint of not exciding the thrust saturation level as shown by Thomas et al [134]. Alternatively, a modified model which takes into account the high frequency fluctuations should be developed and implemented.

In general the current study attempts to fulfill the three requirements set for the applicability of the body force distributions as appropriate models of the actuator performance:

- The implementation of the experimental body force distributions in a numerical flow solver accurately provides the originally measured flow field for the same external conditions (quiescent flow).
- The experimental body force distribution provides accurate representation of the actuator effect in cases which are independent from the conditions of the original force measurement. This requirement is fulfilled partially since no indication of the influence of a given external flow exists.
- The assumption concerning the quasi-steady character of the body force does not to significantly affect the numerical results.

An open remaining question involves the second requirement. More specifically it has not been proven that the experimental body force obtained in conditions of quiescent flow can accurately represent the effect of the actuator in conditions of non-zero external flow.

Part III

Application

If you're going to try, go all the way. There is no other feeling like that. You will be alone with the gods, and the nights will flame with fire. You will ride life straight to perfect laughter. It's the only good fight there is.

Charles Bukowski, *Factotum*

Part III

Application

Chapter 9

Transition Control using DBD Actuators

A promising concept for the utilization of plasma actuators is the cancellation of Tollmien-Schlichting waves in a transitional boundary layer. This technique aims at tackling the instability waves while still in linear amplification stage. At this stage the waves have little energy content with typical amplitudes of 0.01 % of the freestream velocity [118]. Through the damping of TS waves, the process leading to turbulent breakdown is postponed and consequently skin friction is reduced. This technique has been investigated experimentally [128, 133] as well as numerically [6, 21]. In recent studies[50] artificially introduced TS waves were successfully canceled using plasma actuators. It must be stressed that TS wave cancellation is not a drag reduction technique on its own. On one hand TS waves are not the only instability mechanism that leads to transition in relevant industrial applications such as airplane wings. On the other hand the cancellation concept must be used in conjunction with other natural laminar flow techniques in order to extract the full potential of the method. Despite these issues the tackling of TS waves is the first and an important step in the development of an integrated, efficient drag reduction system.

In this chapter a numerical investigation on the TS wave cancellation concept is performed based on the knowledge gathered in the Diagnostics and Model-

ing parts of this work. More specifically the actuator is used as a counter-wave generator operating in a laminar boundary layer in which turbulence-inducing instabilities are propagating. In the 2D case the instabilities propagating in the laminar boundary layer correspond to the unsteady Tollmien-Schlichting modes. Through correctly phased unsteady actuation the amplitude of the modes can be reduced leading to a delay of transition and overall skin friction drag decrease. To simulate the unsteady actuation effect, the plasma actuator is used through the concept of the volume distributed body force. In this study both a generic force distribution as well as the experimentally derived body forces (Chapter 7) are used. For the selection of the correct actuation signal a stand-alone automatic control system employing the filtered-x LMS algorithm [80] is implemented in the flow solver. The control system runs in parallel to the flow solver and the actuation is done in real time.

9.1 Methodology

9.1.1 Numerical flow solver

In order to resolve all the spatial and temporal scales involved in the transition problem, a full Navier-Stokes solution is pursued. Furthermore a reduced approach is followed in which the base flow (laminar boundary layer) is considered fixed while the NS equations are solved for the TS perturbations. A more detailed discussion on the solver as well as the numerical techniques employed within is given in Chapter 3. Here a brief reminder of the governing equations is given for the fluctuating flowfield $(\mathbf{u}, p)$:

$$\frac{\partial \mathbf{u}}{\partial t} + (\mathbf{u}\cdot\nabla)\mathbf{u} + (\mathbf{U_0}\cdot\nabla)\mathbf{u} + (\mathbf{u}\cdot\nabla)\mathbf{U_0} - \nu\nabla^2\mathbf{u} = -\frac{\nabla p}{\rho} + \frac{\mathbf{f_b}}{\rho} \quad (9.1)$$

9.1.2 Automatic control system

A description of the filtered-x LMS control system used for the cancellation of the TS waves is given in Chapter 3. Additionally, the implementation in the OpenFOAM source code is shown in Appendix A. Here a brief reminder of the working principle of the filtered-x LMS algorithm is given. The system

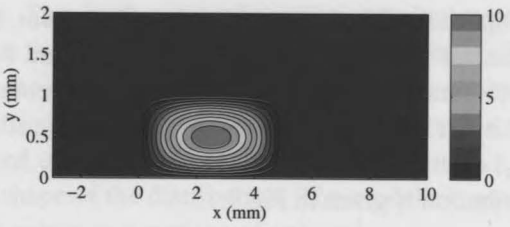

Figure 9.1: Example of a generic body force distribution with $l = 4\ mm$, $h = 1\ mm$ and $A_x = 10\ mN/mm^2$.

involves a feed-forward loop for the estimation of the control signal which drives the actuator (in this case the voltage amplitude of the DBD actuator). More specifically, the system uses a reference and an error signal which in the investigated case are pressure values at the flat plate wall. In the numerical framework these are read directly within OpenFOAM. The reference signal is read upstream of the actuator in order to sense the incoming instabilities while the error sensor is downstream of the actuator in order to sense the instability after manipulation.

9.1.3 Body force implementation

Generic force distribution

To effectively capture the effect of the plasma actuator a distributed volume body force is applied as described earlier. The magnitude and spatial distribution of the body force have been subject of numerical and experimental investigations. For this study two levels of approximations are applied to the force description. Firstly a generic force distribution with arbitrary amplitude and spatial extent is used in order to gain insight into the interaction between the three main components (stability, body force and controller) of the investigation. The force shape is chosen as a half-sinus distribution in both x and y directions given by:

$$f_x(x,y) = A_x \cdot sin(\pi(\frac{x - x_s}{l})) \cdot sin(\pi(\frac{y - y_s}{h}))$$
$$for: \quad x_s \leq x \leq x_s + l, \quad y_s \leq y \leq y_s + h \qquad (9.2)$$

where A_x is the amplitude of the horizontal force component, x_s and y_s define the starting coordinates of the force distribution and l and h the length and height of the distribution respectively. The vertical force component f_y is set to zero for simplicity. It should be noted here that the controller controls only the amplitude (A_x) of the force and not the spatial extend. An example of the generic force distribution is given in Fig.9.1.

Plasma force distribution

For the second level of approximation, the body force implementation is extended to incorporate the experimentally derived force distributions from actual plasma actuators as described in Chapter 7. In contrast to the generic force distribution, the plasma force distributions present additional complexities in implementation. More specifically, the control parameter here is not the amplitude of the force but the value of the applied voltage. This in turn defines not only the amplitude of the force distribution but also the spatial extent and the shape. The available experimental results cover a range of applied voltages from 8 to 16 kV_{pp} with steps of 2 kV as well as cases of varying carrier frequency. For this work only the applied voltage variations are considered. In total 5 different force distributions are available. For implementation of these forces in the solver as a function of voltage, an interpolation based on 2D Bernstein surfaces is carried out and the generated coefficients are stored in the controller environment as lookup tables. This enables the on-line calculation of the body force for every value of applied voltage within the range of 8 to 16 kV_{pp}. For values less than 8 kV_{pp} the body force is set to zero while for values larger than 16 kV_{pp} the force remains constant and equal to the 16 kV_{pp} case.

A correlation model for the variation of the body force under changing applied voltage is developed based on the experimental results. The overall body force distributions for the five tested cases are shown in the left hand side of Fig.9.4. The model construction and implementation is based on observations on the variation of both the magnitude and spatial distribution of the body force with voltage.

The goal of this interpolation procedure is to find a relationship between the applied voltage and the body force, in terms of both the magnitude and the spatial distribution, and subsequently to mathematically describe the force field in

an efficient way. This is all accomplished by one single optimization routine, to guarantee that the best overall fit is found. The essential characteristics to be captured by the correlation model are easily inferred by visual inspection of the force distribution. More specifically it appears that the force field can be fully expressed using the magnitude, the spatial extent in x and y directions and the overall shape of the distribution. The modeling approach will attempt to capture these values as functions of voltage[1].

The first step involves the scaling of the force fields using a scaling factor for each case. This is done to bring the order of magnitude of the fields close to unity which in turn simplifies the optimization procedure. Consider the scalar fields $F_{bx}(x, y, V)$ and $F_{by}(x, y, V)$ which correspond respectively to the horizontal and vertical component of the experimentally measured body force. The scaling is done by dividing the fields by a scaling factor which is a function of voltage. This factor is connected with voltage using a second order polynomial relation. The fields are scaled as follows:

$$\begin{aligned} \hat{F}_{bx}(x, y, V) &= \frac{F_{bx}(x, y, V)}{A_x(V)} \\ \hat{F}_{by}(x, y, V) &= \frac{F_{by}(x, y, V)}{A_y(V)} \end{aligned} \tag{9.3}$$

where the scaling factors are expressed as a quadratic function of voltage:

$$\begin{aligned} A_x(V) &= a_1 \cdot V^2 + a_2 \cdot V + a_3 \\ A_y(V) &= a_4 \cdot V^2 + a_5 \cdot V + a_6 \end{aligned} \tag{9.4}$$

where A_x and A_y are the scaling factors of the horizontal and vertical body force respectively and V is the applied voltage. Use of Eq.9.3 to Eq.9.4 allows the segregation of the amplitude of the force field from the spatial distribution which is desirable for the following modeling steps. The scaling factors are presented in Fig.9.2.

The next step is the spatial stretching of the force fields in order to fall in a non-dimensional domain spanning from 0 to 1 in both horizontal and vertical directions. This is achieved by a linear coordinate transformation scheme which employs a quadratic voltage relation for the horizontal coordinate and

[1]The author is grateful to Michiel Straathof for his assistance with the Bernstein optimization routine

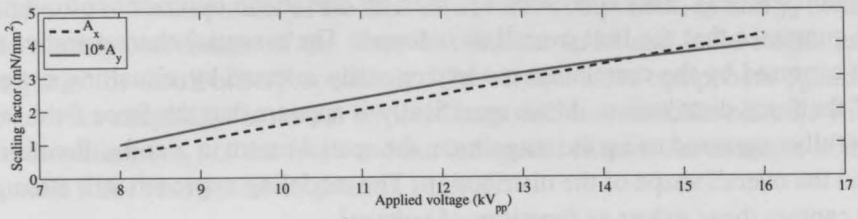

Figure 9.2: Scaling factors for the horizontal (A_x) and vertical (A_y) force fields as functions of voltage.

a voltage independent relation for the vertical coordinate.

$$\begin{aligned} \hat{F}_{bx}(\xi, \psi, V) &= \hat{F}_{bx}(x, y, V) \\ \hat{F}_{by}(\xi, \psi, V) &= \hat{F}_{by}(x, y, V) \end{aligned} \tag{9.5}$$

where:

$$\begin{aligned} \xi &= \frac{x}{b_1 \cdot V^2 + b_2 \cdot V + b_3} + \frac{2}{9} \\ \psi &= \frac{y}{c} \end{aligned} \tag{9.6}$$

where ξ and ψ are the transformed horizontal and vertical coordinates respectively. To be noted that an offset factor of $\frac{2}{9}$ is used on the normalized domain. The relation for the vertical coordinate is considered independent of voltage and it is fixed prior to the optimization.

The last step involves the representation of the normalized and stretched force field in a consistent, accurate and simple way. To this goal, the shape is represented by a surface which is constructed by a summation of a set of Bernstein surfaces which are 3D generalizations of Bernstein polynomials. This approach has been chosen due to the high accuracy of the approximation as well as the inherent smoothness Bernstein surfaces present [95, 127]. The Bernstein surfaces are each multiplied by a coefficient and summed up in order to create the final surface as shown in Eq.9.7 to Eq.9.8. Here $S_x(\xi, \psi)$ and $S_y(\xi, \psi)$ are the final surfaces for the horizontal and vertical force fields respectively, BX_{ij} and $BY_{i,j}$ are the coefficients of the Bernstein surfaces, Px_i and Py_j are the Bernstein polynomials in x and y directions respectively, and n_x and n_y are their indices. Note that ξ and ψ are the normalized spatial variables which run from 0 to 1.

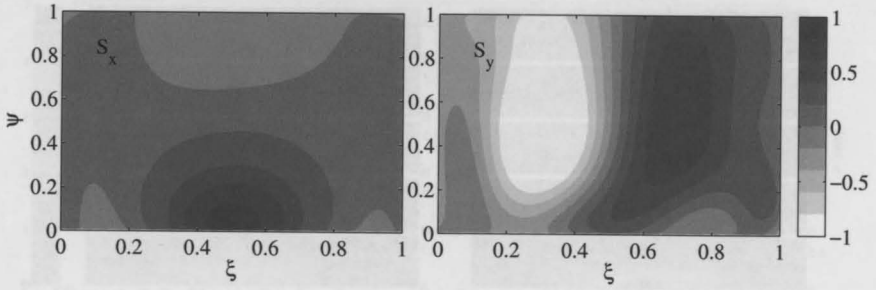

Figure 9.3: Bernstein surfaces for the representation of the horizontal (S_x) and vertical (S_y) force fields.

$$S_x(\xi,\psi) = \sum_{i=0}^{n_x}\sum_{j=0}^{n_y} BX_{ij}\cdot Px_i(\xi)\cdot Py_j(\psi)$$
$$S_y(\xi,\psi) = \sum_{i=0}^{n_x}\sum_{j=0}^{n_y} BY_{ij}\cdot Px_i(\xi)\cdot Py_j(\psi) \tag{9.7}$$

where:

$$Px_i(\xi) = \binom{n_x}{i}\xi^i(1-\xi)^{n_x-i}$$
$$Py_j(\psi) = \binom{n_y}{j}\psi^j(1-\psi)^{n_y-j} \tag{9.8}$$

The final surfaces for the horizontal and vertical fields, as resulting from the optimization procedure, are shown in Fig.9.3.

The unknowns of the problem are now the coefficients in BX_{ij} and $BY_{i,j}$ and the polynomial coefficients a_1 to a_6 and b_1 to b_3. For the calculation of these coefficients MATLAB's sequential quadratic programming algorithm *fmincon* was used, which employed an active-set algorithm and finite differences were used to compute the derivatives. The following cost function was used:

$$\{\sum_{i=1}^{k} \text{abs}[S(\xi,\psi) - \tilde{F}_b(\xi,\psi,V_i)]\}^2 \tag{9.9}$$

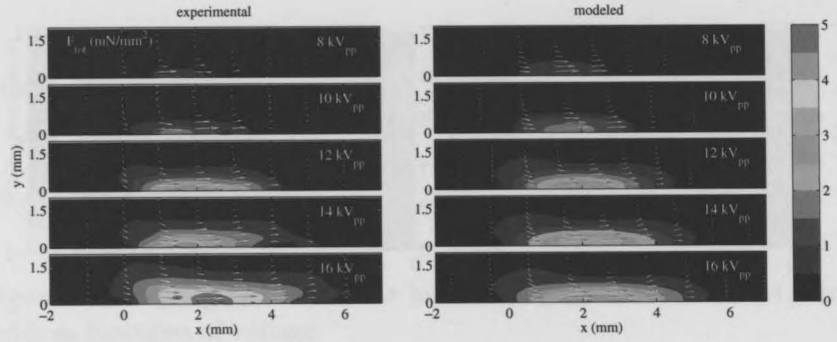

Figure 9.4: Experimental and modeled body force distributions for different applied voltages.

Where $\hat{F}_b(\xi, \psi, V_i)$ is the normalized and stretched force field using the relations defined in Eq.9.3 to Eq.9.5 and $k = 5$ is the number of different voltage cases. Due to the way the formulation of the problem is set, the optimizer is automatically choosing the scaling, stretching and Bernstein representation of the fields as a function of voltage. To be noted that for both scaling Eq.9.3 and stretch polynomials Eq.9.5 constraints are set such that their maximum values do not become larger than 1. This is to ensure that there is minimum interference with the Bernstein surface. After the stretching procedure, the resulting force field is cropped in order to have the same domain for each value of V and be able to compute the difference between the scaled force field and the Bernstein surface, as indicated in Eq.9.9.

Integrating the results of the discussed optimization procedure leads to the formulation of the final corellation model for the body force field of the plasma actuator. Specifically for the voltage range under consideration and the current geometric configuration of the actuator the force field is given by the following relations:

$$\begin{aligned} F_x(\xi, \psi, V) &= A_x(V) \cdot S_x(\xi, \psi) \\ F_y(\xi, \psi, V) &= A_x(V) \cdot S_y(\xi, \psi) \end{aligned} \tag{9.10}$$

where the spatial coordinates are given by:

$$\begin{aligned} x &= (\xi - \frac{2}{9}) \cdot (b_1 \cdot V^2 + b_2 \cdot V + b_3) \\ y &= \psi \cdot c \end{aligned} \tag{9.11}$$

where the scaling factors A_x and A_y are given in Eq.9.4. Eq.9.10 gives the

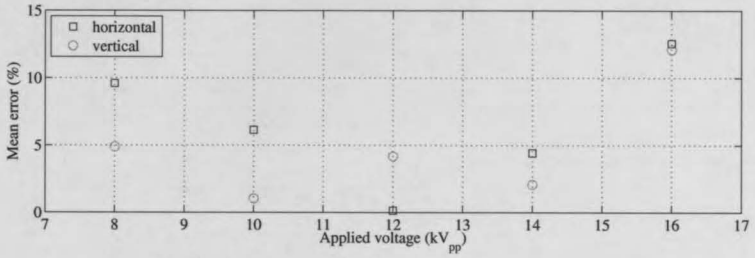

Figure 9.5: Error for horizontal and vertical body force models.

force field in a non-dimensional spatial domain which spans from 0 to 1 in x and y directions. The transformation to the physical domain is given by Eq.9.6. The coefficients for the scaling factor, stretching factor and Bernstein polynomials are given in Appendix B along with the value of the constant c. It must be noted here that the correlation model, as formulated, accepts input values of voltage in kV_{pp} and produces force values in mN/mm^2 and spatial coordinates in mm. An overall comparison between the original and experimental data is given in Fig.9.4. The modeling approach appears to capture most characteristics of the force field sufficiently. The mean error of the approximation is shown in Fig.9.5.

9.1.4 Test cases and mesh

For the entire numerical study, flat plate boundary layers with zero pressure gradient at two freestream velocities are considered. These correspond to 10 and 30 m/s. This choice has been made for several reasons. Firstly, the 10 m/s case (case A) is used to develop the controller system and gain insight on the synergy of several parameters such as convergence constant and length of the body force and their influence on the final control performance. Furthermore, case A has been used for the verification of the numerical flow solver through various grid and boundary conditions studies. The body force used for the cancellation of the TS waves in case A is exclusively the generic sinusoidal distribution. Case B involves the implementation of the experimentally derived body force distributions. As it is already mentioned, no control over the amplitude of this force exists other than the selection of the applied voltage. To this reason case B involves laminar flow at a larger Reynolds number in order to facilitate the increased force amplitude.

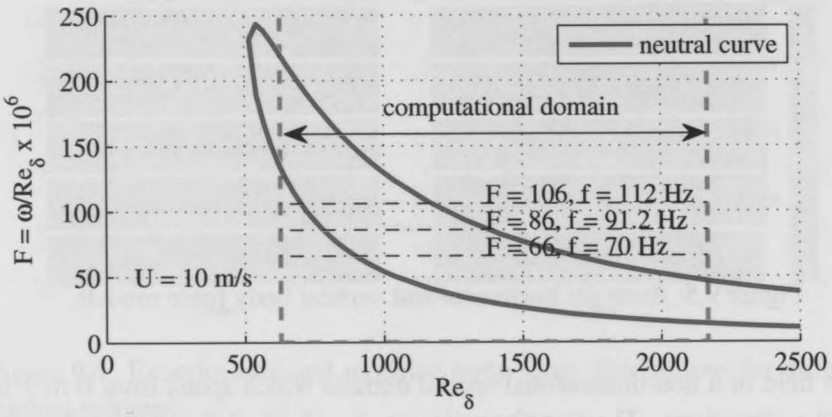

Figure 9.6: Stability diagram for case A with respective modes.

For all cases a Reynolds number based on the inflow displacement thickness is defined:

$$Re_0^* = \frac{U_\infty \delta_0^*}{\nu} \tag{9.12}$$

For case A, Re_0^* is 658 with an inflow displacement thickness $\delta_0^* = 0.98\ mm$. Three single frequency and one multi frequency stability and control sub cases are ran. A frequency number is set based on the Reynolds number at the inflow:

$$F = \frac{\omega_0}{Re_0^*} \times 10^6 \tag{9.13}$$

where $\omega = \frac{2\pi\delta^*}{U f_r}$ is the local non-dimensional frequency of the mode. The three single frequency sub cases correspond to $F = 66$, 86 and 106. Respective physical frequencies (f_r) are 70, 91.2, and 112 Hz respectively while the multi frequency case is a combination of the tree modes with equal initial amplitudes. These modes have been chosen such that at the spatial position of introduction in the solution domain they are still upstream of the neutral curve and thus stable. Stability diagrams for case A, indicating the computational domain and the position of the investigated modes, is shown in Fig.9.6.

Case B involves a higher inflow Reynolds number of $Re_0^* = 1539$. For this case one single and one multiple frequency sub case is ran. The single frequency case corresponds to mode $F = 25$ while the multi frequency case involves the

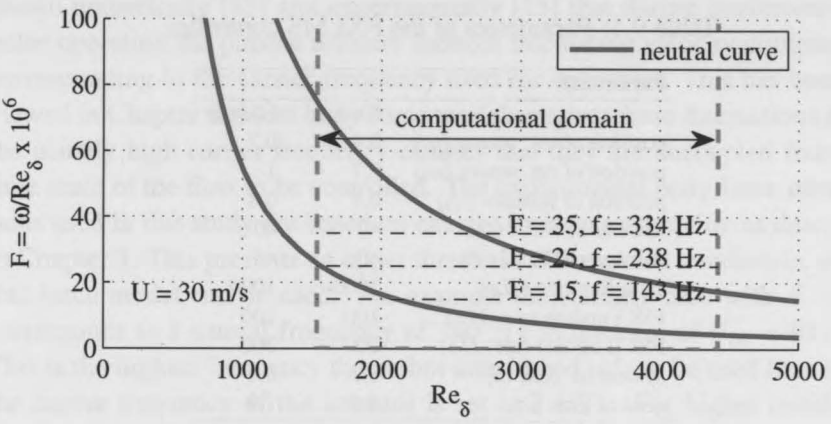

Figure 9.7: Stability diagram for case B with respective modes.

summation of modes F = 15, 25 and 35 with equal amplitudes during introduction. The respective physical frequencies for these modes are f_r = 143, 238, and 334 Hz. The stability diagram for case B is shown in Fig.9.7.

Both cases are run on structured rectangular meshes. For both cases the total number of tetrahedral cells used is approximately 0.1 million. For case A the mesh extends from x = 0.2 to 1.2 m and y = 0 to 0.025 m while for case B the mesh extents from x = 0.4 to 1.4 m and y = 0 to 0.025 m. The mesh is clustered linearly near the wall along the entire domain. Furthermore a more dense mesh is used in the vicinity of the body force distribution. For the highest frequency case (F = 35) the grid density corresponds to approximately 20 cells per TS wavelength. Finally, a buffer region of smoothly increasing cell size in streamwise direction is added at the downstream end of the computational domain in order to avoid reflections from the outflowing disturbances. The length of the buffer layer is fixed at 0.2 m while the stretch factor of the cells in the x direction is 10. Most of the controller settings are mainly fixed for the two cases apart from the convergence constant β which is adjusted per sub-case in order to achieve the best control performance. For case A the reference sensor is located at $x = 0.4$ m while the error sensor is at $x = 0.7$ m. The actuator (body force distribution) is located at $x = 0.5$ m. For case B the reference sensor is located at $x = 0.7$ m while the error sensor is at $x = 1$ m. The actuator (body force distribution) is located at $x = 0.8$ m. For both cases the FIRI and FIRII filters employ 40 weight coefficients and the sampling rate

Table 9.1: Parameters of the FXLMS controller.

Parameter	Case A	Case B
position of ref. sensor (m)	0.4	0.7
position of err. sensor (m)	0.7	1
position of actuator (m)	0.5	0.8
number of FIR I tabs	40	40
number of FIR II tabs	40	40
sampling rate (Hz)	1000	1000
FIR I update rate (Hz)	100	100
FIR II update rate (Hz)	200	200
system id. time (s)	0.2	0.1
control time (s)	0.8	1.9

of the controller is 1 kHz. The update rate for the FIR I filter coefficients is 100 Hz. An overview of the FXLMS controller parameters for both test cases is given in Tab.9.1

9.2 Results

9.2.1 Verification and modeling considerations

The numerical framework of this study is comprised of three discreet computational modules which are coupled together in order to achieve the final transition control goal. These are the flow solver, the forcing mechanism and the adaptive control system. Due to the multiple models used in this approach, it is desirable to identify, evaluate and address possible sources of error. This is done via a verification and validation approach wherever is possible.

A short description on the verification and validation of the flow solver is given in Chapter 3. In contrast to the flow solver, the body force model presents difficulties in verification and validation. A comprehensive validation effort for the specific body force distributions is described in Chapter 8. Nevertheless, several remarks can be made on the possible modeling errors. The representation of the plasma actuator through a volume distributed body force has been a popular method for implementing this type of devices in numerical studies. Yet it should be stressed here that such models must be used with caution especially for high receptivity areas such as the transition domain. It has been

shown numerically [85] and experimentally [15] that during continuous and pulse operation the plasma actuator induces fluctuating velocity components corresponding to the carrier frequency used for operation. This has been reviewed in Chapter 6. Most body force models neglect these fluctuations since the usually high carrier frequency ensures that they are decoupled from the time scale of the flow to be controlled. The experimental body force distributions used in this study are based on exactly such an assumption as described in Chapter 7. This presents an upper threshold of Reynolds numbers in which this force model can be used. For example the stability case with $F = 35$ corresponds to a natural frequency of 340 Hz in the case of U_∞ = 30 m/s. This is the highest frequency the author considered safe to be used here since the carrier frequency of the actuator is set at 2 kHz. For higher instability frequencies which are comparable to the carrier frequency of the actuator, a model that takes the latter into account is necessary in order to accurately capture the effect of the actuator.

On the other hand the limitations of the actuator itself must be taken into account. In Chapter 5 it was shown that an operational envelope exists in which the actuator is able to induce considerable and deterministic fluctuating components in a given external flow situation. Additionally, this envelope is also a function of the external flow velocity. Again in similar numerical or experimental efforts employing unsteady actuation, such envelopes should be consulted in order to define the operational spectrum of the actuator.

9.2.2 Parametric study on control performance

Prior to the actual control cases, a parametric investigation on the operation of the controller is performed. Two separate studies are conducted involving the convergence constant (β) and the streamwise length of the generic body force distribution l. For both cases all other parameters are kept constant.

For the investigation of the convergence constant the single frequency case F = 86 is used. The generic force distribution employs l = 0.02 m and y = 0.003 m. The error signal for all tested values of β is shown in Fig.9.8 along with the respective amplitude of the body force as is autonomously selected by the controller. All cases have a system identification procedure for the first 0.2 s of simulation based on identical settings. The results are shown here only for the control period (starting at t = 0.2 s). Two effects are evident here which

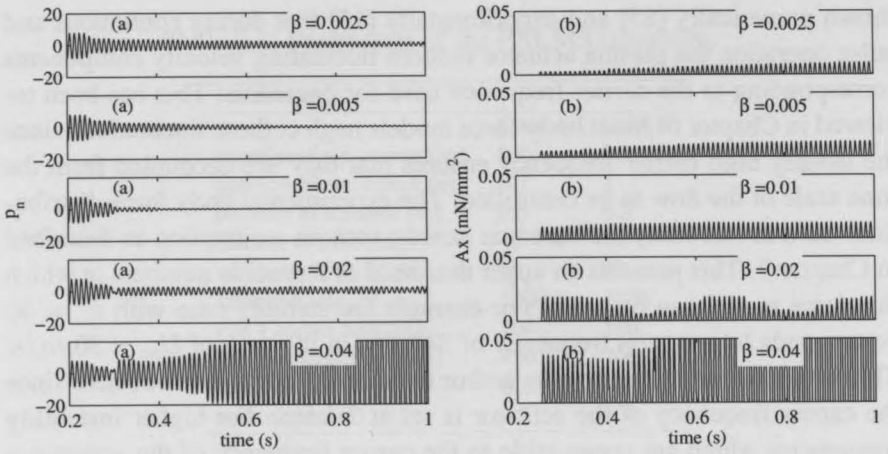

Figure 9.8: (a) Signal measured by the error sensor and (b) respective body force actuation value for different convergence constant (β). ($F = 86$).

are typical for the FXLMS algorithm. Firstly, if the convergence coefficient is too low the algorithm is converging to the optimum solution slowly and in some extreme cases ($\beta = 0.0025$)it might stop converging all together. On the other hand if the convergence constant is too large then the algorithm becomes unstable and the force amplitude starts to oscillate around the near optimal value ($\beta = 0.02$). Although the controller still manages to reduce the error signal, the performance is degrading. In a more extreme case ($\beta = 0.04$) the controller fails altogether with very large force values which respectively increase the error.

The second parameter investigated is the streamwise length of the force distribution. This is an important value in the transition control efficiency as the length of the optimum forcing distribution is expected to be strongly dependent on the wavelength of the incoming TS wave. Two more factors further increase the complexity of this interaction. Firstly, in cases of natural transition control, more than one frequencies of unstable modes are expected in the boundary layer. As such the wavelength of the modes in the wavetrain is not constant which adds one more degree of freedom in the system. Secondly, in the case of plasma actuation, the length of the forcing region is coupled to the applied voltage and the amplitude of the forcing itself as can be seen in Fig.9.9. Combining these two effects, the force distribution in normal oper-

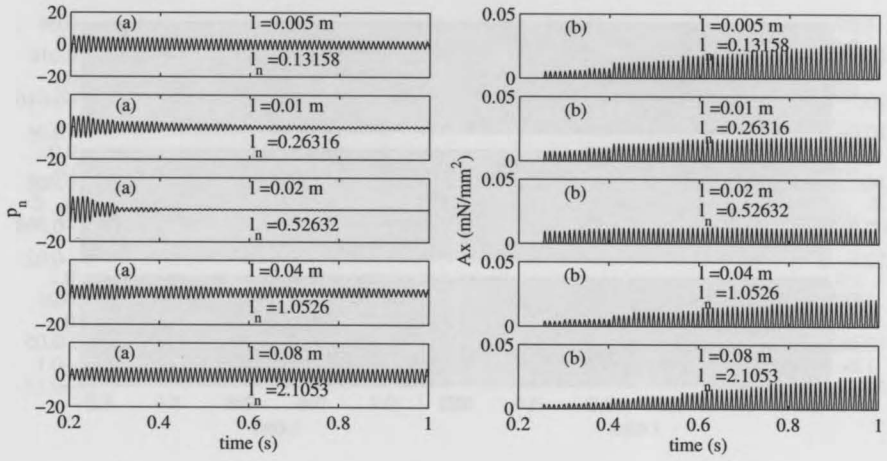

Figure 9.9: (a) Signal measured by the error sensor and (b) respective body force actuation value for different body force lengths (l). ($F = 86$).

ation conditions will have almost certainly sub-optimal characteristics. More discussion on this topic is given in section 9.2.4. Results for all tested values of l and l_n is shown in Fig.9.9. Here l_n is the force length l normalized with the streamwise wavelength of the incoming TS wave (0.038 m for $F = 86$). For all cases β is 0.01.

The results indicate that force lengths around half of the incoming TS wavelength produce the best control performance. This is partly expected as the TS wave is spatially fluctuating in x direction with half the wavelength occupied by positive velocity and the other half by negative velocity components. Since the force is always positive and directed downstream, destructive interference can only occur when the negative velocity half-wavelength is over the actuator. For larger force lengths (l = 0.04 and 0.08 m) the controller fails to reduce the error while for smaller lengths (l = 0.005 and 0.01 m) error reduction is registered although the performance is suboptimal.

9.2.3 Control case A: generic force distribution

The generic force distribution is applied in case A. Three control scenarios are investigated comprising of two single frequency and one multi frequency sub-cases. The controller is operating in single frequency cases corresponding

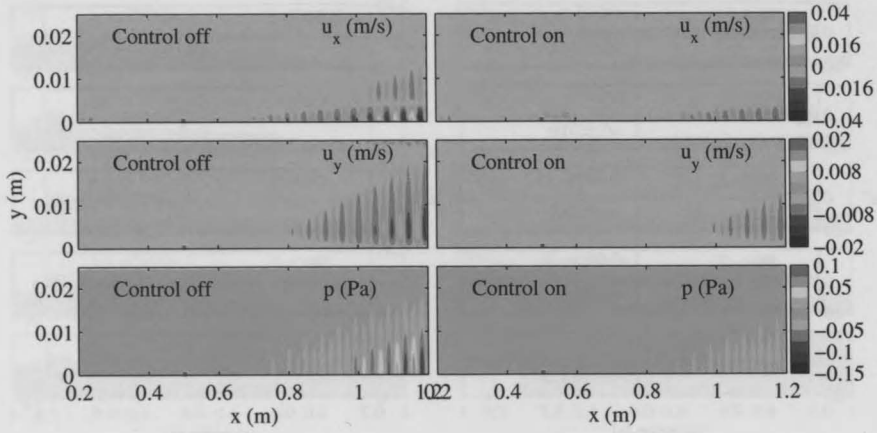

Figure 9.10: Snapshots of horizontal (u_x) and vertical (u_y) components of disturbance velocity and pressure (p) with and without control. ($F = 66$). (Position of the actuator is indicated by the small red rectangle)

to $F = 66$ and 86 while the multi frequency case consists of a wavetrain which is a combination of modes $F = 66$, 86 and 106 of equal initial amplitudes.

Snapshots of the velocity and pressure disturbance flowfield are presented in Figs.9.10 and 9.11 for the cases of $F = 66$ and $F = 86$ respectively. Additionally the value of the maximum horizontal velocity component are presented in Fig.9.13(b) and Fig.9.13(a). The comparison between the controlled and uncontrolled cases indicates the effect of the body force actuation. Both the horizontal and vertical components of the disturbance velocity as well as the pressure fluctuations are reduced downstream the actuation region. In the case of $F = 66$ amplification of the residual disturbances continues after the actuation since the entire domain is located within the instability region.

On the contrary the case of $F = 86$ appears to have an almost total wave cancellation since the TS waves cross the upper neutral curve approximately after $x = 0.9$. To be noted here that the settings of the controller are kept the same for these two cases apart from the convergence constant β. This is adjusted specifically for each case in order to achieve optimal performance from the controller.

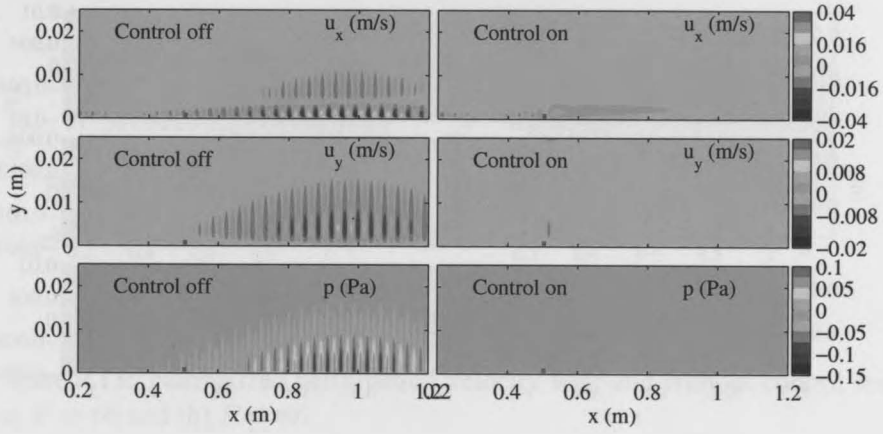

Figure 9.11: Snapshots of horizontal (u_x) and vertical (u_y) components of disturbance velocity and pressure (p) with and without control. ($F = 86$).(Position of the actuator is indicated by the small red rectangle)

Apart from the reduction of the fluctuating velocity components, an interesting aspect is the mean flow component present close to the forcing region. This is an artifact of the unidirectionality of the body force. More specifically, the generic body force is restricted to take only positive (downstream) values. In the case where the controller instructs it to be negative the force is automatically set to zero. This is to ensure that the overall forcing mechanism resembles the unidirectional plasma actuation. In both single frequency cases the mean flow disturbance appears to diffuse downstream.

Velocity and pressure field snapshots for the multi frequency sub-case are presented in Fig.9.12. Additionally the maximum horizontal velocity component is presented in Fig.9.14. This case involves the development of a wavetrain consisting of three modes at F = 66, 86 and 106 respectively. Contrary to the single frequency cases the disturbances are introduced in the domain via a distributed body force as previously explained. The weights for all the modes are set to be equal. It is apparent here that while the controller still manages to reduce the amplitude of the traveling wavetrain, the large values of amplitude reduction achieved for the single frequency cases are not possible. This can be explained by considering the nature of the forcing mechanism.

Although the controller attempts to regulate the amplitude of the imposed

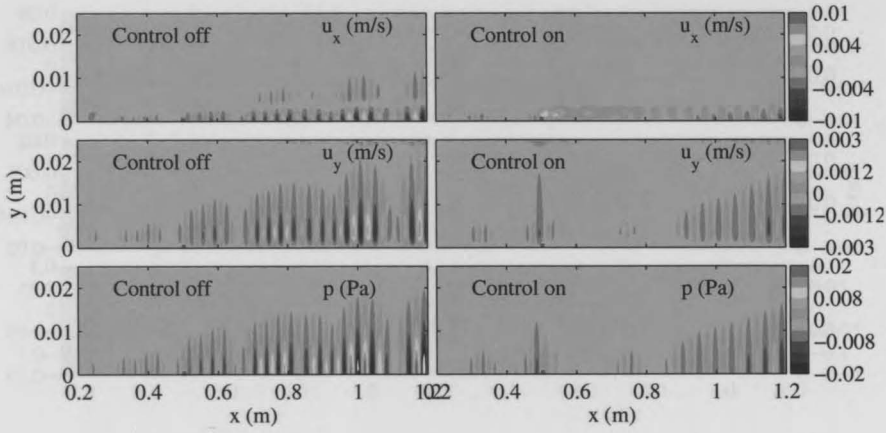

Figure 9.12: Snapshots of horizontal (u_x) and vertical (u_y) components of disturbance velocity with and without control for the multi frequency subcase ($F = 66, 86, 106$).(Position of the actuator is indicated by the small red rectangle)

body force, no authority exists over the spatial distribution, location and shape of the body force. On the other hand the incoming disturbances present multiple wavelengths, amplitudes and frequencies. As was shown in section 9.2.2 the wavelength of the imposed force has considerable influence on the final performance of the controller. It is thus expected that in a scenario where multiple frequencies are to be controlled a predefined force distribution will lead the controller to a sub-optimal operation stage. This is of high importance in actual plasma cases where the spatial extent and shape of the force distribution cannot be explicitly controlled as it is a function of the applied voltage. This is further demonstrated in case B.

The temporal evolution of the reference and error signal along with the respective amplitude of the body force (A_x) are shown in Figs.9.15 - 9.17 for the two single frequency cases and one multi frequency case respectively. As already mentioned the system identification time is 0.2 s in all cases. During this time the body force is directly driven by the reference pressure signal while the system identification algorithm builds the digital representation of the cancellation path. It is interesting to note that during this stage the error signal is reduced in the case of F = 66 while it is increased in the case of

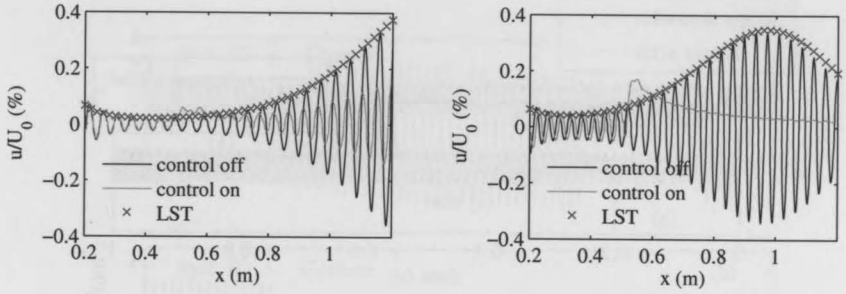

Figure 9.13: Normalized perturbation velocity with and without control for (a) $F = 66$ and (b) $F = 86$.

F = 86. This emphasizes the role of the system ID part in which a random signal which can have either positive or negative effects can be used to drive the actuator.

The difference in control performance between the two single frequency cases is also evident here. Apart from the final reduction in amplitude, the convergence of the controller to the final operation state is considerably faster for the case of F = 86. This again has to do with the relation between the spatial extent and shape of the body force distribution compared to the wavelength of the incoming instability. For the multi frequency case results indicate that although the controller converges relatively fast to the final state of operation, the complete elimination of the fluctuating disturbances is not possible.

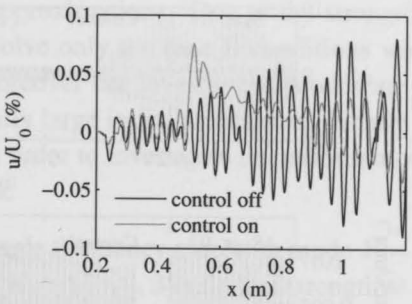

Figure 9.14: Normalized perturbation velocity with and without control for the multi frequency case case $F = 66, 86, 106$.

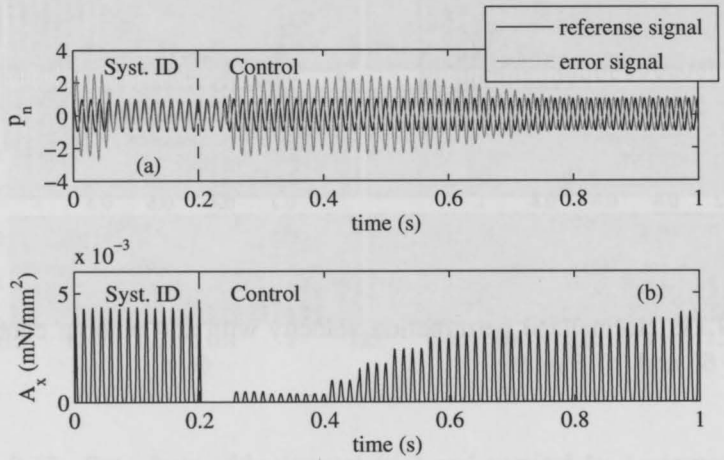

Figure 9.15: (a) Normalized reference and error signals during controller operation and (b) respective body force amplitude (A_x) for the case of $F = 66$

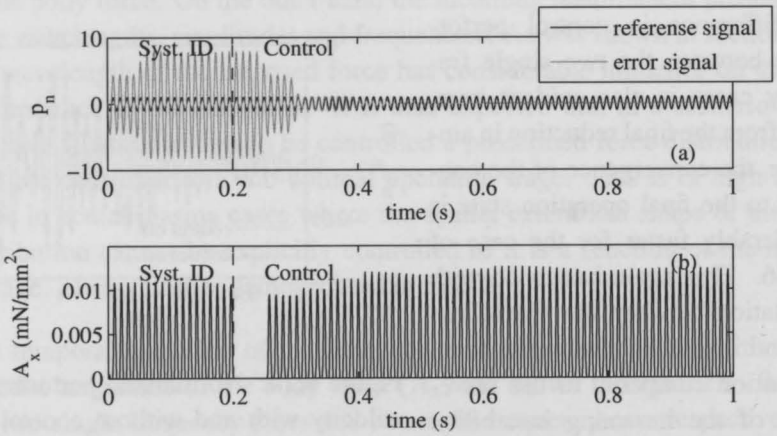

Figure 9.16: (a) Normalized reference and error signals during controller operation and (b) respective body force amplitude (A_x) for the case of $F = 86$

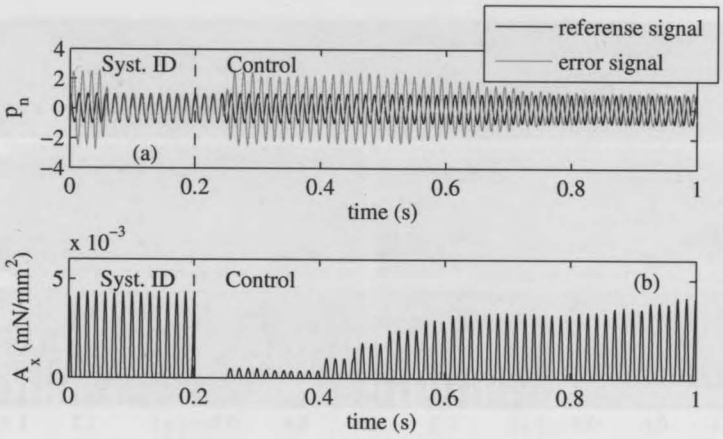

Figure 9.17: (a) Normalized reference and error signals during controller operation and (b) respective body force amplitude (A_x) for the multi frequency case ($F = 66, 86, 106$)

9.2.4 Control case B: plasma force distribution

The experimentally derived plasma body force distributions have been implemented in the numerical framework with the use of a continuous voltage function based on Bernstein surface approximations. Due to the strength of the actuator itself, the tested cases involve only the case B conditions where the freestream velocity is $30m/s$. Moreover the investigated modes are introduced in the domain with intentionally large initial amplitudes. Finally the actuator is placed more downstream in order to investigate its performance in tackling heavily amplified disturbances.

Two sub-cases are studied, namely a single frequency case with mode $F = 25$ and a multi frequency case with modes $F = 15, 25, 35$ of equal strength at the disturbance introduction. Snapshots of the evolved flowfield for the single frequency case are shown in Fig.9.18 while the respective maximum amplitude of the disturbance is shown in Fig.9.20(a). Some comments can be made on this case. The stability characteristics of this case are significantly more adverse than the sub cases of case A. Mode $F = 25$ has an N factor which almost reaches 9 by the end of the computational domain. This signifies the transitional state of this boundary layer. Additionally, at approximately $x = 1.1$ the first harmonic of the mode starts to show significant values departing the

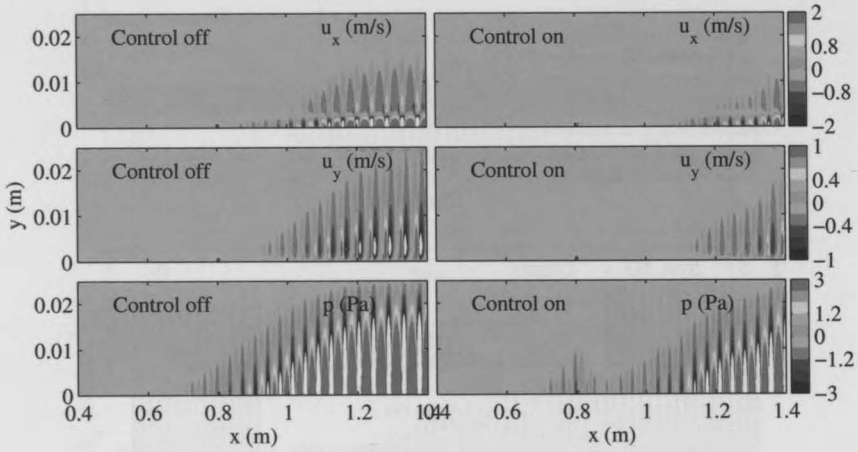

Figure 9.18: Snapshots of horizontal (u_x) and vertical (u_y) components of disturbance velocity and pressure (p) with and without control. ($F = 25$).(Position of the actuator is indicated by the small red rectangle)

maximum disturbance amplitude from the sinusoidal shape. This additionally signifies the initial parts of non-linear amplification in which a 2D simulation is destined to fail. As such results for the unactuated case should be considered valid only until $x = 1m$. The controller achieves significant reduction on the amplitude of the TS mode. Nevertheless, downstream of the actuator the boundary layer is already deep in the instability region and the residual disturbances after actuation quickly amplify again. This effect raises the importance of multiple successive actuators in the case of practical applications.

Snapshots of the flowfield for the multi frequency case are presented in Fig.9.19 while the maximum amplitude of the disturbance is shown in Fig.9.20(b). It is evident that the actuator can respond well to the existence of multiple frequencies in the spectrum of TS waves. Additionally a pronounced mean flow disturbance is evident which nevertheless is significantly reduced within approximately 6 TS wavelengths downstream.

The reference, error and voltage signals as measured by the controller are presented in Figs.9.21 and 9.22 for the single and multi frequency cases respectively. For the single frequency case a relatively large time span is spent

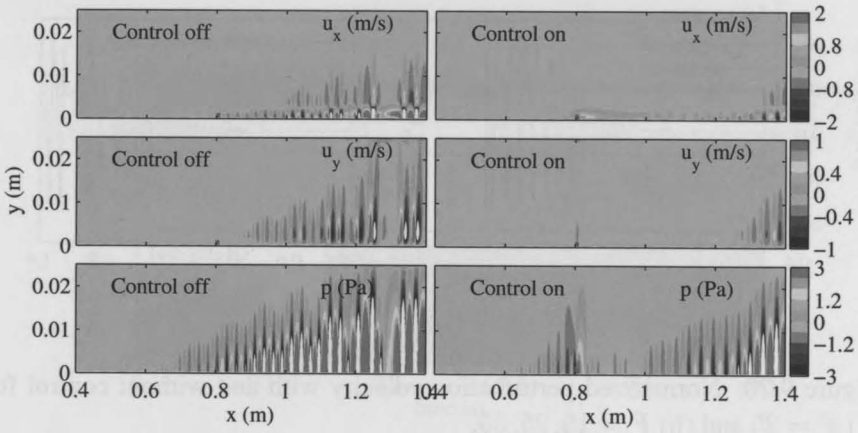

Figure 9.19: Snapshots of horizontal (u_x) and vertical (u_y) components of disturbance velocity and pressure (p) with and without control for the multi frequency case. ($F = 15, 25, 35$).(Position of the actuator is indicated by the small red rectangle)

in which the actuator does not operate. This is due to the fact the required voltage decided by the control algorithm lies below the threshold value of 8 kV_{pp}. In these cases the controller automatically restricts the voltage to a zero value.

For the multi frequency case the effect is opposite. Due to the strength of the incoming disturbances the actuator is requested to operate with at voltages that lye above the maximum threshold of 16 kV_{pp}. In this case the maximum voltage is restricted to 16 kV_{pp}. This cutoff voltage effectively renders the actuation signal shape to trapezoidal rather than sinusoidal. In spite this the actuator achieves significant reduction of the TS amplitude. An overview of the test cases, respective force model and TS strength reduction is presented in Tab.9.2 Here Δu_{max} is the reduction of the maximum horizontal velocity component of the TS mode at $x = 1\ m$ while Δp_e is the reduction of the error signal as this is registered by the controller.

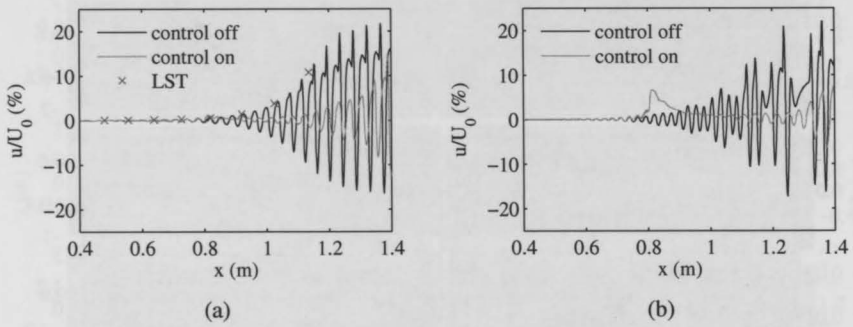

Figure 9.20: Normalized perturbation velocity with and without control for (a) $F = 25$ and (b) $F = 15, 25, 35$.

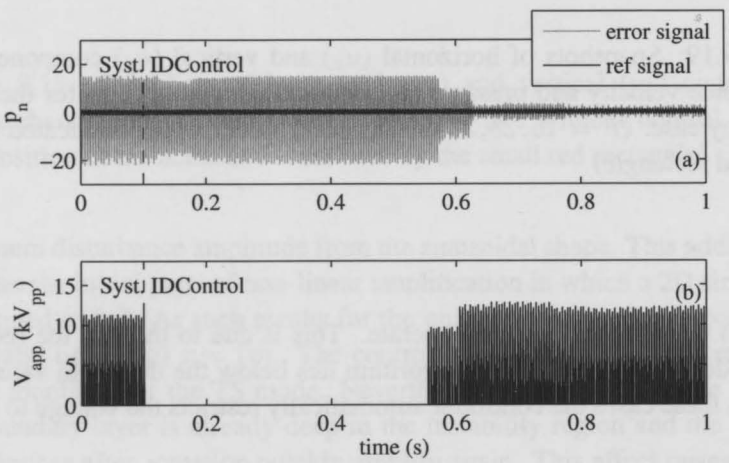

Figure 9.21: (a) Normalized reference and error signals during controller operation and (b) respective applied voltage value (V_{app}) for the case of $F = 25$

Table 9.2: Overview of test cases with respective force model and reduction in TS wave strength.

case	**frequency** (F)	**force**	Δu_{max} at $x =$ 1 m (%)	Δp_e (%)
A. 1	single (66)	generic	61	55
A. 2	single (86)	generic	90	98
A. 3	multi (66, 86, 106)	generic	62	69
B. 1	single (25)	plasma	84	79
B. 2	multi (15, 25, 35)	plasma	83	93

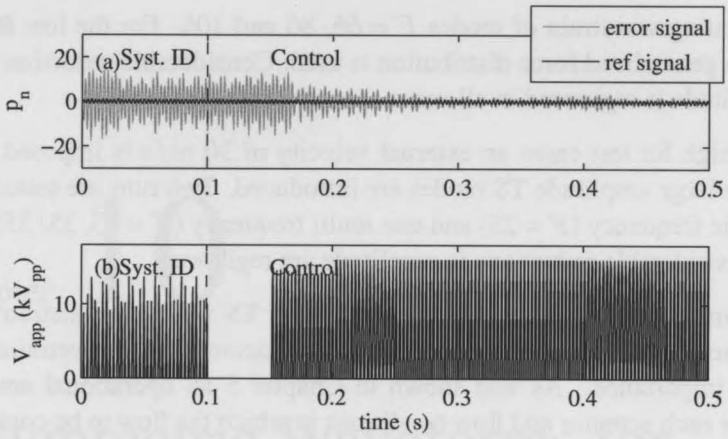

Figure 9.22: (a) Normalized reference and error signals during controller operation and (b) respective applied voltage value (V_{app}) for the case of $F = 15, 25, 35$

9.3 Conclusions

A numerical investigation on the use of plasma actuators for transition control is presented. The numerical framework involves the solution of the full unsteady 2D incompressible Navier Stokes equations using a finite volume formulation. Prior to the actual test cases an exploratory parametric study is conducted in order to clarify some aspects of the FXLMS controller and the body force-TS wave interaction. On the first aspect the effect of the convergence constant is demonstrated. Smaller than optimum values cause the controller to converge slowly while in extreme cases convergence is stopped altogether. Larger than optimum values cause unwanted fluctuations in the control action and eventually lead to controller instability.

A second aspect investigated, is the relation between the spatial wavelengths of the body force and TS modes. It has been found that an optimum control performance is achieved when the force wavelength is near half of the incoming TS wave.

Two different sets of control test cases are simulated. Firstly, low Re number cases at freestream velocity of 10 m/s. These involve two single frequency cases of modes F = 66 and 86 and one multi frequency case comprising of

a propagating wavetrain of modes F = 66, 86 and 106. For the low Re test cases the generalized force distribution is used. Considerable reduction in the TS amplitude is registered in all cases.

For the high Re test cases an external velocity of 30 m/s is imposed. Furthermore large amplitude TS modes are introduced. Two runs are tested with one single frequency (F = 25) and one multi frequency (F = 15, 25, 35) case. Again considerable reductions in amplitude are registered.

Several insights are gained into the process of TS wave cancellation using plasma actuators. The spectral content of the incoming TS wavetrains is of primary importance. As was shown in Chapter 5 an operational envelope exists for each actuator and flow conditions in which the flow to be controlled must be confined. Additionally, a maximum limit on the frequency of the unsteady TS modes must be set based on the carrier frequency of the actuator. As was demonstrated in Chapters 6 and 8 the time invariant force assumption can only be applied when the carrier frequency and the receptivity spectrum of the controlled flow are sufficiently decoupled.

A second point is the spatial relation of the wavelengths of the forcing mechanism (plasma actuator) and the structure to be controlled (TS wave). Especially in the case of plasma actuation the spatial extent of the body force is not constant but a function of applied voltage. This is coupled to the change of amplitude with voltage which presents one more degree of freedom. The control situation is further complicated in the case of natural transition where a wavetrain of several TS wavelengths is present. All these issues render the problem almost impossible to be addressed in the optimum way and a set of sub-optimum settings must be imposed.

Finally, exactly because of the high volatility of the system, the FXLMS algorithm appears to be ideal for this kind of problems. While relatively simple to implement, either numerically or experimentally, it provides the control engineer with a large degree of autonomy, frequency response and accuracy needed not only in the case of TS wave cancellation but also in a large variety of unsteady flow control applications.

Chapter 10

Asymmetric Waveforms for Improvement of DBD Actuation

The second chapter on DBD application involves the extension of the knowledge gathered in Chapter 6 for the improvement of DBD performance. This has been a major topic for past research on plasma actuators as their only relevant disadvantage is the limited momentum input to the flow for a given electrical power consumption. This handicap starts becoming significant and even limiting for applications at high Reynolds numbers where the energy content of the global flow instabilities is high. This chapter presents a study towards obtaining stronger and more efficient actuation.

Chapter 6 and previous investigations have demonstrated that the momentum transfer sequence and in consequence the plasma exerted body force is highly unsteady and periodic in respect to the driving High Voltage (HV) signal which is applied to the exposed electrode of the actuator. Several studies have focused on determining the actual magnitude and direction of the body force during the HV cycle. It has been shown in Chapter 6 that the momentum transfer is asymmetric between the two HV half cycles when the driving signal is sinusoidal. Using a different technique [37] showed the negative half cycle (*forward stroke*) to be responsible for the majority of momentum

transfer. A PUSH-push scenario has also been verified from recent numerical studies [85, 17]. To be noted that the term PUSH-push refers to the direction of the forcing during the forward and *backward stroke* and is used in the same context as [32]. The term in capital letters indicates the strongest of the two events. This terminology will be used throughout the chapter. In the forcing mechanisms study described in Chapter 6 the author demonstrated the forcing sequence for four different waveforms using a technique based on phase reconstruction of time resolved PIV snapshots of the plasma induced flowfield. It was shown that the shape of the waveform has dramatic effects on the momentum transfer sequence with PUSH-push and PUSH-pull scenarios possible depending on the shape of the waveform. It was suggested that such effects can be exploited for the improvement of performance of plasma actuators.

The current chapter is an extension and continuation of the previous work on the effect of the waveform shape on the actuator's performance. More specifically, it is recognized that the effect of the shape of the waveform influences both the magnitude and duration of the upstream and downstream body force components as well as the consumed electrical power. For example the conventional sinusoidal waveform is shown to produce a strong push event during the *forward stroke* and weak push event during the *backward stroke*. In contrast, a square shaped waveform produces strong push and pull events during the initial phases of the forward and *backward stroke*s. Yet the square waveform is overall stronger than the sine waveform since the push event is responsible for significantly higher momentum input compared to the respective push event of the sine waveform. On the other hand the square waveform is shown to consume considerably more power than the sine waveform which must be additionally taken into account.

This work is focused on the investigation of waveforms which present an asymmetry in shape between the two half cycles. A systematic combination of the sine and square shapes is performed based on the results of the aforementioned study of Chapter 6. This is achieved through a parametric thrust measurement study. Additionally, electrical power consumption is measured in order to have a measure of efficiency for the different cases. Finally, the best performing waveform is selected and analyzed using the previously developed phase reconstruction technique in conjunction with time resolved PIV measurements. The reference cases of sinusoidal and square waveforms are analyzed in a similar way in order to have a concrete base of comparison with

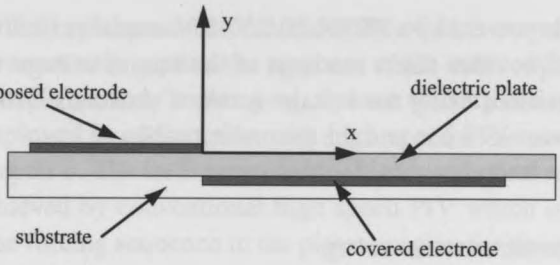

Figure 10.1: The geometrical configuration of the actuator with the corresponding coordinate system (not to scale).

the optimized asymmetric waveform.

The structure of the chapter follows a description of the experimental setup, including the actuator operating parameters and the employed measurement techniques. In the next section the groups of results are presented and discussed. Finally, conclusions are presented.

10.1 Experimental Setup

10.1.1 The actuator

For this study a Dielectric Barrier Discharge (DBD) configuration employing thick electrodes is used. The actuators consist of thin rectangular copper electrodes made out of self-adhesive copper tape separated by a dielectric layer (Fig.10.1). The thickness of both electrodes is 60 μm. The width of the exposed electrode is 10 mm while the grounded electrode is 20 mm. No horizontal gap exists between the two electrodes. Their effective spanwise length (along which plasma is generated) is 220 mm. The electrodes are separated by a clear Plexiglass (PMMA) plate acting as a dielectric. The thickness of the plate is 3 mm. The lower electrode is covered by three layers of Kapton tape and an additional plate of PMMA in order to prevent plasma to be formed on the lower side. The geometric parameters of the actuator are chosen to correspond to the actuator used by Forte et al.[42] since, to the authors knowledge, this actuator has achieved the highest induced velocities to date for the given applied voltage.

The actuator is powerd by a TREK 20/20C HV amplifier ($\pm 20\ kV$, $\pm 20\ mA$). The amplifier provides direct readings of the output voltage while the output current is measured using the voltage across a resistance (100 Ω) placed between the lower electrode and the grounding cable.

10.1.2 Measurements setup

The measurements for this study are performed in quiescent flow conditions. To ensure such conditions, measurements are conducted in a closed box made from Plexiglass (PMMA) to provide optical access. Two diagnostic techniques are applied for quantifying the effect of the waveform shape on the performance of the actuator. These consist of direct thrust measurements and time-resolved Particle Image Velocimetry (PIV) measurements respectively.

For the initial parametric study, a large number of test cases is executed. Consequently, direct thrust measurements are conducted due to the speed and accuracy such technique provides. The concept of thrust measurements has been previously applied for the characterization of plasma actuators in Chapter 4 and it relies on the direct measurement of the reaction force due to the acceleration of fluid from the plasma operation. For the current study the plasma actuator is placed on a frictionless air bearing which is able to slide in the x direction. The entire system is fitted in the closed PMMA box. A highly sensitive ME-messsysteme KD-40S strain-gage load cell is then connected to the bearing which registers the reaction force from the induced jet due to the plasma actuation. The nominal force range of the load cell is $\pm$ 2 N with an accuracy of 0.1% (2 mN). The connections of the active and grounded electrodes to the power supply are established via thin copper wires to minimize signal contamination from external vibrations. The thrust value is sampled at 100 Hz for ten seconds during actuation while reference measurements are taken before and after every measurement sequence. All measurement tests are repeated three times to minimize any error due to load cell relaxation or external vibrations.

For the second part of this investigation the selected waveform, which is established through the parametric study based on thrust, is further analyzed. Additionally the two reference cases of sinusoidal and square shapes are similarly analyzed. The analysis is based on the spatio-temporal resolution of the in-

duced flowfield under plasma actuation respective of each waveform. As such it is desirable to accurately capture the response of the induced flow within the time scales of the HV period. To this goal, a phase shifting and reconstruction technique is employed in conjunction with high speed PIV measurements as described in Chapter 6. The technique enables higher temporal resolution than what can be achieved by conventional high speed PIV which is necessary to fully describe the forcing sequence in the plasma region for the studied carrier frequency (625 Hz).

The phase shifting and reconstruction technique requires data from time-resolved PIV measurements. For the time-resolved PIV tests the plasma actuator is placed flushed on the bottom of the Plexiglas box. A Photron Fastcam SA1 high speed camera of 1024×1024 pixels is used to image the field-of-view (FOV). Image acquisition has been conducted at 6 KHz rate in double-frame mode. Time separation of 75 μs has been applied between successive images. A Micro-Nikkor 105 mm objective is set at f-stop 4 in order to achieve 0.67 magnification and a FOV of 30.9×15.0 mm using a cropped sensor of 1024×496 pixels. The air in the Plexiglas box is seeded with olive oil droplets of approximately 1 μm diameter generated by a TSI atomizer. Due to the quiescent flow conditions particle accumulation near the wall could introduce errors. To avoid this, forced mixing through an air blower is introduced before each measurement to ensure homogeneity of the seeding particles. The air is let to settle before actuation. Additionally, the homogeneity is visually confirmed from the PIV snapshots for every case. No near wall accumulation is observed. The particles at the mid span of the actuator are illuminated by a light sheet of 2 mm thickness generated by a Quantronix Darwin-Duo laser system with an average output of 80 W at 3 kHz. The images are analyzed using Davis 7.4 (Lavision GmbH) by cross-correlating successive images. Final interrogation window size of 12×12 pixels and overlap factor of 75% are used. The interrogation windows are elongated in the wall normal direction using a 4:1 aspect ratio in order to obtain higher spatial resolution. The velocity vectors are returned on a grid of 11×11 vectors per mm^2.

10.1.3 Test cases

The experimental investigation in this study is comprised of two parts. Firstly, a parametric study is conducted based on direct thrust measurements. Initially two reference cases are tested employing the conventionally used sinusoidal

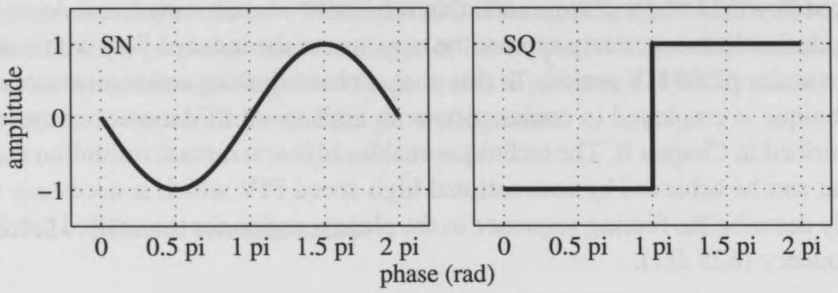

Figure 10.2: Shapes of the two reference waveforms used in this study.

shape waveform and a square waveform respectively. Based on the results of Chapter 6 the two waveforms present different forcing behavior in duration and magnitude. Specifically, the sinusoidal waveform produces a strong positive forcing component during the *forward stroke*. A a smaller but still positive component is present during the *backward stroke*. On the contrary, the square waveform produces two short in duration but strong forcing peaks at the start of each stroke. The *forward stroke* presents a positive forcing while the *backward stroke* gives a negative forcing. Based on these differences, the waveforms for this study are constructed based on a systematic transition between the two reference waveforms of sinusoidal and square shapes respectively. The rationale behind this approach is the exploitation of the favorable features of each of the reference shapes in order to optimize the performance of the final waveform. Since it is shown that, depending on the shape of the waveform, both a push and a pull regimes can exist within the actuation period, it becomes clear that the shape of the optimized waveform should be such that the push action is enhanced while the pull action is abated or completely removed.

It should be noted here that the findings in Chapter 6 serve only as a starting point since for this study a series of parameters is changed. More specifically the dielectric material is changed from Kapton to Plexiglass while its thickness is much larger. Additionally, due to the thicker dielectric, the applied voltage is also larger. These differences are enough to produce changes in the discharge regime as demonstrated by [85]. Therefore, the reference cases of sine and square waveforms are re-investigated in this study.

Three families of waveforms are created for the parametric study based on

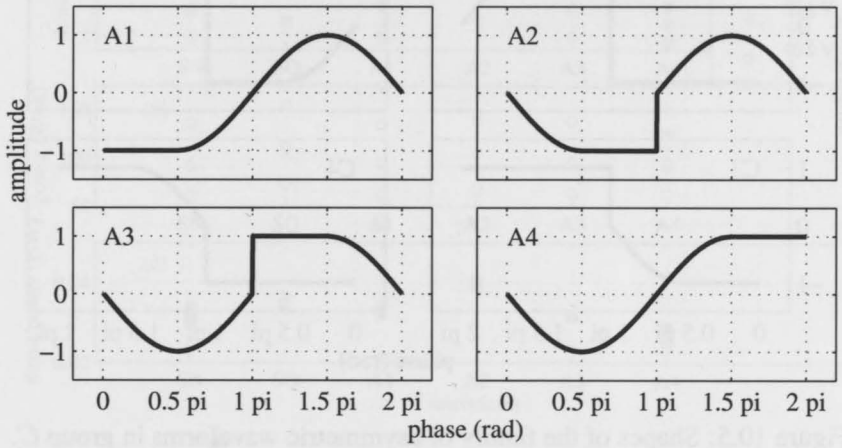

Figure 10.3: Shapes of the family of asymmetric waveforms in group A.

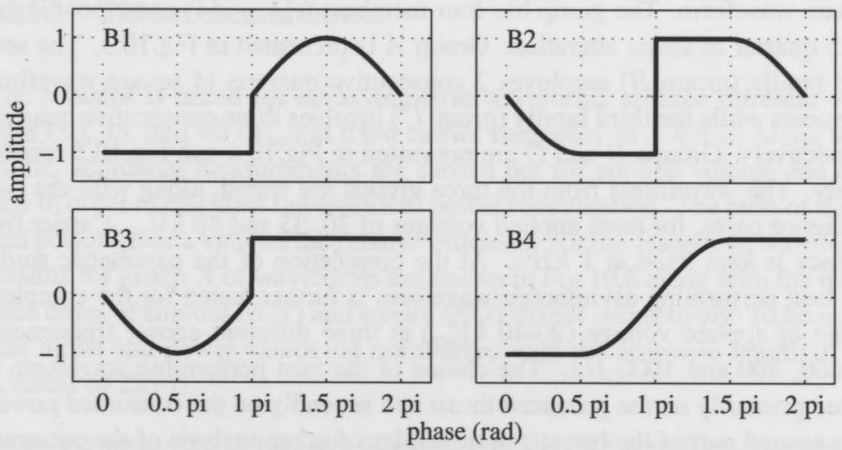

Figure 10.4: Shapes of the family of asymmetric waveforms in group B.

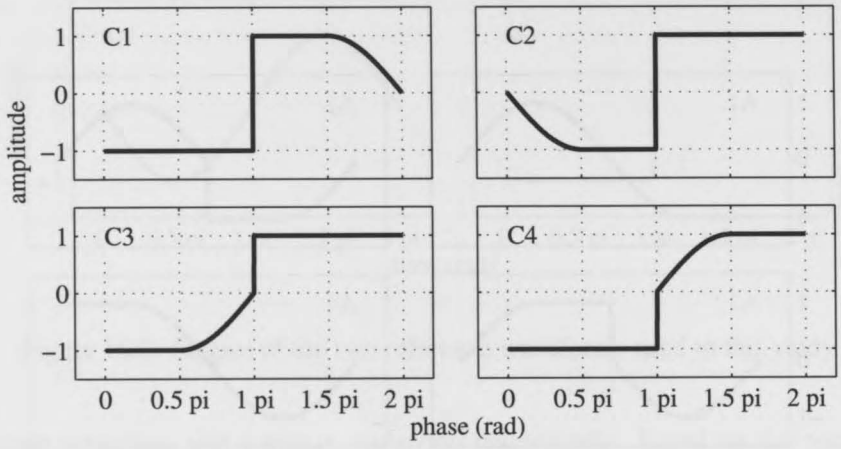

Figure 10.5: Shapes of the family of asymmetric waveforms in group C.

thrust. These are combinations of the two reference cases of sinusoidal (SN) and square (SQ) shapes. The reference cases are presented in Fig.10.2. The first family of waveforms (group A) consists of sinusoidal shapes where one quarter of the period is replaced by the shape of the respective period of a square waveform. The group has four members ($A1 - A4$) corresponding to each quarter of shape alteration. Group A is presented in Fig.10.3. The second family (group B) employes 2 consecutive quarters of square waveform segments while the third family (group C) involves three consecutive quarters respectively. Groups B and C are presented in Fig.10.4 and Fig.10.5 respectively. The waveforms from the three groups are tested, along with the two reference cases, for three applied voltages of 30, 35 and 40 kV_{pp}. Carrier frequency is kept fixed at 1 kHz. At the completion of the parametric study, the best performing asymmetric waveform is further tested for the complete range of applied voltage (20-40 kV_{pp}) at three different carrier frequencies of 600, 800 and 1000 Hz. The choice of the best performing waveform is based primarily on the produced thrust and secondly on the consumed power. The second part of the investigation involves further analysis of the optimum asymmetric waveform using the previously mentioned PIV and phase shifting technique. The asymmetric waveform extracted from the parametric study is tested along with the two reference cases at applied voltage of 40 kV_{pp} and carrier frequency of 625 Hz.

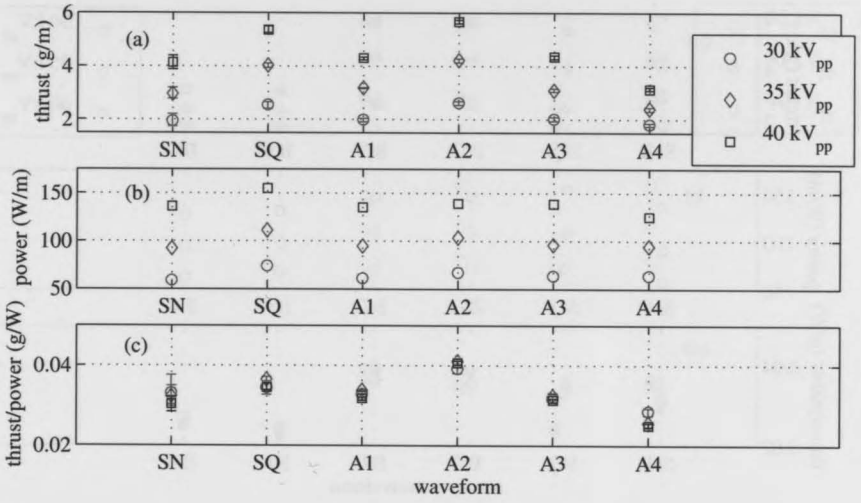

Figure 10.6: (a) Thrust, (b) power consumption and (c) relative efficiency for the waveforms in group A.

10.2 Results

10.2.1 Thrust measurement

The actuator is tested for all asymmetric waveforms at three different voltages (30, 35, and 40 kV_{pp}) at fixed carrier frequency of 1 kHz. Along with thrust, additional measurements are carried out for applied voltage and current in order to calculate the electrical power consumption. The ratio of thrust and power gives a view of the relative efficiency for the respective waveform. Results for group A of waveforms are shown in Fig.10.6 along with the reference cases of sinuous (SN) and square (SQ) shapes respectively. To be noted that thrust and power values are normalized with the spanwise length of the actuator (0.22 m).

From the measured thrust, it is obvious that the SQ waveform is more effective than the conventionally used SN. This is already observed from the results of Chapter 6 although the dielectric material and thickness as well as applied voltage were different. Nevertheless, SQ also appears to consume more power than SN for the same voltage. Nevertheless, the difference in

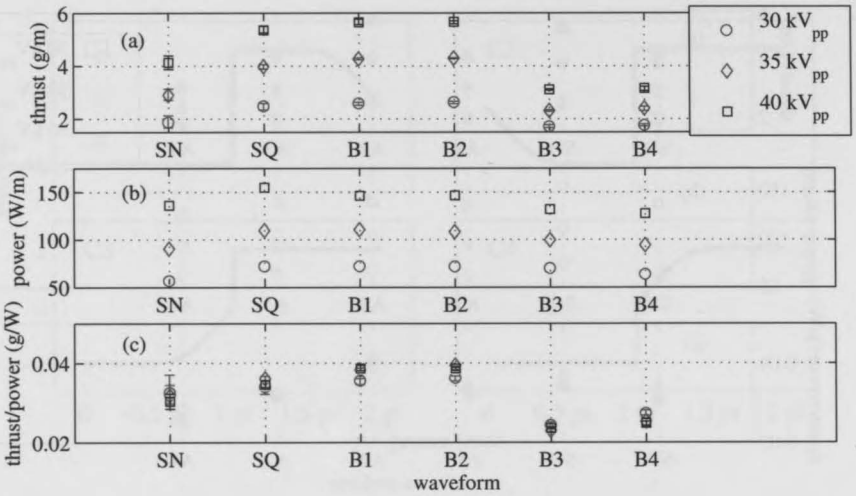

Figure 10.7: (a) Thrust, (b) power consumption and (c) relative efficiency for the waveforms in group B.

thrust is disproportionate to the respective difference in power consumption. This is reflected on the relative efficiency values (thrust to power ratio). SQ is approximately 15 % more efficient than SN.

For the asymmetric waveforms in group A some interesting observations can be established. Waveform $A2$ appears to provide slightly more thrust than SQ with power consumption which is comparable to the SN shape. This brings the overall efficiency improvement up to 30 % compared with the conventional SN. $A1$ and $A3$ do not present significant changes compared to SN while $A4$ is significantly lower in terms of thrust than all other waveforms of group A.

A correlation appears to exist between produced thrust, consumed power and the shape of the respective waveforms. The better performing $A2$ employs a square waveform during the second quarter of the HV cycle. This effectively creates a long plateau of negative voltage with a steep ascent at phase π as opposed to the smooth rise of SN for the same quarter. Waveforms $A1$ and $A3$ have the square waveform shape in the first and third quarter respectively which appears to have no effect on thrust or power. In contrast waveform $A4$ has the square shape and steep voltage reversal at the start of the *forward*

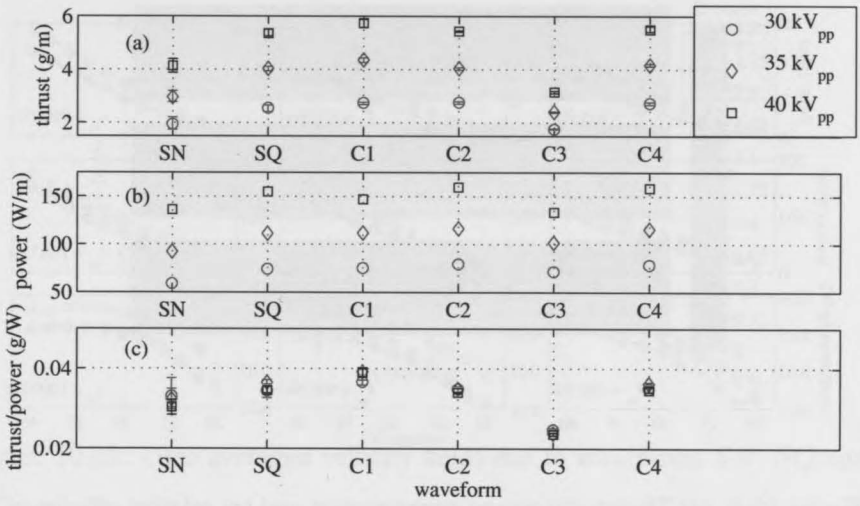

Figure 10.8: (a) Thrust, (b) power consumption and (c) relative efficiency for the waveforms in group C.

stroke. This has a degrading effect in thrust production which is even lower than the sine waveform. On the other hand the power consumption of waveform $A4$ is significantly lower than all other waveforms of group A.

Results for group B of asymmetric waveforms are presented in Fig.10.7. $B1$ and $B2$ are providing slightly higher thrust than SQ with comparable power consumption to SN. On the contrary $B3$ and $B4$ have significantly poorer performance in terms of thrust while their power consumption is relatively low. The observations for group A are verified for group B as well. Shapes that present a steep voltage rise during the start of the *backward stroke* provide higher thrust than SN while steep voltage drop at the start of the *forward stroke* degrades the performance significantly.

The correlation observed for group A appears to hold for group B as well. More specifically, shapes that employ a steep voltage rise at the *backward stroke* ($B1$ and $B2$) outperform the sine reference case and are even marginally better than the square waveform in both terms of produced thrust and relative efficiency. On the contrary, waveforms which employ the steep voltage drop at the beginning of the *forward stroke* ($B3$ and $B4$) are significantly weaker. Their power consumption is also lower although not proportionally as can be

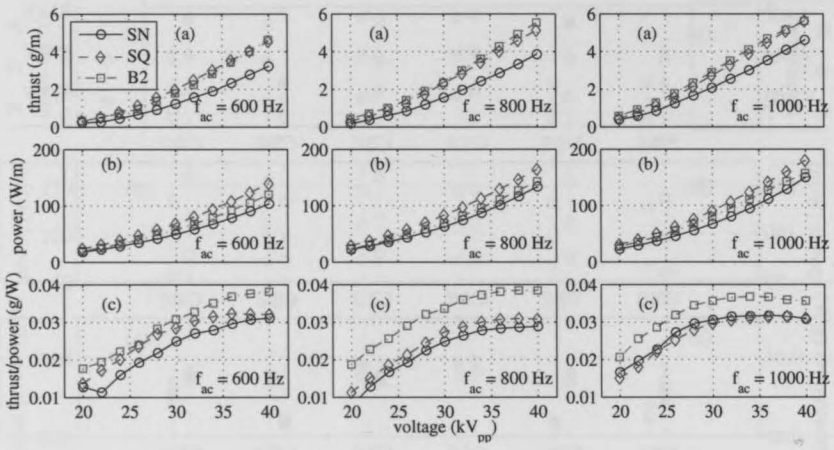

Figure 10.9: (a) Thrust, (b) power consumption and (c) relative efficiency for the waveforms SN, SQ and $B2$.

seen from the relative efficiency values which are even lower than the SN reference case.

The results for the group C are presented in Fig.10.8 and further demonstrate the importance of steep voltage rise at the start of the *backward stroke*. Shapes $C1$, $C2$ and $C4$ produce thrust on par with the SQ waveform. On the contrary $C3$, which employs a steep voltage drop at the beginning of the *forward stroke* is significantly weaker.

In general two major observations can be deduced from the results of groups A, B and C. Firstly, the performance of the actuator is defined by the shape of the waveform at specific phase intervals. More specifically, the beginning of the *forward stroke* (0 - 0.2 π) and *backward stroke* (1 - 1.2 π) seem to be of major importance while the shape at all other phases does not affect performance in any way. Secondly, the actual shape of the waveform at these intervals seems to have an enhancing or degrading effect on the performance in terms of thrust and power consumption compared to the reference case of SN. Sharp voltage changes, associated with the square shape, during the *forward stroke* (0 - 0.2 π) reduce thrust production compared to the sine shape (waveforms $A4$, $B3$, $B4$ and $C3$). Additionally, power consumption for these shapes is also reduced. Waveforms that employ sharp voltage changes at phases other than the relevant *active* periods (0 - 0.2 π and 1 - 1.2 π) do not present any

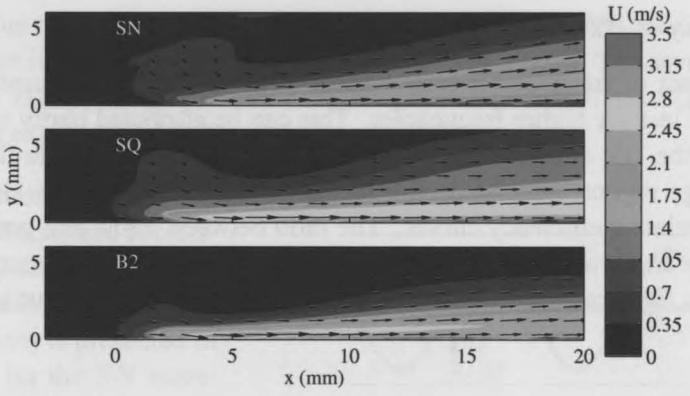

Figure 10.10: Time averaged velocity fields due to waveforms SN, SQ and $B2$.

difference from SN. Finally, if the steep voltage change is applied at the beginning of the *backward stroke* (1 - 1.2 π), thrust is increased to the levels of the square waveform while the consumed power remains approximately the same (waveform $A2$).

The main driving mechanism behind thrust improvement appears to be the temporal gradient of the voltage signal. For the *forward stroke* the effects of steeper voltage drop are detrimental for the performance while the exact opposite occurs for the *backward stroke*. The effect of the slew rate of the HV amplifier should also be mentioned here since not all desired shapes can be reproduced. Yet it seems that even small differences on the slope of voltage can lead to significant changes in produced thrust. This is further discussed in the next section.

In order to gain more insight into the characteristics of the different shapes, three waveforms are selected for more detailed analysis. Waveform $B2$ is selected as the most optimum shape among the ones tested and is promoted for further analysis. Additionally, the reference cases SN and SQ are also tested. Thrust measurements are performed for the full voltage range of 20 to 40 kV_{pp} at three different carrier frequencies of 600, 800 and 1000 Hz. Results are presented in Fig.10.9. Several observations here verify the previous parametric study. Waveform $B2$ produces comparable thrust values to the SQ waveform. Nevertheless, the power consumption of $B2$ is slightly above SN and considerably less than SQ. This effectively shows an increase in relative

efficiency of $B2$ compared to both reference cases.

The effect of frequency is also evident. The thrust improvement seems to become less for higher frequencies. This can be attributed partly to the slew rate of the HV amplifier and partly due to the transition to the filamentary discharge regime associated with increased frequency. This is also evident on the relative efficiency curves. The ratio between thrust and power seems to reach an asymptotic plateau at high voltages. The plateau starts at lower voltages for increasing carrier frequencies. Still the highest thrust is achieved at 1 kHz.

10.2.2 Forcing mechanism analysis

A clear description of the forcing mechanisms due to the differences in shape is not possible with only the thrust measurements since thrust data are averaged in time and space by default. It is, thus, essential to further expand the analysis to the spatio-temporal behavior of the induced velocity. This can be achieved with the phase shift and reconstruction technique as was explained in the experimental setup section and in more detail demonstrated in Chapter 6.

Three waveforms are chosen for the forcing mechanism analysis. These consist of the two reference waveforms (SN and SQ) along with the asymmetric waveform $B2$ which exhibited the best performance in terms of thrust and relative efficiency during the thrust parametric study. For each waveform the applied voltage is held fixed at $40kV_{pp}$ and the carrier frequency at 625 Hz to comply with the phase shift technique requirements. A time-resolved PIV measurement is conducted for all the waveforms with the actuator placed in the closed PMMA box to ensure quiescent flow conditions. Sampling rate is fixed at 6 kHz which in combination with the selected carrier frequency provides a reconstructed signal of 48 frames within the actuation period. A total of 50 reconstructed cycles are measured and phase averaged to provide the final result.

Prior to the time resolved analysis, the flowfields are averaged in time and presented in Fig.10.10. As suggested from the trhust measurements, SQ and $B2$ produce significantly stronger jets than SN. Maximum mean velocities are 3.03 and 3.35 m/s for SQ and $B2$ respectively, while the respective value for SN is 2.41 m/s. This implies an improvement of 40 % in maximum induced

velocity due to the asymmetric waveform $B2$ compared to SN. Additionally a difference in the thickness of the produced jet is registered. The asymmetric waveform $B2$ appears to produce a thinner jet than both SN and SQ. There is no clear explanation for this phenomenon at this point.

The evolution of the instantaneous velocity and acceleration at a point in the vicinity of the actuator (x = 5 mm, y = 0.4 mm) is presented in Fig.10.11 for the SN waveform. Additionally, snapshots of the velocity and acceleration fields at four selected instants are presented in Fig.10.12. The behavior of the flowfield generally resembles that of the actuator tested in Chapter 6 although several parameters such as dielectric material, thickness and applied voltage are different. On the other hand some important differences between the two cases exist as is explained in following paragraphs.

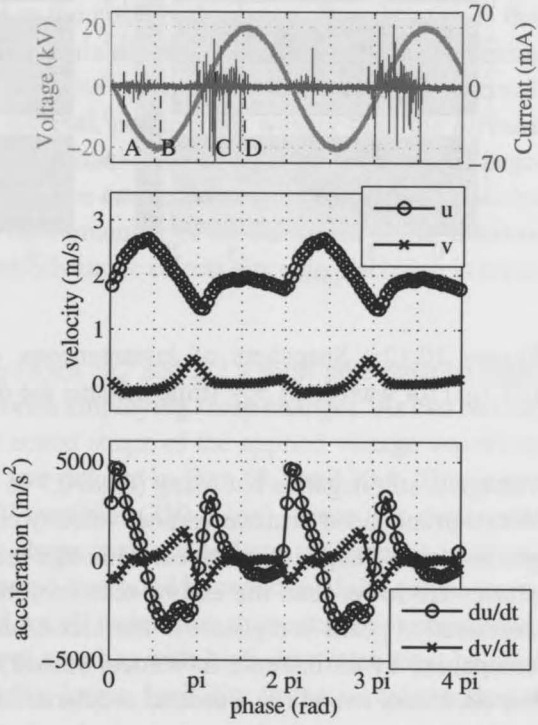

Figure 10.11: Evolution of the velocity and acceleration within the HV period for the SN waveform (values probed at x = 5 mm, y = 0.4 mm).

The majority of experimental [37, 71] and numerical [17, 85] investigations on the DBD forcing mechanisms discuss the sinusoidal waveform, albeit for different electrical and geometrical parameters. Here a phenomenological description of the three tested waveforms flowfield evolution is given followed by a conceptual scenario of the underlying forcing mechanisms. At the beginning of the *forward stroke* strong acceleration of fluid is observed near the exposed electrode (instant A). Simultaneously the positive discharge is ignited as is evident by the current peaks. While the

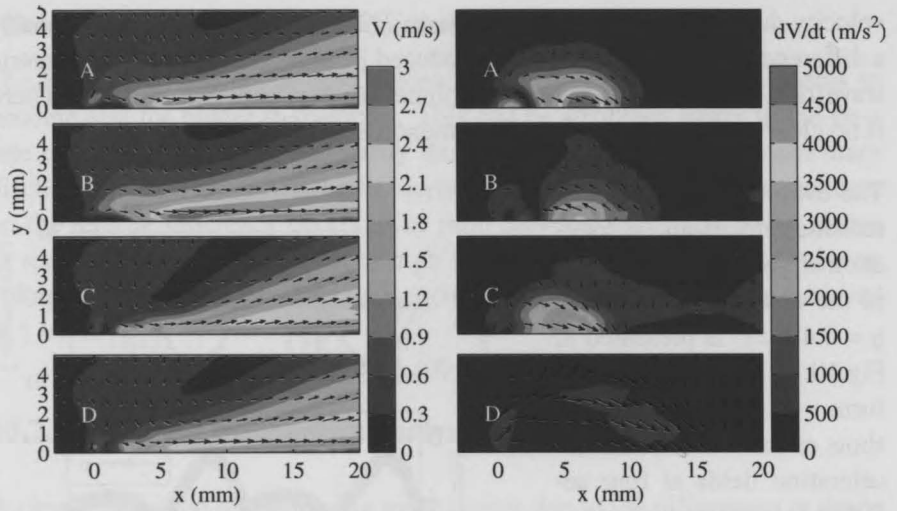

Figure 10.12: Snapshots of instantaneous velocity (V) and acceleration (dV/dt) for waveform SN (time instants are defined in Fig.10.11).

voltage is still negative but rising (from 0.7 to 1 π) a deceleration is observed with a pronounced positive vertical velocity component (instant B). At these phases no discharge is registered. Although the values of deceleration at these phases are lower than the earlier acceleration, the existence of two discreet deceleration peaks is registered. The second deceleration peak (near π) is accompanied by an increase in vertical velocity as well. At the beginning of the *backward stroke* (π) a second acceleration event is occurring (instant C) while the negative discharge is ignited as indicated from the strong current peaks which occupy most of the period between π and 1.5 π. For the remainder of the negative stroke (1.5 - 2 π) no substantial velocity variation is further registered.

The sine waveform flowfield evolution presents similarities as well as differences with the lower voltage, thin dielectric case of Chapter 6. The overall scenario still follows the PUSH-push scenario with strong positive acceleration at the beginning of the *forward stroke* and weak but still positive acceleration at the beginning of the *backward stroke*. More specifically form 0 to 0.5 π the discharge event appears to produce strong positive horizontal force. This can be related to emission of negative ions from the exposed electrode towards the dielectric. From 0.5 to 0.9 π the flow decelerates and as no dis-

charge is registered during this period, the deceleration can be attributed to hydrodynamic stresses and pressure effects.

On the other hand, of great interest is the apparently negative forcing component responsible for the second deceleration peak (1 π). Since intuitively there is no reason for the second peak to be related to hydrodynamic effects it can be assumed to be related to the positive discharge. Possibly this is due to negative ions which have accumulated over the dielectric surface during the *forward stroke* and begin to move upstream as the voltage is reversed. Immediately after the voltage reversal, positive but weaker than the *forward stroke* acceleration is registered simultaneously with the majority of the negative discharge (π to 1.5 π). This can be attributed to the dominance of positive ions moving downstream. For the remainder of the *backward stroke* the flow smoothly decelerates due to hydrodynamic effects since no discharge is registered.

Prior to the description of waveforms SQ and $B2$ a short note must be made considering the shape of waveforms employing sharp changes. As can be seen from Figs.10.13 and 10.15 the actual shape of the applied voltage waveform is far from the ideal shape that was defined in Figs.10.2 and 10.4. This is due to the finite slew rate of the HV amplifier (350 $V/\mu s$). Since it is shown that small differences in waveform shape can lead to large differences in actuator performance it must be stressed that good knowledge of the actual waveform shape must be established for all tests either numerical or experimental. Furthermore, amplifiers or power supplies with high slew rates must be used wherever possible since they offer larger flexibility in the waveform shapes sellection.

The respective temporal evolution of velocity and acceleration for the SQ waveform is shown in Fig.10.13. Additionally snapshots of the velocity and acceleration fields for four different instants are shown in Fig.10.14. At the beginning of the *forward stroke* a strong horizontal acceleration peak is registered (instant A) simultaneously to current peaks indicating the ignition of the positive discharge. The maximum value of the acceleration peak is twice the respective peak of the SN case although the duration of the period where the acceleration is active is half in comparison. For the remainder of the *forward stroke* the flow decelerates smoothly while no discharge is registered (instant B). At instant C the voltage is sharply reversed from negative to positive values with strong current peaks indicating the negative discharge. At the same

time a fluctuating behavior is observed in the flowfield evolution with two almost equal in value deceleration and acceleration events succeeding one another. As soon as the voltage reaches the positive plateau (1.5 π) the discharge terminates and the flow smoothly decelerates (instant D).

The overall evolution of the SQ waveform signifies some differences compared to SN. It appears that the forcing effects are compressed to the short time intervals governing the sharp voltage reversals at the beginning of both strokes. At the start of the forward stroke (0 π) strong positive force dominates the event most possibly related to movement of negative ions from the exposed electrode towards the dielectric surface. For the remainder of the *forward stroke* the lack of current peaks signifies the absence of any discharge event. At this period (0.2 - 1 π) the flow appears to decelerate smoothly due hydrodynamic stresses and pressure. At the beginning of the *backward stroke* (pi) the fluctuating behavior of the flow signifies a negative force component which is immediately succeeded with a positive force component. The two components appear to be of similar strength since the acceleration which they produce is of the same order of magnitude. A speculation on the origin of these components can be made. The initial negative component can be attributed to the dominance of accumulated negative species

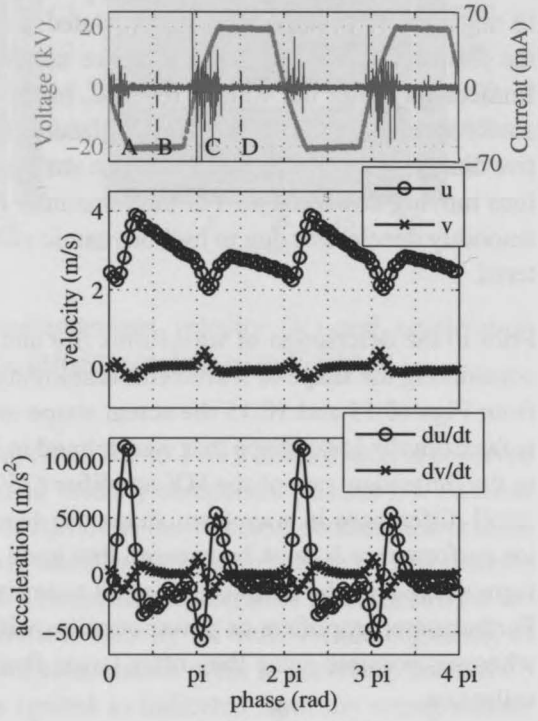

Figure 10.13: Evolution of the velocity and acceleration within the HV period for the SQ waveform (values probed at $x = 5\ mm$, $y = 0.4\ mm$).

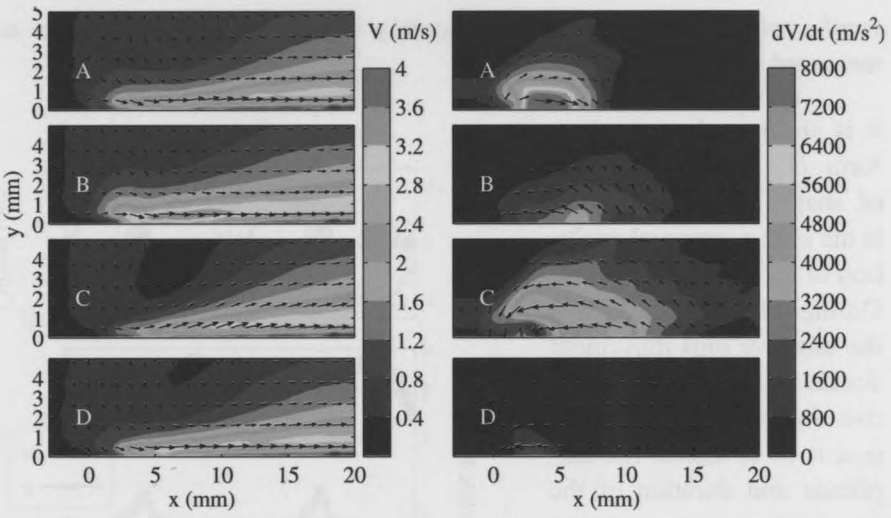

Figure 10.14: Snapshots of instantaneous velocity (V) and acceleration (dV/dt) for waveform SQ (time instants are defined in Fig.10.13).

which begin to move upstream at π. As the negative discharge progresses, positive ions which move downstream begin to dominate hence providing the positive force component. Again, the *backward stroke* forcing events appear to be restricted only to the short time interval it takes for the voltage to reverse from negative to positive. During the remainder of the stroke the flow smoothly decelerates due to hydrodynamic effects while no discharge is registered.

The temporal evolution of velocity and acceleration for the $B2$ waveform is shown in Fig.10.15. Additionally snapshots of the velocity and acceleration fields for four different instants are shown in Fig.10.16. At the beginning of the *forward stroke* (instant B) the positive discharge is initiated as indicated by the current peaks. at the same time the flowfield is accelerated downstream. The velocity reaches the maximum at 0.5 π where the discharge stops. During the remainder of the *forward stroke* no discharge is registered while the flow decelerates moderately (instant B). At the beginning of the *backward stroke* (π) similar fluctuating behavior as with waveform SQ is observed with a sharp deceleration (instant C) and sharp acceleration (instant D) event succeeding one another during the sharp voltage reversal. at the same time strong current peaks indicate the negative discharge. For the remainder of the *back-*

ward stroke the flow decelerates smoothly while no discharge currents are measured.

It is apparent that as waveform $B2$ is a combination of shapes SN and SQ so is the spatio-temporal evolution of its induced flowfield. During the *forward stroke* the negative ions movement dominates as strong positive force components appear to be in effect. The amplitude and duration of the acceleration is very similar to the respective SN waveform as would be expected. In the same way the *backward stroke* is dominated by the succeeding negative and positive forcing components associated with the square waveform. Again the amplitude and duration of the respective acceleration is very similar to the SQ waveform case.

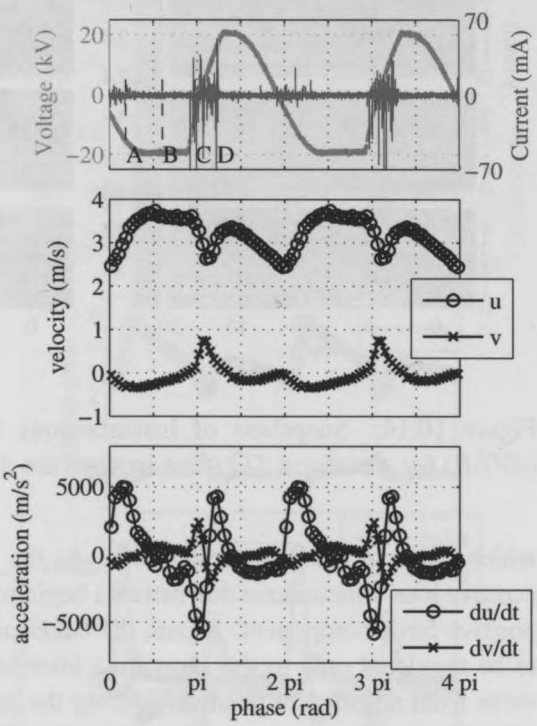

Figure 10.15: Evolution of the velocity and acceleration within the HV period for the $B2$ waveform (values probed at $x = 5\ mm$, $y = 0.4\ mm$).

Gathering observations on all three tested waveforms a conceptual model can be attempted on the superiority of shapes SQ and $B2$ over SN in terms of thrust production as well as the relative efficiency gain which $B2$ attains over the other two shapes. It is apparent that the initial parts of both *forward* and *backward* strokes are defining the forcing behavior.

The thrust production is a function of two discreet events. Firstly, during the *forward stroke* a pure push event is occurring for all three waveforms. This can be attributed to the dominance of negatively charged species which move

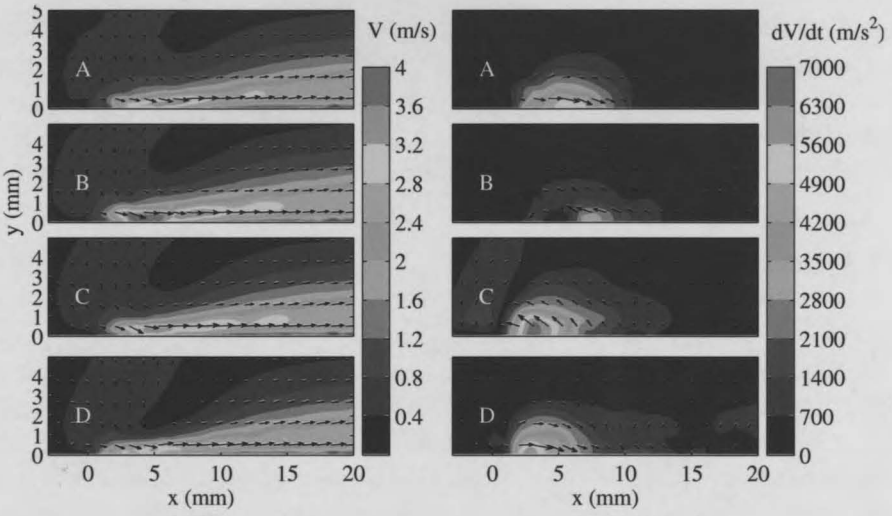

Figure 10.16: Snapshots of instantaneous velocity (V) and acceleration (dV/dt) for waveform $B2$ (time instants are defined in Fig.10.15).

from the exposed electrode towards the dielectric. The difference between the waveforms lies in the amplitude and the duration of the force as is suggested by the acceleration evolution. SN and $B2$ waveforms produce weaker but more spread in time force components compared to SQ. In any case, both the sine and square shape appear to couple positive momentum values of the same order during the *forward stroke*. Secondly, at the beginning of the *backward stroke* both a pull and a push event are occuring in the case of waveforms SQ and $B2$. These events are short in time and of the same order of magnitude. On the other hand, the SN waveform appears to have a pronounced pull event which even starts from within the *forward stroke*. By comparison the deceleration occurring at π in both SQ and $B2$ is much shorter in time than in SN. Therefore, it is exactly this negative forcing, which appears to be suppressed by the sharp voltage rise of shapes SQ and $B2$, which makes waveform SN weaker compared to the other two shapes.

The waveform shape is also the main factor behind the consumed power differences observed between the three waveforms during the thrust parametric study. The discharge can be divided in two regimes depending on the polarity of the voltage at the exposed electrode[14, 32]. During the *forward stroke* the exposed electrode is negative and gives electrons towards the dielectric sur-

face. Since the electrode is a finite source of electrons, the latter are given in a multitude of small microdischarges. This can be named the *glow regime*. On the other hand, at the *backward stroke* the exposed electrode is positive and draws electrons from the dielectric surface. Since the dielectric is a finite source of electrons the latter come in fewer and larger microdischarges (streamers). This is called the *streamer regime*.

The intensity of the *glow regime* is defined by the amplitude and temporal gradient of the applied voltage. On the other hand the *streamer regime* is more insensitive to the voltage variation due to its filamentary nature. The effect of temporal gradient of the voltage seems to be the one of the driving factors behind power consumption of different waveforms. SN and $B2$ waveforms employ a smooth shape change during the *forward stroke*. This in turn reduces the temporal gradient of the applied voltage which consequently reduces the intensity of the *glow regime*. This is clearly visible in the current peaks in Figs.10.11 and 10.15. In comparison waveform SQ appears to produce much larger current peaks (Fig.10.13) which seem to be responsible for the increased power consumption of this waveform. A second factor influencing the power consumption is the instantaneous values of the applied voltage which are generally higher than the other two forms due to the morphology of the shape itself.

10.3 Conclusions

Shape variations of the High Voltage waveform which drives plasma actuators appear to have significant impact on the produced body force and consumed power. It is shown that the time gradient of the voltage plays a significant role. Waveforms which have steep voltage drop (square shape) during the initial stages of the *forward stroke* produce significantly less thrust than waveforms which employ a smooth voltage change (sinusoidal shape). On the other hand, waveforms which have a steep voltage rise at the start of the *backward stroke* have increased thrust compared to the smooth sinusoidal rise.

The shape of the applied voltage signal has been found to affect consumed electrical power as well. It is shown that steep voltage changes cause larger current peaks which reflect the underlying discharge regimes. During the *forward stroke*, a microdischarge regime appears with consecutive electron avalanches active due to electron emission from the exposed electrode (*glow*

regime). These are shown in the form of multiple and weak current peaks and seem to increase with the steepness of voltage. During the *backward stroke*, large and fewer current peaks appear since electrons are traveling from the dielectric surface to the exposed electrode (*streamer regime*). Again, smoother voltage changes seem to decrease the number and intensity of these peaks.

It is found from the parametric study that one of the best performing waveforms is $B2$. This is a waveform which consists out of a sinusoidal voltage drop at the start of the *forward stroke* and a steep voltage rise at the start of the *backward stroke*. The produced thrust for waveform $B2$ is approximately 30 % more than the conventionally used sinusoidal shape. Additionally, power consumption is in the same order as with the sine waveform due to the smooth voltage drop during the *glow regime*. Further analysis has been conducted on the forcing mechanism of waveform $B2$. This is based on the spatio-temporal resolution of the induced flowfield using time resolved PIV measurements in conjunction with a phase shift technique (Chapter 6). It is found that for the asymmetric waveform $B2$ as well as for the reference cases of sinusoidal and square shapes, push and pull events are present in the actuation period. Furthermore, it is clear that during the voltage drop, positive forces develop in the plasma region, while both positive and negative force succeed one another during the voltage rise. All three waveforms appear to couple positive momentum to the fluif of the same order of magnitude during the *forward stroke*. What differentiates the different waveforms in term of net effect is the relation between the push and the pull event during the *backward stroke*. More specifically, the sinusoidal waveform presents a more spread in time pull event compared to the other waveforms. This is a major source of inefficiency in the net momentum transfer. On the other hand waveforms SQ and $B2$ has a similar in strength push event but significantly weaker pull event comared to SN.

In general, careful manipulation of the shape of the waveform could be a promising tool for improving the performance and efficiency of plasma actuators. The range of tested waveforms in this study is limited to fundamental shapes and a more expanded waveform collection could provide with better results. Nevertheless, using asymmetric waveform $B2$ an improvement in induced velocity of nearly 40 % compared to the conventional sinusoidal shape is achieved. Since the consumed power is only marginally increased, relative thrust efficiency is also increased by almost 25%.

Epilogue

Κουφός ο Σάλαχ το κατάστρωμα σαρώνει.
-Μ' ένα ξυστρί καθάρισέ με απ' τη μοράβια.
Μα είναι κάτι πιο βαθύ που με λερώνει.
-Γιε μου, που πας; -Μάνα, θα πάω με τα καράβια.

Κι έτσι μαζί με τους εφτά κατηφοράμε.
Με τη βροχή, με τον καιρό που μας ορίζει.
Τα μάτια σου ζούνε μια θάλασσα, θυμάμαι...
Ο πιο στερνός μ' ένα αυλό με νανουρίζει.

Νίκος Καββαδίας, Οι εφτά νάνοι στο SS-Κερύνεια

Salah, deaf, wipes the deck.
-Clean the paint off me with a scraper.
But there's something deeper, staining me.
-Son, where are you going? -Mother, I'll sail off.

And so, together with the seven we go.
Along the rain, the weather, which govern us.
Your eyes live a sea, I remember...
With a flute, the last one is lulling me.

Nikos Kavadias, *The seven dwarfs aboard the SS-Kerynia*

Chapter 11

Conclusions and Recommendations

The work in the present thesis has been conducted towards obtaining new insights into the operation of Dielectric Barrier Discharge actuators intended for flow control. A multi-dimensioned effort has been carried out towards advanced *Diagnostics*, *Modeling* and *Application* of DBD actuators. Experimental as well as numerical methods have been employed to attack the problems and objectives specified in Chapter 1. This final chapter aims at presenting a summary of the major conclusions this work has arrived at. Additionally, based on the findings, a list of recommendations for possible pathways towards future research in the area of DBD flow control is compiled.

11.1 Conclusions

The first major part of the research presented in this thesis is concerned with diagnostics on the DBD actuator operation. Several parameters and metrics of performance have been investigated with a multitude of experimental techniques. These include the induced flowfield resulting from the DBD actuation, integrated thrust values, power consumption and mechanical efficiency. Major conclusions from the *Diagnostics* part are:

The conventional configuration of the DBD actuator (as investigated here) has been shown to induce a wall-jet-like flowfield. The intensity, shape and general topology of this flowfield are subject to a large selection of control parameters including geometrical, electrical and material variables. Additionally to the globally induced flowfield a secondary phenomenon has been observed in an area at the vicinity of the actuator corresponding to the ionization region. Strong deterministic velocity fluctuations at the primary carrier frequency are registered, indicating the underlying momentum transfer processes within one HV cycle.

The actuators have been investigated in both continuous and pulse operation. While in continuous operation the induced flowfield is relatively steady, in pulse operation a different topology is observed. The actuator has demonstrated the ability for inducing large coherent structures under pulse operation. In the specific case of no external flow conditions these structures correspond to convecting and periodic vortices. Strong relation exists between the pulsation parameters (pulse frequency and duty cycle) and the morphology of the induced unsteady flowfield.

The study of the pulse operation reveals the inherent favorable features of DBD actuators as flow control devices. The operation is performed in electrical rather than mechanical time-scale, the flow responds extremely fast to the input signal while power consumption is relatively low. Furthermore, the actuator is mechanically robust with no moving parts, ease of construction and virtually no additional roughness imposed on the aerodynamic surface.

The pulse operation has been investigated in the case of an imposed external flowfield and more specifically a laminar boundary layer. The ability of the actuator to perturb the flow in an unsteady manner has been demonstrated. Additionally an operating envelope for this kind of application is devised. More specifically, limits of operating parameters such as pulse frequency and duty cycle have been identified within which the control authority of the actuator is maximized.

The previously mentioned secondary fluctuations effect has been further investigated. Employing an experimental technique to resolve the spatio-temporal evolution of the fluctuation region, aspects of the underlying forcing mechanisms have been revealed. It is established that the forcing of the plasma region is unsteady and periodic within the alternating HV cycle. Additionally, an asymmetry in forcing intensity exists between the two halves of the HV

AC cycle. It is concluded that the forcing is strongly dependent on the shape of the HV waveform. For the conventionally used sinusoidal waveform the forcing is directed from the exposed electrode towards the covered electrode in both half cycles while the first half cycle (exposed electrode is negative) is considerably stronger.

The second part of this work involves an integrated effort towards an accurate and efficient model for the operation of the actuator. This is achieved with the formulation, implementation and evaluation of a new experimental technique for the measurement of the plasma exerted body force field. Additionally a validation effort for the developed model is attempted. Major conclusions from the *Modeling* part are:

The exerted body force field can be used as an efficient and convenient way of modeling DBD actuation. In this study body force fields have been measured using time-resolved PIV and NS term decomposition techniques. It is demonstrated that the obtained results are in agreement with well-established benchmark measurements. The developed techniques are capable of capturing the value as well as the spatial distribution of the plasma body force for a variety of electrical and geometrical properties of the actuator.

Body force fields have been measured for eight different cases employing the same actuator with varying applied voltage and carrier frequency values. These force fields have been implemented in a numerical flow solver in an effort to validate the force measurement technique. The original measured velocity fields are reproduced within the error margins involved in the technique's assumptions. Additionally, it is shown that the force fields can accurately model the DBD actuators in cases of pulse operation as well.

One of the major assumption of the force measurement technique is the considering of a quasi-steady character for the force field. The latter has been shown to strongly fluctuate within the HV cycle in the *Diagnostics* part. Based on the large time-scale separation between the electrostatic force fluctuation and the external flowfield, the force is assumed steady within the HV cycle. This assumption carries on to the developed DBD force model. As such the model is to be used with caution, especially in applications involving DBD carrier frequencies lying close to natural flow receptivity areas.

The third and last part of this work involves the application of the gained knowledge on practical cases of DBD operation. This is demonstrated on two

concepts, involving a flow control scenario and a performance improvement study respectively. The flow control concept is based on a numerical investigation of TS wave cancellation using DBD actuators while the second concept aims at maximizing the performance of the DBD actuator using asymmetric HV waveforms. Major conclusions of the *Application* part are:

The actuators are used in pulse mode in order to damp convecting TS instabilities within a laminar boundary layer. The DBD operation is controlled autonomously using an automatic control system with adaptive capabilities. The system appears capable of tackling single-frequency and multi-frequency modes in a range of freestream frequencies. The used FXLMS system demonstrates positive behavior, strengthening its potential for practical application in such concept.

The derived DBD models from the Modeling part have been used to simulate the actuators in the TS control case. The actuators demonstrate strong capabilities of efficient and accurate control, even in scenarios of strongly amplified TS modes. Furthermore, intrinsic behavior of the plasma force field as a function of applied voltage appears not to pose serious problems for the operation of the FXLM algorithm.

The second application concept is a parametric study aiming at the improvement of the performance of the DBD. This is attempted based on observations made during the *Diagnostics* part regarding the effect of the HV waveform on the forcing mechanisms. More specifically, a range of asymmetric waveforms has been tested using thrust and power measurements. It has been found that a waveform made of a specific combination of sine and square shapes results in a better thrust-to-power ration than comparable symmetric shapes.

Using the time-resolved PIV diagnostics from the Diagnostics part, the mechanism for performance improvement using asymmetric waveforms has been revealed. More specifically, waveforms employing a sharp voltage rise from the negative half-cycle to the positive half-cycle minimize and mitigate the negative forcing component which is present during this period. A strong phenomenological effect exists also during the voltage drop although the shape influence on the averaged forcing during this period is minimal.

11.2 Recommendations

This thesis has been occupied with several aspects of DBD actuation both from a fundamental as well as application point of view. Several findings and conclusions have been obtained. Nevertheless, this is a finite work and as such several interesting points remain untouched giving room for potential future research. A brief list of recommendations for possible directions of future research on DBDs is given here.

The PIV measurement technique has been thoroughly used in the present study. It has been proven invaluable for the achievement of some objectives and indispensable in the fundamental understanding of DBDs. The technique involves a complicated setup, which increases resource and time consumption. On the other hand, once experience has been built, the effort becomes minimal. Using PIV systems with time-resolving capabilities, a diagnostic tool of great value instantly becomes available in the field of DBD actuator research. It is therefore essential to further use and verify this technique in the field. Especially issues of electromagnetic interference, seeding particles charging and frequency response should be rigorously identified and evaluated. Given enough confidence in the system, the last grey areas remaining in the diagnostics of DBD operation could be solved.

Successful active flow control is based on local flow instabilities manipulation rather than global flow effects [119]. This is especially important when efficiency is a priority. A mitigating factor is the usually low energy content of local flow instabilities, especially in instability manipulation concepts. This is an area where the DBD actuator excels. This is partly circumstantial since the DBD actuator has an inherently low momentum transfer capability. On the other hand the excellent frequency response, mechanical robustness and low power consumption of the actuator render it ideal for these concepts. Further investigation in the pulse mode operation of the DBD actuator is essential in order to fully map the behavior of this device. This is a necessary condition prior to any successful flow control application.

The forcing mechanisms and behavior of DBD actuators within the HV cycle has been one of the most debated and controversial issues in published literature [32]. Although many questions have been clarified, some issues remain ambiguous. The effects of carrier frequency, voltage amplitude, geometric configuration and material properties should be carefully established.

It is essential that this is an integrated and complementary effort using both numerical and experimental tools.

The search for an efficient and accurate model for the DBD operation has occupied a significant portion of the published research [61]. Several models have been proposed ranging from low-order simple phenomenological approaches to high-order computationally intensive concepts. A new approach is proposed in this thesis based on experimental observations. The approach should be further developed in various directions. Firstly, the method can be used to built a database of force models for a variety of test cases, mapping parameters such as geometry, materials and electrical properties. Such a database can serve as the basis for a reduced order modeling approach as well as a benchmark validation dataset for numerical plasma force models. Secondly, the existing method can be improved by taking into account the electrostatic velocity fluctuations in the vicinity of the actuator. This can be done explicitly by modifying the technique or implicitly by the use of correction factors.

The first application concept investigated in the present work is involved with active cancellation of TS waves. Although a first proof of the capability of the DBD actuator in such concept is demonstrated, several points remain unclear. Firstly, this approach must be studied in the case of an external, adverse pressure gradient which is typically the flow condition over airfoils. Secondly, three dimensional cases must be investigated again simulating conditions over true aircraft wings. Last and most important is the implementation of such concept in an experimental framework in order to truly validate the capabilities of DBD actuators in active transition delay.

The second application concept involves the improvement of performance of the actuator using asymmetric waveforms. This is an interesting topic which potentially could lead to significant step changes in the ability of the DBD to provide significant forcing. The present study was only an initial exploratory study using combinations of only two basic waveform shapes. More generic combinations must be investigated in order to find a truly optimum shape in terms of forcing and power consumption.

Bibliography

[1] *Open FOAM developer's guide.*

[2] *Open FOAM user's guide.*

[3] T. Abe, Y. Takizawa, S. Sato, and N. Kimura. Experimental study for momentum transfer in a dielectric barrier discharge plasma actuator. *AIAA Journal*, 46(9):2248–2256, 2008.

[4] C. Airiau, A. Bottaro, S. Walther, and D. Legendre. A methodology for optimal laminar flow control: Application to the damping of tollmien-schlichting waves in a boundary layer. *Physics of Fluids*, 15(5):1131–1145, 2003.

[5] Jung W. Akhavan, R. and N. Mangiavacchi. Control of wall turbulence by high frequency spanwise oscillations. *AIAA paper*, 93-3282, 1993.

[6] T. Albrecht, R. Grundmann, G. Mutschke, and G. Gerbeth. On the stability of the boundary layer subject to a wall-parallel lorentz force. *Physics of Fluids*, 18(9), 2006.

[7] J.D. Anderson. *Fundamentals of Aerodynamics*. McGraw-Hill, 2005.

[8] D. Arnal and C. Bulgubure. Drag reduction by boundary layer laminarization. *La Recherche Aerospatiale*, 3:157–165, 1996.

[9] G. Artana, L. Leger, E. Moreau, and G. Touchard. Flow control with electrohydrodynamic actuators. *AIAA Journal*, 40(9):1773–1778, 2002.

[10] M. Bajura, R. ad Catalano. Transition in a two-dimensional plane wall jet. *J. Fluid Mechanics*, 70:773–799, 1975.

[11] N. Balcon, N. Benard, Y. Lagmich, J. . Boeuf, G. Touchard, and E. Moreau. Positive and negative sawtooth signals applied to a dbd plasma actuator - influence on the electric wind. *Journal of Electrostatics*, 67(2-3):140–145, 2009.

[12] N. Balcon, N. Benard, and E. Moreau. Formation process of the electric wind produced by a plasma actuator. *IEEE Transactions on Dielectrics and Electrical Insulation*, 16(2):463–469, 2009.

[13] R. W. Barnwell and M. Hussaini. *Natural Laminar Flow and Laminar Flow Control*. 1992.

[14] N. Benard, A. Mizuno, and E. Moreau. A large-scale multiple dielectric barrier discharge actuator based on an innovative three-electrode design. *Journal of Physics D: Applied Physics*, 42(23), 2009.

[15] N. Benard and E. Moreau. Capabilities of the dielectric barrier discharge plasma actuator for multi-frequency excitations. *Journal of Physics D: Applied Physics*, 43(14), 2010.

[16] J. P. Boeuf, Y. Lagmich, Th Callegari, and L. C. Pitchford. Ehd force in dielectric barrier discharges parametric study and influence of negative ions. In *45th AIAA Aerospace Sciences Meeting and Exhibit*, volume 4, pages 2170–2180, 2007.

[17] J. P. Boeuf, Y. Lagmich, and L. C. Pitchford. Contribution of positive and negative ions to the electrohydrodynamic force in a dielectric barrier discharge plasma actuator operating in air. *Journal of Applied Physics*, 106(2), 2009.

[18] J. P. Boeuf and L. C. Pitchford. Electrohydrodynamic force and aerodynamic flow acceleration in surface dielectric barrier discharge. *Journal of Applied Physics*, 97(10), 2005.

[19] P. Boon. Plasma actuators for active transition delay. Master's thesis, TU Delft, 2009.

[20] V. Boucinha, P. Magnier, R. Weber, A. Leroy-Chesneau, B. Dong, and D. Hong. Characterization of the ionic wind induced by a sine dbd actu-

ator used for laminar-to-turbulent transition delay. In *4th Flow Control Conference*, number AIAA-2008-4210, 2008.

[21] W. W. Bower, J. T. Kegelman, A. Pal, and G. H. Meyer. A numerical study of two-dimensional instability-wave control based on the orr–sommerfeld equation. *Physics of Fluids*, 30(4):998–1004, 1987.

[22] J. Bridges and P. J. Morris. Differential eigenvalue problems in which the parameter appears nonlinearly. *J. Comput. Phys.*, 437:222–224, 1984.

[23] A. M. H. Brooker, J. C. Patterson, and S. W. Armfield. Non-parallel linear stability analysis of the vertical boundary layer in a differentially heated cavity. *Journal of Fluid Mechanics*, 352:265–281, 1997.

[24] D M Bushnell. Aircraft drag reduction - a review. *J. Aerospace Engineering*, 217, 2003.

[25] D. M. Bushnell, M. Malik, and W. D. Harvey. Transition prediction in external flows via linear stability theory. *In Symposium Transsonicum 3*, pages 225–242, 1989.

[26] D. M. Bushnell and M. H. Tuttle. Survey and bibliography on attainment of laminar flow control in air using pressure gradient and suction. *NASA RP-1035*, 1979.

[27] H. Choi, P. Moin, and J. Kim. Active turbulence control for drag reduction in wall-bounded flows. *J. Fluid Mechanics*, 262:75–110, 1994.

[28] P.G. Ciarlet and J.L. Lions. *Handbook of Numerical Analysis*. Elsevier, 2002.

[29] F. S. Collier Jr. An overview of recent subsonic laminar flow control flight experiments. *AIAA paper*, 93-2987, 1993.

[30] G. Comte-Bellot. Hot-wire anemometry. *Annu. Rev. Fluid Mech.*, 8, 1976.

[31] L. Cordier and M. Bergmann. Proper orthogonal decomposition: an overview. *ENSEM -2*, 2000.

[32] T. C. Corke, C. L. Enloe, and S. P. Wilkinson. Dielectric barrier discharge plasma actuators for flow control. *Annual Review of Fluid Mechanics*, 42:505–529, 2010.

[33] T. C. Corke, M. L. Post, and D. M. Orlov. Single dielectric barrier discharge plasma enhanced aerodynamics: physics, modeling and applications. *Experiments in Fluids*, pages 1–26, 2008. Article in Press.

[34] J. Cousteix, D. Arnal, and E. Coustols. Reduction of aerodynamic skin friction drag. *Nouvelle Revue d'Aeronautique et d'Astronautique*, 1:23–31, 1993.

[35] B. Dong, J. M. Bauchire, J. M. Pouvesle, P. Magnier, and D. Hong. Experimental study of a dbd surface discharge for the active control of subsonic airflow. *Journal of Physics D: Applied Physics*, 41(15), 2008.

[36] B. Eliasson and U. Kogelschatz. Nonequilibrium volume plasma chemical processing. *Plasma Sci.*, 19:1063-77, 1991.

[37] C. L. Enloe, M. G. McHarg, and T. E. McLaughlin. Time-correlated force production measurements of the dielectric barrier discharge plasma aerodynamic actuator. *Journal of Applied Physics*, 103(7), 2008.

[38] C. L. Enloe, T. E. McLaughlin, R. D. VanDyken, K. D. Kachner, E. J. Jumper, and T. C. Corke. Mechanisms and responses of a single dielectric barrier plasma actuator: Plasma morphology. *AIAA Journal*, 42(3):589–594, 2004.

[39] C.L. Enloe, T.E. McLaughlin, R.D. VanDyken, K.D. Kachner, E.J. Jumper, T.C. Corke, M. Post, and O. Haddad. Mechanisms and responses of a single dielectric barrier plasma actuator: geometric effect. *AIAA Journal*, 42:595–604, 2004.

[40] G. I. Font, C. L. Enloe, and T. E. McLaughlin. Plasma volumetric effects on the force production of a plasma actuator. *AIAA Journal*, 48(9):1869–1874, 2010.

[41] G. I. Font and W. L. Morgan. Recent progress in dielectric barrier discharges for aerodynamic flow control. *Contributions to Plasma Physics*, 47(1-2):103–110, 2007.

[42] M. Forte, J. Jolibois, J. Pons, E. Moreau, G. Touchard, and M. Cazalens. Optimization of a dielectric barrier discharge actuator by stationary and non-stationary measurements of the induced flow velocity:

Application to airflow control. *Experiments in Fluids*, 43(6):917–928, 2007.

[43] M. Forte, L. Leger, J. Pons, E. Moreau, and G. Touchard. Plasma actuators for airflow control: measurement of the non-stationary induced flow velocity. *Journal of Electrostatics*, 63(6-10):929 – 936, 2005. 10th International Conference on Electrostatics.

[44] M. Gad el Hak, A. Pollard, and J. P. Bonnet. *Flow Control: Fundamentals and Practices*. 1998.

[45] R. Giepman. On transition delay with plasma actuators. piv diagnostics, reduced order modeling and adaptive control. Master's thesis, TU Delft, 2011.

[46] M.B. Glauert. The wall jet. *J. Fluid Mechanics*, 1:625–643, 1956.

[47] A. Glezer, M. Amitay, and A. M. Honohan. Aspects of low- and high-frequency actuation for aerodynamic flow control. *AIAA Journal*, 43(7):1501–1511, 2005.

[48] M. E. Goldstein. Evolution of tollmien-schlichting waves near a leading edge. *Journal of Fluid Mechanics*, 127:59–81, 1983.

[49] S. Grundmann and C. Tropea. Experimental transition delay using glow-discharge plasma actuators. *Experiments in Fluids*, 42(4):653–657, 2007.

[50] S. Grundmann and C. Tropea. Active cancellation of artificially introduced tollmien-schlichting waves using plasma actuators. *Experiments in Fluids*, 44(5):795–806, 2008.

[51] S. Grundmann and C. Tropea. Experimental damping of boundary-layer oscillations using dbd plasma actuators. *International Journal of Heat and Fluid Flow*, 30(3):394–402, 2009.

[52] C.H. Hansen. *Understanding Active Noise Cancellation*. Spon Press, 2001.

[53] R Henke. The airbus a320 hlf fin programme. *Nouvelle Revue d'Aeronautique et d'Astronautique*, 2:53–55, 1998.

[54] A.T. Hjemfelt and L.F. Mockros. Motion of discrete particles in a turbulent fluid. *Appl. Sci. Res.*, 16 149, 1996.

[55] A. R. Hoskinson, Hershkowitz, and D. E. Ashpis. Force measurements of single and double barrier dbd plasma actuators in quiescent air. *Journal of Physics D: Applied Physics*, 41(24), 2008.

[56] F.B. Hsiao and S.S. Sheu. Double-row vortical structures in the near-field region of a plane wall jet. *Experiments in Fluids*, 17:291–301, 1994.

[57] J. L. van Ingen. A suggested semi-empirical method for the calculation of the boundary layer transition region. In *Report VTH-74 TU Delft*, 1956.

[58] J.L. van Ingen. The en method for transition prediction. historical review of work at tu delft. In *38th AIAA Fluid Dynamics Conference and Exhibit*, 2008.

[59] R. I. Issa. Solution of the implicitly discretized fluid flow equation by operator splitting. *J. Comput. Phys.*, 62:40–65, 1986.

[60] B. Jayaraman, Y. . Cho, and W. Shyy. Modeling of dielectric barrier discharge plasma actuator. In *38th AIAA Plasmadynamics and Lasers Conference*, volume 2, pages 1019–1038, 2007.

[61] B. Jayaraman and W. Shyy. Modeling of dielectric barrier discharge-induced fluid dynamics and heat transfer. *Progress in Aerospace Sciences*, 44(3):139–191, 2008.

[62] B. Jayaraman, S. Thakur, and W. Shyy. Modeling of fluid dynamics and heat transfer induced by dielectric barrier plasma actuator. *Journal of Heat Transfer*, 129(4):517–525, 2007.

[63] R. D. Joslin, G. Erlebacher, and M. Y. Hussaini. Active control of instabilities in laminar boundary layers - overview and concept validation. *Journal of Fluids Engineering, Transactions of the ASME*, 118(3):494–497, 1996.

[64] T. N. Jukes and K. . Choi. Flow control around a circular cylinder using pulsed dielectric barrier discharge surface plasma. *Physics of Fluids*, 21(8), 2009.

[65] T. N. Jukes, K. . Choi, T. Segawa, and H. Yoshida. Jet flow induced by a surface plasma actuator. *Proceedings of the Institution of Me-*

chanical Engineers.Part I: Journal of Systems and Control Engineering, 222(5):347–356, 2008.

[66] T. N. Jukes, K. Choi, G. A. Johnson, and S. J. Scott. Turbulent drag reduction by surface plasma through spanwise flow oscillation. In *3rd AIAA Flow Control Conference*, volume 3, pages 1687–1700, 2006.

[67] W. J. Jung, N. Mangiavacchi, and R. Akhavan. Suppression of turbulence in wall bounded flows by high frequency spanwise oscillations. *Physics of Fluids*, 4(8):1605–1607, 1992.

[68] S. Kanazawa, M. Kogoma, T. Moriwaki, and SJ. Okazaki. Stable glow plasma at atmospheric pressure. *Journal of Physics D: Applied Physics*, 21:838-40, 1988.

[69] S. Kanazawa, M. Kogoma, T. Moriwaki, and SJ. Okazaki. The improvement of atmospheric pressure glow plasma method and the deposition of organic films. *Journal of Physics D: Applied Physics*, 23:374-77, 1990.

[70] S. Kanazawa, M. Kogoma, SJ. Okazaki, and T. Moriwaki. Glow plasma treatment at atmospheric pressure for surface modification and film deposition. *Nucl. Inst. Methods Phys. Res. B*, 37:842-45, 1989.

[71] W. Kim, H. Do, M. G. Mungal, and M. A. Cappelli. On the role of oxygen in dielectric barrier discharge actuation of aerodynamic flows. *Applied Physics Letters*, 91(18), 2007.

[72] U. Kogelschatz. Filamentary, patterned and diffuse barrier discharges. *IEEE Trans. Plasma Sci.*, 30:1400-8, 2002.

[73] U. Kogelschatz, B. Eliasson, and W. Egli. Dielectric-barrier discharges: principles and applications. *J. Phys. IV (France)*, 7:C4-47-66, 1997.

[74] M. Kogoma and SJ. Okazaki. Raising of ozone formation efficiency in a homogeneous glow discharge plasma at atmospheric pressure. *Journal of Physics D: Applied Physics*, 27:1985-87, 1994.

[75] J. Kostas, J. Soria, and M.S. Chong. A comparison between snapshot pod analysis of piv velocity and vorticity data. *Experiments in Fluids, 3rd IAHR International meeting*, 38, 2005.

[76] M. Kotsonis, S. Ghaemi, L. Veldhuis, and F. Scarano. Measurement of the body force field of plasma actuators. *Journal of Physics D: Applied Physics*, 44(4), 2011.

[77] L. D. Kral and H. F. Fasel. Numerical investigation of three-dimensional active control of boundary-layer transition. *AIAA journal*, 29(9):1407–1417, 1991.

[78] E. Kunhardt. Electrical breakdown of gases: the pre-breakdown stage. *IEEE Trans. Plasma Sci.*, 8:130-38, 1980.

[79] EE. Kunhardt and L. Luessen. *Electrical Breakdown and Discharges*. New York: Plenum, 1981.

[80] S.M. Kuo and D.R. Moran. *Active noise control systems*. John Wiley, New York., 1996.

[81] F. Laadhari, L. Skandaji, and R. Morel. Turbulence reduction in a boundary layer by a local spanwise oscillating surface. *Physics of Fluids*, 6(10):3218–3220, 1994.

[82] Y. Lagmich, Th Callegari, L. C. Pitchford, and J. P. Boeuf. Model description of surface dielectric barrier discharges for flow control. *Journal of Physics D: Applied Physics*, 41(9), 2008.

[83] L.D. Landau and E.M. Lifshitz. *Electrodynamics of Continuous Media*. Oxford: Pergamon, 1984.

[84] I Langmuir. Oscillations in ionized gases. *Proc. Natl. Acad. Sci.*, 14:627-37, 1928.

[85] A. V. Likhanskii, M. N. Shneider, S. O. MacHeret, and R. B. Miles. Modeling of dielectric barrier discharge plasma actuator in air. *Journal of Applied Physics*, 103(5), 2008.

[86] A. V. Likhanskii, M. N. Shneider, D. F. Opaits, R. B. Miles, and S. O. Macheret. Numerical modeling of dbd plasma actuators and the induced air flow. In *38th AIAA Plasmadynamics and Lasers Conference*, volume 2, pages 1060–1072, 2007.

[87] J. Little, M. Nishihara, I. Adamovich, and M. Samimy. High-lift airfoil trailing edge separation control using a single dielectric barrier discharge plasma actuator. *Experiments in Fluids*, 48(3):521–537, 2010.

[88] F. Llewellyn-Jones. *The Glow Discharge and an Introduction to Plasma Physics*. New York: Methuen, 1966.

[89] D. V. Maddalon, D. W. Bartlett, and F. S. Collier Jr. Fifty years of laminar flow flight testing. *SAE paper*, 88-1393, 1988.

[90] D. V. Maddalon and A. L. Braslow. Simulated airline service fight tests of laminar flow control with perforated surface suction system. *NASA TP-2966*, 1990.

[91] F. Massines, A. Rabehi, P. Decomps, R. B. Gadri, P. Sigur, and C. Mayoux. Experimental and theoretical study of a glow discharge at atmospheric pressure controlled by dielectric barrier. *Journal of Applied Physics*, 83(6):2950–2957, 1998.

[92] A. Melling. Seeding gas flows for laser anemometry. *Proceedings on the Conference of Advanced Instrumentation for Aero Engine Components*, AGARD CP-399, 8.1, 1986.

[93] A. Melling. Tracer particles and seeding for particle image velocimetry. *Me*, 8:1406–1416, 1997.

[94] E. Moreau. Airflow control by non-thermal plasma actuators. *Journal of Physics D: Applied Physics*, 40(3):605–636, 2007.

[95] M.E. Mortenson. *Geometric Modeling*. Wiley, 1997.

[96] Y. Murakami, I. Stilman, and E. Levich. Reducing turbulence by phase juggling. *Physics of Fluids*, 4(8):1776–1781, 1992.

[97] G. Nati. Suppression of vortex shedding from a truncated trailing edge by plasma actuation. Master's thesis, TU Delft, 2011.

[98] SJ. Okazaki, M. Kogoma, M. Uehara, and Y. Kimura. Appearance of stable glow discharge in air, argon oxygen and nitrogen at atmospheric pressure using 50 hz source. *Journal of Physics D: Applied Physics*, 26:889-92, 1993.

[99] D. F. Opaits, M. N. Shneider, R. B. Miles, A. V. Likhanskii, and S. O. MacHeret. Surface charge in dielectric barrier discharge plasma actuators. *Physics of Plasmas*, 15(7), 2008.

[100] H. Opfer. *Active cancellation of 3D Tollmien-Schlichting waves in the pressence of sound and vibrations*. PhD thesis, Gottingen University, 2002.

[101] D. M. Orlov, T. C. Corke, and M. P. Patel. Electric circuit model for the aerodynamic plasma actuator. *AIAA Paper No.2006-1206*, 2006.

[102] D.M. Orlov. *Modeling and simulation of single dielectric barrier discharge plasma actuators*. PhD thesis, University of Notre Dame, 2006.

[103] W. Pfenninger and J. W. Bacon Jr. Investigation of methods for re-establishment of a laminar boundary layer from turbulent flow. *Northrop Norair Report NOR 65-48 (BLC-161)*, 1965.

[104] J. Pons, E. Moreau, and G. Touchard. Asymmetric surface barrier discharge in air at atmospheric pressure: electric properties and induced airflow characteristics. *Journal of Physics D: Applied Physics*, 38 3635-42, 2005.

[105] C.O. Porter, J.W. Baughn, T.E. McLaughlin, C.L. Enloe, and G.I. Font. Temporal measurements on an aerodynamic plasma actuator. In *AIAA Meeting (Reno, USA, January 2006)*, 2006.

[106] M. L. Post and T. C. Corke. Separation control using plasma actuators: Dynamic stall vortex control on oscillating airfoil. *AIAA Journal*, 44(12):3125–3135, 2006.

[107] J. Priest and J. Reneaux. Recent developments in international laminar flow research programs for transport aircraft. *Onera TP P-1992-163*, 1992.

[108] M. Raffel, C. Willert, and J. Kompenhans. *Particle image velocimetry: a practical guide*. Springer-Verlag, Berlin, Germany., 2007.

[109] Y.P. Raizer. *Gas Discharge Physics*. Berlin: Springer-Verlag, 1991.

[110] J.R. Roth. Electrohydrodynamically induced airflow in a one atmosphere uniform glow discharge surface plasma. 1998.

[111] J.R. Roth. Electrohydrodynamically induced airflow in a one atmosphere uniform glow discharge surface plasma. In *25th IEEE Int. Conf. Plasma Science (Raleigh, USA)*, 1998.

[112] J.R. Roth and X. Dai. Optimization of the aerodynamic plasma actuator as an ehd electrical device. In *AIAA Meeting (Reno, USA, January 2006)*, 2006.

[113] J.R. Roth, D. M. Sherman, and S. P. Wilkinson. Electrohydrodynamic flow control with a glow-discharge surface plasma. *AIAA journal*, 38(7):1166–1172, 2000.

[114] J.R. Roth, D.M. Sherman, and S.P. Wilkinson. Boundary layer flow control with a one atmosphere uniform glow discharge surface plasma. In *AIAA meeting, Reno*, 1998.

[115] S. Roy and D. V. Gaitonde. Modeling surface discharge effects of atmospheric rf on gas flow control. pages 5815–5823, 2005.

[116] A. Santhanakrishnan and J. D. Jacob. Flow control with plasma synthetic jet actuators. *Journal of Physics D: Applied Physics*, 40(3):637–651, 2007.

[117] A. Santhanakrishnan, D. A. Reasor Jr., and R. P. LeBeau Jr. Characterization of linear plasma synthetic jet actuators in an initially quiescent medium. *Physics of Fluids*, 21(4), 2009.

[118] H. Schlichting and K. Gersten. *Boundary Layer Theory*. Springer, 2000.

[119] A. Seifert, D. Greenblatt, and I. J. Wygnanski. Active separation control: An overview of reynolds and mach numbers effects. *Aerospace Science and Technology*, 8(7):569–582, 2004.

[120] A. Seraudie, E. Aubert, N. Naude, and J. P. Cambronne. Effect of plasma actuators on a flat plate laminar boundary layer in subsonic conditions. volume 2, pages 1065–1073, 2006.

[121] W. Shyy, B. Jayaraman, and A. Andersson. Modeling of glow discharge-induced fluid dynamics. *Journal of Applied Physics*, 92(11):6434–6443, 2002.

[122] K. P. Singh and S. Roy. Physics of plasma actuator operating in atmospheric air. *Applied Physics Letters*, 92(11), 2008.

[123] L. Sirovich. Turbulence and the dynamics of coherent structures. *Appl. Math.*, XLV, 1987.

[124] V. R. Soloviev and V. M. Krivtsov. Surface barrier discharge modelling for aerodynamic applications. *Journal of Physics D: Applied Physics*, 42(12), 2009.

[125] J. G. Spangler. Effects of periodic blowing through flush transverse slots on turbulent boundary layer skin friction. *LTV Report 0-71100/6R-6*, 1966.

[126] E. Stephen, A. Campbell, J. Nygard, M. Selby, C. Hennig, and T McLaughlin. Assessment of a corner plasma actuator for flow control using periodic jets. In *29th AIAA Applied Aerodynamics Conference*, 2011.

[127] M.J.L. Voskuil M. Koren B. Straathof, M.H. Van Tooren. Aerodynamic shape prameterisation and optimisation of novel configurations. In *Proceedings of the 2008 Royal Aeronautical Society Annual Applied Aerodynamics Research Conference, London, 27-28 October*, 2008.

[128] D. Sturzebecher and W. Nitsche. Active cancellation of tollmien-schlichting instabilities on a wing using multi-channel sensor actuator systems. *International Journal of Heat and Fluid Flow*, 24(4):572–583, 2003.

[129] Y.B. Suzen and P.G. Huang. Simulation of flow separation control using plasma actuators. In *AIAA Aerosp. Sci. Meet. Exhibit, 44th, Reno, AIAA Pap. No. 2006-877*, 2006.

[130] Y.B. Suzen, P.G. Huang, J.D. Jacob, and D.E. Ashpis. Numerical simulations of plasma based flow control applications. In *AIAA Fluid Dyn. Conf. Exhibit, 35th, Toronto, AIAA Pap. No. 2005-4633*, 2005.

[131] J. Thibert, J. Reneaux, and V. Schmitt. Onera activities on drag reduction. In *17th ICAS Congress*, pages 1053–1064, 1990.

[132] A. S. W. Thomas. Active wave control of boundary layer transition. *AIAA Prog. Astronaut. Aeronaut.*, 123:179–199, 1990.

[133] Andrew S. W. Thomas. Control of boundary-layer transition using a wave-superposition principle. *Journal of Fluid Mechanics*, 137:233–250, 1983.

[134] F. O. Thomas, T. C. Corke, M. Iqbal, A. Kozlov, and D. Schatzman. Optimization of dielectric barrier discharge plasma actuators for active aerodynamic flow control. *AIAA Journal*, 47(9):2169–2178, 2009.

[135] M. R. Turner and P. W. Hammerton. Asymptotic receptivity analysis and the parabolized stability equation: A combined approach to boundary layer transition. *Journal of Fluid Mechanics*, 562:355–381, 2006.

[136] M. H. Tuttle and D. V. Maddalon. Laminar flow control (1976-1991). *NASA TM-107749*, 1993.

[137] R. Van Dyken, T. E. McLaughlin, and C. L. Enloe. Parametric investigations of a single dielectric barrier plasma actuator. pages 9503–9514, 2004.

[138] M. R. Visbal and D. V. Gaitonde. Control of vortical flows using simulated plasma actuators. volume 9, pages 6132–6155, 2006.

[139] R. D. Wagner, D. V. Maddalon, and D. F. Fisher. Laminar flow control leading edge systems in simulated airline service. *Journal of Aircraft*, 27(3):239–244, 1990.

[140] P. D. Welch. The use of fast fourier transform for the estimation of power spectra: A method based on time averaging over short, modified periodograms. *Modern Spectrum Analysis*, pages 17–20, 1978.

[141] J. Westerweel. Fundamentals of digital particle image velocimetry. *Meas. Sci. Technol.*, 8:1379–1392, 1997.

[142] J. B. Wilke. *Aerodynamic flow-control with dielectric barrier discharge plasma actuators*. PhD thesis, DLR Deutsches Zentrum fur Luft- und Raumfahrt e.V. - Forschungsberichte, 2009.

[143] S. P. Wilkinson. Interactive wall turbulence control. *AIAA Prog. Astronaut. Aeronaut.*, 123:479–509, 1990.

[144] T. Yokoyama, M. Kogoma, T. Moriwaki, and SJ. Okazaki. The mechanism of the stabilization of glow plasma at atmospheric pressure. *Journal of Physics D: Applied Physics*, 23:1125-28, 1990.

List of Publications

Journal Articles

Kotsonis, M. and Veldhuis, L. Experimental study on dielectric barrier discharge actuators operating in pulse mode. *Journal of Applied Physics*, 108, 2010.

Kotsonis, M., Ghaemi, S., Veldhuis, L. and Scarano, F. Measurement of the body force field of plasma actuators. *Journal of Physics D: Applied Physics*, 44, 2011.

Giepman, R. and Kotsonis, M. On the mechanical efficiency of dielectric barrier discharge plasma actuators. *Applied Physics Letters*, 98, 2011.

Kotsonis, M. and Ghaemi, S. Forcing Mechanisms of DBD Plasma Actuators at Carrier Frequency of 625 Hz. *Journal of Applied Physics*, 110, 2011.

Kotsonis, M, and Ghaemi, S. Performance Improvement of Plasma Actuators using Asymmetric High Voltage Waveforms. *Journal of Physics D: Applied Physics* , 45, 2012.

Book Chapters

Kotsonis, M., Veldhuis. L. and Bijl, H. Plasma Assisted Aerodynamics for Transition Delay. *Proceedings of the 7th IUTAM Symposium on Laminar-*

Turbulent Transition, 2009, Springer.

Conference Proceedings

Kotsonis, M., Boon, P. and Veldhuis, L. Plasmas for Transition Delay. In *Proc.* 10^{th} *International Conference on Fluid Control, Measurements and Visualization*, 2009, Moscow, Russia.

Kotsonis, M., Ghaemi, S., Giepman, R. and Veldhuis, L. Experimental Study on the Body Force Field of Dielectric Barrier Discharge Actuators. In *Proc.* 41^{st} *AIAA Plasmadynamics and Laser Conference*, 2010, Chicago, USA.

Kotsonis, M., Giepman, R. and Ghaemi, S. Numerical Study on Control of Tollmien-Schlichting Waves Using Plasma Actuators. In 29^{th} *AIAA Applied Aerodynamics Conference*, 2011, Honolulu, USA.

van Ingen, J. and Kotsonis, M. A two-parameter method for e^N transition prediction. In 6^{th} *AIAA Theoretical Fluid Mechanics Conference*, 2011, Honolulu, USA.

Curriculum Vitae

Marios Kotsonis was born in Nicosia, Cyprus in August 1984. He exhibited an early interest in dismantling toys and mechanisms to discover their working principles, which formed a strong basis for his future fascination with engineering. He had his school education in Cyprus until the age of 18. Afterwards, he moved to Greece where he enrolled in the Mechanical and Aerospace Engineering Department of the University of Patras in 2002. There, he attained the Diploma in Aerospace Engineering in 2007 with a graduation thesis on helicopter aerodynamics. In October 2007 he migrated to the Netherlands after being hired by the TU Delft in a PhD research position within the CleanEra project. He carried out his research in the Department of Aerodynamics under the supervision of dr. Leo Veldhuis and Prof. Fulvio Scarano. His research interests include hydrodynamic stability, flow control, DBD actuators and applied aerodynamics. He can be currently found somewhere in the dark corners of the Aerodynamics Laboratories of TU Delft, playing with extremely expensive equipment.

Appendix

Appendix

Appendix A

Reduced NS solver source code

A description is given here of the main source code file for the reduced NS solver described in Chapter 3 and implemented in Chapter 9 for the numerical investigation of TS wave cancellation using plasma actuators. This solver version contains three distinct modules:

- The reduced flow solver based on the perturbation analysis of the NS for the simulation of the propagation of 2D TS waves in a laminar boundary layer (Chapter 3)
- The implementation of the filtered-x LMS algorithm for the autonomous operation of the plasma actuator (Chapter 3)
- The representation of the plasma body force mode in the form of a function of Bernstein surface polynomials (Chapter 9). The tables containing the coefficients for the full expression of the model are given in Appendix B.

The source code is based on the existing $icoFoam$ solver in the distribution 1.7.1 of OpenFOAM. Here only a description of the added or changed parts is given. The interested reader is reffered to [2, 1] for more information on the basic $icoFoam$ solver.

- **lines 33 - 34:** `iostream` and `fstream` are native C++ headers in order to be able to export velocity and pressure values from selected cells at all time steps
- **line 48:** `createBodyForceGen.H` is a subroutine to initialize the body force field used for introducing the TS waves in the solution domain and to allocate it to the specific cells.
- **lines 51 - 61:** initialization of several variables needed for the control sequence
- **line 63:** `createBodyForcePlasmaInit.H` is a subroutine to initialize the plasma actuator force field and to allocate it to the specific cells.
- **line 67:** `controlInit.H` is a subroutine to initialize the filtered-x LMS algorithm. Here positions of reference and error sensors, length of filters, sampling and update rates and convergence constants are set.
- **lines 88-98:** Sequence to produce the body force used to introduce the TS waves in the domain (Eq.3.38).
- **line 99:** Start of the control sequence.
- **line 108:** Header `sensor.H` used to read the reference and error signals at the specific time step
- **lines 110-115:** System Identification procedure
- **lines 115-119:** Adaptive control procedure
- **line 129:** Calculation of the applied voltage value
- **lines 133-144:** Reduced NS equation (Eq.3.37)

```
/*---------------------------------------------------------------------------*\
  =========                 |
  \\      /  F ield         | OpenFOAM: The Open Source CFD Toolbox
   \\    /   O peration     |
    \\  /    A nd           | Copyright (C) 1991-2009 OpenCFD Ltd.
     \\/     M anipulation  |
-------------------------------------------------------------------------------
License
    This file is part of OpenFOAM.

    OpenFOAM is free software; you can redistribute it and/or modify it
    under the terms of the GNU General Public License as published by the
    Free Software Foundation; either version 2 of the License, or (at your
    option) any later version.

    OpenFOAM is distributed in the hope that it will be useful, but WITHOUT
    ANY WARRANTY; without even the implied warranty of MERCHANTABILITY or
    FITNESS FOR A PARTICULAR PURPOSE.  See the GNU General Public License
    for more details.

    You should have received a copy of the GNU General Public License
    along with OpenFOAM; if not, write to the Free Software Foundation,
    Inc., 51 Franklin St, Fifth Floor, Boston, MA 02110-1301 USA

Application
    bodyForceIcoFoamBlMultFreqPlasma

Description
    Transient solver for incompressible, laminar flow of Newtonian fluids.

```

```
31  \*---------------------------------------------------------------------------*/
32
33  #include <iostream>
34  #include<fstream>
35  #include "fvCFD.H"
36
37  // * * * * * * * * * * * * * * * * * * * * * * * * * * * * * * * * * * * * * //
38
39  int main(int argc, char *argv[])
40  {
41      #include "setRootCase.H"
42      #include "createTime.H"
43      #include "createMesh.H"
44      #include "createFields.H"
45      #include "initContinuityErrs.H"
46
47      // one extra header files that are needed  mk
48      #include "createBodyForceGen.H"
49      // initialization
50
51      scalar currentTime=0;
52      scalar initialTime=0;
53      scalar currentPhase=0;
54      scalar currentGenPhase=0;
55      scalar aux_time1=0;
56      scalar aux_time2=0;
57      scalar period=0;
58      scalar sigPow=0;
59      scalar convFactorControl=0;
60      scalar firstRun=0;
```

```
61      scalar voltage=0;
62
63      #include "createBodyForcePlasmaInit.H"
64
65  // ***** initialize the controller
66
67      #include "controlInit.H"
68
69  // ***************************
70
71      Info<< "\nStarting time loop\n" << endl;
72
73      while (runTime.loop())
74      {
75          if (firstRun==0)
76          {
77          initialTime=runTime.timeOutputValue()-runTime.deltaTValue();
78          firstRun=1;
79          }
80
81          Info<< "Time=" << runTime.timeOutputValue() << nl << endl;
82
83          #include "readPISOControls.H"
84          #include "CourantNo.H"
85
86          currentTime=runTime.timeOutputValue();
87
88          // force generator
89
90          currentGenPhase=0;
```

```
91
92          for (int itm=0; itm<sizeModeWeights; itm++)
93          {
94          currentGenPhase+=modeWeights[itm]*\\
95                          Foam::sin(2*(mathematicalConstant::pi)*\\
96                          modeFreqs[itm]*currentTime);
97          }
98
99          //filtered-x LMS controller
100
101                 aux_time1 +=runTime.deltaTValue();
102                 aux_time2 +=runTime.deltaTValue();
103                 Info<< "controller sub-time = " << aux_time1  << nl << endl;
104
105                 if (aux_time1+0.5*runTime.deltaTValue()>samplingPeriod)
106                 {
107
108                 #include "sensor.H"
109
110                 if (currentTime<=systIdTime+initialTime)
111                 {
112                 Info<< "System ID" << nl << endl;
113                 #include "systemID.H"
114                 }
115                 else
116                 {
117                 Info<< "Control" << nl << endl;
118                 #include "controlLoop.H"
119                 }
120
```

```
121             Info<< "uSens = " << sSens << nl << endl;
122             Info<< "sigPow = " << sigPow << nl << endl;
123             Info<< "convFactor = " << convFactorControl << nl << endl;
124
125             aux_time1 = 0;
126
127             }
128
129         voltage=currentPhase/voltageRatio;
130
131         #include "createBodyForcePlasma.H"
132
133         fvVectorMatrix UEqn
134         (
135             fvm::ddt(U)
136           + fvm::div(phi, U)
137           + fvm::div(phi0, U)
138           + fvc::div(phi, U0)
139           - fvm::laplacian(nu, U)
140           - bodyForce/rho
141            -currentGenPhase*bodyForceGen/rho
142         );
143
144         solve(UEqn == -fvc::grad(p));
145
146
147         // --- PISO loop
148
149         for (int corr=0; corr<nCorr; corr++)
150         {
```

```
151             volScalarField rUA = 1.0/UEqn.A();
152
153             U = rUA*UEqn.H();
154             phi = (fvc::interpolate(U) & mesh.Sf())
155                 + fvc::ddtPhiCorr(rUA, U, phi);
156
157             adjustPhi(phi, U, p);
158
159             for (int nonOrth=0; nonOrth<=nNonOrthCorr; nonOrth++)
160             {
161                 fvScalarMatrix pEqn
162                 (
163                     fvm::laplacian(rUA, p) == fvc::div(phi)
164                 );
165
166                 pEqn.setReference(pRefCell, pRefValue);
167                 pEqn.solve();
168
169                 if (nonOrth == nNonOrthCorr)
170                 {
171                     phi -= pEqn.flux();
172                 }
173             }
174
175             #include "continuityErrs.H"
176
177             U -= rUA*fvc::grad(p);
178             U.correctBoundaryConditions();
179         }
180
```

```
181         runTime.write();
182
183         Info<< "ExecutionTime = " << runTime.elapsedCpuTime() << " s"
184             << "  ClockTime = " << runTime.elapsedClockTime() << " s"
185             << nl << endl;
186
187     }
188
189         #include "sensor.H"
190         if (iSens>=0)
191         {
192                 for (int i=0; i<Tabs; i++)
193                 {
194                 str66<< secPathWeights[i] << nl;
195                 str77<< firFilterWeights[i] <<nl;
196                 }
197         }
198     return 0;
199 }
200
201
202 // ************************************************************************* //
```

Appendix B

Plasma correlation model coefficients

For the plasma body force correlation model three sets of coefficients are needed. These are the Bernstein coefficients B_{ij} necessary for the construction of the force field shape as in Eq.9.8, the polynomial coefficients for the scaling factor and the stretch factor as in Eq.9.4. The Bernstein, scaling and stretch factor coefficients are given in Tables B.2 to B.1 respectively.

Table B.1: Coefficients for scaling and stretch factor polynomials

Scaling coef.	value	Stretch coef.	value	Transf. const.	value
a1	$-1.0909 \cdot 10^{-4}$	b1	$1.7385 \cdot 10^{-3}$	c	2
a2	0.4499	b2	0.2317		
a3	-2.9033	b3	4.8480		
a4	$-1.9698 \cdot 10^{-3}$				
a5	0.0841				
a6	-0.4459				

Table B.2: Bernstein coefficient values for the horizontal force field shape construction

$i \rightarrow$	0	1	2	3	4	5	6	7	8	9
$j \downarrow$										
0	-0.0102	0.0527	0.0263	0.0111	-0.0037	0.0020	0.0354	0.0698	0.0875	0.1581
1	0.0479	0.0780	0.0943	0.1155	0.1220	0.1016	0.0596	0.0057	-0.1088	-0.1077
2	0.0684	0.0599	0.0591	0.0799	0.0715	0.0150	-0.0434	-0.0953	-0.2529	-0.6628
3	-0.0131	-0.0690	-0.0676	-0.0219	0.0078	0.0068	0.1420	0.4612	0.7153	0.5286
4	-0.1441	-0.1993	-0.1730	-0.0553	0.0250	0.1130	0.4230	1.0457	1.6434	1.7642
5	-0.1223	-0.1762	-0.1298	0.0012	0.0827	0.1732	0.4667	1.0715	1.6125	1.5993
6	-0.0040	-0.0505	-0.0207	0.0588	0.0991	0.0961	0.2337	0.5874	0.8222	0.5082
7	0.0260	0.0322	0.0405	0.0798	0.0626	-0.0061	-0.0396	0.0494	0.0367	-0.2516
8	0.0273	0.0473	0.0552	0.0699	0.0565	0.0150	-0.0258	-0.0229	-0.0844	-0.0644
9	0.0066	0.0486	0.0143	0.0054	0.0157	0.0417	0.0854	0.1190	0.0576	0.0323

Table B.3: Bernstein coefficient values for the vertical force field shape construction

$i \rightarrow$	0	1	2	3	4	5	6	7	8	9
$j \downarrow$										
0	-0.2881	-0.3288	-0.0247	-0.4781	-0.2231	0.0046	-0.2340	-0.5660	-0.4940	-0.0328
1	-0.2655	-0.3964	0.2085	0.1155	-0.1817	1.0255	0.8081	2.3666	1.1584	0.2230
2	0.0919	-0.1423	-0.0547	0.6010	-0.3121	-1.4490	-1.2610	-2.3376	-0.4500	0.1190
3	-2.3961	-2.0719	-2.7894	-3.7133	-3.8805	-4.0091	-3.8187	-3.7912	-2.7701	-2.5376
4	-1.2585	-2.2614	-2.0879	-1.9870	-2.3873	-2.7095	-2.6232	-0.6599	2.4847	2.0080
5	1.5127	1.9342	2.0173	2.3242	2.9842	2.9839	3.3620	3.8403	3.8745	1.9955
6	1.3131	1.7604	1.8319	1.9061	2.1053	2.1581	2.2186	1.3952	-0.4822	-1.8155
7	0.1981	-0.2080	0.4460	0.5411	-0.1931	-0.0903	-0.0541	-1.3361	-3.0783	-0.5190
8	0.3402	1.0486	0.0392	0.3893	0.0192	0.6587	0.8062	1.7826	1.2166	1.0234
9	0.1980	0.1224	0.3248	0.1201	0.7225	-0.2746	-0.5221	0.7989	0.2824	-0.2644

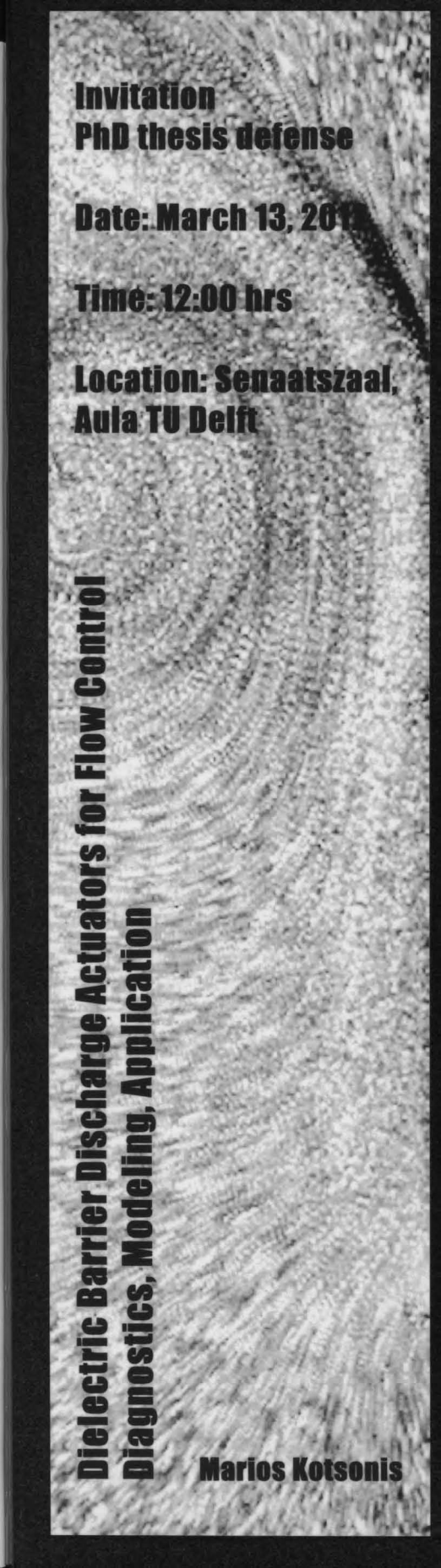
Invitation
PhD thesis defense
Date: March 13, 201
Time: 12:00 hrs
Location: Senaatszaal,
Aula TU Delft
Dielectric Barrier Discharge Actuators for Flow Control
Diagnostics, Modeling, Application
Marios Kotsonis

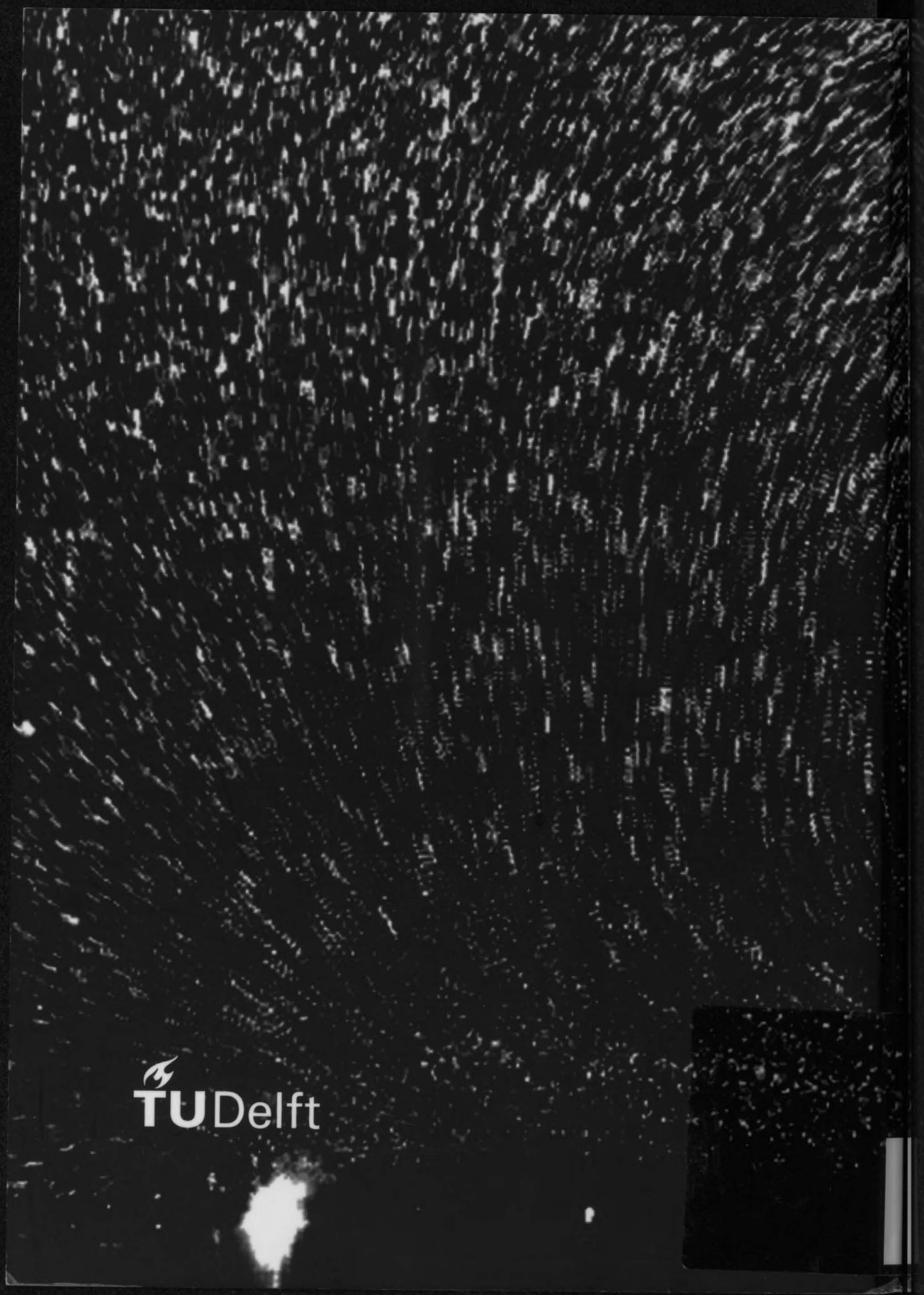
TUDelft